Modulation dynamics of InP-based quantum dot lasers and quantum cascade lasers

Cheng Wang

Thèse

THESE INSA Rennes
sous le sceau de l'Université européenne de Bretagne
pour obtenir le titre de
DOCTEUR DE L'INSA DE RENNES
Spécialité : Physique optoélectronique

présentée par
Cheng WANG
ECOLE DOCTORALE : *SDLM*
LABORATOIRE : *FOTON*

Modulation Dynamics of InP-Based Quantum Dot Lasers and Quantum Cascade Lasers

Thèse soutenue le 17.03.2015
devant le jury composé de :

Didier Erasme
Professeur, Télécom ParisTech / Président
Marc Sciamanna
Professeur, Supélec / Rapporteur
Guang-Hua Duan
Directeur de Recherche / HDR, III-V Lab / Rapporteur
Marek Osiński
Professor, University of New Mexico / Examinateur
Mariangela Gioannini
Associate Professor HDR, Politecnico di Torino / Examinateur
Kathy Lüdge
Associate Professor HDR, Technische Universität Berlin / Examinateur
Frédéric Grillot
Maitre de conférences / HDR, Télécom ParisTech / Co-Directeur de thèse
Jacky Even
Professeur, INSA de Rennes / Co-Directeur de thèse

Modulation Dynamics of InP-Based Quantum Dot Lasers and Quantum Cascade Lasers

Cheng Wang

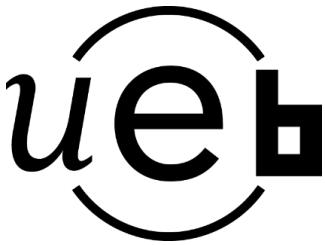

En partenariat avec

To my parents and Leming

Acknowledgements

Here I would like to express my sincere gratitude and appreciation to my supervisors, Dr. Frédéric Grillot and Professor Jacky Even, for their excellent guidance and support throughout my Ph.D. study. I have learned a lot from their profound knowledge, professional approach, and rigorous attitude towards scientific research. I thank them for supporting me on international mobilities and conferences, which helped me to catch the latest and hottest research topics and advances, as well as to build the social networks in the scientific society. The great experience with them will benefit a lot to my future career.

I would like to thank Dr. Kathy Lüdge and Professor Eckehard Schöll from Technische Universität Berlin, Berlin, Germany, as well as Dr. Mariangela Gioannini and Professor Ivo Montrosset from Politecnico di Torino, Torino, Italy for hosting me in their renowned groups. Their deep insights in optoelectronics impressed me a lot. I gained a lot from the collision of disparate ideas under their kind guidance on my research work.

I appreciate all our collaborators Professor Didier Erasme from Télécom ParisTech, France, Professor Alain Le Corre and Dr. Thomas Batte from INSA de Rennes, France, Professor Vassilios I. Kovanis from the Air Force Research Laboratory, USA, Professor Marek Osiński from University of New Mexico, Albuquerque, USA, Dr. Jean-Guy Provost and Dr. Guang-Hua Duan from III-V Lab, France, Dr. Philip Poole from the National Research Council, Canada, Prof. Marc Sciamanna from Supélec, France, Prof. Fan-Yi Lin from National Tsing Hua University, Taiwan, Prof. Sheng-Kwang Hwang from National Cheng Kung University, Taiwan, Dr. Nelson Sze-Chun Chan from City University of Hong Kong, Dr. Joshua D. Bodyfelt from Ohio State University, Columbus, USA, Dr. Paolo Bardella from Politecnico di Torino, Italy, Dr. Schires Kévin from Télécom Paristech, France, Dr. Christian Otto and Benjamin Lingnau from Technische Universität Berlin, Germany, Dr. Martin Virte from Vrije Universiteit Brussel, Belgium and Supélec, France, and Dr. Ivan Aldaya from Instituto Tecnológico y de Estudios Superiores de Monterrey, Mexico for helpful scientific discussions.

I would like to thank all the professors, all the colleagues and all my friends from GTO group, Télécom ParisTech, and from FOTON lab, INSA de Rennes, who leads me a colorful life in France.

I acknowledge the China Scholarship Council for funding my Ph.D. work.

Last but not least, I am highly grateful to my parents for their persistent support and encouragement. My special thank to Leming, for her help on the thesis manuscript and the defense slides, as well as her love, understanding and support.

Abstract

High performance semiconductor lasers are strongly demanded in the rapidly increasing optical communication networks. Low-dimensional nanostructure lasers are expected to be substitutes of their quantum well (Qwell) counterparts in the next-generation telecommunication optical links. Many efforts have been devoted during the past years to achieve nanostructure lasers with broad modulation bandwidth, low frequency chirp, and near-zero linewidth enhancement factor. Particularly, 1.55-μm InP-based quantum dash (Qdash)/ dot (Qdot) lasers are preferable for long-haul transmission in contrast to the 1.3-μm laser sources.

In the first part of this dissertation, we investigate the dynamic characteristics of InP-based quantum dot semiconductor lasers operating under direct current modulation, including the amplitude (AM) and frequency (FM) modulation responses, the linewidth enhancement factor (also known as α-factor), as well as large-signal modulation response. Through the rate equation analysis of the AM response in a semi-analytical approach, it is found that the modulation bandwidth of the quantum dot laser is strongly limited by the finite carrier capture and relaxation rates, and the latter is also responsible for the large damping factor.

In order to study the α-factor and chirp properties of the quantum dot laser, we develop an improved rate equation model, which takes into account the contribution of carrier populations in off-resonant states to the refractive index change. It is demonstrated that the α-factor of quantum dot lasers is strongly dependent on the pump current as well as the modulation frequency, in comparison to the case of Qwell lasers. We point out that the α-factor remains constant at low modulation frequencies (<0.1 GHz) and is consistent with that operating under DC condition. The values are higher than that at high modulation frequencies (beyond several GHz) obtained from the FM/AM technique. These features are mostly attributed to the carrier populations in off-resonant states. Further simulations show that the α-factor can be reduced by enlarging the energy separation between the resonant ground state (GS) and off-resonant states, or by enhancing the carrier scattering rates.

Instead of GS emission in quantum dot lasers, lasing from the excited state (ES) can be a promising alternative to enhance the laser's dynamic performance. Calculations show that the ES laser exhibits a broader modulation response associated with a much lower frequency chirping in comparison with the GS emission laser. In addition, the α-factor of the quantum dot laser can be reduced by as much as 40% in the ES lasing operation.

On the other hand, optical injection technique is attractive to improve the laser's dynamical performance, including bandwidth enhancement and chirp reduction. These are demonstrated

both theoretically and experimentally. The phase-amplitude coupling property is altered as well in comparison with the free-running laser. Another important feature of optical injection is that it tunes the optical gain depending on the injection strength and the frequency detuning. Using this feature, we propose an improved Hakki-Paoli method--- *Optical Injection-Hakki-Paoli* method--- which is capable of measuring the α-factor of semiconductor lasers both below and above threshold. On the other hand, we theoretically demonstrate that the α-factor in nanostructure lasers exhibits a threshold discontinuity, which restrains its reduction towards zero. This is mainly attributed to the unclamped carrier populations in the off-resonant states.

Quantum cascade (QC) lasers rely on intersubband electronic transitions in the conduction band of multi-quantum well heterostructures. They find applications in the mid- and far-infrared spectral regions, such as gas spectroscopy or free-space optical communication. Interestingly, QC lasers show flat and broadband AM response (tens of GHz) without resonance. Surprisingly, calculations show that the QC lasers exhibit an ultrabroad FM bandwidth on the order of tens of THz, which is three orders of magnitude larger than the AM bandwidth. Optically injection-locked QC lasers also exhibit specific characteristics by comparison to interband semiconductor lasers. Both positive and negative frequency detunings enhance the modulation bandwidth and raise a peak in the modulation response.

List of abbreviations

Abbreviation	Phrase
AFM	Atomic force microscopy
AM	Amplitude modulation
ASE	Amplified spontaneous emission
α-factor	Linewidth enhancement factor
BER	Bit error rate
BT	Bogdanor-Takens
CBE	Chemical beam epitaxy
CDP	Carrier density pulsation
CH	Carrier heating
CPR	Chirp-to-power ratio
CW	Continuous wave
DC	Direct current
DFB	Distributed feedback
DH	Double heterostructure
DM	Directly modulated
EA	Electro-absorption
EL	Electroluminescence
EO	Electro-optical
ES	Excited state
ESA	Electrical spectrum analyzer
FP	Fabry Perot
FM	Frequency modulation, chirp
FSO	Free-space optical
FSR	Free spectral range
FWHM	Full-width of half maximum
FWM	Four-wave mixing
GS	Ground state
GSG	Ground-signal-ground
IM	Intensity modulation
LIDAR	Light illumiated detection and ranging
LO	Longitudinal optical
MBE	Moleculor beam epitaxy
MIR	Mid infrared
MPRE	Multi-population rate equation
MOCVD	Metal-organic chemical vapor deposition
MZ	Mach-Zehnder
NCE	Normalized conversion efficiency
NDFWM	Non-degenerate four-wave mixing
NIR	Near infrared
NRZ	Non return zero
OIHP	Optical Injection-Hakki-Paoli
OSA	Optical spectrum analyzer
PC	Polarization controller
PL	Photoluminescence
PMF	Polarization maintaining fiber
PRBS	Pseudo-random binary sequence
QC	Quantum cascade
Qdash	Quantum dash
Qdot	Quantum dot
Qwell	Quantum well
Qwire	Quantum wire
RIE	Reactive ion etching
RS	2D carrier reservoir/ wetting layer
SCH	3D separate confinement heterostructure, barrier
SHB	Spectral hole burning

List of abbreviations (continued)

SL	Superlattice
SMSR	Side mode suppression ratio
SN	Saddle-node
SOA	Semiconductor optical amplifier
TEC	Thermo-electric cooler
TRPL	Time-resolved photoluminescence
ZH	Zero Hopft
VNA	Vector network analyzer

The thesis is organized in two parts. Part I consists of Chapters 1-5, and investigates nanostructure semiconductor lasers. Part II including Chapters 6-8 is devoted to quantum cascade lasers. Chapter 9 presents the summary of the thesis and discusses the outlook.

Table of Contents

Part I. Quantum Dot (Qdot) Laser

Chapter 1. Introduction to Qdot lasers

1.1. Development of InP-based Qdot lasers

Semiconductor lasers play a crucial role in optical datacom and telecom applications. Nowadays, high-definition television, video-on-demand, broadband internet and mobile phones are available all around the globe. The exponential rise in cost-effective information transmission would not have been possible without the introduction of optical transmission sytems, which in turn are enabled by semiconductor lasers. A hundred million new semiconductor lasers are deployed in communication systems every year, generating several billion dollars of annual revenue at the component level [Murphy10]. Higher performance semiconductor laser sources are strongly demanded due to the increasing data traffic in the Wide Area Networks (WANs), Metropolitan Area Networks (MANs), and Local Area Networks (LANs), which drives the development of the novel semiconductor laser technologies. In addition, silicon based semiconductor laser devices and integrated circuits have undergone rapid and significant processes during the last decade, transiting from laboratory research topics to product development in corporations. Silicon photonics is anticipated to be disruptive optical technologies for data communication, with applications such as intra-chip or inter-chip interconnects, and short range communications in datacenters and supercomputers [Richman14]. It also finds applications in telecommunications on metro coherent and long-haul optical transmissions [Dong14], [Duan14].

Figure 1.1 shows the history of active layer structure with evolutions. Since the first demonstration of semiconductor laser in 1962, significant development took place from bulk-structure lasers, through Qwell lasers to the advanced nanostructure quantum wire (Qwire), Qdash and Qdot lasers. In 1960s, the 3D bulk laser was developed based on semiconductor heterostructures, which provide efficient confinement of charged carriers in the active region [Kroemer57]. In particular, the double heterostructure (DH), which also yields optical confinement, transformed semiconductor lasers from laboratory research into industrial applications [Alferov63]. The quantum confinement occurs when one or more spatial dimensions of a nanocrystal approach the de Broglie wavelength of the carrier (on the order of 10 nm). The confinement of carriers leads to the quantization of the density of states, and splits the energy band of bulk semiconductors into energetic subbands [Dingle76]. In 1970s, the first Qwell laser (2D system), in which carriers are confined in one dimension, was demonstrated [van der Ziel75]. The recognized advantages over DH lasers were the reduced threshold current

by decreasing the thickness of the active layer as well as the tunability of the wavelength via changing the Qwell thickness.

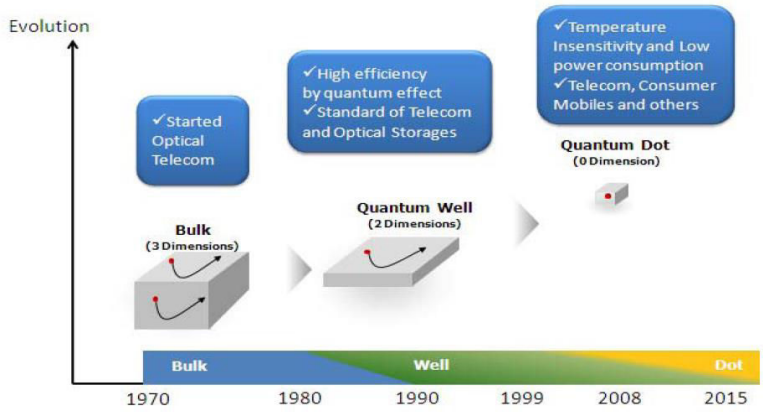

Fig. 1.1. The history of evolutions and structure of active layers in lasers, after [QD Laser, Inc., 08]

Further decrease of the degrees of freedom leads to low-dimensional nanostructures such as Qwire (1D) and Qdash or Qdot structures (0D). Ideally, 0D systems exhibit atom-like density of states hence resulting with an ultimate carrier confinement. The concept of Qdot semiconductor laser was originally proposed by Arakawa and Sakaki in 1982 [Arakawa82], predicting temperature independence of the threshold current. Henceforth, reduction in threshold current density, high spectral purity, enhancement of differential gain and chirp-free properties were theoretically discussed in 1980s [Asada86]. The most straightforward technique to produce array of Qdots is to fabricate suitably sized mesa-etched quantum wells grown by metal-organic chemical vapor deposition (MOCVD) or by molecular beam epitaxy (MBE). However, the nonradiative defects produced during the etching procedure lead to a degradation of the material quality, which results in unsuitable structures for lasers. In the 1990's, both selective growth and self-assembled growth technique, which can avoid nonradiative defects were well developed. Particularly, the Stranski-Krastanow growth mode was very successful for InGaAs/GaAs systems [Bimberg98], [Arakawa01]. The strain-induced self-organization of InGaAs/GaAs Qdot lasers [Kirstaedter94], [Bimberg96], [Huffaker98] yielded threshold current densities as low as ~60 A/cm^2 at room temperature [Ledentsov96]. Extensive work on the GaAs based Qdot system has been carried out and the laser performance has been improved a lot since then [Crowley12]. A low threshold density of 17 A/cm^2 [Liu04] and a high output power of 7 W (broad area) have been achieved in InAs/GaAs lasers [Maksimov04]. Nowadays, the InAs/GaAs Qdot products already become commercialized in the market [Bimberg98], [Zhukov12]. Meanwhile, several self-assembled growth techniques, such as solid-state MBE [Joyce02], gas source MBE [Chang03], metalorganic vapor phase epitaxy (MOVPE)

[Oshinowo94], and chemical-beam epitaxy (CBE) [Poole09], have been improved and successfully used to grow the Qdot materials.

However, the GaAs-based Qdot laser devices emit usually in the O band (1260-1360 nm) of the telecommunication windows and can hardly reach the desirable long haul communication window around 1.55 µm. Instead, InAs active region grown on InP substrates allows the realization of laser devices emitting in the C band window (1530-1565 nm) because of the smaller lattice mismatch. In the current market, InP-based 1.55 µm Qwell laser devices have shown substantial improvement in the optical characteristics in comparison with their DH counterparts. In order to improve upon the Qwell laser performance, InAs Qdots grown on InP substrates attract a lot of attention in the research field. However, the formation of nanostructures on InP is much more challenging than on the GaAs substrate [Bertru10]. Although the InAs/InP and the InAs/GaAs systems have the same material in the Qdots, they differ in three aspects: (a) The lattice mismatch for InAs/InP (3%) is smaller than that for InAs/GaAs (7%); (b) InAs/InP Qdots exhibit less confinement potential for electrons, but a stronger confinement for holes; (c) The InAs/InP material shares the same cation (In), while the InAs/GaAs shares the same anion (As) on the interface [Gong08]. The small lattice mismatch and the complex strain distribution can result in the formation of a new class of self-assembled Qdash nanostructures instead of Qdots. These are elongated dot-like structures exhibiting interesting mixed characteristics in between the Qwell and the Qdot [Wang01]. Strongly anisotropic Qdash nanostructures are even closer to the electronic properties of Qwire [Miska04]. Therefore, realization of true InAs/InP Qdots does require specific epitaxial growth procedures. This can be done by employing conventional or miscut (100) InP substrates, as well as a misoriented (311) InP substrate along with various innovations in the growth process [Khan14]. Nevertheless, reduction of the dot size and suppression of the size dispersion due to the self-assembled growth procedure still pose challenges in achieving high quality epitaxial material and hence better device performance. Currently, the size dispersion, characterized by the full width at half maximum (FWHM) of the photoluminescence (PL) linewidth, is ~20 meV at 10 K for Qdots, and ~50 meV at room temperature for Qdashes [Reithmaier07], [Zhou08], [Zhou09], [Sichkovskyi13] and Qdots [Paranthëon01]. Further improvements of the material quality are still required to be competitive with the matured InAs/GaAs Qdot systems. InAs dots formed on the (100) InP substrate usually have a lower dot density on the order of 10^9~10^{10}/cm^2 [Kotani09]. These laser structures usually require multiple stacked layers for sufficient material gain. In contrast, dots grown on the high index (311)B substrate can lead to a higher Qdots density, commonly in the 5×10^{10}~10^{11}/cm^2 range [Homeyer07], [Cornet06].

Figure 1.2 shows atomic force microscopy (AFM) images of InAs/InP Qdashes (left), Qdots (middle) on (100) substrate and Qdots (right) on (311)B substrates. Carlin *et al.* were the first to report the Qdot formation in the ultra-thin InAs/InP Qwells grown by CBE [Carlin91]. The first InAs/InP Qdot laser emitting at ~1.9 µm at 77 K was reported by Ustinov *et al.* in 1998 [Ustinov98], [Ustinov98a]. Room temperature operation was then realized by Nishi *et al.* [Nishi98]. In the following, we review the development of the InAs/InP Qdot lasers on both (311)B and (100) InP substrates employing the InAs/InGaAsP or InAs/InGaAlAs active material regions.

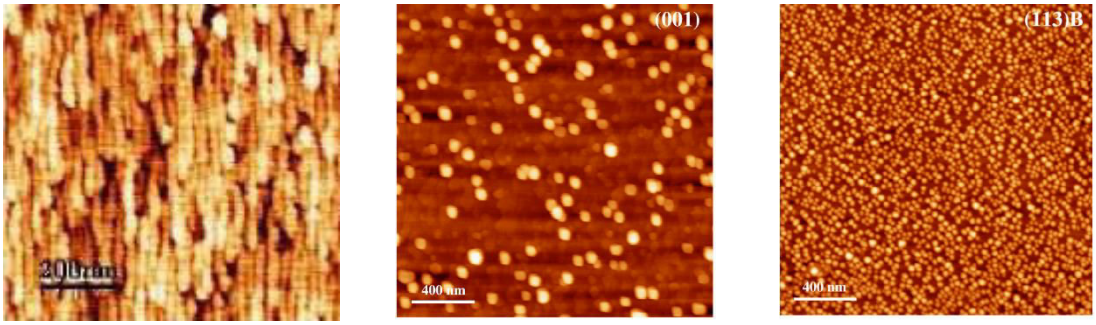

Fig. 1.2. AFM image of InAs Qdashes (left), Qdots (middle) formed on (100) InP substrate, and Qdots (right) on (311)B InP substrate, after [Alghoraibi06].

1.1.1. Lasers on (311)B InP substrate

High indexed (311)B InP substrates can offer a high density of nucleation points for the Qdot islands, which strongly reduces surface migration effects and leads to the formation of more symmetric Qdots in the planar direction. As a reslut, high density and uniform distribution of Qdots can be obtained. In order to reach higher density of Qdots, various studies have been carried out on the InP(311)B substrate and a relatively high density of 5-13×10^{10} cm^{-2} has been obtained [Nishi98], [Li00], [Miska03], [Alghoraibi06]. The inhomogeneous linewidth broadening can be constrained within 50 meV by using the double capping layer technique [Paranthoen01], [Paranthoen03]. The typical size of dots is about 30-50 nm in base diameter and about 3 nm in height [Li13].

Using the InAs/InGaAsP active region, Nishi *et al.* demonstrated a Qdot laser with 7 stack layers grown by MBE [Nishi98]. The laser device emitting at 1.4 µm at room temperature had a dot density of 2×10^{10} cm^{-2} and a threshold current density of 4.8 kA/cm^2. By using a double capping technique, Caroff *et al.* achieved a dot density of 1.1×10^{11} cm^{-2} with a lasing emission close to 1.55 µm at room temperature [Caroff05]. The laser had a high modal gain of 7 cm^{-1} per dot layer while the threshold and transparency current densities were 190A/cm^2 (63 A/cm^2 per layer) and 68A/cm^2 (23 A/cm^2 per layer), respectively. These results still represent the best

threshold performance reported for the InP(311B) material system. Homeyer *et al.* reported a broad area laser emitting at 1.54 µm at room temperature with a high internal quantum efficiency of 62% [Homeyer07a]. The laser consisting of only two Qdot stack layers had a modal gain of 8 cm^{-1} per layer and a dot density as high as ~1.0×10^{11} cm^{-2}. A single active layer laser device with a gain of 13 cm^{-1} was further demonstrated in 2007, but lasing was observed only up to 295 K [Homeyer07]. Recently, a Qdot laser including 9 stack layers was reported with internal loss as low as 6 cm^{-1} and a total modal gain of 25 cm^{-1} [Klaime13]. However, the InAs/InGaAsP material system usually has a poor temperature stability, with a characteristic temperature T_0 of only 25-50 K at room temperature due to the low conduction band offset [Caroff05], [Khan14]. It is reminded that the laser threshold I_{th} increases exponentionally with temperature (T in Kelvin) as $I_{th} = I_{th0}\exp(T/T_0)$. T_0 (typically 60 to 150 K) is a measure of the temperature sensitivity of laser devices. Higher values of T_0 imply that the threshold current density and the external differential quantum efficiency of the device increase less rapidly with increasing temperatures.

Employing the InAs/InGaAlAs active region, Saito *et al.* first demonstrated a Qdot laser at a wavelength of 1.63 µm with a threshold current density of 660 A/cm^2 (132 A/cm^2 per layer) [Saito01]. The extracted internal loss was 3.6 cm^{-1}, which is the lowest value ever reported for the InAs/InP system. Nine years later, by exploiting the Al atoms in the spacer layers and employing the strain compensation technique, Akahane *et al.* demonstrated a 30 stack-layer laser with a threshold current density of 2.7 kA/cm^2 (90 A/cm^2 per layer) [Akahane10]. Subsequently, by improving the material growth quality, the threshold current density of a 30 stacked laser was reduced down to 1.72 kA/cm^2 (57.4 A/cm^2 per layer) with an extremely high temperature stability. The characteristic temperature T_0 was 114 K for temperature operation in the range of 20-75℃ and was further improved to 148 K (for 25-80℃) with a 20-stack layer laser [Akahane12]. However, due to the imperfect coupling of the optical mode with the multi-stack gain medium, the laser exhibited a high internal loss value of ~ 26 cm^{-1}.

1.1.2. Lasers on (100) InP substrate

The formation of self-assembled Qdots on the (100)InP substrate is more complicated [Elias09]. The formation of the dots or dashes strongly depends on the growth conditions and the thickness of InAs layers. One of the major problems encountered on the road to obtain lasers with good performance is the low Qdot density provided by this kind of substrate.

In the InAs/InGaAsP material system, the growth of dots is mostly based on CBE or MOCVD techniques. Allen *et al.* reported a CBE-grown Qdot laser, which was operated in a

pulsed mode at room temperature [Allen05]. Employing the dot height trimming procedure with growth interruptions, the pulsed threshold current density was 3.56 kA/cm^2 (713 A/cm^2 per layer). Then, by using a higher-energy barrier, the dot density was increased to 3-6×10^{10} cm^{-2}. On the other hand, Lelarge *et al.* used a hybrid growth technique with MBE grown active region in conjunction with MOCVD-grown p-doped cladding and contact layers [Lelarge05]. The CW threshold current density was 1.4 kA/cm^2 (240 A/cm^2 per layer) and T_0 was 56 K at room temperature. Particularly, the laser showed a very high modal gain of 64 cm^{-1} (10.7 cm^{-1} per layer). The laser grown by MOCVD exhibited a reduced threshold current density of 615 A/cm^2 (123 A/cm^2 per layer) [Anantathanasarn06]. The transparency current density was also as low as 30 A/cm^2 with internal loss of only 4.2 cm^{-1}.

In the InAs/InGaAlAs material system, Kim *et al.* first demonstrated a Qdot laser using an assisted growth technique of a thin Gas underlying layer before the growth of InAs dots in InGaAlAs matrix [Kim04], [Kim04a]. The achieved dot density was 6.0×10^{10} cm^{-2}, and the laser exhibited a threshold current density of 2.8 kA/cm^2 (400 A/cm^2 per layer). Measured T_0 was 377 K fro temperatures up to 200 K, and 138 K above 200 K. More recently, Gilfert *et al.* reported a high gain Qdot laser using MBE method [Gilfert11]. A low internal loss coefficient of 4 cm^{-1} combined with a high modal gain of 15 cm^{-1} per layer was reported. The lasing threshold current density was 1.95 kA/cm^2 (325 A/cm^2 per layer).

Very recently, Mollet *et al.* reported a very high modal gain of 97 cm^{-1} of an InAs/InP(100) Qdash laser. However, the internal loss coefficient was also as high as 23 cm^{-1} [Mollet14]. Generally, the performance of the InAs/InP lasers has been improved significantly since its first demonstration. However, it still needs further development in order to be comparable with that of InAs/GaAs laser devices.

1.2. Dynamic performance of InP-based Qdot laser

In the fiber optic links, the laser transmitter may either be directly modulated, known as directly modulated (DM) laser, or externally modulated using a modulator. Fig. 1.3 shows an illustration of the direct and external modulations. In the DM scheme (top), the driving current carries the transmitted data and is directly applied to the laser. In the external modulation scheme (bottom), the laser subjected to a constant bias current emits a continuous wave (CW) while an external modulator switches the optical power on or off according to the data stream.

In the external modulation scheme, electro-optical (EO) or electro-absorption (EA) modulators are commonly used [Peucheret09], [Ngo12]. The EO modulators, such as Mach-Zehnder modulators, utilize a signal-controlled crystalline material exhibiting the electro-

optical effect (Pockels effect) to modulate the CW laser light. The electro-optic effect is the change in the refractive index of the material resulting from the application of a DC or low-frequency electric field. The EA modulator controls the intensity of a laser beam via an electric voltage. Its operation can be based on the Franz–Keldysh effect [Seraphin65], i.e., a change in the absorption spectrum caused by an applied electric field, which changes the bandgap energy but usually does not involve the excitation of carriers by the electric field. However, most EA modulators are made in the form of a waveguide with electrodes for applying an electric field in a direction perpendicular to the modulated light beam. For achieving a high extinction ratio, one usually exploits the quantum-confined Stark effect, which describes the effect of an external electric field upon the light absorption spectrum or emission spectrum of a quantum well structure. Both EO and EA modulators are operated on voltages of a few volts (below 10 V). In comparison with EO modulators, a convenient feature of EA modulators is that it can be integrated with the laser on a single chip to create a data transmitter in the form of a photonic integrated circuit [Kechaou12], [Erasme14].

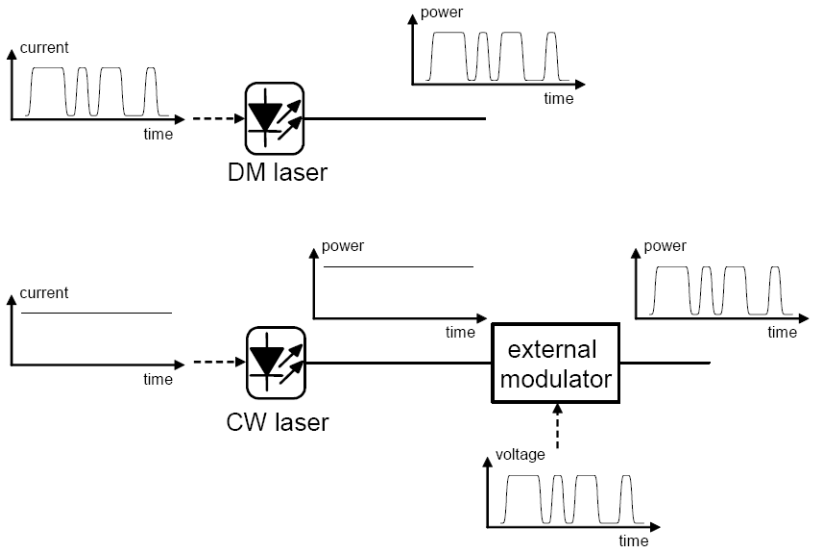

Fig. 1.3. Direct (top) and external (bottom) modulation schemes of the laser transmitter.

In contrast, DM lasers are the most common, particularly for short reach systems. DM lasers do constitute a low cost solution and offer least energy consumption, whereas they usually suffer from poor frequency chirp characteristics [Tucker11]. DM lasers generally produce more chirp for higher extinction ratios, leading to an optimum setting for trading off signal to noise ratio and chirp penalty. In addition, the DM scheme is helpful to understand peculiar physical characteristics of semiconductor lasers. Aiming to realize chirp-free DM lasers, many efforts have been devoted to the development of nanostructure semiconductor lasers. Table 1.1 summarizes the reported dynamical performance of InP-based Qdot and Qdash lasers in

literature, including the 3-dB modulation bandwidth and the α-factor, which is linked with the frequency chirp under direct modulation.

Table 1.1. Dynamic characteristics of Qdot or Qdash lasers grown on InP substrate

Reference	material	Bandwidth	α-factor, <=I_{th}	α-factor, >I_{th}	Differential gain, Gain compression factor
Martinez08	Qdot, (311)B InP	4.8 GHz	~1.8	~6	7.3×10^{-15} cm^2 6.4×10^{-16} cm^3
Gready12	Qdot, (100) InP	5 GHz 15 Gbps			
Gready14	Qdot, (100) InP	9 GHz 22 Gbps			
Bhowmick14	Qdot, (100) InP p-doped & tunnel injection	14.4 GHz	~0		0.8×10^{-15} cm^2 5.4×10^{-17} cm^3
Kaiser05	Qdash, (100) InP	7.6 GHz			
Mi06	Qdash, (100) InP	6 GHz @undoped 8 GHz @p-doped 12 GHz @p-doped & tunnel injection	~1 @p-doped ~0 @p-doped & tunnel injection		
Hein07	Qdash, (100) InP p-doping	8 GHz			
Lelarge07	Qdash, (100) InP	9.6 GHz 10 Gbps		5-7	
Zou10	Qdash, (100) InP p-doped	10 GHz			1.1×10^{-15} cm^2
Chimot13	Qdash, (100) InP	10 GHz 20 Gbps			
Joshi14	Qdash, (100) InP p-doped	10 Gbps		2.2	
Mollet14	Qdash, (100) InP	~10 GHz		~5 @undoped ~2.7 @p-doped	$1\text{-}2\times10^{-15}$ cm^2

Martinez *et al.* reported a Qdot laser grown on the (311)B InP substrate with a modulation bandwidth of 4.8 GHz. The above-threshold α-factor was about 6 and did not change significantly with the bias current [Martinez08]. However, most reported dynamics of 1.55 µm lasers are for nanostructures grown on (100) InP substrate. Gready *et al.* demonstrated an InAs/InGaAlAs/InP Qdot laser with a 3-dB bandwidth of 5 GHz [Gready12]. Interestingly, the laser showed a much higher large signal modulation capability: 15 Gbps with a 4-dB extinction ratio. The discrepancy between the small and large signal performances was attributed to the large nonlinear gain compression effect [Gready13]. Through the optimization of the barrier width and the number of stack layers, the performance of the structure was improved--- the small-signal modulation bandwidth was increased to 9 GHz and the large signal modulation was operated up to 22 Gbps with an extinction ratio of 3 dB [Gready14]. The best performance of InAs/InP Qdot laser was achieved by Bhowmick *et al.* recently [Bhowmick14]. The laser material system was InAs/InGaAlAs and the active zone was grown on (100) InP substrate. Tunnel injection and p-doping techniques enhanced the modulation bandwidth up to 14.4 GHz, and a near-zero α-factor was reported in this structure. For Qdash lasers realized on (100) InP substrate, most work employed the p-doping technique to improve the modulation bandwidth and to reduce the α-factor [Mi06], [Mollet14], [Joshi14], [Joshi14a]. Mi *et al.* showed that the modulation bandwidth was increased from 6 GHz for the undoped laser to 8 GHz with p-doping laser [Mi06]. Mollet *et al.* demonstrated that the α-factor was reduced from 5 down to 2.7 by p-doping [Mollet14]. On the other hand, the tunnel injection technique further increased the modulation bandwidth more than 10 GHz, and reduced the α-factor towards zero [Mi06], [Bhowmick14]. Consequently, a low chirp of 60 pm at a modulation frequency of 8 GHz was achieved in the Qdash laser, and the same chirp level at 10 GHz in a Qdot one.

1.3. Motivation and overview

As mentioned previously, in order to face the traffic increase, one timely innovating solution relies on the development of low cost and small foot print optical components while simultaneously enhancing their high-speed performances and reducing their thermal sensitivity and power consumption [Cisco10]. Since future optical networks are about to operate at 40 Gbps and 100 Gbps, development of "greener and faster optical components" incorporating Qdot material is also highly expected. In order to cope with these societal challenges, DM lasers do still provide a unique low cost and ultra-compact solution. Direct modulation makes however the output light strongly dependent on the lasers' nonlinear characteristics. An external modulator could certainly overcome these problems providing a larger bandwidth with higher

linearity and lower chirp but external modulation still does suffer from a high cost and power consumption.

Based on the review of literatures, Qdot lasers are demonstrated to have the following advantages in comparison with their Qwell counterparts:

- Low threshold current density [Liu99]
- High temperature stability [Mikhrin05]
- High material gain [Maximov04]
- High differential gain in the range of 10^{-15}~10^{-13} cm^2, which is one or two orders of magnitude lager than that of Qwell lasers [Bhattacharyya99], [Bhattacharya00]
- Potential for reduced α-factor [Saito00]

On the other hand, Qdot lasers are also found to have the following characteristics, which can be drawbacks limiting the lasers' dynamical performances:

- Large inhomogenous broadening (30~80 meV) of the optical spectra due to the fluctuation of the dot size [Bhattacharya00]
- High gain compression on the order of 10^{-16}~10^{-14} cm^3, which is also one or two orders of magnitude larger than that of Qwell lasers [Zhukov13]

These unique features can significantly alter the static and dynamic characteristics of Qdot lasers. For instance, not as expected from the theoretical prediction of the 'ideal' Qdot lasers, the modulation bandwidth is not necessarily that high and shown to be less than 10 GHz [Bhattacharya00a], [Fathpour05]. This limitation is inherently limited by several factors such as phonon bottleneck associated with relatively slow carrier relaxation rates, the inhomogeneous gain broadening and hot carrier effects. As such, the modulation performance of standard Qdot lasers made without any artificial solutions such as tunnel-injection or p-doping does remain lower than the best values reported on Qwell lasers. In addition to that, Qdot lasers have also been touted to exhibit an increased dynamic gain as well as a reduced α-factor, which in theory should make them superior for implementation in ultra-fast and chirp-free transmitter modules. The reported α-factor varies in a wide range from near-zero value [Newell99] up to more than 10 [Dagens05], which indicates the frequency chirping of modulated Qdot lasers is not necessarily low.

Nowadays, it is known that achieving a simultaneous high 3-dB modulation bandwidth and chirp-free operation in conventional DM lasers, if theoretically proven to be possible, is practically very challenging. Besides, the inherent benefit of having small value of the α-factor is not maintained at high current densities where the large bandwidths are potentially accessible.

Thus, it is of prime significance to properly to understand the underlying physical mechanism of QD laser that can be leveraged to our benefits for enhancing their dynamical performance. As far as direct modulation is concerned, chirp-free operation is crucial to overcome the chromatic dispersion arising in standard single mode fibers. The frequency chirp property being directly connected with the α-factor, it is therefore still of great significance to engineer novel and reliable high-speed Qdot laser sources with much broader bandwidth, highly reduced α-factor and ultra-low frequency chirp.

Meanwhile, in order to further improve the Qdot laser's dynamic performance, one possible approach is to introduce external control such as optical feedback or optical injection. Residual optical feedback to the semiconductor laser in optical fiber links is detrimental. Even a weak back-reflection from the optical fiber pigtail or optical connectors could degrade the laser's modulation characteristics and increase the intensity noise [Grillot10]. Usually expensive optical isolators are required to guarantee the stable operation. On the other hand, with proper control on the feedback strength, phase and time delay, the semiconductor laser subject to optical feedback exhibits numerous nonlinear dynamics from stable regime, over periodic oscillation or pulsation to chaotic behaviors [Lüdge11]. Optical injection technique can also produce rich nonlinear dynamics. In particular, the period one oscillation has been demonstrated to be a promising microwave signal sources [Hwang04] for radio-over-fiber applications [Chan07]. In the stable injection-locked regime, optical injection is very robust to enhance the modulation bandwidth [Simpson97], to reduce the frequency chirp [Lau09], to suppress the relative intensity noise [Simpson95] as well as the nonlinear distortion [Seo02].

Based on the above introduction and motivations, this thesis investigates the dynamics of nanostructure InP-based semiconductor lasers using both theoretical and experimental approaches. Part I of the thesis is organized as follows:

Chapter 2 presents fundamental properties of Qdot structures and lasers, including the electronic structure, carrier scattering processes, gain and refractive index, as well as the homogeneous and inhomogeneous broadenings. These fundamentals are required to understand the physics and the semi-empirical modeling proposed in the following chapters.

Chapter 3 deals with the modulation dynamics of the free running Qdot laser, where three different rate equation models are introduced. Model-I was already introduced in 2007 [Veselinov07], and is re-used in section 3.1 for the study of the amplitude modulation response of free-running lasers. However, this model is not capable of studying the linewidth enhancement factor. As such, in sections 3.2-3.6, we develop an improved rate equation model Model-II in collaboration with Technische Universität Berlin, Germany. This novel model takes

into account the phase change of the electric field due to the carrier injection, and allows investigating the linewidth enhancement factor and hence the frequency chirping characteristics of Qdot lasers. The above two models can be implemented in a semi-analytical approach for the analysis of the Qdot laser dynamics owing to its simplicity. Sections 3.7-3.8 introduce a multiple population rate equation (MPRE) model Model-III developed in collaboration with Politecnico di Torino, Italy [Gioannini07]. This model includes the homogeneous and inhomogeneous broadening effects, and is used to study the large-signal modulation properties of the laser.

Chapter 4 discusses the effects of optical injection locking on the modulation dynamics. We show the improvement of the modulation bandwidth, large-signal modulation capability and reduction of frequency chirp in the stable locking regime. The properties of linewidth enhancement factor under optical injection are discussed as well. In this chapter, section 4.2 employs Model-I to analyze the injection-locking diagram. Sections 4.3-4.5 use Model-II for the small-signal analysis and section 4.6 utilize Model-III for the large-signal analysis.

Chapter 5 experimentally characterizes the dynamic properties of nanostructure semiconductor lasers. Particularly, we propose in section 5.2 an improved Hakki-Paoli method using optical injection, named as *Optical Injection-Hakki-Paoli* method, which is capable of measuring the α-factor of the lasers operating above threshold.

Chapter 2. Fundamentals of Qdot laser

In the semi-classical quantum theory, the laser field is treated classically with the Maxwell's equations, and the gain medium is described quantum mechanically by the optical Bloch equations or semiconductor Bloch equations. In semiconductor (Class B) lasers based on interband transitions, the polarization dephasing occurs much faster than changes in carrier population and light intensity, which allows adiabatic elimination of the polarization dynamics and results in a simplified rate equation description [Chow13], [Arecchi84].

In order to properly model the static and dynamic characteristics of Qdot lasers, basic and crucial features of Qdot laser have to be taken into account. On one hand, these features can be microscopically described, which is usually complex but helpful for understanding the physics. On the other hand, for device engineering applications, these models can be simplified by introducing some phenomenological concepts and empirical parameters. This section deals with the fundamental features of the Qdot laser and describes the state-of-the-art of the Qdot laser modeling.

2.1. Qdot electronic structure and carrier scattering processes

Schematically, the active region of a Qdot laser often consists of a 3D separate confinement heterostructure (SCH, also known as barrier), a 2D carrier reservoir (RS, roughly corresponding to the wetting layer) and dots spatially confined in three dimensions. The electronic band structure calculation of semiconductor lasers can be performed using multiband **k·p** theory [Cornet06], [Even08]. Figure 2.1 shows an illustration of the electronic structure in a Qdot laser. Carriers in the barrier and the wetting layer can be treated as quasi-free particles. Thus, quasi-continuum electronic states are formed in the SCH and the RS. The densities of states for the SCH (per volume) and that for the RS (per area) are respectively given by [Gioannini07]:

$$\rho_{SCH} = 2\left(2\frac{m^*_{SCH}}{\hbar^2}\pi k_B T\right)^{3/2} \tag{2.1}$$

$$\rho_{RS} = \frac{m^*_{RS}}{\pi\hbar^2} k_B T \tag{2.2}$$

with m^* being the effective mass of either electrons or holes. The quasi-continuum carrier reservoir coupling with the localized energy states of the dots results in smaller energy separations and thus states overlapping at higher energies [Cornet05]. The discrete states lying

at lower energies are separated by a few tens of meV in the conduction band (CB), while smaller in the valence band (VB) due to heavier effective hole masses.

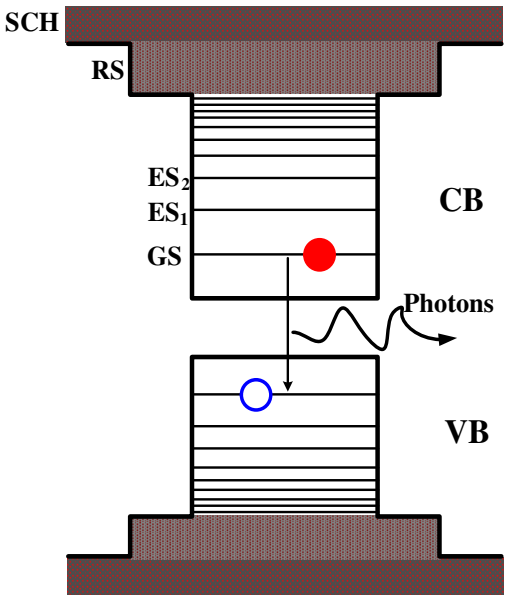

Fig. 2.1. Schematic of a Qdot laser electronic band structure of electrons and holes.

Due to the Coulomb interaction, electrons and holes in the semiconductor can be bounded into electron-hole pairs, known as excitons. The distance between the electron and the hole within an exciton is called Bohr radius of the exciton. Typical exciton Bohr radius of semiconductors is of a few nanometers [Nozik08]. The exciton nature can be modified by the confinement structure and thus exhibits different optical properties. Within the framework of a simplified excitonic picture, the electronic structure of Qdot laser is illustrated in Fig. 2.2. The exciton approximation can significantly simplify the semi-empirical modeling of Qdot lasers because it reduces half of the rate equations regarding the carrier populations. This approximation enables direct input from experimental data and can give intuitive images of physical processes. The assumption holds as long as electron and hole populations do not exhibit significant deviations. In some cases, it is necessary to utilize more sophisticated approaches [Lüdge09], [Gioannini11].

In a Qdot device, once the current injection generates charge carriers in the SCH layer, the carriers will transport across the 3D barrier and reach the 2D RS, which acts as a carrier reservoir for the localized Qdot states. The carrier capture process refers to the subsequent carrier capture from the RS to the ESs of dots. In the dots, carriers relax from high energetic ESs down to the GS level. Finally, radiative recombination of electrons-holes and lasing occurs ofen on the GS. In addition, carrier capture directly from the RS into the GS is possible as well (not shown in Fig. 2.1 or Fig. 2.2) [Wu14]. This direct channel accelerates the carrier indirect

process (via ES) to the lasing GS, and plays an important role on the dual (GS and ES) lasing process as already pointed out in InAs/InP Qdot lasers [Veselinov07]. Moreover, those electronic states also exhibit inter-dot electronic coupling [Cornet05].

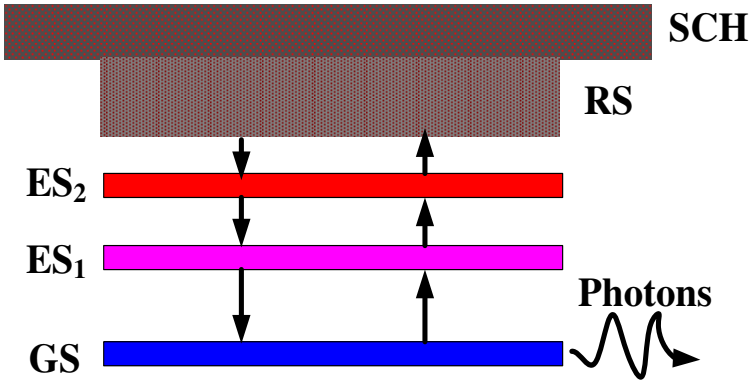

Fig. 2.2. Exciton picture of Qdot laser's electronic structure.

As in Qwell lasers, the carrier transport process plays an important role in determining the Qdot laser's dynamics as well, which induces a parasitic-like roll-off that is indistinguishable from an RC roll-off in the modulation response, and thus limits the modulation bandwidth. [Nagarajan92], [Coldren95]. Time-resolved photoluminescence (TRPL) shows that the carrier transport time across barrier to the RS is several picoseconds (1~5 ps) depending on the thickness of the SCH layer [Siegert05], [Marcinkevicius99].

The carrier capture and relaxation transition processes are supported mainly by two physical mechanisms: Coulomb interaction induced carrier-carrier scattering (Auger process), and carrier-LO phonon scattering. The scattering behavior is different at low and high excitation carrier densities. At low excitation density, the carrier interaction with LO phonons can provide efficient scattering channels provided that energy conservation is fulfilled. While the energy separation of Qdot states typically does not match the LO phonon energy, this scattering mechanism is often possible for holes due to their dense states [Nielsen04]. When high-density carrier plasma is created in the carrier reservoir, carrier-carrier scattering accounts for the efficient capture from the RS into the localized Qdot states as well as the relaxation between the discrete Qdot states [Lorke06]. The Auger scattering can be categorized into three types, according to the initial electronic states of the carriers involved. Type I involves two carriers in the RS states [Magnusdottir03], type II is with one carrier in an ES state while the other in the RS [Bockelmann92], and type III has both carrier occupied the ES [Ferreira99].

In TRPL experiments, the capture and relaxation processes can be identified by varying the excitation energy. The carrier-phonon interaction process is shown to be temperature-dependent,

the scattering rate increases at high temperature. In contrast, the Auger process is temperature-independent, but carrier-density dependent [Ohnesorge96], [Ignatiev00], [Miska08]. From the analysis of PL rise time at room temperature, both the capture and relaxation times are found to vary in a wide range from 0.1 up to 100 ps relying on the excitation intensity [Ohnesorge96], [Uskov98]. However, for moderate RS carrier density of 10^{11}~10^{12} cm^{-2}, the typical carrier scattering times are of the order of 1~10 ps [Siegert05], [Uskov97]. For the processes related to Coulomb many-body interactions, relaxation within the Qdot is typically on a faster time scale than the carrier capture from the WL into the Qdot. Processes involving holes are faster than the corresponding processes involving electrons and capture to the excited states is more efficient than capture to the ground states. Hence in a dynamical scenario, first the holes are captured to the excited Qdot states and immediately scattered via relaxation to the Qdot ground states. Capture of electrons is somewhat slower, the subsequent relaxation for electrons is only slightly slower than for holes [Nielsen04].

In the rate equation modeling of Qdot lasers, carrier distributions in all states are assumed to be under the quasi-equilibrium condition with the Fermi-Dirac distribution, which is quite suitable for sufficiently rapid intraband relaxation process [Chow05]. Carrier occupations at least in a lasing GS and a reservoir (RS) must be modeled in order to distinguish the Qdot case from the Qwell one. However, for achieving better accuracy and connections with experimental data in the InAs/InP system, it is necessary to incorporate the carrier dynamics in the first (and the second) ES, which can have significant influence on the laser's static and dynamic characteristics. Inclusion of more states would be even more accurate but at a price of losing simplicity, and no direct experimental evidence of such ESs lying at higher energy have been obtained by the TRPL in InAs Qdot on InP substrate.

Rigorous calculation of carrier scattering rates is a stiff task, which requires sophisticated many-body quantum theory that treat intraband collision processes [Chow99], [Chow05]. [Berg01] proposed a phenomenological formula to take into account the carrier-dependent capture and relaxation time in a semi-empirical model:

$$\tau_i = \frac{1}{A_i + C_i N_{RS}} \tag{2.3}$$

where i denotes the capture or relaxation process, A_i is the phonon-assisted scattering rate, and C_i is the coefficient determining the Auger-assisted scattering by carriers in the RS (N_{RS}). Although this expression leads to good agreement with the TRPL experiments in [Miska08], parameters A_i and C_i can be quite different from device to device [Veselinov07], hence limiting the applicability of this expression. However, due to the fact that once the laser is pumped above

its threshold, there is a large density of carriers in the RS which does not vary a lot with the bias current, it is a reasonable approximation to assume the carrier scattering time as a constant value, which simplifies the rate equation model for the study of Qdot laser dynamics.

2.2. Gain, refractive index and linewidth enhancement factor

The laser field and the semiconductor gain medium are coupled by the gain and the carrier-induced refractive index, or equivalently, by the complex optical susceptibility. To determine these quantities, it is necessary to solve the quantum mechanical gain medium equations of motion for the microscopic polarization. In principle, these dynamical equations should be derived using the full system Hamiltonian, which includes contributions from the kinetic energies, the many-body Coulomb interactions, the electric-dipole interaction between the carriers and the laser field, as well as the interactions between the carriers and phonons. The effects of injection current pumping should also be included [Chow99].

The connection between the classical electrodynamics and quantum mechanics is performed through the macroscopic polarization P and the microscopic polarization p_α:

$$\mathrm{P} = \frac{1}{V}\sum_{\alpha}\mu_\alpha p_\alpha \tag{2.4}$$

where μ_α is the dipole matrix element for the α transition. In QD lasers, the processes include the GS, ES, RS and barrier transitions. V is the active region volume and the polarization summation is performed over all interband optical transitions. The complex optical susceptibility χ is connected with the polarization via:

$$\chi = \frac{1}{\varepsilon_0 n_b^2}\frac{P}{E} \tag{2.5}$$

where ε_0 is the vacuum permittivity of the light, n_b is the refractive index without carrier injection, and E is the amplitude of the electric field. The gain g and the carrier-induced refractive index δn in the model are defined by:

$$\frac{d}{dt}E(t) = \Gamma_p \frac{cg}{2n_b}E(t) + j\frac{\omega\delta n}{n_b}E(t) \tag{2.6}$$

where ω and c are the laser frequency and velocity of light, and Γ_p is the optical confinement factor. We can obtain the following relation between the gain, refractive index, susceptibility and the polarization [Chow11]:

$$g = -\frac{\omega n_b}{c}\mathrm{Im}\{\chi\} = -\frac{\omega}{\varepsilon_0 n_b c}\frac{\mathrm{Im}\{P\}}{E} \tag{2.7}$$

$$\delta n = \frac{n_b}{2}\mathrm{Re}\{\chi\} = \frac{1}{2\varepsilon_0 n_b}\frac{\mathrm{Re}\{P\}}{E} \tag{2.8}$$

Introducing the differential gain a, the phenomenological gain with linear approximation can be expressed as:

$$g = a(N - N_{tr}) \tag{2.9}$$

with N and N_{tr} being the injected carrier density and transparency carrier density of zero gain, respectively.

In semiconductor lasers, the nonlinear gain phenomenon plays an important role in both static and dynamic characteristics such as spectral properties, modulation bandwidth and frequency chirping [Takahashi91]. The main physical mechanisms behind nonlinear gain can be attributed to the spectral hole burning, spatial hole burning and carrier heating [Willatzen91], [Klotzkin14]. However, these mechanisms for gain compression are still not fully understood. Furthermore, the gain nonlinearity was found to be enhanced by the quantum confinement of carriers and carrier relaxation processes [Lam94]. Spectral hole burning is the formation of a dip in the gain spectrum due to stimulated emission. The dip occurs by the recombination of electrons and hole at a specific energy and the subsequent redistribution of carrier energies due to carrier-carrier scattering. The scattering process takes place on a time scale of the order of 50-100 fs and leads to a dip width of about 20-40 meV. It also ensures that the temperature equilibrium is established among the carriers within the same time scale. The spatial hole burning is referred to the non-uniform photon density in the laser cavity. For higher photon density at certain locations (at the facets in Fabry-Perot lasers, or anywhere in DFB lasers) depletes the carriers and hence reduces the net gain [Morthier91], [Duan92], [Wentworth93]. Carrier heating is related to the fact that, the carrier temperatures can be different from the lattice temperature due to the stimulated emission and free carrier absorption [Willatzen91]. The carrier temperatures relax towards the lattice temperature by electron-phonon scattering processes within a time scale of 0.5-1 ps. The nonlinear gain effect is usually characterized by a phenomenological gain compression factor ξ as:

$$g_{nl} = \frac{g}{1+\xi S} \approx g(1-\xi S) \tag{2.10}$$

with S being the photon density. This expression shows that the linear gain g is reduced at high power density.

The refractive index change related to the optical interband transition as expressed in Eq. (2.8) is known as anomalous dispersion [Schneider02]. Another important contribution to the

index change is the free carrier plasma originating from intraband transitions [Uskov04]. In Qwell lasers, this contribution to the refractive index is well described by the Drude model [Hegarty05]:

$$\delta n_{FC} = -\frac{\Gamma_p e^2 N}{2 n_b \varepsilon_0 m^* \omega^2} \tag{2.11}$$

with e the electronic charge. Analog transitions in Qdot lasers can be envisaged between bound Qdot states and the continuum levels of the RS and the barrier. It has been shown that the Drude formula can also be applied to the case of Qdot lasers when the Qdot carriers are not tightly confined and when working at photon energies within the 0.8-1.0 eV region [Uskov04].

In semiconductor lasers, it is well known that any change in the imaginary part of the susceptibility (gain) will be accompanied by a corresponding change in its real part (refractive index) via the Kramers-Krönig relations. The linewidth enhancement factor or α-factor describes the coupling between the carrier-induced variation of real and imaginary parts of susceptibility and is defined as [Henry82], [Osinski87]:

$$\alpha_H = \frac{\partial Re\{\chi\}/\partial N}{\partial \mathrm{Im}\{\chi\}/\partial N} \tag{2.12}$$

Employing the relation in Eqs. (2.7) and Eqs. (2.8), the above definition is equivalent to the following often-used expression:

$$\alpha_H = -2\frac{\omega}{c}\frac{dn/dN}{dg/dN} \tag{2.13}$$

In practical case, the variation of the carrier concentration is usually small, this justifies taking the derivatives at the operating point and assuming a linear dependence of g(N) and n(N). Equation (2.13) would thus be written as:

$$\alpha_H = -2\frac{\omega}{c}\frac{\Delta n}{\Delta g} \tag{2.14}$$

Through the relation between the refractive index and the frequency variations $\Delta n = -n_b \Delta\omega/\omega$, we can obtain the following equivalent formula:

$$\alpha_H = 2\frac{n_b}{c}\frac{\Delta\omega}{\Delta g} \tag{2.15}$$

The α-factor plays a crucial role in driving fundamental features of semiconductor lasers such as the spectral linewidth [Duan90], frequency chirp [Duan87], mode stability [Agrawal89] as well as nonlinear dynamics subject to optical injection [Wieczorek02] or optical feedback [Haegeman02], [Sciamanna04], [Panajotov12]. Typical Qwell lasers often exhibit α-factor values in the order of 2~5 [Coldren12]. For Qdot lasers, earlier analyses have suggested a zero

or near-zero α-factor due to the delta-function like discrete density of states. A symmetrical gain spectrum indeed leads to a dispersive curve of the refractive index with a zero value at the gain peak. However, experimental α-factor values in Qdot lasers vary over a wide range from zero up to more than 10, and especially a giant value as high as 60 was also reported [Newell99], [Mi05], [Dagens05]. The non-zero α-factor is attributed to the large inhomogeneous broadening, the off-resonant bound and continuum states as well as the free carrier plasma effect. These mechanisms will be discussed in details in the following chapters.

2.3. Homogeneous and inhomogeneous broadenings

The homogenous broadening in semiconductor Qdots is inversely proportional to the polarization dephasing time, which is the decay time of the optical polarization associated with an interband transition. In principle, the dephasing of the optical polarization involves not only the particular electron-hole pair but also other electron-hole polarizations [Schneider04]. However, in the quasi-equilibrium carrier system, the dephasing time (T_2) can be treated as a time constant, which is simply twice the total carrier scattering time [Haug98]. There are a number of mechanisms responsible for the homogeneous broadening, such as carrier-carrier scattering, carrier-phonon scattering, and the radiative electron-hole recombination lifetime. Thus the full width at half maximum (FWHM) of homogeneous broadening for a confined QD bound state can be expressed as [Nilsson05]

$$2\hbar\Gamma_{\text{hom}} = \frac{2\hbar}{T_2} = \hbar\left(\frac{1}{\tau_{hh}} + \frac{1}{\tau_{he}} + \frac{1}{\tau_{ee}} + \frac{1}{\tau_{eh}}\right) + \hbar\frac{1}{\tau_{phon}} + \hbar\frac{1}{\tau_{recom}} \tag{2.16}$$

where the first term is due to the Auger scattering process among electrons and holes. The second term is the contribution from the carrier-phonon interaction, and the last term is attributed to the radiative recombination. The homogeneous broadening of optical gain is characterized by a Lorentzian function as [Sugawara00]

$$B_{cv}(E - E_{opt}) = \frac{\hbar\Gamma_{\text{hom}} / \pi}{(E - E_{opt})^2 + (\hbar\Gamma_{\text{hom}})^2} \tag{2.17}$$

where E_{opt} is the optical interband transition energy. The homogeneous broadening has been demonstrated to be responsible for the temperature dependence of lasing spectra [Veselinov08]. Dots are lasing independently at low temperature due to the carrier spatial localization as well as the atom-like gain, while at room temperature the dot ensemble contributes to a narrow-line lasing correlatively via the broadened homogeneous broadening of optical gain as well as the carrier redistribution between the dots [Sugawara00], [Gready11], [Cornet06a].

Meanwhile, the homogeneous broadening of refractive index is given by [Gioannini07]

$$D_{cv}(E-E_{opt}) = \frac{(E-E_{opt})/\pi}{(E-E_{opt})^2 + (\hbar\Gamma_{\text{hom}})^2} \tag{2.18}$$

Figure 2.3 illustrates profiles of $B_{cv}(E-E_{opt})$ and $D_{cv}(E-E_{opt})$ as a function of energy E. We observe that for the same value of $\hbar\Gamma_{\text{hom}}$, the refractive index broadening function $D_{cv}(E-E_{opt})$ (dash) is wider than the gain broadening function $B_{cv}(E-E_{opt})$ (solid). Therefore, carrier population in off-resonant QD states that has little gain contribution to the stimulated emission may nevertheless cause significant variation of refractive index of the lasing mode.

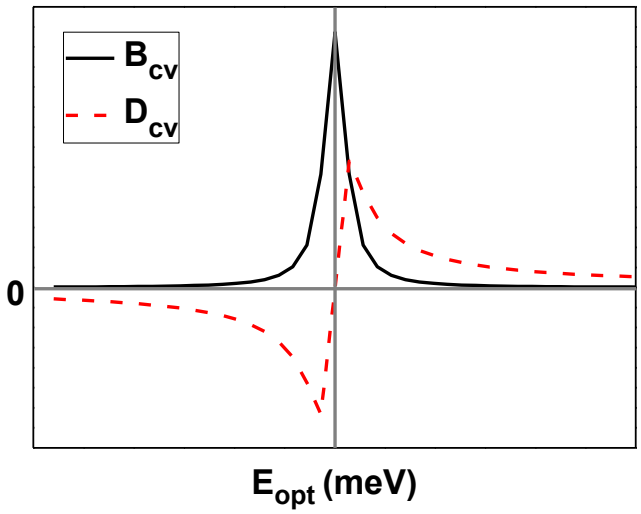

Fig. 2.3. Homogeneous broadening function of gain $B_{cv}(E-E_{opt})$ and of refractive index variation $D_{cv}(E-E_{opt})$.

The inhomogeneous broadening originates from the size fluctuation and the composition variation of self-assembled Qdots, which yields different confined energies of state. Considering a usual Gaussian-shape distribution of the dot size, the energy fluctuation of dots can be thereby represented by the Gaussian function as [Sugawara00]

$$G_{cv}(E-E_{opt}) \frac{1}{\sqrt{2\pi}\xi_{inh}} \exp\left(-\frac{(E-E_{opt})^2}{2\xi_{inh}^2}\right) \tag{2.19}$$

whose FWHM is given as $2.35\xi_{inh}$. Figure 2.4 shows an illustration of a Gaussian distribution. The dot inhomogeneous broadening is known to significantly reduce the gain and differential gain of the Qdot laser and thus degrade the laser dynamic performance [Dery05].

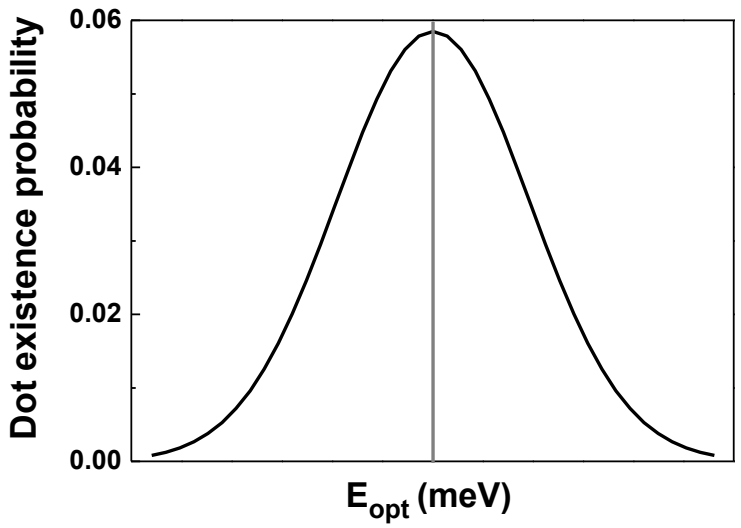

Fig. 2.4. Inhomogeneous broadening function $G_{cv}(E-E_{opt})$ of dot size or energy fluctuation.

In summary, this chapter introduces fundamental knowledge of Qdot nanostructure semiconductor lasers, including the electronic structures, the carrier scattering processes, gain and refractive index, the linewidth enhancement factor as well as the homogeneous and inhomogeneous broadenings. These understandings are helpful for the various analyses conducted in the following chapters.

Chapter 3. Modulation dynamics of free-running Qdot lasers

This chapter will discuss the small-signal modulation characteristics of Qdot lasers, including the amplitude response, frequency chirp, as well as the linewidth enhancement factor. The analysis is based on a semi-analytical approach of a set of coupled rate equations. We show how rate equations account for the contributions of off-resonant states on the refractive index change. In order to enhance the laser's dynamic performance, the Qdot laser operating on the excited state is also discussed.

3.1. Amplitude modulation response

In this section, the theoretical analysis of the laser is based on a previously developed empirical model for InAs/InP Qdot lasers (FOTON lab) named as Model-I in this thesis [Veselinov07]. This numerical model holds under the assumption that the active region consists of only one Qdot ensemble, where the nanostructures are interconnected by the 2D RS. The Qdot density of states contains two energy levels: a two-fold degenerate GS and a four-fold degenerate ES. This simplified picture corresponds to early direct TRPL experimental observations in this material system [Miska02]. The Qdots are implicitly assumed to be always neutral, electrons and holes are treated as electron-hole (eh) pairs, which mean that the system is only composed by excitonic energy states. Carriers are supposed to be injected directly from the contacts into the RS levels, so the carrier dynamics in the barrier are not taken into account in the model.

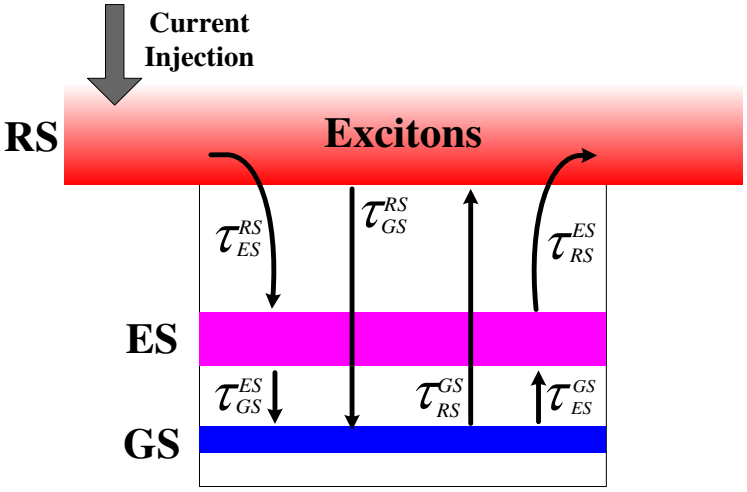

Fig. 3.1. Sketch of carrier dynamics model including a direct relaxation channel

Fig. 3.1 shows the schematic of the carrier dynamics in the conduction band. Firstly, the external injected carrier fills directly into the RS reservoir, some of the carriers are then either captured into the ES within time τ_{ES}^{RS} or directly into the GS within time τ_{GS}^{RS}, and some of them recombine spontaneously with a spontaneous emission time τ_{RS}^{spon}. Once in the ES, carriers can relax into the GS within time τ_{GS}^{ES} or recombine spontaneously. On the other hand, carriers can also be thermally reemitted from the ES to the RS with an escape time τ_{RS}^{ES}, which is governed by the Fermi distribution for the quasi-thermal equilibrium without external excitation [Grillot09]. Similar dynamic behavior is followed for the carrier population on the GS level with regards to the ES. Direct injection from the RS to the GS was introduced to reproduce the experimental results [Veselinov07]. Stimulated emission occurs from the GS when the threshold is reached, and that from the ES is not taken into account in the model. Following the sketch of Fig. 3.1, the four coupled rate equations on carrier and photon densities are described as follows:

$$\frac{dN_{RS}}{dt} = \frac{I}{qV} + \frac{N_{ES}}{\tau_{RS}^{ES}} - \frac{N_{RS}}{\tau_{ES}^{RS}}(1-\rho_{ES}) - \frac{N_{RS}}{\tau_{GS}^{RS}}(1-\rho_{GS}) - \frac{N_{RS}}{\tau_{RS}^{spon}} + \frac{N_{GS}}{\tau_{RS}^{GS}} \tag{3.1}$$

$$\frac{dN_{ES}}{dt} = \frac{N_{RS}}{\tau_{ES}^{RS}}(1-\rho_{ES}) + \frac{N_{GS}}{\tau_{ES}^{GS}}(1-\rho_{ES}) - \frac{N_{ES}}{\tau_{RS}^{ES}} - \frac{N_{ES}}{\tau_{GS}^{ES}}(1-\rho_{GS}) - \frac{N_{ES}}{\tau_{ES}^{spon}} \tag{3.2}$$

$$\frac{dN_{GS}}{dt} = \frac{N_{RS}}{\tau_{GS}^{RS}}(1-\rho_{GS}) + \frac{N_{ES}}{\tau_{GS}^{ES}}(1-\rho_{GS}) - \frac{N_{GS}}{\tau_{ES}^{GS}}(1-\rho_{ES}) - \frac{N_{GS}}{\tau_{GS}^{spon}} - \frac{N_{GS}}{\tau_{WL}^{GS}} - g_{GS}v_g S_{GS} \tag{3.3}$$

$$\frac{dS_{GS}}{dt} = \Gamma_p g_{GS} v_g S_{GS} - \frac{S_{GS}}{\tau_P} + \beta_{SP}\frac{N_{GS}}{\tau_{GS}^{spon}} \tag{3.4}$$

where $N_{RS,ES,GS}$ are carrier densities in the RS, ES, GS, and S_{GS} is photon density in the cavity with GS resonance energy. β_{SP} is the spontaneous emission factor, Γ_p the optical confinement factor, τ_p the photon lifetime and v_g the group velocity. V is the volume of the laser's active region. The GS gain is given by:

$$g_{GS} = a_{GS}\frac{N_B}{H_B}\left(\frac{2N_{GS}}{2N_B/H_B} - 1\right) \tag{3.5}$$

where a_{GS} is the differential gain, N_B is the total Qdot surface density and H_B is the height of the dots. In what follows, it is important to stress that effects of gain compression are not taken into account. In (3.1)-(3.3), $\rho_{GS,ES}$ are the carrier occupation probabilities in the GS and the ES, respectively:

$$\rho_{GS} = \frac{N_{GS}}{2N_B / H_B}; \qquad \rho_{ES} = \frac{N_{ES}}{4N_B / H_B} \tag{3.6}$$

Since the carrier escape from the GS to the RS has little effects on lasing properties [Veselinov07], the N_{GS} / τ_{RS}^{GS} term in (3.1) and (3.3) can be neglected.

The rate equations can be linearized through a small signal analysis. Assuming a sinusoidal current modulation $dI = I_1 e^{j\omega t}$ with modulation frequency ω, the corresponding carrier and photon variations are of the form

$$\begin{aligned} dN_{RS,ES,GS} &= N_{RS1,ES1,GS1} e^{j\omega t} \\ dS_{GS} &= S_{GS1} e^{j\omega t} \end{aligned} \tag{3.7}$$

Combining (3.7) into the rate equations, we obtain

$$\begin{bmatrix} \gamma_{11} + j\omega & -\gamma_{12} & 0 & 0 \\ -\gamma_{21} & \gamma_{22} + j\omega & -\gamma_{23} & 0 \\ -\gamma_{31} & -\gamma_{32} & \gamma_{33} + j\omega & -\gamma_{34} \\ 0 & 0 & -\gamma_{43} & \gamma_{44} + j\omega \end{bmatrix} \begin{bmatrix} N_{RS1} \\ N_{ES1} \\ N_{GS1} \\ S_{GS1} \end{bmatrix} = \frac{I_1}{qV} \begin{bmatrix} 1 \\ 0 \\ 0 \\ 0 \end{bmatrix} \tag{3.8}$$

with

$$\begin{aligned} &\gamma_{11} = \frac{1-\rho_{ES}}{\tau_{ES}^{RS}} + \frac{1-\rho_{GS}}{\tau_{GS}^{RS}} + \frac{1}{\tau_{RS}^{spon}}; \quad \gamma_{12} = \frac{1}{\tau_{RS}^{ES}} + \frac{N_{RS}}{\tau_{ES}^{RS}} \frac{1}{4N_B / H_B} \\ &\gamma_{21} = \frac{1-\rho_{ES}}{\tau_{ES}^{RS}}; \quad \gamma_{22} = \frac{1-\rho_{GS}}{\tau_{GS}^{ES}} + \frac{1}{\tau_{RS}^{ES}} + \frac{N_{RS}}{\tau_{ES}^{RS}} \frac{1}{4N_B / H_B} + \frac{N_{GS}}{\tau_{ES}^{GS}} \frac{1}{4N_B / H_B} + \frac{1}{\tau_{ES}^{spon}} \\ &\gamma_{23} = \frac{1-\rho_{ES}}{\tau_{ES}^{GS}} + \frac{N_{ES}}{\tau_{GS}^{ES}} \frac{1}{2N_B / H_B}; \quad \gamma_{31} = \frac{1-\rho_{GS}}{\tau_{GS}^{RS}}; \quad \gamma_{32} = \frac{1-\rho_{GS}}{\tau_{GS}^{ES}} + \frac{N_{GS}}{\tau_{ES}^{GS}} \frac{1}{4N_B / H_B} \\ &\gamma_{33} = \frac{1-\rho_{ES}}{\tau_{ES}^{GS}} + \frac{N_{ES}}{\tau_{GS}^{ES}} \frac{1}{2N_B / H_B} + v_g a_{GS} S_{GS} + \frac{1}{\tau_{GS}^{spon}}; \quad \gamma_{34} = -v_g g_{GS} \\ &\gamma_{43} = \frac{\Gamma_p \beta_{SP}}{\tau_{GS}^{spon}} + \Gamma_p v_g a_{GS} S_{GS}; \quad \gamma_{44} = \frac{1}{\tau_p} - \Gamma_p v_g g_{GS} \end{aligned} \tag{3.9}$$

Then, we can extract a new modulation transfer function for the Qdot laser as:

$$H_{QD}(\omega) = \frac{R_0}{\Delta} \equiv \frac{R_0}{R_0 + j\omega R_1 - \omega^2 R_2 - j\omega^3 R_3 + \omega^4} \tag{3.10}$$

where Δ is the determinant of the matrix, and the four parameters which characterize $H_{QD}(\omega)$ are given by:

$$\begin{aligned} R_0 &= \omega_R^2 \omega_{R0}^2 - \gamma_{23}\gamma_{44}(\gamma_{31}\gamma_{12} + \gamma_{11}\gamma_{32}) \\ R_1 &= \omega_R^2 \Gamma_0 + \Gamma \omega_{R0}^2 - \gamma_{23}\gamma_{32}(\gamma_{11} + \gamma_{44}) - \gamma_{31}\gamma_{12}\gamma_{23} \\ R_2 &= \omega_R^2 + \Gamma\Gamma_0 + \omega_{R0}^2 - \gamma_{23}\gamma_{32} \\ R_3 &= \Gamma + \Gamma_0 \end{aligned} \tag{3.11}$$

The relaxation resonance frequency ω_R and damping factor Γ are approximately defined as

$$\omega_R^2 = \gamma_{33}\gamma_{44} - \gamma_{34}\gamma_{43} \tag{3.12}$$

$$\Gamma = \gamma_{33} + \gamma_{44} \tag{3.13}$$

And the other two new parameters are:

$$\omega_{R0}^2 = \gamma_{11}\gamma_{22} - \gamma_{12}\gamma_{21} \tag{3.14}$$

$$\Gamma_0 = \gamma_{11} + \gamma_{22} \tag{3.15}$$

Using the set of (3.9), the above parameters can be re-expressed as follows:

$$\omega_R^2 = \frac{v_g a_{GS} S_{GS}}{\tau_p} + \frac{\Gamma_p \beta_{SP} N_{GS}}{\tau_{GS}^{spon} S_{GS}} \left(\frac{H_B}{2N_B} \frac{N_{ES}}{\tau_{GS}^{ES}} + \frac{1-\rho_{ES}}{\tau_{ES}^{GS}} + \frac{1-\beta_{SP}}{\tau_{GS}^{spon}} \right) + \frac{\beta_{SP}}{\tau_{GS}^{spon} \tau_p} \tag{3.16}$$

$$\Gamma = v_g a_{GS} S_{GS} + \frac{H_B}{2N_B} \frac{N_{ES}}{\tau_{GS}^{ES}} + \frac{1-\rho_{ES}}{\tau_{ES}^{GS}} + \frac{1}{\tau_{GS}^{spon}} + \frac{\Gamma_p \beta_{SP} N_{GS}}{\tau_{GS}^{spon} S_{GS}} \tag{3.17}$$

where the steady-state relationship $1/\tau_p - \Gamma_p v_g g_{GS} = \Gamma_p \beta_{SP} N_{GS} / (\tau_{GS}^{spon} S_{GS})$ has been used.

Equations (3.16) and (3.17) constitute new relationships giving the resonance frequency and the damping factor for Qdot lasers. Because ω_R^2 and Γ contain the additional term due to the existence of ES, these equations differ from those obtained from the conventional model of Qwell lasers [Coldren95]. Since the first term in ω_R^2 dominates over all the other terms, the resonance frequency can be reduced to $\omega_R^2 \approx \Gamma_p v_g S_{GS} a_{GS} / \tau_p$. Employing this simplified definition of ω_R^2 the damping factor can be rewritten as:

$$\Gamma = K f_R^2 + \frac{H_B}{2N_B} \frac{N_{ES}}{\tau_{GS}^{ES}} + \frac{1-\rho_{ES}}{\tau_{ES}^{GS}} + \frac{1}{\tau_{GS}^{spon}} + \frac{\Gamma_p \beta_{SP} N_{GS}}{\tau_{GS}^{spon} S_{GS}} \tag{3.18}$$

where the so-called K-factor is as follows:

$$K = 4\pi^2 \tau_p \tag{3.19}$$

The expression of the K-factor is identical to that of Qwell lasers. However, the offset of the damping factor in (3.18) contains additional terms that are due to the carrier relaxation and escape. These terms are in fact comparable to $K f_R^2$ even at high powers meaning that such offset cannot be neglected for Qdot lasers.

In order to identify the influences of the RS and the ES, Eq. (3.11) can be simplified by neglecting small contributions terms:

$$\begin{aligned} R_0 &\approx \omega_R^2 \omega_{R0}^2; \qquad R_1 \approx \omega_R^2 \Gamma_0 + \Gamma \omega_{R0}^2 \\ R_2 &\approx \omega_R^2 + \Gamma\Gamma_0 + \omega_{R0}^2; \quad R_3 = \Gamma + \Gamma_0 \end{aligned} \tag{3.20}$$

Based on these expressions, the modulation transfer function (3.10) can be rewritten as

$$H_{app}(\omega) \approx \frac{\omega_R^2}{\omega_R^2 - \omega^2 + j\omega\Gamma} \frac{\omega_{R0}^2}{\omega_{R0}^2 - \omega^2 + j\omega\Gamma_0} \tag{3.21}$$

This novel expression reveals that the two additional terms ω_{R0}^2 and Γ_0 play a similar role in the modulation response as the resonance frequency ω_R^2 and the damping factor Γ, respectively. It is important to point out the effects of ω_{R0}^2 and Γ_0 on the modulation dynamics, as well as the underlying physical mechanism. The results will be discussed in the following section.

Then, the modulation bandwidth f_{3dB} can be obtained by solving $\left|H_{QD}(\omega)\right|^2 = 1/2$, i.e.

$$2R_0^2 = \left(\omega^4 - R_2\omega^2 + R_0\right)^2 + \left(R_3\omega^3 - R_1\omega\right)^2 \tag{3.22}$$

and the maximum possible bandwidth $f_{3dB}\big|_{\max}$ occurs when $\Gamma^2 = 2\omega_R^2$ so the value can be extracted by:

$$2\omega_R^4\omega_{R0}^4 = \left[\omega^4 + \omega_R^4\right]\left[\left(\omega^2 - \omega_{R0}^2\right)^2 + \left(\omega\Gamma_0\right)^2\right] \tag{3.23}$$

Table 3.1. Material and laser parameters used in the simulation of the AM response

Symbols	Simulation parameters	Values	Symbols	Simulation parameters	Values
E_{RS}	RS energy	0.97 eV	L	Active region length	0.11 cm
E_{ES}	ES energy	0.87 eV	W	Active region width	3×10^{-4} cm
E_{GS}	GS energy	0.82 eV	N	Number of QD layers	5
τ_{ES}^{RS}	Capture time from RS to ES	25.1 ps	N_B	QD density	5×10^{10} cm^{-2}
τ_{GS}^{ES}	Relaxation time from ES to GS	11.6 ps	Γ_p	Optical confinement factor	0.06
τ_{RS}^{spon}	Spontaneous time of RS	500 ps	β_{SP}	Spontaneous emission factor:	1×10^{-4}
τ_{ES}^{spon}	Spontaneous time of ES	500 ps	α_i	Internal modal loss	6 cm^{-1}
τ_{GS}^{spon}	Spontaneous time of GS	1200 ps	R_1=R_2	Mirror reflectivity	0.3
			a_{GS}	Differential gain	8.3×10^{-14} cm^2

All the material and Qdot laser parameters used in the calculations are summarized in Table 3.1. The direct carrier capture time from the RS to the GS τ_{GS}^{RS} is observed to be larger than the capture time τ_{ES}^{RS} in the low excitation regime [Bockelmann92], while under strong excitation

τ_{GS}^{RS} becomes approximately the same as τ_{ES}^{RS} ($\tau_{GS}^{RS} \approx \tau_{ES}^{RS}$) [Miska08]. In the calculation, the direct carrier capture time is kept as $\tau_{GS}^{RS} = 1.5\tau_{ES}^{RS}$.

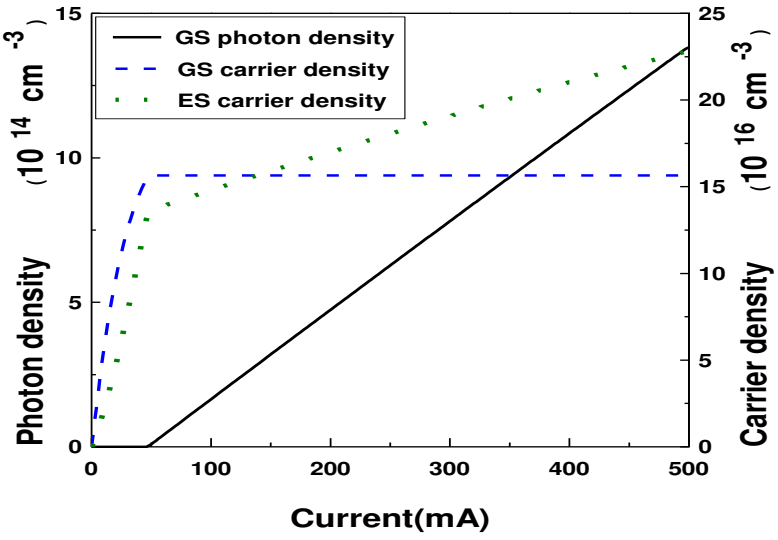

Fig. 3.2. Photon and carrier densities versus injected current.

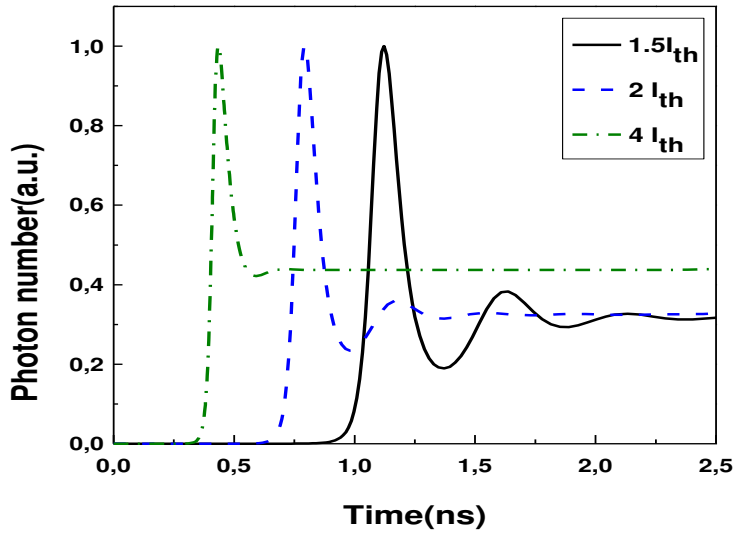

Fig. 3.3. Turn-on delay properties at various injected currents.

In order to validate the semi-analytical approach, the steady-state properties of the system are at first studied by numerically solving the four rate equations (3.1)-(3.4). The results depicted in Fig. 3.2 show that both the GS and the ES carrier populations increase with the injected current. Then, for an injected current larger than 48 mA, the GS population are clamped which leads to the occurrence of the GS lasing emission while the ES population keeps

increasing with a reduced slope efficiency. Fig. 3.3 illustrates the turn-on delay properties for various injected currents. With the increase of the pump current, the delay time becomes shorter which means that the effective carrier lifetime is decreased [Agrawal86]. Both the oscillation frequency and the damping factor increase with the current. The oscillation frequencies at $1.5I_{th}$, $2I_{th}$ and $4I_{th}$ are 1.94 GHz, 2.64 GHz and 3.52 GHz, respectively.

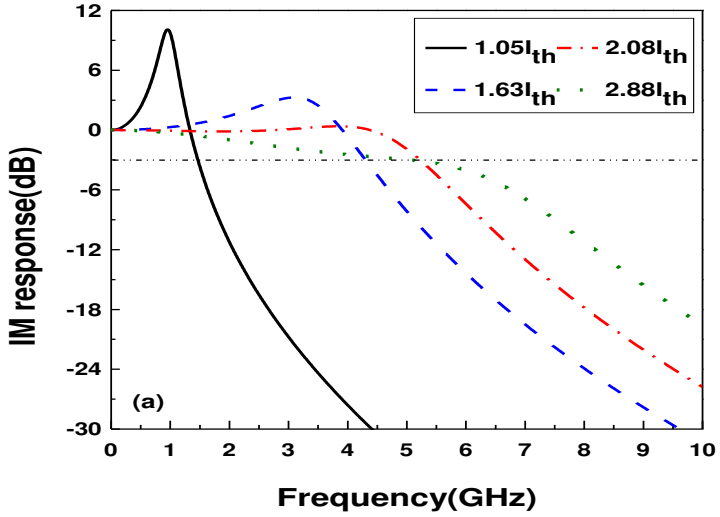

Fig. 3.4. Modulation responses at several injected currents, which are calculated from the new analytical expression (3.10).

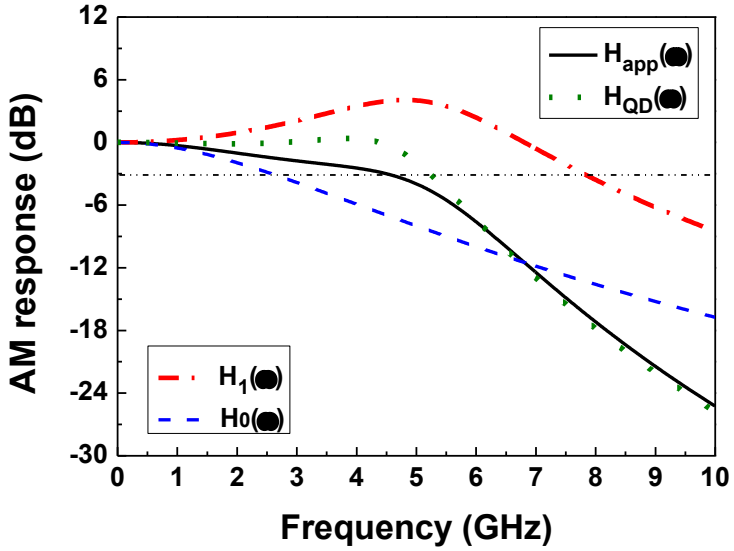

Fig. 3.5. Comparisons of analytical approximation (solid) calculated from (3.24) for modulation response and the precise value (dot) calculated from (3.10). Dashed line indicates contribution of $H_0(\omega)$ to the total modulation response, and dash-dot line is contribution of $H_1(\omega)$.

Based on the steady-state as well as on the transient response results, the modulation responses are calculated from the analytical expression (3.10) for various current levels and depicted in Fig. 3.4. Numerical results show that the relaxation frequency and the damping factor increase with the injected current. At an injected current of around $2.9I_{th}$, the modulation bandwidth reaches the maximum value ~5.5 GHz, which is in good agreement with the commonly measured values [Sugawara05], [Bhattacharya07], [Krebs01].

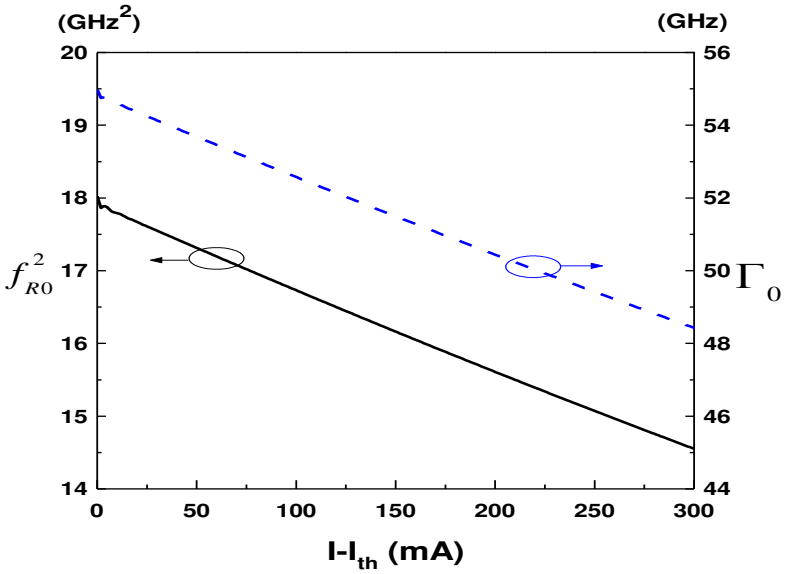

Fig. 3.6. Evolutions of f_{R0}^2 and Γ_0 as a function of the current (I-I_{th}).

According to (3.21), the modulation response $20\log\left|H_{app}(\omega)\right|$ can be divided into

$$20\log\left|H_{app}(\omega)\right| = 20\log\left|H_1(\omega)\right| + 20\log\left|H_0(\omega)\right| \tag{3.24}$$

where

$$H_1(\omega) = \frac{\omega_R^2}{\omega_R^2 - \omega^2 + j\omega\Gamma} \tag{3.25}$$

$$H_0(\omega) = \frac{\omega_{R0}^2}{\omega_{R0}^2 - \omega^2 + j\omega\Gamma_0} \tag{3.26}$$

The analytical approximation of modulation response at $2.08I_{th}$ calculated from (3.24) is shown in Fig. 3.5 (solid line), and is compared with the exact solution given by (3.10). Both are found in good agreement except around the resonance peak for which the approximated value is slightly smaller than the exact solution. The behavior of $H_1(\omega)$ to the IM response (dash-dot line) is similar to that of QW lasers, and the characteristics of ω_R^2 and Γ characterizing $H_1(\omega)$

will be discussed in the following section. Since the modulation bandwidth of $H_0(\omega)$ is much smaller than that of $H_1(\omega)$, the total modulation bandwidth of the Qdot laser is limited by $H_0(\omega)$. According to the expression of ω_{R0}^2 in $H_0(\omega)$ associated with (3.9), the results point out that the finite carrier capture time τ_{ES}^{RS} and τ_{GS}^{RS}, finite carrier relaxation time τ_{GS}^{ES} as well as the Pauli blocking $(1-\rho_{ES})$ and $(1-\rho_{GS})$ are the physical limitations for the enhancement of the modulation bandwidth. Equivalently, it is the finite carrier scattering time [Lüdge10] that limits the modulation bandwidth. In order to further analyze the characteristics of f_{R0}^2 and Γ_0, their evolutions are plotted in Fig. 3.6 as a function of the current (I-I_{th}). Inversely to the behaviors of f_R^2 and Γ, both f_{R0}^2 and Γ_0 decrease linearly with the increased current. This is attributed to the reduced Pauli blocking factor $(1-\rho_{ES})$. The relation of the two parameters is fitted as $\Gamma_0 = 1.9 f_{R0}^2 + 20.8$ (GHz), and the maximum f_{R0} at threshold is only 4.2 GHz associated with a large Γ_0 value of 55.0 GHz, which result in the small bandwidth of $H_0(\omega)$.

In order to further test the model, we compare the simulation results with the experiment. The device under study is an InAs/InP(311B) Qdot laser [Martinez08], where the heterostructure is grown by MBE on a (311)B oriented InP substrate. The active region consists of 5 Qdot layers, and the measured Qdot density is ~10^{11}cm^2 [Massé07]. The length and width of the ridge wave-guide laser are 1.1 mm and 3×10^{-3} mm, respectively. The laser's facets are as-cleaved. The experiment shows that the GS lasing peaks at 1.52 μm at room temperature under continuous wave (cw) operation. The photon lifetime is measured to be about 5.8 ps. In order to compare with the experimental results, we use the new analytical transfer function (3.10) to simulate the laser modulation performance. In the calculations, the differential gain a_{GS} is the only one fitting parameter, which is adjusted to 4.2×10^{-14} cm^2. All other parameters are set to the experimental values.

Fig. 3.7 depicts the resonance frequency f_R as a function of the current $(I-I_{th})^{1/2}$, while the inset shows the modulation response at two different pump currents (50 mA and 77 mA). Theoretical results (solid lines) obtained from the Qdot model lead to a relative good agreement with the experimental ones (dot lines). However, at large current injections, the calculated resonance frequency (lines) is found to be higher than the experimental one. Such a discrepancy is attributed to the gain compression, which is not considered in the present simulations.

Analytical calculations also point out that the carrier relaxation and escape between the ES to the GS induce a non-zero resonance frequency around 1 GHz at low bias powers. Based on Eq. (3.16), we see that the frequency offset at threshold is inversely proportional to the carrier relaxation time. This resonance frequency offset is larger than the one due to the spontaneous emission in Qwell lasers (dash-dot line) [Coldren95]. In the inset, the theoretical modulation responses (solid lines) match relatively well with the experimental results (dots).

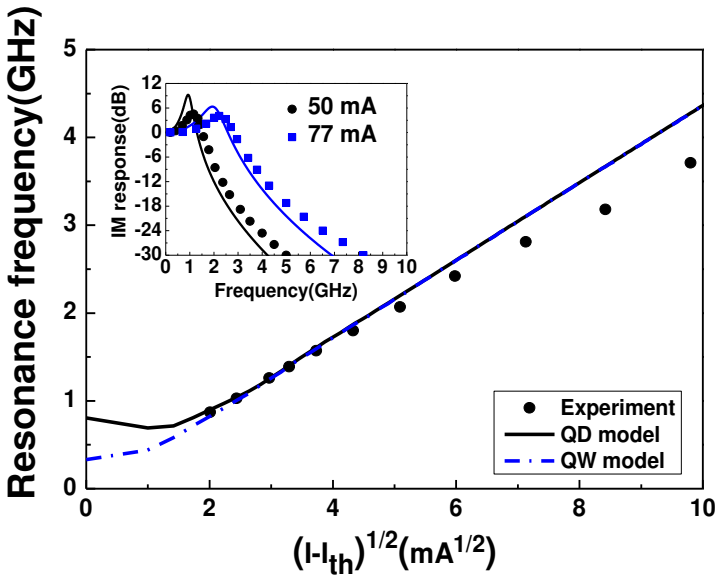

Fig. 3.7. Resonance frequency as a function of the current $(I-I_{th})^{1/2}$ and intensity modulation response at 50 mA and 77 mA (inset). Dots denote experimental results. Solid lines are theoretical results from Qdot model, compared with those from Qwell model (dash-dot lines).

Fig. 3.8 shows the evolution of damping factor as a function of the resonance frequency. According to (3.18), their relationship can be fitted as $\Gamma = 0.20 f_R^2 + 14.9$ (GHz), in comparison with the result from the conventional Qwell model (inset), which is $\Gamma = 0.23 f_R^2 + 0.066$ (GHz). The two K-factors are nearly the same ~0.2 ns, which is 3 times smaller than the experimental value (0.6 ns) [Martinez08]. Once again, such a discrepancy can be attributed to the fact that the simulation does not take into account the gain saturation effects [Coldren95]. The offset occurring in the Qdot model is also found to be much larger than that of Qwell one, confirming the strong damping in nanostructure lasers and the reason that Qdot lasers are less sensitive to external perturbations [Kuntz02], [Malic06], [O'Brien04]. According to (3.17), it is clear that the carrier relaxation and escape processes are responsible for this large damping factor. The deviation from linearity at low relaxation resonance frequency is attributed to the spontaneous emission term $(\Gamma_p \beta_{SP} N_{GS}) / (\tau_{GS}^{spon} S_{GS})$ in the damping factor expression. This phenomenon has

also been observed in InGaAsP bulk lasers via a parasitic-free optical modulation technique [Su92].

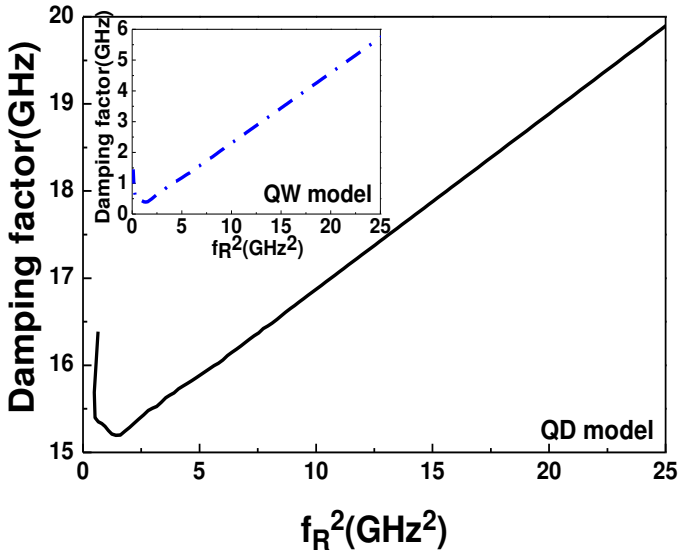

Fig. 3.8. Comparisons of damping factors calculated from the Qdot model and the QW model.

In summary, based on a set of four rate equations, a new analytical modulation transfer function of Qdot lasers has been introduced via a small-signal analysis. This numerical study clarifies the roles of the RS and of the ES in the modulation response: finite carrier capture time, finite carrier relaxation time and Pauli blocking have been found to be the physical limitations to the enhancement of the modulation bandwidth. The model has been used to recast the definitions of the resonance frequency and of the damping factor. These results give intuitive insights into the relevant material and nanostructure parameters and are of first importance for further improvements of the Qdot laser dynamic properties.

3.2. Linewidth enhancement factor (α-factor)

As mentioned in Chapter 2, the linewidth enhancement factor plays an important role in determining fundamental features of semiconductor lasers. It is also known as *α-factor, amplitude-phase coupling factor* and *chirp factor*, and hereafter we use the name α-factor instead in the following chapters. Although the Qdot laser is predicted to have delta-function like discrete density of states, the measured α-factor values in experiments vary over a wide range from zero up to more than 10. The non-zero α-factor in Qdot lasers is partly attributed to the asymmetric gain spectrum because of the inhomogeneous broadening [Oksanen03], as well as the carrier population in off-resonant states [Melnik06]. On the other hand, the free carrier

plasma effect in the barrier and in the RS is reported to contribute almost half of the total refractive index change [Uskov04], [Hegarty05].

In order to characterize the α-factor variation of Qdot lasers, Melnik *et al.* empirically introduced the off-resonant RS contribution to the refractive index change [Melnik06]. Gioannini *et al.* macroscopically derived the index variation due to the carrier population in localized states of the dots through the Kramers-Krönig relationship [Gioannini06]. In 2008, Grillot *et al.* proposed an analytical expression for the α-factor based on the analysis of the nonlinear gain [Grillot08]. Recent work by Lingnau *et al.* microscopically pointed out that the real and imaginary parts of the optical susceptibility in Qdot lasers are desynchronized because the resonant state contributes primarily to the gain change, while the off-resonant states mainly influence the refractive index [Lingnau12],[Lingnau13]. The microscopic rate equation model provides an accurate description of the Qdot laser physics. On the other hand, in order to bridge the gap between the theoretical approaches and experimental investigations, this work proposes a simplified electric field model taking into account the contribution of off-resonant states on the refractive index change, which allows a semi-analytical study of the α-factor features in combination with the dot carrier dynamics in the Qdots. The model can explore the crucial physical mechanisms driven the Qdot laser's α-factor.

Conventional model describing the complex electric field of semiconductor lasers is given by:

$$\frac{dE(t)}{dt} = \frac{1}{2}\left(\Gamma_P v_g g - \frac{1}{\tau_P}\right)E(t) + j\Delta\omega_N E(t) \tag{3.27}$$

where the first term on the right hand gives the gain and the photon loss of the laser cavity. The second term $\Delta\omega_N$ describes the carrier induced frequency shift of the laser field with respect to the frequency at the lasing threshold. $\Delta\omega_N$ is usually expressed by the α-factor α_H as:

$$\Delta\omega_N = \frac{1}{2}(\Gamma_P v_g g - \frac{1}{\tau_P})\alpha_H \tag{3.28}$$

This model is able to study the impacts of a non-zero α-factor on the modulation dynamics and nonlinear dynamics of Qdot lasers [Wieczorek05], but does not allow the study of α_H itself for different operating conditions. In order to investigate the α-factor, we need to obtain the expression of the gain and the refractive index separately. In the semi-classical theory, the semiconductor laser system can be fully described by the optical Bloch equations together with the Maxell's equations [Chow03]. The RS is treated as a discrete energy state of degeneracy $D_{RS} = k_B T m^* A_{RS} / (\pi\hbar^2)$, with m^* the reduced carrier mass and A_{RS} the RS surface area (see

section 3.1) [Markus03]. The active region consists of only one Qdot ensemble. In addition, the electrons and holes are treated as neutral pairs (excitons). Two discrete states --- the ground state (GS) and the first excited state (ES) --- are considered in the dots. With these assumptions, the slowly varying electric field $E(t)$ is given by [Lingnau13]:

$$\frac{d}{dt}E(t)=\frac{j\omega_{LS}^{0}\Gamma_{P}}{2\varepsilon_{bg}\varepsilon_{0}}\frac{1}{A_{RS}H_{B}}\sum_{X=GS,ES,RS}\left(\mu_{X}^{*}P_{X}\right)-\frac{1}{2\tau_{P}}E(t) \tag{3.29}$$

where ω_{LS}^{0} is the lasing frequency in the cold cavity, ε_{bg} and ε_{0} are the background and vacuum permittivity, respectively. Γ_{P} is the optical confinement factor and H_{B} is the height (equals to the dot's height). The sum over X (X=GS, ES, RS) includes all possible optical transitions, with μ_{X} being the corresponding dipole transition matrix element and P_{X} being the microscopic polarization. τ_{P} is the photon lifetime in the laser cavity. Assuming a sufficiently short dephasing time T_{D} and adiabatically eliminating the interband polarization, yield the quasi-static relation

$$P_{X}(t)=-j\frac{\mu_{X}T_{D}}{2\hbar}(2\rho_{X}-1)\frac{1+j(\omega_{X}-\omega_{LS}^{0})T_{D}}{1+(\omega_{X}-\omega_{LS}^{0})^{2}T_{D}^{2}}E(t) \tag{3.30}$$

where ρ_{X} denotes the carrier occupation probability and $\hbar\omega_{X}$ gives the transition energy of each state. Inserting Eq. (3.30) into Eq. (3.29), we obtain the complex gain

$$\tilde{G}(\omega_{LS}^{0},t)=\left(2\mu_{GS}^{*}\frac{j\omega_{LS}^{0}\Gamma_{P}}{2\varepsilon_{0}\varepsilon_{bg}}\frac{2N_{B}}{H_{B}}\frac{P_{GS}(t)}{E(t)}\right)+\left(4\mu_{ES}^{*}\frac{j\omega_{LS}^{0}\Gamma_{P}}{2\varepsilon_{0}\varepsilon_{bg}}\frac{2N_{B}}{H_{B}}\frac{P_{ES}(t)}{E(t)}\right)+\left(\frac{j\omega_{LS}^{0}\Gamma_{P}}{2\varepsilon_{0}\varepsilon_{bg}}\frac{2}{A_{RS}H_{B}}D_{RS}\mu_{RS}^{*}\frac{P_{RS}(t)}{E(t)}\right) \tag{3.31}$$

The optical susceptibility can be derived from the complex gain expression (3.31) through the relationship $\chi(\omega_{LS}^{0},t)=2\varepsilon_{bg}\tilde{G}(\omega_{LS}^{0},t)/(j\omega\Gamma_{P})$. The real part of Eq. (3.31) is related to the laser gain while the imaginary part gives the instantaneous frequency shift of the electric field. The three terms on the right hand give contributions of the GS, the ES and the RS, respectively. Introducing the differential gain (a_{X}):

$$\begin{aligned}a_{GS}&=\frac{2\mu_{GS}\mu_{GS}^{*}\omega_{GS}\mathrm{T}_{D}}{\hbar v_{g}\varepsilon_{0}\varepsilon_{bg}}\\ a_{ES}&=\frac{4\mu_{ES}\mu_{ES}^{*}\omega_{ES}\mathrm{T}_{D}}{\hbar v_{g}\varepsilon_{0}\varepsilon_{bg}}\\ a_{RS}&=\frac{\mu_{RS}\mu_{RS}^{*}\omega_{RS}\mathrm{T}_{D}}{\hbar v_{g}\varepsilon_{0}\varepsilon_{bg}}\end{aligned} \tag{3.32}$$

with v_{g} being the group velocity of the light. The material gain of each state is then given by:

$$
\begin{aligned}
g_{GS} &= \frac{a_{GS}}{1+\xi S_{GS}} \frac{N_B}{H_B}\left(\frac{2N_{GS}}{2N_B/H_B}-1\right) \\
g_{ES} &= a_{ES} \frac{N_B}{H_B}\left(\frac{2N_{ES}}{4N_B/H_B}-1\right) \\
g_{RS} &= a_{RS} \frac{D_{RS}}{A_{RS}H_B}\left(\frac{2N_{RS}}{D_{RS}/(A_{RS}H_B)}-1\right)
\end{aligned}
\tag{3.33}
$$

where N_X is the carrier density in each state, S_{GS} is the photon density in the GS, and ξ denotes the gain compression factor. Because the real part of the complex gain approaches zero very quickly when off resonance, the field gain originates mainly from the resonant state. Considering the lasing emission in resonance with the GS transition $\omega_{LS}^0 = \omega_{GS}$, we obtain

$$
\mathrm{Re}\left[\tilde{G}(\omega_{GS})\right] \approx \Gamma_P v_g g_{GS} \tag{3.34}
$$

In contrast, the imaginary part of the complex gain decays slowly for off-resonant frequencies (see Fig. 2.3). Thus, the off-resonant states can significantly influence the refractive index change, even though their gain contribution to the GS lasing is almost null. Carrier populations in the off-resonant ES and RS induced frequency shifts of the laser field respectively are

$$
\Delta\omega_N^{ES} = \frac{1}{2}\Gamma_P v_g g_{ES} F_{ES}^{GS} \tag{3.35}
$$

$$
\Delta\omega_N^{RS} = \frac{1}{2}\Gamma_P v_g g_{RS} F_{RS}^{GS} \tag{3.36}
$$

with coefficients

$$
F_{ES,RS}^{GS} = \frac{\omega_{GS}}{\omega_{ES,RS}} \frac{(\omega_{ES,RS}-\omega_{GS})T_D}{1+(\omega_{ES,RS}-\omega_{GS})^2 T_D^2} \tag{3.37}
$$

From Eq. (3.31), the resonant GS has no contribution to the refractive index change, which is the case when the laser is operated at the gain peak together with a symmetric gain distribution. Nevertheless, as mentioned in the introduction due to the asymmetric Qdot size dispersion the resonant state induces a finite α-factor α_H^{GS}, and the corresponding frequency shift with respect to the cold cavity can be expressed by:

$$
\Delta\omega_N^{GS} = \frac{1}{2}\Gamma_P v_g g_{GS} \alpha_H^{GS} \tag{3.38}
$$

Employing Eqs. (3.33)-(3.38), the electric field (3.29) is re-expressed as

$$
\frac{dE(t)}{dt} = \frac{1}{2}\left(\Gamma_P v_g g_{GS} - \frac{1}{\tau_P}\right)E(t) + j\left(\Delta\omega_N^{GS} + \Delta\omega_N^{ES} + \Delta\omega_N^{RS}\right)E(t) \tag{3.39}
$$

With carrier injection, the lasing frequency becomes $\omega_{LS} = \omega_{th}^{LS} + \Delta\omega_N^{LS}$, where $\Delta\omega_N^{LS} = \Delta\omega_N^{GS} + \Delta\omega_N^{ES} + \Delta\omega_N^{RS}$ gives the total frequency shift of the electric field from its threshold value (ω_{th}^{LS}). Through the $E(t) = \sqrt{S(t)V/\Gamma_P}\, e^{j\phi(t)}$ relationship, the photon density $S(t)$ and the phase $\phi(t)$ can be separately described. Combining with the equations describing the carrier dynamics in Qdot lasers, the laser system is finally given by:

$$\frac{dN_{RS}}{dt} = \frac{I}{qV} + \frac{N_{ES}}{\tau_{RS}^{ES}} - \frac{N_{RS}}{\tau_{ES}^{RS}}\left(1-\rho_{ES}\right) - \frac{N_{RS}}{\tau_{RS}^{spon}} \tag{3.40}$$

$$\frac{dN_{ES}}{dt} = \left(\frac{N_{RS}}{\tau_{ES}^{RS}} + \frac{N_{GS}}{\tau_{ES}^{GS}}\right)\left(1-\rho_{ES}\right) - \frac{N_{ES}}{\tau_{GS}^{ES}}\left(1-\rho_{GS}\right) - \frac{N_{ES}}{\tau_{RS}^{ES}} - \frac{N_{ES}}{\tau_{ES}^{spon}} \tag{3.41}$$

$$\frac{dN_{GS}}{dt} = \frac{N_{ES}}{\tau_{GS}^{ES}}\left(1-\rho_{GS}\right) - \frac{N_{GS}}{\tau_{ES}^{GS}}\left(1-\rho_{ES}\right) - v_g g_{GS} S_{GS} - \frac{N_{GS}}{\tau_{GS}^{spon}} \tag{3.42}$$

$$\frac{dS_{GS}}{dt} = \left(\Gamma_p v_g g_{GS} - \frac{1}{\tau_P}\right) S_{GS} + \beta_{SP}\frac{N_{GS}}{\tau_{GS}^{spon}} \tag{3.43}$$

$$\frac{d\phi}{dt} = \Delta\omega_N^{GS} + \Delta\omega_N^{ES} + \Delta\omega_N^{RS} \tag{3.44}$$

where τ_{GS}^{spon} is the spontaneous emission time and β_{SP} is the spontaneous emission factor. Carriers in the RS are scattered into the dots through the phonon-assisted and Auger-assisted processes [Ohnesorge96], [Ignatiev00]. The latter one makes the scattering rates nonlinearly depend on the carrier density in the RS. However, for the sake of simplicity, the carrier capture time τ_{ES}^{RS} and the relaxation time τ_{GS}^{ES} are both treated as constants in this work. On the other hand, the carrier-escape times (τ_{RS}^{ES} , τ_{ES}^{GS}) are governed by the Fermi distribution for a quasi-thermal equilibrium system [Grillot08]. For semiconductor lasers operating under small-signal modulation with frequency ω , the bias current change δI induces variations of the carriers δN_X , the photon δS_{GS} and the phase $\delta\phi$. In order to perform analytical analyses, the differential rate equations are derived as follows:

$$\begin{bmatrix} \gamma_{11}+j\omega & -\gamma_{12} & 0 & 0 & 0 \\ -\gamma_{21} & \gamma_{22}+j\omega & -\gamma_{23} & 0 & 0 \\ 0 & -\gamma_{32} & \gamma_{33}+j\omega & -\gamma_{34} & 0 \\ 0 & 0 & -\gamma_{43} & \gamma_{44}+j\omega & 0 \\ -\gamma_{51} & -\gamma_{52} & -\gamma_{53} & -\gamma_{54} & j\omega \end{bmatrix} \begin{bmatrix} \delta N_{RS} \\ \delta N_{ES} \\ \delta N_{GS} \\ \delta S_{GS} \\ \delta\phi \end{bmatrix} = \frac{\delta I}{qV} \begin{bmatrix} 1 \\ 0 \\ 0 \\ 0 \\ 0 \end{bmatrix} \tag{3.45}$$

where

$$\gamma_{11}=\frac{1-\rho_{ES}}{\tau_{ES}^{RS}}+\frac{1}{\tau_{RS}^{spon}};\ \gamma_{12}=\frac{1}{\tau_{RS}^{ES}}+\frac{1}{4N_B}\frac{N_{RS}}{\tau_{ES}^{RS}};\ \gamma_{21}=\frac{1-\rho_{ES}}{\tau_{ES}^{RS}};\ \gamma_{22}=\frac{1-\rho_{GS}}{\tau_{GS}^{ES}}+\frac{1}{\tau_{RS}^{ES}}+\frac{1}{\tau_{ES}^{spon}}+\frac{1}{4N_B}\frac{N_{RS}}{\tau_{ES}^{RS}}+\frac{1}{4N_B}\frac{N_{GS}}{\tau_{ES}^{GS}};$$
$$\gamma_{23}=\frac{1-\rho_{ES}}{\tau_{ES}^{GS}}+\frac{1}{2N_B}\frac{N_{ES}}{\tau_{GS}^{ES}};\ \gamma_{32}=\frac{1-\rho_{GS}}{\tau_{GS}^{ES}}+\frac{1}{4N_B}\frac{N_{GS}}{\tau_{ES}^{GS}};\ \gamma_{33}=\frac{1-\rho_{ES}}{\tau_{ES}^{GS}}+\frac{1}{\tau_{GS}^{spon}}+\frac{1}{2N_B}\frac{N_{ES}}{\tau_{GS}^{ES}}+v_g aS_{GS};$$
$$\gamma_{34}=-v_g g_{GS}+v_g a_P S_{GS};\ \gamma_{43}=\Gamma_p v_g aS_{GS}+\frac{\Gamma_p\beta_{SP}}{\tau_{GS}^{spon}};\ \gamma_{44}=-\Gamma_p v_g g_{GS}+\frac{1}{\tau_p}+\Gamma_p v_g a_P S_{GS};\ \gamma_{51}=\Gamma_p v_g a_{RS}F_{RS};$$
$$\gamma_{52}=\frac{1}{4}\Gamma_p v_g a_{ES}F_{ES};\ \gamma_{53}=\frac{1}{2}\Gamma_p v_g a\alpha_H^{GS};\ \gamma_{54}=-\frac{1}{2}\Gamma_p v_g a_P\alpha_H^{GS}; \tag{3.46}$$

with

$$a=\frac{\partial g_{GS}}{\partial N_{GS}}=\frac{a_{GS}}{1+\xi S_{GS}};\ a_P=-\frac{\partial g_{GS}}{\partial S_{GS}}=\frac{\xi}{1+\xi S_{GS}}g_{GS} \tag{3.47}$$

Based on the above differential rate equations, the α-factor of the Qdot laser is derived as

$$\alpha_{H,QD}^{GS}(\omega)=\frac{2}{\Gamma_P v_g}\frac{\delta\left[\Delta\omega_N^{LS}(N)\right]}{\delta g_{GS}(N)}\equiv\alpha_H^{GS}+\frac{1}{2}F_{ES}\frac{a_{ES}\delta N_{ES}}{a\delta N_{GS}}+2F_{RS}\frac{a_{RS}\delta N_{RS}}{a\delta N_{GS}} \tag{3.48}$$

Following the definition in Eq. (2.12), it is noted that only the carrier contribution (δN) is included in the above equation, while the photon contribution (δS) is excluded. In the following, it will be shown that the α-factor of Qdot lasers presents peculiar characteristics under direct modulation.

Over the last decades, various techniques have been proposed for the measurement of the α-factor. In this work, we employ the well-kown "FM/AM" technique for the above-threshold and the widely used "Hakki-Paoli" method for the below-threshold analyses, respectively [Osinski87]. The "FM/AM" technique relies on the direct current modulation of the laser, which generates both the optical frequency (FM) and amplitude (AM) modulations [Provost11]. With respect to the linearized rate equations, the ratio of the FM-to-AM index is derived as

$$2\frac{\beta(\omega)}{m(\omega)}=2\frac{\delta\omega_{LS}/\omega}{\delta S_{GS}/S_{GS}}$$
$$\equiv\frac{j\omega+\left(1/\tau_P-\Gamma_P v_g g_{GS}+\Gamma_p v_g a_P S_{GS}\right)}{j\omega}\times\left[\alpha_H^{GS}\left(1-\frac{a_P\delta S_{GS}}{a\delta N_{GS}}\right)+\frac{1}{2}F_{ES}\frac{a_{ES}\delta N_{ES}}{a\delta N_{GS}}+2F_{RS}\frac{a_{RS}\delta N_{RS}}{a\delta N_{GS}}\right] \tag{3.49}$$

where the relation $\delta\omega_{LS}=j\omega\delta\phi$ is used in the above derivation. In this approach, the laser's α-factor is usually extracted through the formula $\alpha_{H,QD}^{FM/AM}=\min\left\{2\beta(\omega)/m(\omega)\right\}$. This is indeed true for Qwell or bulk lasers, however, this work will show that the α-factor of Qdot lasers is dependent on the modulation frequency but we still take the minimum value to characterize the Qdot laser as reported in [Melnik06].

For semiconductor lasers operating below threshold, the "Hakki-Paoli" method relies on the direct measurement of the optical spectra of amplified spontaneous emission (ASE) in the laser cavity. Tuning the pump current slightly step by step (ΔI), the gain change can be extracted by

the Hakki-Paoli method and the wavelength variation can be directly recorded using an optical spectrum analyzer. Correspondingly, the below-threshold α-factor is calculated as

$$\alpha_{H,QD}^{ASE} = \alpha_H^{GS} + \frac{1}{2} F_{ES}^{GS} \frac{a_{ES}}{a_{GS}} \frac{\Delta N_{ES}}{\Delta N_{GS}} + 2 F_{RS}^{GS} \frac{a_{RS}}{a_{GS}} \frac{\Delta N_{RS}}{\Delta N_{GS}} \tag{3.50}$$

The laser parameters used in the simulation are listed in Table 3.2 [Martinez08], [Miska08], [Cornet04]. It is noted that the carrier occupation in the GS has a small contribution to the α-factor (less than 1) [Mi07], hence we assume the value α_H^{GS}=0.5 in the simulation. Figure 3.9 depicts the carrier density variations in the three states under small signal modulation. For low frequencies smaller than 0.1 GHz, all the carrier density variations remain almost constant, but the variations of the ES (δN_{ES}) and RS (δN_{RS}) populations are 15 dB larger than that of the GS (δN_{GS}) one. The small variation of the GS carrier population is associated with the gain clamping above threshold. Both δN_{GS} and δN_{ES} exhibit resonances around 7 GHz. Beyond the resonance frequency, δN_{GS} decays faster than δN_{ES} and δN_{RS}. These features significantly impact the behaviour of the α-factor as described in Eq. (3.48).

Table 3.2. Qdot material and laser parameters for study of the α-factor

Symbol	Description	Value	Symbol	Description	Value
L	Active region length	5×10^{-2} cm	τ_{ES}^{RS}	Capture time from RS to ES	6.3 ps
W	Active region width	4×10^{-4} cm	τ_{GS}^{ES}	Relaxation time from ES to GS	2.9 ps
R_1=R_2	Mirror reflectivity	0.32	a_{GS}	GS differential gain	5×10^{-15} cm^2
n_r	Refractive index	3.5	a_{ES}	ES differential gain	10×10^{-15} cm^2
α_i	Internal modal loss	6 cm^{-1}	a_{RS}	RS differential gain	2.5×10^{-15} cm^2
N_B	Dot density	10×10^{10} cm^{-2}	ξ	Gain compression factor	2×10^{-16} cm^3
H_B	Dot height	5×10^{-7} cm	α_H^{GS}	GS induced α-factor	0.5
E_{RS}	RS transition energy	0.97 eV	T_D	Dephasing time	0.1 ps
E_{ES}	ES transition energy	0.87 eV	Γ_p	Optical confinement factor	0.06
E_{GS}	GS transition energy	0.82 eV	β_{SP}	Spontaneous emission factor	1×10^{-4}

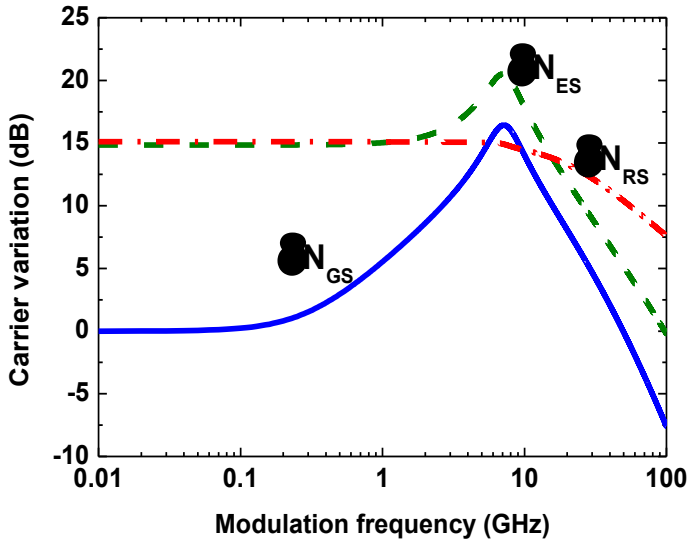

Fig. 3.9. Small-signal carrier density variations in the GS (solid line), ES (dashed line), and RS (dash-dot line) versus modulation frequency. The bias current is $I=1.2\times I_{th}$, with the threshold current I_{th}=49 mA. The carrier variation is normalized to the value δN_{GS} of 0.01 GHz.

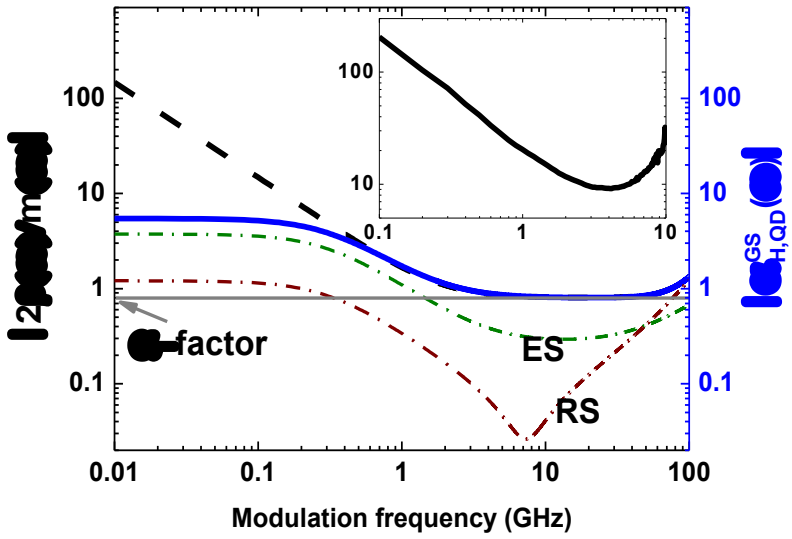

Fig. 3.10. Modulation-frequency dependence of the FM-to-AM ratio (dash) and of the α-factor (thick solid). The minimum level indicated by the horizontal line gives the laser's conventional α-factor. The thin dash-dotted curve represents the sole contribution of the ES or the RS to the α-factor, respectively. The inset shows an experimental curve of the FM-to-AM ratio for a Qdot laser.

Fig. 3.10 compares the difference between the α-factor $\left|\alpha_{H,QD}^{GS}(\omega)\right|$ and the ratio $\left|2\beta(\omega)/m(\omega)\right|$ as a function of the modulation frequency. At low frequencies smaller than 0.1 GHz, there is a large discrepancy between the two parameters. As expected, $\left|2\beta(\omega)/m(\omega)\right|$ exhibits large values due to the gain compression and the large carrier variations in the ES and

in the RS. Nevertheless, $\left|\alpha_{H,QD}^{GS}(\omega)\right|$ remains constant. Increasing the modulation frequency beyond several GHz, the two values of both parameters decrease down to a plateau, which gives the conventional α-factor indicated by the horizontal line. As can be seen, $\alpha_{H,QD}^{FM/AM}$ is almost the same as $\left|\alpha_{H,QD}^{GS}\right|$, which indicates that the FM/AM method is a reliable technique for the measurement of Qdot laser's α-factor. Further increase of the modulation frequency raises again both the two values as observed experimentally in a Qdot laser (inset of Fig. 3.10) [Gerhard08]. It is emphasized that such a situation is not encountered in Qwell lasers [Provost11]. This behavior is attributed to the different decay rates (versus modulation frequency) of carrier variations in each state as shown in Fig. 3.9. In addition, Fig. 3.10 (dash-dotted curves) shows that the ES contributes more to the α-factor $\left|\alpha_{H,QD}^{GS}\right|$ than the RS due to its smaller energy separation with the resonant GS.

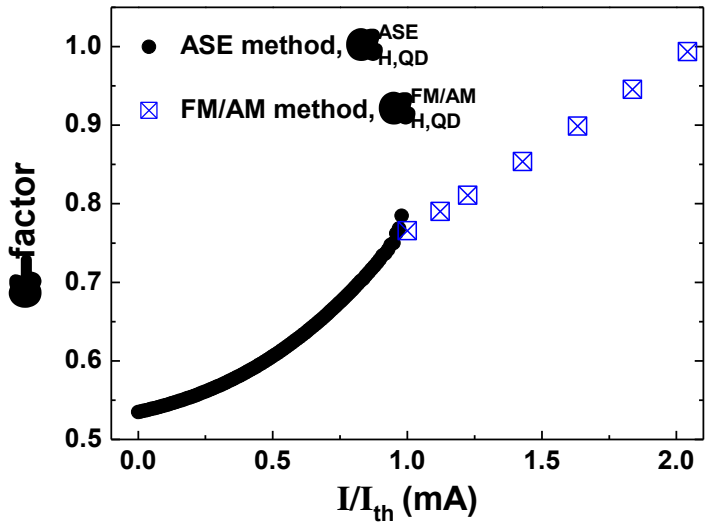

Fig. 3.11. α-factor as a function of the normalized bias current I/I$_{th}$.

Based on the ASE and the FM/AM methods, Fig. 3.11 illustrates the α-factor as a function of the normalized pump current I/I$_{th}$. Below threshold, carrier populations in both the resonant and off-resonant states increase with the pump current. In consequence, the α-factor increases nonlinearly. Above threshold, the carrier population in the GS is clamped, while the off-resonant state populations keep increasing. Thus, the α-factor varies almost linearly above threshold as usually measured in experiments [Martinez08], [Gioannini07]. At threshold, the α-factor extracted from the ASE method is similar to that using the FM/AM technique. In addition, the α-factor is larger than the sole GS-induced value of α_H^{GS} =0.5 both below and above threshold, which means the off-resonant ES and RS contribute to the increase of the α-factor in

the Qdot laser. This is explained by the fact that the coefficients F_{ES}^{GS} and F_{RS}^{GS} are both positive since the ES and RS have higher energies than the GS (see Eq. (3.37)).

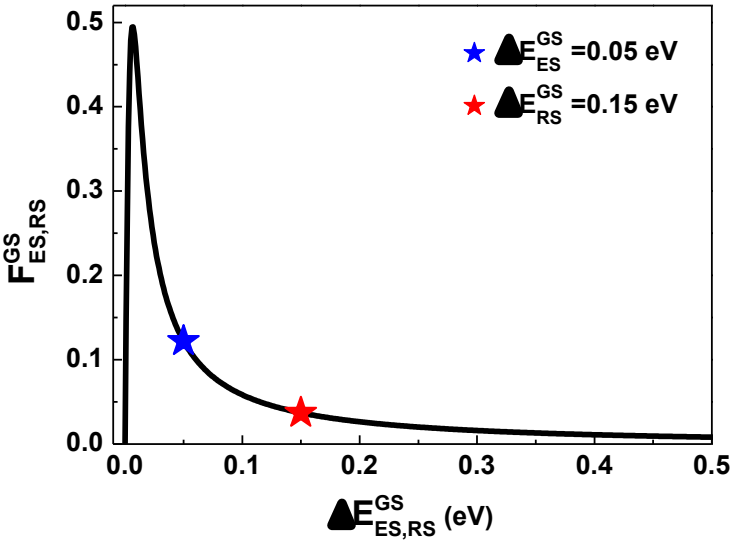

Fig. 3.12. $F_{ES,RS}^{GS}$ dependence on the GS-ES separation ΔE_{ES}^{GS} and the GS-RS separation ΔE_{RS}^{GS}. The stars indicate the values used in Fig. 3.10.

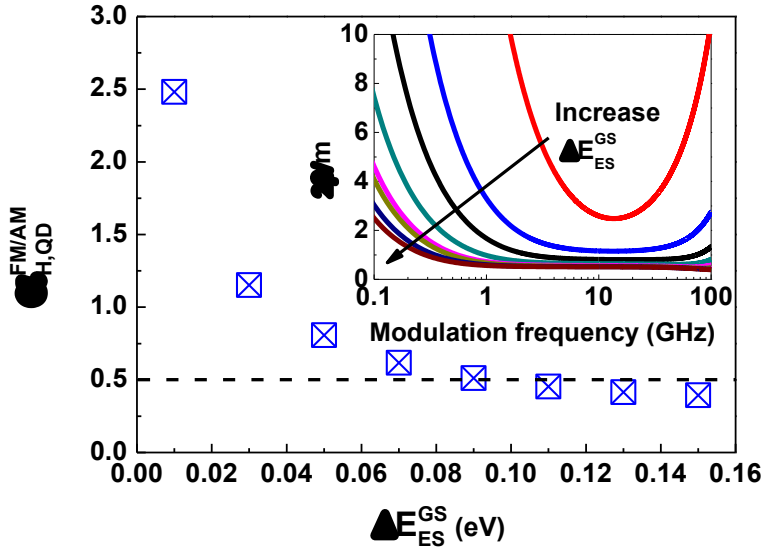

FIG. 3.13. $\alpha_{H,QD}^{FM/AM}$ dependence on the GS-ES separation ΔE_{ES}^{GS} using Eq. (16). The GS transition energy is E_{GS}=0.82 eV, and the GS-RS separation is kept as $\Delta E_{RS}^{GS} = 3 \times \Delta E_{ES}^{GS}$. Inset shows the corresponding dependence of $2\beta/m$ on the modulation frequency. The simulated range is from 10 meV up to 150 meV.

In addition, Eq. (3.37) points out that the α-factor coefficients $F_{ES,RS}^{GS}$ strongly rely on the energy separation between the GS and the off-resonant states. As presented in Fig. 3.12, $F_{ES,RS}^{GS}$ undergo a drastic increase at small energy separation and peaks around a separation of 0.01 eV.

Then, the $F_{ES,RS}^{GS}$ values decrease toward zero when increasing the energy separation. Thus, for large separations (>0.3 eV), the ES and the RS have little contribution to the laser's α-factor, which is therefore mainly limited by the symmetry of the inhomogeneous broadening.

Figure 3.13 depicts the α-factor dependence on the GS-ES separation ΔE_{ES}^{GS}, where the GS-RS separation is kept as $\Delta E_{RS}^{GS} = 3 \times \Delta E_{ES}^{GS}$. It is noted that the carrier capture and relaxation times are fixed as shown in Table 3.2, since the carrier scattering rates are weakly dependent on the energy separation [Schuh13]. For a small separation ΔE_{ES}^{GS}=0.01 eV, the laser exhibits a large α-factor with a value of 2.5 due to the contribution of carrier populations in the ES and the RS, which is 5-fold higher than α_H^{GS}. Enlarging the energy separation reduces the value of α-factor [Molina06]. The value can be even slightly smaller than α_H^{GS} due to the gain compression as shown in Eq. (3.48). The inset of Fig. 3.13 presents the corresponding variation of $2\beta / m$ as a function of the modulation frequency. It shows for the first time that Qdot lasers of larger energy separation not only exhibit a smaller α-factor, but also a lower FM-to-AM index ratio over all the low and high frequencies. Especially, a large energy separation significantly suppresses the re-increase of $2\beta / m$ at high modulation frequencies due to the decoupling between the GS and the off-resonant states. Therefore, the simulations unveil that strongly confined Qdots are more favorable to realize low chirp laser devices with small α-factor. A trade-off between this condition and the required 1.55 μm GS emission has however to be considered. Growth optimization of InAs/InP to meet both requirements can be achieved via a careful tuning of the radius and thickness of the Qdot.

3.3. Frequency chirp

As we saw in the previous sections, direct current modulation of a semiconductor laser results in the modulation of both photon and carrier densities. The modulation of the carrier density modulates the gain as well as the refractive index. As a result, the optical length of the cavity is modulated by the current, causing the resonant mode to shift back and forth in frequency. This frequency chirping broadens the modulated spectrum of the laser, hindering its effectiveness in optical fiber communications. The frequency chirp property of semiconductor lasers can be characterized either by the frequency modulation (FM) response ($\delta\omega_{LS} / \delta I$) or by the chirp-to-power ratio (CPR). Since the frequency chirping level is dependent on the laser intensity variation, here we employ the latter measurement. Following the analysis in Section 3.2, the CPR is defined as:

$$CPR_{GS}(\omega)=\frac{\delta\omega_{LS}(\omega)}{\delta S_{GS}(\omega)}\approx\frac{\alpha_{H,QD}^{GS}}{2S_{GS}}\left(j\omega+\Gamma_p v_g a_{GS}^{p} S_{GS}\right) \tag{3.51}$$

Employing this formula, Fig. 3.14 shows the CPR of the Qdot laser for various bias condition from $1.1I_{th}$ up to $2.9I_{th}$. In the adiabatic chirp regime, the gain compression effect dominates and the CPR can be approximated by $\Gamma_p v_g a_{GS}^{p}\alpha_{H,QD}^{GS}/2$. As the thermal effect is not included, the CPR remains constant (less than 1 GHz/mW) for modulation frequencies below 1 GHz. In this regime, the CPR value is roughly the same for all the bias currents. For higher modulation frequencies, the CPR rises almost parabolically with the modulation frequency following the relation $j\omega\alpha_{H,QD}^{GS}/(2S_{GS})$. It is shown that higher bias current effectively reduces the CPR of Qdot lasers.

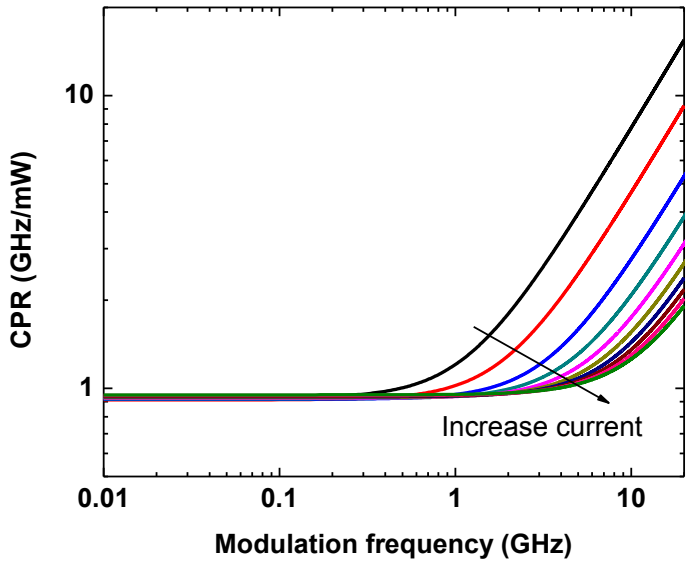

Fig. 3.14. CPR of the Qdot laser for various bias currents.

3.4. Qdot laser operating on the excited state

Qdot lasers are usually engineered to operate on the GS optical transition because of its low operation current in contrast to the higher-energy bound states. Nevertheless, as discussed in the previous sections, there are several limitations for Qdot lasers operating on the GS: On one hand, the modulation bandwidth is inherently limited by the slow carrier dynamics [Wu13], the low differential gain as well as the large gain compression factor [Martinez08], [Zhukov13]. On the other hand, the GS lasing laser does not necessarily exhibit a small α-factor, which is a good prerequisite for chirpless operation in fiber-based optical telecommunication.

Alternatively, exploiting the stimulated emission from ES nanostructures could be a promising option to enhance the laser's dynamic performance.

In practice, the ES emission can be achieved by increasing the bias current, shortening the cavity length, coating the cavity facets or via coupling gratings [Stevens09], [Lee11], [Lv10], [Lin12], [Parantheon03], [Grillot11], [Naderi10]. However, ES lasing devices draw less attention because of the high operation current as well as the short wavelength located out of the C-band optical communication window in the fibre (1530 nm-1565 nm). However, in the InAs/InP Qdot material system, the GS laser has natural potential to emit at 1.60~1.65 μm, longer than the C-band wavelengths. Consequently, since the ES has a higher optical transition energy than the GS, it is indeed possible to tune the ES emission back within the C band through proper band energy engineering and growth optimizations like the double cap procedure [Paranthoen01], [Cornet06]. On the other hand, the ES in Qdots shows faster carrier capture rates from the surrounding carrier reservoir as well as a higher saturated gain than the GS [Stevens09], [Lee11]. Indeed, Qdot lasers operating on the ES has shown a broader modulation bandwidth and the K-factor limited bandwidth is estimated almost twice of that in the GS lasing [Xu10]. A recent experimental work has demonstrated an ES emission InAs/GaAs Qdot laser with a large-signal modulation capability up to 22.5 Gbps [Arsenijevi14]. In addition, the ES emission exhibits a smaller α-factor in comparison with the GS emission in a Qdot laser [Xu12], [Xiao13].

In order to compare the performance of the Qdot laser operating on the ES with that on the GS, we reuse rate equations (3.40)-(3.44) by considering stimulated emission on the ES instead of the GS. The gain terms are the same as Eq. (3.33), while the different contributions to the instantaneous electric field frequency shift (3.35)-(3.38) are revised as:

$$\Delta\omega_N^{GS} = \frac{1}{2}\Gamma_P v_g g_{GS} F_{GS}^{LS} \tag{3.52}$$

$$\Delta\omega_N^{ES} = \frac{1}{2}\Gamma_P v_g g_{ES} \alpha_H^{ES} \tag{3.53}$$

$$\Delta\omega_N^{RS} = \frac{1}{2}\Gamma_P v_g g_{RS} F_{RS}^{LS} \tag{3.54}$$

with the coefficient

$$F_{GS,RS}^{LS} = \frac{\omega_{LS}^0}{\omega_{GS,RS}} \frac{(\omega_{GS,RS} - \omega_{LS}^0)T_D}{1 + (\omega_{GS,RS} - \omega_{LS}^0)^2 T_D^2} \tag{3.55}$$

Correspondingly, the phase-amplitude coupling of the electric field in the ES emission laser is given by:

$$\alpha_{QD}^{ES}(j\omega)=\alpha_{H}^{ES}+2F_{GS}^{ES}\frac{a_{GS}}{a_{ES}}\frac{\delta N_{GS}}{\delta N_{ES}}+4F_{RS}^{ES}\frac{a_{RS}}{a_{ES}}\frac{\delta N_{RS}}{\delta N_{ES}} \tag{3.56}$$

The α-factor extracted from the FM/AM technique is expressed as:

$$\alpha_{H,QD}^{FM/AM}=\left\{\frac{j\omega+(1/\tau_p-\Gamma_p v_g g_{ES}+\Gamma_p v_g a_P S_{ES})}{j\omega}\left[\alpha_H^{ES}\left(1-\frac{a_P\delta S_{ES}}{a_{ES}\delta N_{ES}}\right)+2F_{GS}^{ES}\frac{a_{GS}}{a_{ES}}\frac{\delta N_{GS}}{\delta N_{ES}}+4F_{RS}^{ES}\frac{a_{RS}}{a_{ES}}\frac{\delta N_{RS}}{\delta N_{ES}}\right]\right\}_{\min} \tag{3.57}$$

The below-threshold α-factor obtained from the Hakki-Paoli method is calculated by

$$\alpha_{H,QD}^{ASE}=\alpha_{H}^{ES}+2F_{GS}^{ES}\frac{a_{GS}}{a_{ES}}\frac{\Delta N_{GS}}{\Delta N_{ES}}+4F_{RS}^{ES}\frac{a_{RS}}{a_{ES}}\frac{\Delta N_{RS}}{\Delta N_{ES}} \tag{3.58}$$

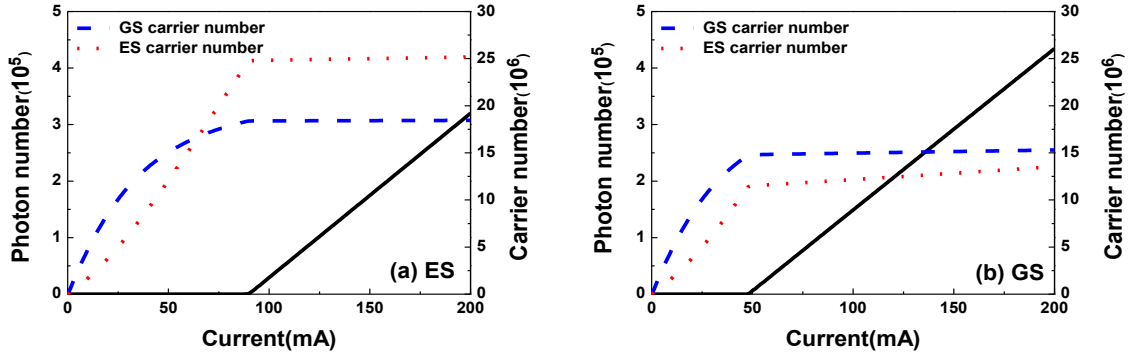

Fig. 3.15. Steady-state solution for (a) lasing in the ES and (b) lasing in the GS. Solid lines denote the photon number, dashed and dotted lines represent the carrier number in the GS and ES, respectively.

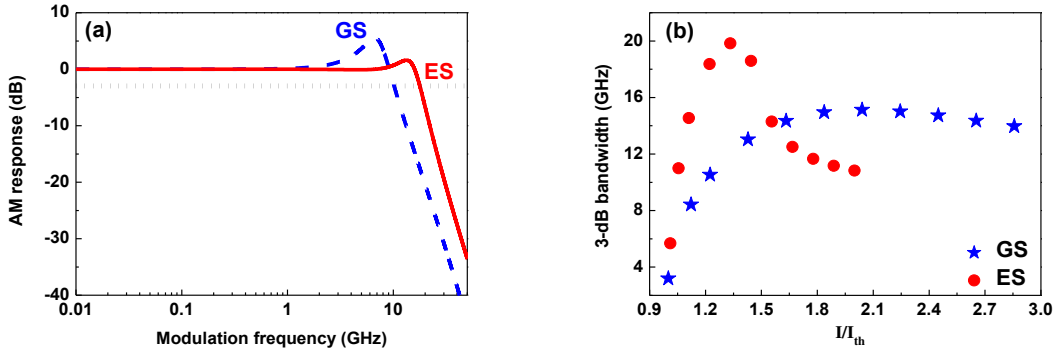

Fig. 3.16. (a) Intensity modulation response versus modulation frequency. The dotted line indicates the 3-dB modulation bandwidth. (b) 3-dB bandwidth for stimulated emissions in the ES and GS, respectively. The bias currents are set at I_{ES}=1.2×$I_{th,ES}$ and I_{GS}=1.2×$I_{th,GS}$.

Figure 3.15 compares the steady-state solutions of lasing in the ES (Fig. 3.15(a)) and in the GS (Fig. 3.15(b)). The threshold current of ES lasing is about 90 mA, which is 1.8-fold larger than that of the GS. In Fig. 3.15(a), carriers both in ES and GS are clamped above threshold, and the former population is larger due to the higher degeneracy of ES than GS. Thus, despite a higher threshold current, the ES does provide a larger saturated gain. In Fig. 3.15(b), however, the carrier population in the ES keeps increasing when the GS laser reaches the threshold current.

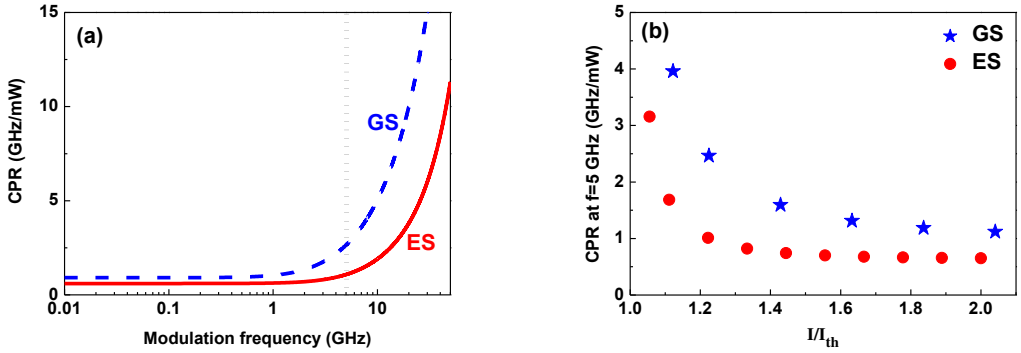

Fig. 3.17. (a) CPR response versus the modulation frequency. The bias currents are set at $I_{ES}=1.2\times I_{th,ES}$ and $I_{GS}=1.2\times I_{th,GS}$, respectively. The dotted line indicates CPR at modulation frequency f=5.0 GHz (b) CPR variation as a function of the normalized bias current (I/I_{th}) at f=5.0 GHz.

The computed AM responses for GS and ES lasing operations are shown in Fig. 3.16(a), respectively. As observed, the ES response indeed exhibits a broader and flatter response in contrast to the GS one. The broader bandwidth is partly attributed to the faster carrier capture time [Stevens09], as well as to the higher ES differential gain (a_{ES}) [Lee11], which is set two-fold larger than the GS one (a_{GS}). The lower resonance peak in the ES response indicates a stronger damping factor. From the AM response curve, the 3-dB modulation bandwidth is extracted and depicted in Fig. 3.16(b) as a function of the normalized bias current (I/I_{th}). The ES and GS bandwidths firstly increase with the bias current and then reach a maximum value. The calculated maximum ES bandwidth is about 5 GHz larger than the GS case. Further increase of the bias current reduces the bandwidth because the modulation response becomes over-damped [Asryan11]. It is found that the ES bandwidth decreases faster than the GS lasing case, which means that the ES damping factor is more sensitive to the bias current. It is noted that the carrier transport process from the SCH as well as the inhomogeneous broadening in the Qdots can further reduce the 3-dB bandwidth described in Fig. 3.16 [Asryan96]. Besides, the electrical parasitic effects limiting the modulation dynamics are out of the scope of the thesis.

Fig. 3.17(a) presents the CPR responses of the ES laser and of the GS laser. Due to the reduced α-factor in the ES (this will be discussed in the following section), the ES lasing CPR is found always smaller than the GS case. The difference becomes larger at high modulation frequencies. For instance, at 20 GHz the CPR of the ES laser is 60% smaller than that in the GS configuration. Figure 3.17(b) shows the CPR calculated at a fixed modulation frequency (5 GHz) as a function of the bias current. The CPR decreases with the pump current because of the higher output power and finally reaches a finite value. Still, the ES CPR remains lower than the GS CPR level. Since DM semiconductor lasers suffer significantly from the frequency chirp,

these results make the ES lasing transmitters very promising for the optical communication networks.

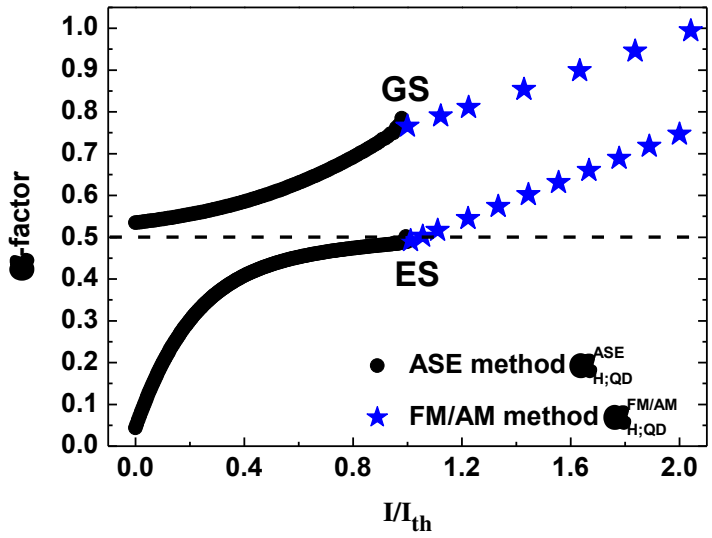

Fig. 3.18. A comparison on the α-factors between the ES and GS emission lasers. The dashed line gives the resonant state contributed part (0.5) of α-factor.

Figure 3.18 compares the variations of ES and GS α-factors with the injected current. Below threshold, carriers in both resonant and off-resonant states increase with the pump current and the α-factors rise nonlinearly. Above threshold, the carrier population in the resonant state is clamped while the α-factor evolution becomes relatively linear. At threshold, it is found that the α-factors extracted from the ASE method and from the FM/AM method are in good agreement. For both below and above threshold, the predicted ES α-factor is found always smaller than the GS one. The ES lasing α-factor at threshold is reduced by about 40% in contrast to the GS lasing case. It is noted that the GS α-factor is always larger than the resonant GS contribution part (α_H^{GS}=0.5), whereas the ES α-factor can be smaller than the resonant ES one (α_H^{ES}=0.5). That is because the energies of ES ($\hbar\omega_{ES}$) and RS ($\hbar\omega_{RS}$) are both higher than the GS one ($\hbar\omega_{GS}$), thus we obtain $F_{ES}^{GS}>0$ and $F_{RS}^{GS}>0$ (see section 3.2). So in the case of the Qdot laser operating on the GS transition, both the ES and the RS contribute to enhance the α-factor [Gioannini06], [Gioannini07]. In contrast for the ES lasing case depicted in Eq. (3.55) where $F_{GS}^{ES}<0$ and $F_{RS}^{ES}>0$, the lower-energy GS contributes to reduce the α-factor of ES laser while the RS remains increases its value. Therefore when the GS contributes more than the RS, the ES lasing α-factor is smaller than the sole resonant ES state induced part.

Figure 3.19 presents the variations of the $F_{GS,RS}^{ES}$ parameters for the ES emission as a function of GS-ES and ES-RS energy separations. For small energy separation values (~0.01 eV) the parameters $F_{GS,RS}^{ES}$ undergo drastic variations, followed by a rapid increase (decrease) with the enlarged energy split. It is also shown that those off-resonant states have little contribution to the α-factor when the energy separation becomes larger than 0.25 eV.

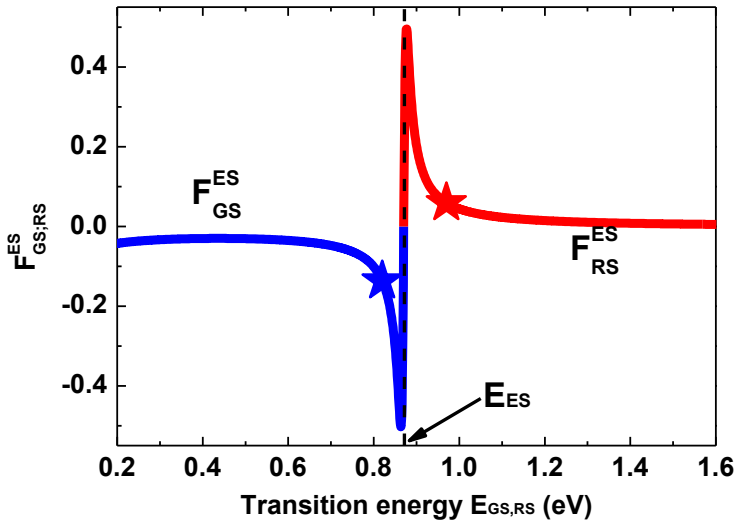

Fig. 3.19. Dependence of the $F_{GS,RS}^{ES}$ parameters on the GS-ES and ES-RS energy separations in the case of a Qdot laser emitting on its excited state. The dashed line indicates the ES emission energy of E_{ES}=0.87 eV, and the stars denote $F_{GS,RS}^{ES}$ values used in this work.

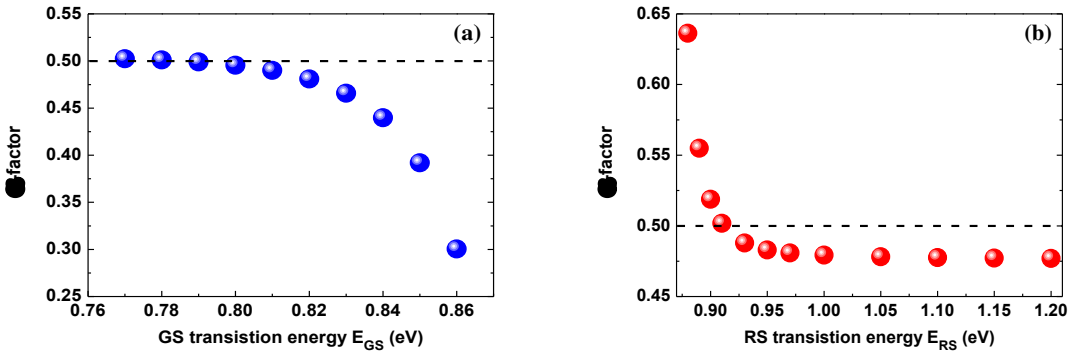

Fig. 3.20. α-factor dependence on the off-resonant state transition energy for the ES emission laser with E_{ES}=0.87 eV (a) as a function of GS transition energy E_{GS}, with E_{RS}=0.97 eV; (b) as a function of RS transition energy E_{RS}, with E_{GS}=0.82 eV. The dashed line indicates the resonant ES contributed part of the α-factor. The bias current is fixed at $I=0.9\times I_{th,ES}$.

Figure 3.20 depicts the below threshold α-factor dependence on the transition energy ($I=0.9\times I_{th,ES}$). Indeed, when the GS is localized far away from the ES, the GS has little influence on the α-factor value (Fig. 3.20(a)). But once the GS-ES separation is less than 60 meV, the α-

factor decreases rapidly with increasing GS transition energy E_{GS}. For a GS-ES separation of 10 meV, the α-factor value is reduced by about 40%. In contrast, Fig. 3.20(b) shows that small energy separation between the RS and the ES leads to a large α-factor. When the separation is less than 40 meV, the laser exhibits a higher value than the ES induced part, which means the RS contributes more than the GS on the α-factor. Increasing the RS energy E_{RS} reduces the α-factor and finally leads to a limit value of about 0.48 when the ES-RS separation is larger than 80 meV. Therefore, in order to reduce the α-factor of the ES emission laser, one potential option is to diminish the energy separation with the ES-GS separation (as opposed to the GS lasing case) while enlarging the ES-RS separation. In InAs/InP or InAs/GaAs material systems, the GS transition energy is mostly determined by the vertical confinement and thus the thickness of the Qdot, while the ES-GS energy splitting is related to Qdot lateral confinement [Garcie97],[Raz03],[Even04]. The simulation results provide some basic guidance for the fabrication of zero α-factors of Qdot lasers through proper quantum engineering of the bound and continuum electronic states.

Finally, regarding the reduction of the lasing threshold, the ES emission can be selected by inhibiting the GS one through a dichroic mirror or by external forcing based on optical inejction or optical feedback. The rear facet reflectivity of the Qdot laser can then be modified by depositing a specific dichroic mirror that has a maximum of reflectivity in resonance with the ES wavelength. In such way this modification will reduce the threshold for the ES lasing and completely inhibit oscillation at the GS optical transition.

In summary, although the ES laser requires a higher operation current, it does provide a larger modulation bandwidth and a lower frequency chirp, which are expected to be much superior to those of GS lasers. In addition, the ES laser exhibits a smaller α-factor due to the contribution of the off-resonant GS. From the semi-analytical analysis, calculations provide a guidance to reduce the ES lasing α-factor to zero through the band energy engineering.

3.5. Impacts of gain compression

Based on rate equations (3.40)-(3.44), as well as the analysis on the modulation dynamics in the previous sections, this part investigates the impacts of gain compression effect on the modulation dynamics of GS lasing Qdot lasers including the AM response, the α-factor and the CPR. The gain compression factor values used for Figs. 3.21-3.23 vary from 10^{-17} cm^3 up to 10^{-14} cm^3 (ξ=1×10^{-17}, 1×10^{-16}, 5×10^{-16}, 1×10^{-15}, 5×10^{-15}, 1×10^{-14} cm^3).

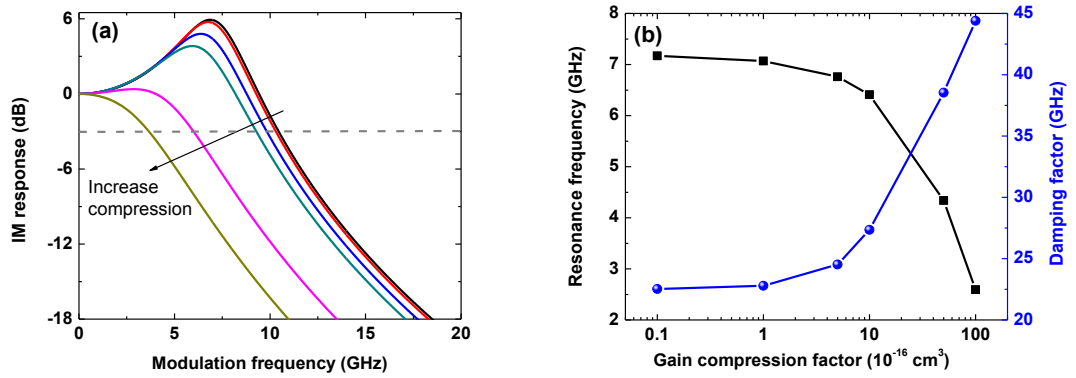

Fig. 3.21. (a) Gain compression effect on the IM response; (b) Resonance frequency and damping factor as a function of gain compression factor.

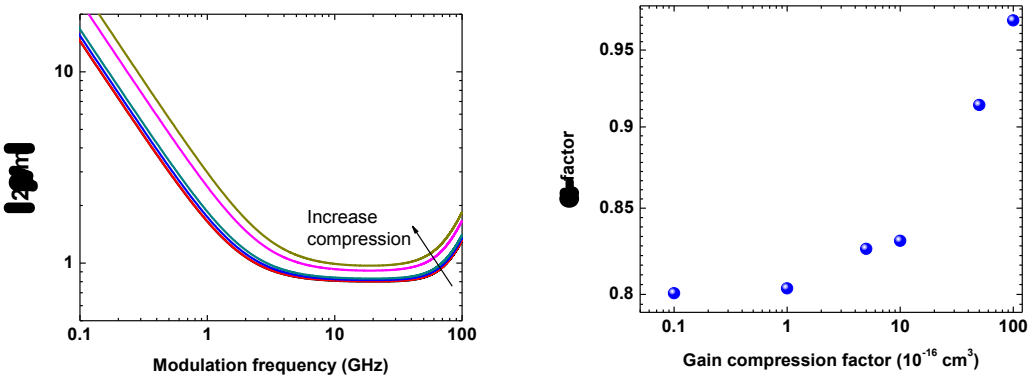

Fig. 3.22. (a) Gain compression effect on the ratio of FM-to-AM index; (b) α-factor variation (extracted from plot (a)) as a function of gain compression factor.

Figure 3.21(a) shows that the gain compression effect suppresses the resonance peak and reduce the 3-dB modulation bandwidth in the AM response. The bandwidth decreases from 10.5 GHz for ξ=1×10^{-17} cm^3 down to 3.7 GHz for ξ=1×10^{-14} cm^3. From the analysis of the eigenvalues of the Qdot laser system, which are obtained by solving the determinant of the coefficient matrix in the differential rate equation system (see Eqs. (3.45)-(3.47)). We extracted the resonance frequency f_R and damping factor Γ from the pair of conjugate complex values $p_{1,2}$ through the relationship $p_{1,2} = -\Gamma/2 + j2\pi f_R$. As shown in Fig. 3.21(b), the resonance frequency decreases with the gain compression factor, while the damping factor increases with the latter. Especially when ξ >10^{-15} cm^3, the gain compression strongly degrades the AM performance of the Qdot laser. Figure 3.22 presents the impacts of the gain compression on the α-factor (Fig. 3.22(b)), which is extracted from the ratio of FM-to-AM index (Fig. 3.22(a)). The α-factor is raised by about 21% from 0.80 to 0.97 with the increasing gain compression factor. As expected in Eq. (3.51), Figure 3.23 shows that high gain compression enhances the adiabatic chirp in the modulation response of the CPR.

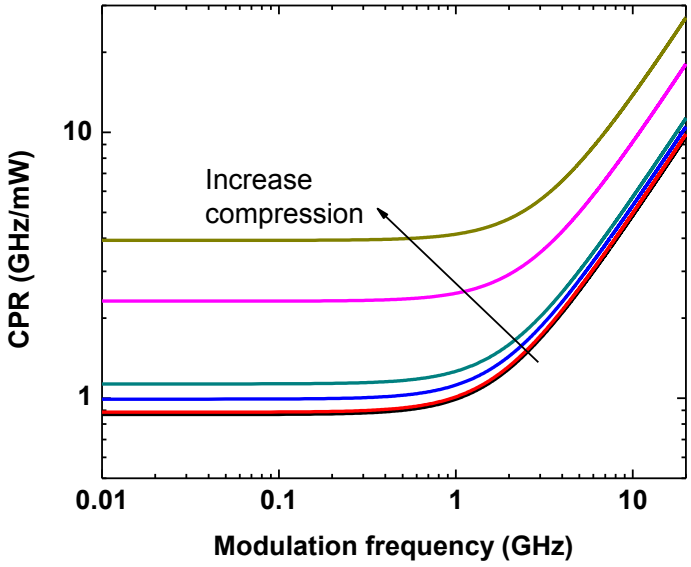

Fig. 3.23. Gain compression effect on the CPR.

3.6. Impacts of carrier capture and relaxation processes

As mentioned in chapter 2, the Qdot laser involves carrier capture process from the 2D RS to the localized ES and carrier relaxation process from the ES to the GS inside the dots. This section discusses the influences of these processes on the lasers' modulation dynamics. The analysis is still based on the rate equations (3.40)-(3.44) as well as the discussions in sections 3.2 and 3.3.

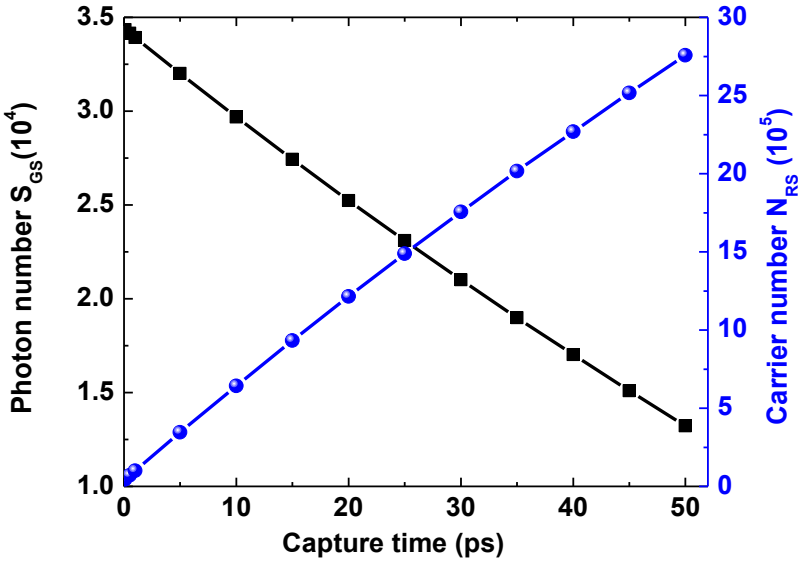

Fig. 3.24. Steady-state solutions as a function of carrier capture time. Carrier populations in the ES N_{ES} and in the GS N_{GS} stay almost constant (not shown).

A) Impacts of the carrier capture time from the RS to the ES

In order to focus on the impacts of the carrier capture process, the carrier relaxation time τ_{GS}^{ES} is fixed at 2.9 ps, while the carrier capture time τ_{ES}^{RS} is varied from 0.1 ps up to 50 ps. We firstly examined the steady-state solutions. It is found that the carrier capture process has little impact on the carrier population in the ES or in the GS (not shown). In contrast, as shown in Fig. 3.24, slow carrier capture process significantly accumulates carriers in the 2D carrier reservoir. The carrier number N_{RS} increases linearly by about two orders of magnitude from 4.5×10^4 for τ_{ES}^{RS} =0.1 ps to 2.8×10^6 for τ_{ES}^{RS} =50 ps. Meanwhile, the emitted photon number S_{GS} is reduced linearly by the slow capture process.

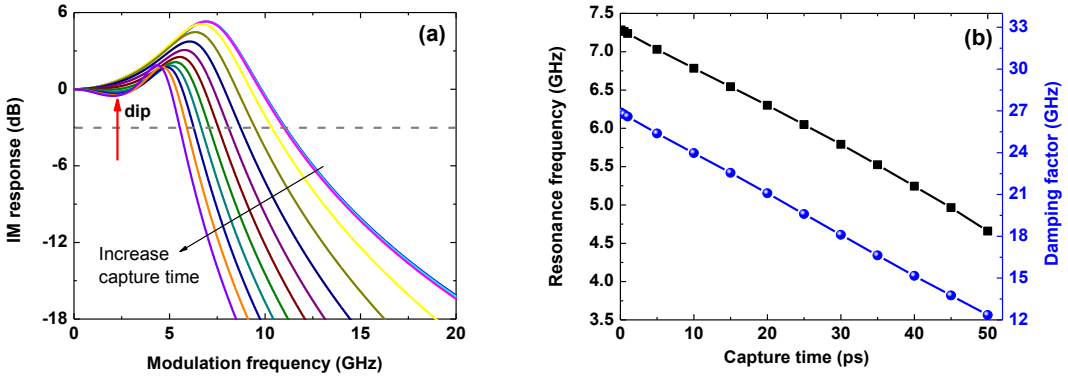

Fig. 3.25. (a) Influence of carrier capture time on the IM response; (b) Resonance frequency and damping factor as a function of the capture time.

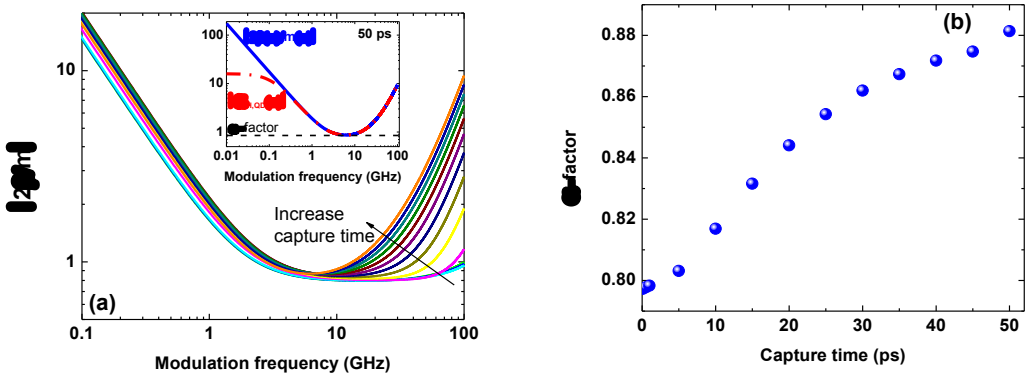

Fig. 3.26. (a) Influence of carrier capture time on the ratio of FM-to-AM index. Inset shows its comparison with the directly calculated α-factor using Eq. (3.48) for τ_{ES}^{RS} =50 ps. (b) α-factor variation (extracted from plot (a)) as a function of the capture time.

Figure 3.25(a) shows the variation of the IM response for different capture times. Slow capture process reduces the 3-dB modulation bandwidth, from 11 GHz down to 7 GHz. Besides, the resonance peak is also slightly reduced. Interestingly, for capture times larger than 30 ps, a parasitic-like roll-off (dip) appears in the response, which is similar to the effect of slow carrier

transport process from the 3D barrier to the 2D RS. [Coldren95]. Figure 3.25(b) describes the resonance frequency f_R and the damping factor Γ extracted from the eigenvalues of the Qdot laser system. It is shown that both f_R and Γ decrease linearly with the carrier capture time.

Figure 3.26(a) illustrates that the ratio of FM-to-AM index $|2\beta/m|$ exhibits a significant re-increase beyond 10 GHz for slow carrier capture process (large capture time). With respect to Eq. (3.48), this can be attributed to the larger carrier variation in the RS δN_{RS} under high frequency modulation since the number of available carriers in the RS is larger (see Fig. 3.24). Figure 3.26(b) indicates that increasing the carrier capture time enhances the α-factor by 11% from 0.80 for τ_{ES}^{RS} =0.10 ps to 0.88 for τ_{ES}^{RS} =50 ps. Because of the large α-factor for slow capture process, the overall CPR in Fig. 3.27 is also enlarged both in the adiabatic and the high modulation frequency regimes.

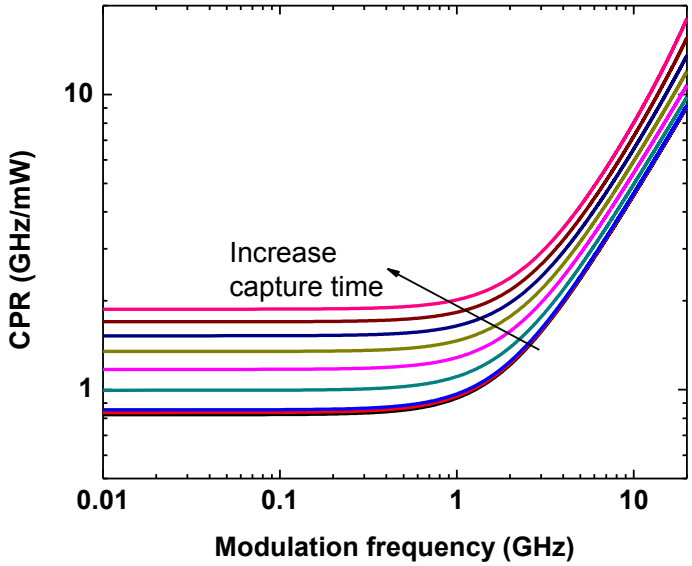

Fig. 3.27. Influence of carrier capture time on the CPR.

B) Impacts of the carrier relaxation time from the ES to the GS

Employing the same approach, the capture time is now fixed in this part at a constant value of 6.3 ps, while the carrier relaxation time is varied from 0.1 ps up to 50 ps. In contrast to the impact of capture process, Fig. 3.28 shows the static solution in which both carriers in the ES and in the RS increases linearly with the relaxation time, while the carrier number in the GS remains constant (not shown). Similarly, the photon number is also reduced by the slow carrier relaxation process.

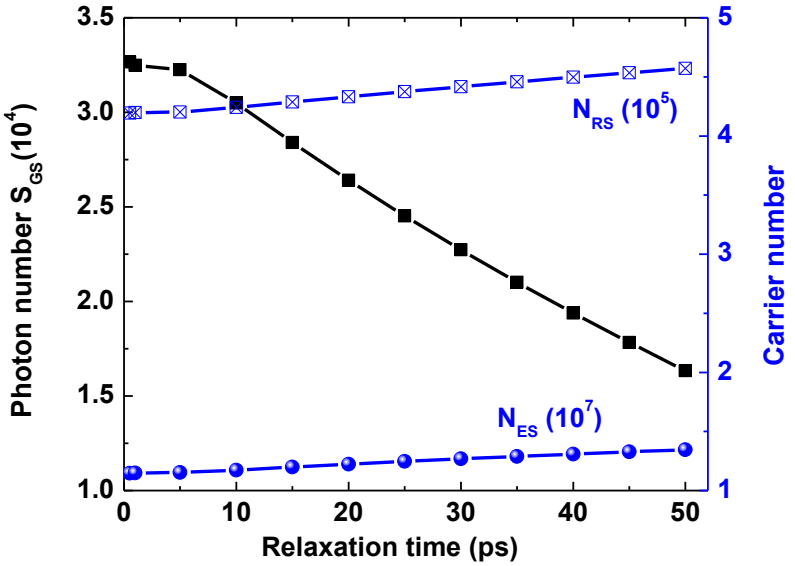

Fig. 3.28. Steady-state solutions as a function of carrier relaxation time. Carrier population in the GS N_{GS} keeps almost constant (not shown).

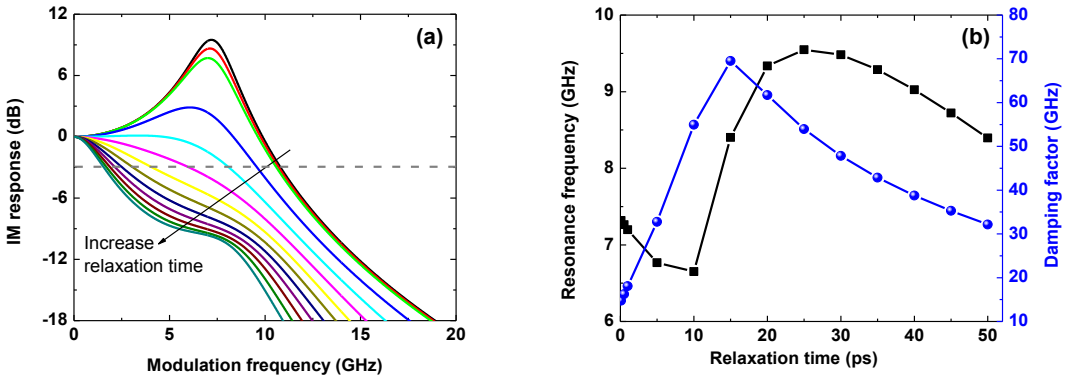

Fig. 3.29. (a) Influence of carrier relaxation time on the IM response; (b) Resonance frequency and damping factor as a function of the capture time.

Figure 3.29(a) shows that the modulation bandwidth is significantly reduced by the slow relaxation process from 10.8 GHz for τ_{GS}^{ES}=0.1 ps to 1.6 GHz for τ_{GS}^{ES}=50 ps. In addition, the response is strongly damped for large relaxation times. It is noted that the evolution of the IM response shape is quite different to that for the capture process in Fig. 3.25(a). For relaxation times τ_{GS}^{ES}>25 ps, the response shows a clear resonance around 8 GHz. Correspondingly, Fig. 3.29(b) presents the resonance frequency and the damping factor extracted from the eigenvalues. The behavior is much more complex than the one of the capture process. The resonance frequency firstly decreases for τ_{GS}^{ES} <10 ps, while the damping factor increases with the relaxation time. At τ_{GS}^{ES}=10 ps, the AM response is rather flat. However, for τ_{GS}^{ES}>10 ps the

resonance re-increase until τ_{GS}^{ES} =25 ps, while the damping factor reaches the maximum at τ_{GS}^{ES} =15 ps. Beyond the peak values, both the resonance and the damping decrease as a function of the relaxation time. Lastly, we note that the damping factors of the Qdot laser both in Fig. 3.25 and in 3.29 are much larger than those of Qwell lasers, which is attributed to the carrier occupation in the off-resonant states as well as the carrier scattering processes [Lingnau12a].

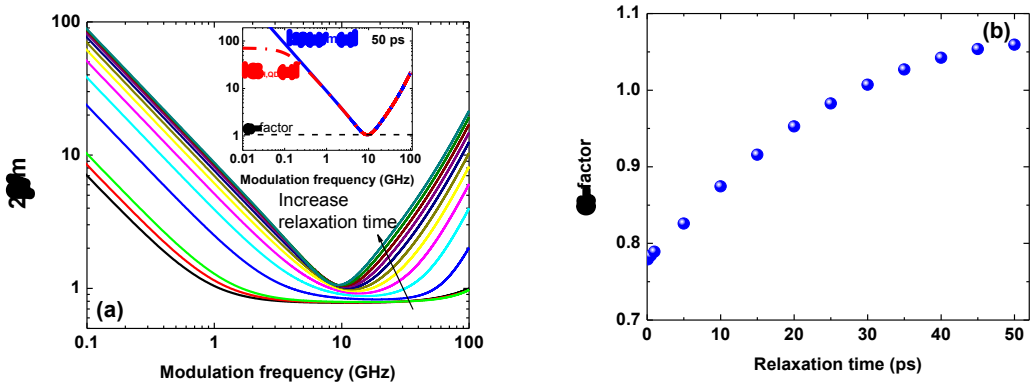

Fig. 3.30. (a) Influence of carrier relaxation time on the ratio of FM-to-AM index. Inset shows its comparison with the directly calculated α-factor using Eq. (3.48) for τ_{GS}^{ES} =50 ps. (b) α-factor variation (extracted from plot (a)) as a function of the capture time.

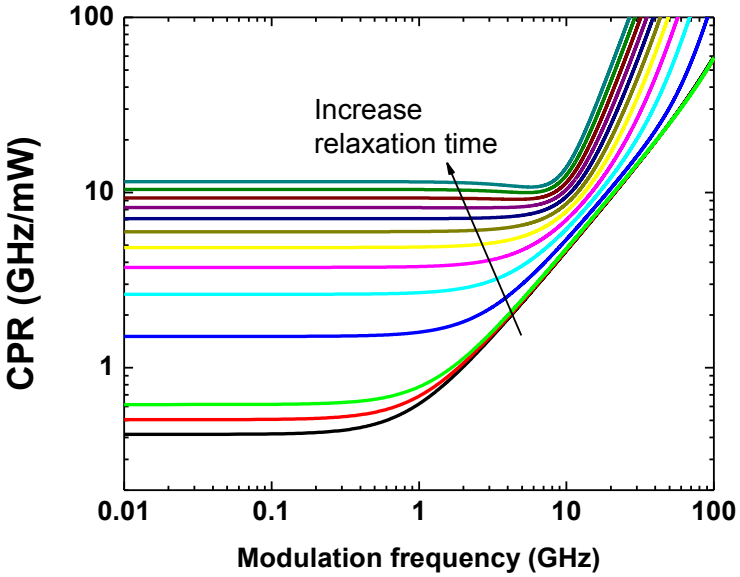

Fig. 3.31. Influence of carrier relaxation time on the CPR.

Figure 3.30(a) depicts that slow carrier relaxation process induces steep re-increase of $2\beta/m$ for modulation frequencies larger than 10 GHz. This is due to the increased carrier populations and variations in the ES and in the RS as shown in Fig. 3.28. Figure 3.30(b) shows the α-factor extracted from the minimum value of $2\beta/m$, which increases by about 36% from

0.78 for τ_{GS}^{ES}=0.1 ps to 1.06 for τ_{GS}^{ES}=50 ps. Figure 3.31 shows the CPR at various relaxation times. It is found that for fast relaxation time, the adiabatic chirp dominates in modulation frequencies only less than 1.0 GHz, while it expands up to 10 GHz for slow relaxation times. On the other hand, the magnitude of the CPR is enhanced by the slow carrier relaxation process due to the increased α-factor.

3.7. Effects of inhomogeneous broadening

Previous implementations of the rate equation model in sections 3.1-3.6 only consider one Qdot ensemble, and thus did not take into account the effect of inhomogeneous broadening. In practice, due to the size and composition fluctuation of the self-assembled dots, Qdot lasers exhibit a broad inhomogeneous broadening of the gain, which is usually characterized by a Gaussian function as in Eq. (2.19). In order to study the influence of the inhomogeneous broadening, we introduce a multi-population rate equation (MPRE) model in this section [Gioannini07]. By contrast to the semi-analytical approach in sections 3.1-3.6, this section analyzes the Qdot laser dynamics employing a numerical approach.

The numerical model is based on the electronic structure shown in Fig. 2.2, including the 3D SCH, the 2D RS, two excited states (ES_1 and ES_2), as well as the GS. It is noted that in comparison with the model presented in previous sections, this model incorporates the SCH state and the ES_2, providing better accuracy. To takes into account the effect of size fluctuation of the dots, we divide the Qdot ensemble into *N* subgroups, and for each group the average energies of the ES_2, ES_1, and the GS are given by $E_{ES1,n}$, $E_{ES2,n}$, and $E_{GS,n}$, respectively (n=1,2,...,N). Correspondingly, the scattering time for the *nth* group is given by τ_{fin}^{ini}, where *ini* and *fin* denote the initial and final states of the transition with energy E_{ini} and E_{fin}, respectively. Thus, a capture or relaxation process occurs when $E_{ini} > E_{fin}$, whereas an escape process does when $E_{ini} < E_{fin}$. Finally, the rate equations describing the carrier dynamics of the *nth* group dots are given by:

$$\frac{dN_{SCH}}{dt} = \frac{\eta_I I}{qV} - \frac{N_{SCH}}{\tau_{RS}^{SCH}} + \frac{N_{RS}}{\tau_{SCH}^{RS}} \tag{3.59}$$

$$\frac{dN_{RS}}{dt} = \frac{N_{SCH}}{\tau_{RS}^{SCH}} - \frac{N_{RS}}{\tau_{SCH}^{RS}} - \frac{N_{RS}}{\tau_{ES2}^{RS}} \sum_{n=1}^{N} (1-\rho_{ES2,n}) G_{cv,n} + \sum_{n=1}^{N} \frac{N_{ES2,n}}{\tau_{RS}^{ES2,n}} \tag{3.60}$$

$$\begin{aligned} \frac{dN_{ES2,n}}{dt} = {} & \frac{N_{RS}}{\tau_{ES2}^{RS}} (1-\rho_{ES2,n}) G_{cv,n} - \frac{N_{ES2,n}}{\tau_{RS}^{ES2,n}} - \frac{N_{ES2,n}}{\tau_{ES1}^{ES2}} (1-\rho_{ES1,n}) + \frac{N_{ES1,n}}{\tau_{ES2,n}^{ES1,n}} (1-\rho_{ES2,n}) \\ & - R_{ES2,n}^{st} - R_{ES2,n}^{Auger} - R_{ES2,n}^{sp} \end{aligned} \tag{3.61}$$

$$\frac{dN_{ES1,n}}{dt}=\frac{N_{ES2,n}}{\tau_{ES1}^{ES2}}(1-\rho_{ES1,n})-\frac{N_{ES1,n}}{\tau_{ES2,n}^{ES1,n}}(1-\rho_{ES2,n})-\frac{N_{ES1,n}}{\tau_{GS}^{ES1}}(1-\rho_{GS,n})+\frac{N_{GS,n}}{\tau_{ES1,n}^{GS,n}}(1-\rho_{ES1,n})$$
$$-R_{ES1,n}^{st}-R_{ES1,n}^{Auger}-R_{ES1,n}^{sp} \tag{3.62}$$

$$\frac{dN_{GS,n}}{dt}=\frac{N_{ES1,n}}{\tau_{GS}^{ES1}}(1-\rho_{GS,n})-\frac{N_{GS,n}}{\tau_{ES1,n}^{GS,n}}(1-\rho_{ES1,n})-R_{GS,n}^{st}-R_{GS,n}^{Auger}-R_{GS,n}^{sp} \tag{3.63}$$

Considering *M* optical modes in interaction with the N subgroup dots, the coupled photon rate equation for the *mth* optical mode is written as follows:

$$\frac{dS_m}{dt}=\Gamma_p v_g S_m\sum_{n=1}^{N}(g_{mn}^{GS}+g_{mn}^{ES1}+g_{mn}^{ES2})-\frac{S_m}{\tau_P}+R_m^{sp} \tag{3.64}$$

where the occupation probability of the state *X* in the subgroup *n* is given by $\rho_{X,n}$. $G_{cv,n}$ is the existence probability of the *nth* subgroup dots, which satisfies the Gaussian distribution as in Eq. (2.19) and $\sum_{n=1}^{N}G_{cv,n}=1$. The gain at lasing energy E_m is given by $g(E_m)=\sum_{X}\sum_{n=1}^{N}g_{mn}^{X}$, with g_{mn}^{X} the material gain at the energy E_m of the photons S_m due to the stimulated emission from the state *X* of the *nth* subgroup dot:

$$g_{mn}^{GS}=\mu_{GS}C_g N_B\frac{\left|P_{GS}^{\sigma}\right|^2}{E_{GS,n}}\left(2\rho_{GS,n}-1\right)G_{cv,n}B_{cv}(E_m-E_{GS,n}) \tag{3.65}$$

$$g_{mn}^{ES1}=\mu_{ES1}C_g N_B\frac{\left|P_{GS}^{\sigma}\right|^2}{E_{ES1,n}}\left(2\rho_{ES1,n}-1\right)G_{cv,n}B_{cv}(E_m-E_{ES1,n}) \tag{3.66}$$

$$g_{mn}^{ES2}=\mu_{ES2}C_g N_B\frac{\left|P_{ES2}^{\sigma}\right|^2}{E_{ES2,n}}\left(2\rho_{ES2,n}-1\right)G_{cv,n}B_{cv}(E_m-E_{ES2,n}) \tag{3.67}$$

where $\mu_{GS}=2$, $\mu_{ES1}=4$, and $\mu_{ES2}=6$ are the degeneracies of the GS, ES_1, and the ES_2 including the spin. C_g is a constant ($C_g=2\pi\hbar q^2/(cn_r\varepsilon 0m_0^2)$)[Gioannini06], [Sugawara00] N_B is the dot density per unit area, $\left|P_X^{\sigma}\right|^2$ is the transition matrix element of the interband recombination [Sugawara00]. $B_{cv}(E_m-E_{X,n})$ is the Lorentzian homogeneous broadening function with width $\hbar\Gamma_{\text{hom}}$ as indicated in Eq. (2.17). Symbols $R_{X,n}^{Auger}$ and $R_{X,n}^{sp}$ represent the Auger and the spontaneous recombination rates of the carriers in the state *X* of the dot group *n*, respectively. The stimulated recombination rate $R_{X,n}^{st}$ is expressed by:

$$R_{X,n}^{st}=\Gamma_p v_g\sum_{m=1}^{M}g_{mn}^{X}S_m \tag{3.68}$$

At room temperature and without stimulated emission, the quasi-thermal equilibrium is characterized by the Fermi distribution of the carriers. In order to ensure this condition, the carrier escape times are related to the carrier capture and relaxation times:

$$\begin{aligned}
\tau_{ES1,n}^{GS,n} &= \tau_{GS}^{ES1}\frac{\mu_{GS}}{\mu_{ES1}}\exp\left(\frac{E_{ES1,n}-E_{GS,n}}{k_BT}\right)\\
\tau_{ES2,n}^{ES1,n} &= \tau_{ES1}^{ES2}\frac{\mu_{ES1}}{\mu_{ES2}}\exp\left(\frac{E_{ES2,n}-E_{ES1,n}}{k_BT}\right)\\
\tau_{RS}^{ES2,n} &= \tau_{ES2}^{RS}\frac{\mu_{ES2}N_B}{\rho_{RS}}\exp\left(\frac{E_{RS}-E_{ES2,n}}{k_BT}\right)\\
\tau_{SCH}^{RS} &= \tau_{RS}^{SCH}\frac{\rho_{RS}N_{layer}}{\rho_{SCH}H_{SCH}}\exp\left(\frac{E_{RS}-E_{ES2,n}}{k_BT}\right)
\end{aligned} \tag{3.69}$$

where ρ_{RS} and ρ_{SCH} are density of state in the RS and in the SCH given in Eqs. (2.1) and (2.2). N_{layer} is the number of Qdot layers and H_{SCH} is the total thickness of the SCH layer. It is noted that the carrier capture and relaxation (scattering-in) times are empirical values while the carrier excape (scattering-out) times are dependent on the state energy separations.

Table 3.3. QD material and laser parameters for study of the inhomogeneous broadening effect

Symbol	Description	Value	Symbol	Description	Value
L	Active region length	8.3×10^{-2} cm	E_{ES2}	Recombination energy	0.905 eV
W	Active region width	4×10^{-4} cm	E_{ES1}	Recombination energy	0.856 eV
R_1=R_2	Mirror reflectivity	0.32	E_{GS}	Recombination energy	0.800 eV
n_r	Refractive index	3.5	τ_{RS}^{SCH}	Transport time	1.2 ps
α_i	Internal modal loss	4 cm^{-1}	τ_{ES2}^{RS}	Capture time	2.1 ps
N_B	Dot density	7×10^{10} cm^{-2}	τ_{ES1}^{ES2}	Relaxation time	1.2 ps
H_B	Dot height	5×10^{-7} cm	τ_{GS}^{ES1}	Relaxation time	1.2 ps
N_{layer}	QD layer number	6	T_D	Dephasing time	0.1 ps
η_i	Current injection efficiency	0.8	Γ_p	Optical confinement factor	0.06
E_{SCH} –E_{RS}	Energy separation	50 meV	β_{SP}	Spontaneous emission factor	1×10^{-4}
E_{RS} –E_{ES2}	Energy separation	40 meV	N	dot subgroup number	41
Homogeneous broadening		5 meV			

As already discussed in chapter 2, the variation of the refractive index in Qdot lasers due to the carrier injection consists of two part contributions. One part is related with the interband

transitions of the states insides the dots (Δn_{QD}) , which follows the Kramer-Krönig relation with the gain change. The other part is attributed to the free-carrier plasma effect in the RS (Δn_{RS}), and is evaluated by the Drude model as in Eq. (2.11). The plasma effect of the 3D SCH barrier is not considered in this work. Thus, the total refractive index variation $\Delta n(E_m)$ at lasing energy E_m is given by

$$\Delta n(E_m) = \Delta n_{dot}(E_m) + \Delta n_{RS}(E_m) \tag{3.70}$$

$$\Delta n_{dot}(E_m) = \Gamma_p \frac{\hbar c}{2E_m} C_g N_B \sum_X \sum_{n=1}^{N} \mu_X \frac{\left|P_X^{\sigma}\right|^2}{E_{X,n}} \left(2\rho_{X,n} - 1\right) G_{cv,n} D_{cv}(E_m - E_{X,n}) \tag{3.71}$$

$$\Delta n_{RS}(E_m) = -\frac{\Gamma_p e^2 N_{RS}}{2n_b \varepsilon_0 m^* \omega_m^2} \tag{3.72}$$

where the homogeneous broadening of the refractive index $D_{cv}(E_m - E_{X,n})$ is given in Eq. (2.18). The change of the refractive index in time induces a fluctuation of the lasing mode frequency:

$$\Delta\omega(t, E_m) = -\frac{\omega_m}{n_b} \Delta n(t, E_m) \tag{3.73}$$

In the simulations, the material and laser parameters used for the study of the inhomogeneous broadening effect are listed in Table 3.3. The dots are divided into 41 subgroup, and the inhomogeneous broadening is varied from 30 meV to 80 meV. We first investigates the effects of inhomogeneous broadenings on the steady-state properties and secondly on the dynamic characteristics.

A) Effects on the steady-state characteristics of a multimode Fabry-Perot laser

In this section, we consider a multimode Fabry-Perot laser, and a group number of 63~98 optical modes are taken into account depending on the inhomogeneous broadening.

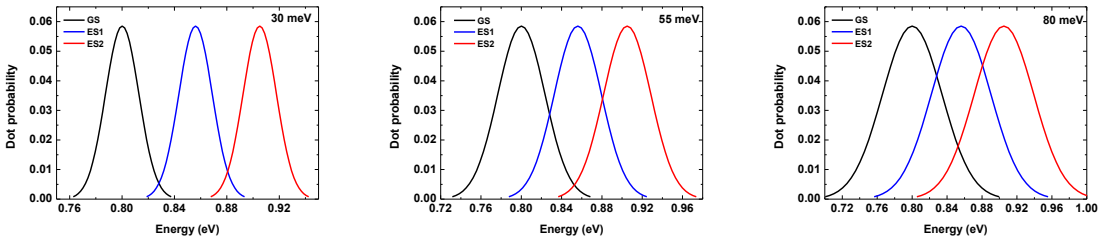

Fig. 3.32. Carrier distributions in each Qdot electronic levels for inhomogeneous broadenings equal to 30, 55 and 80 meV.

Figure 3.32 presents the carrier distributions in each electronic state for broadenings of 30, 55 and 80 meV. It shows that the overlap areas between the GS, the ES_1 and the ES_2 become

larger for higher inhomogeneous broadenings. Consequently, for some optical modes, both the GS and the ES_1 (or ES_1 and ES_2) contributes to the photon emission. Figure 3.33 shows that the threshold current is increased by almost 3 times when the broadening increases from 30 meV to 80 meV. On the other hand, the carrier occupation probabilities of the center subgroup dots for the GS, ES_1, and ES_2 also increases for broadenings smaller than 60 meV, whereas decrease slightly when larger than 60 meV. This is because the mean energy difference between the GS and the ES_1 is 56 mV as shown in Table 3.3. Therefore, for broadenings smaller than this energy difference, only carrier population in the GS contributes to the gain peak. For larger broadenings, not only carriers in the GS contribute to the peak of the gain but also carriers in the ES_1, and thus slightly reducing the carrier occupation probability. This phenomenon is presented in Fig. 3.34, which illustrates the net modal gain spectra (solid curve) at threshold. For the broadening of 30 meV, the laser exhibits one narrow positive gain peak, located slightly below the average recombination energy of the GS E_{GS}. For the broadening of 50 meV, another peak appears due to the carrier population in the ES. It is noted that this peak is not located at E_{ES1}, because the peak position is determined by both the dot existence probability (Gaussian distribution) and the carrier occupation probability (Fermi distribution) for each dot subgroup. For the broadening of 60 meV, the GS (red dash curve) and the ES_1 (blue dash curve) peaks begin to merge. For the 80 meV value, the two peaks merge to form a broad gain spectrum. Carriers in the GS mainly contributes to the low-energy part of the gain, while carriers in the ES_1 contributes to the high-energy part.

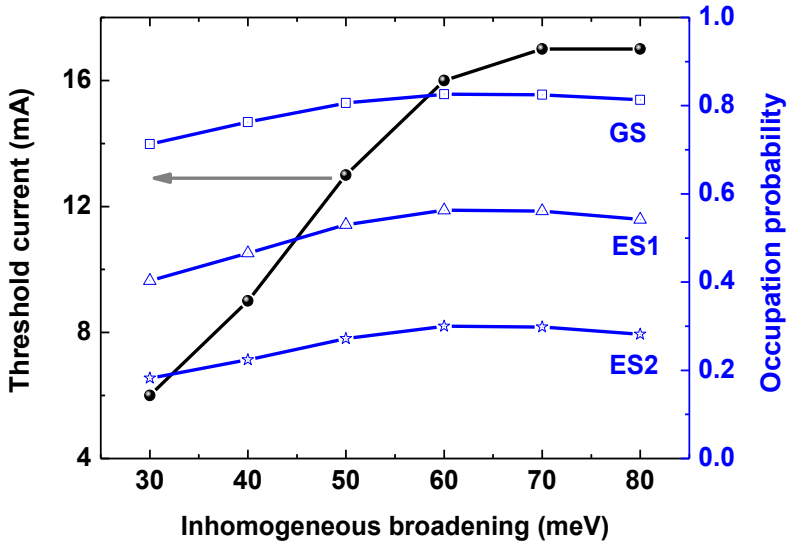

Fig. 3.33. Threshold current of the laser and carrier occupation probabilities of the center (*21th*) group dot as a function of the inhomogeneous broadening width.

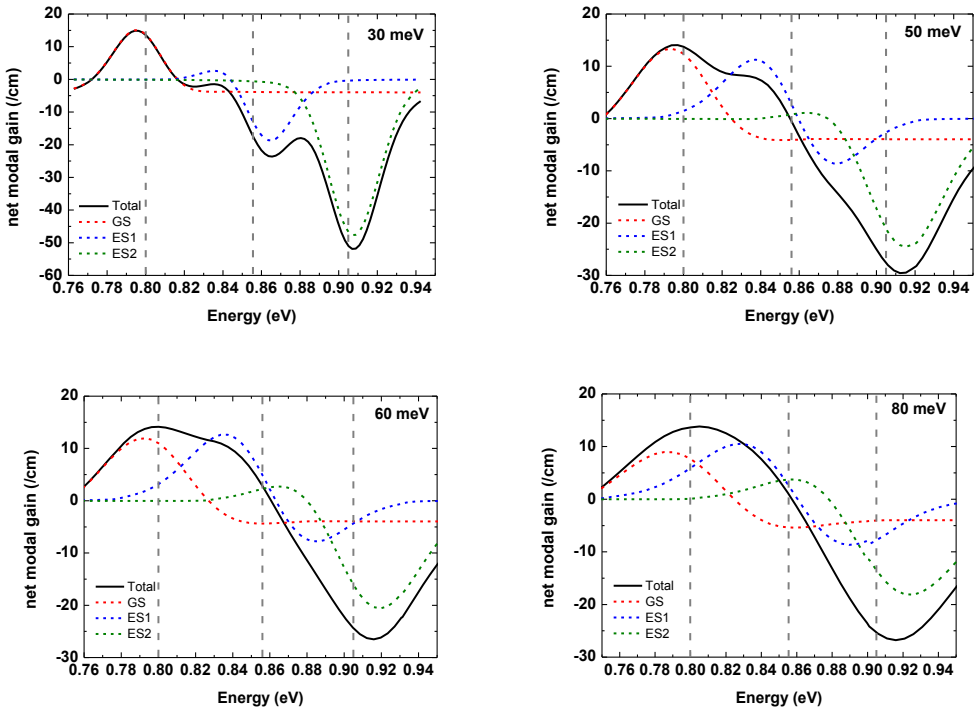

Fig. 3.34. Net modal gain spectra (solid curve) at threshold for inhomogeneous broadenings of 30, 50, 60 and 80 meV. The dashed curves indicate contributions of the GS, the ES_1 and the ES_2, respectively; and the internal loss is included in the GS gain curve. The grey dash lines give the recombination energy of the GS, the ES_1 and the ES_2, respectively.

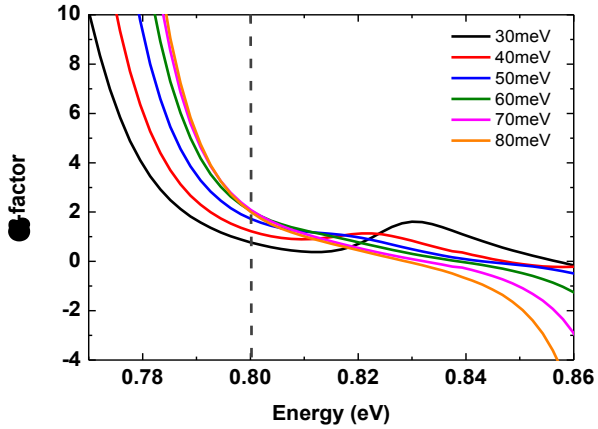

Fig. 3.35. The α-factor at lasing threshold as a function of the photon energy for various inhomogeneous broadenings. The dashed line indicates E_{GS}. The α-factor is computed using the ASE method.

In order to study the α-factor of the laser at the lasing threshold, we impose a small step-function like current (ΔI) to the sub-threshold current, which subsequently induces variation of the gain ($\Delta g(E_m)$) as well as variation of the refractive index ($\Delta n(E_m)$). Then we obtain the α-factor using Eq. (2.14). Figure 3.35 presents the threshold α-factor as a function of the photon energy for various inhomogeneous broadenings. Generally, the α-factor decreases with the

increased photon energy. For low lasing energies, narrow inhomogeneous broadening leads to a smaller α-factor while it is opposite for the high lasing energy case.

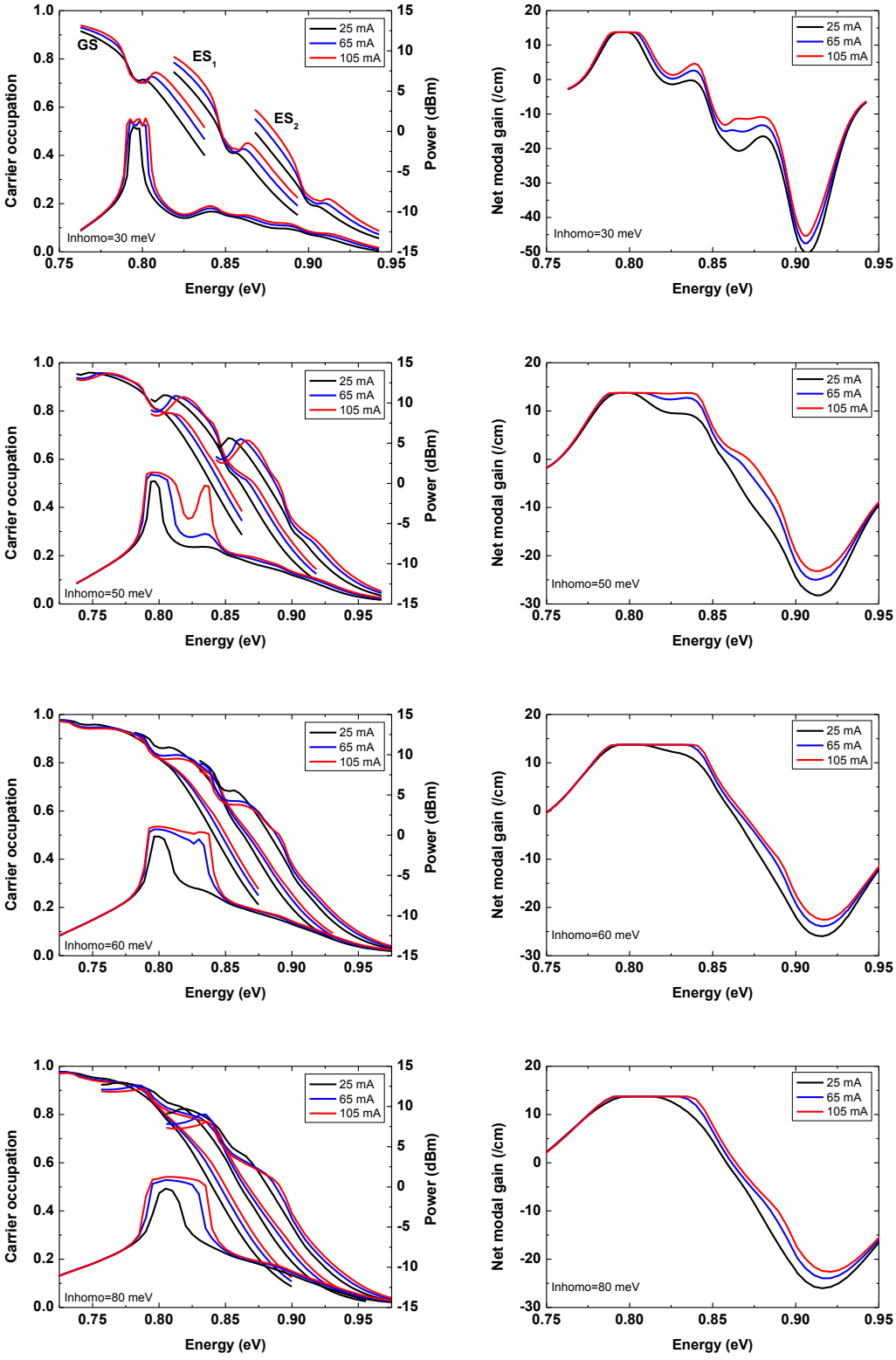

Fig. 3.36. Carrier occupation probability, power (left) and net modal gain spectrum (right) beyond the lasing threshold (25, 65, 105 mA) for inhomogeneous broadenings of 30, 50, 60, 80 meV (from up to down). The corresponding threshold currents can be found in Fig. 3.33.

Figure 3.36 presents the steady-state behavior above threshold. It is shown that the carrier occupation probability (left) of the discrete Qdot states (the center subgroup) generally follows the Fermi-Dirac distribution. Due to the lasing emission, a hole is formed in the population, known as spectral hole burning. For a small inhomogeneous broadening, the spectral hole is narrow and deep, while it becomes broader and shallower for a larger inhomogeneous broadening. On the other hand, the power spectrum also broadens due to the fact that carrier population in higher energy states can be high enough to reach the lasing threshold. This can be seen in the net gain spectrum (right), the flat peak regime of which is broadened by both the large inhomogeneous broadening and the high bias current.

B) Effects on the dynamic characteristics of a single mode DFB laser

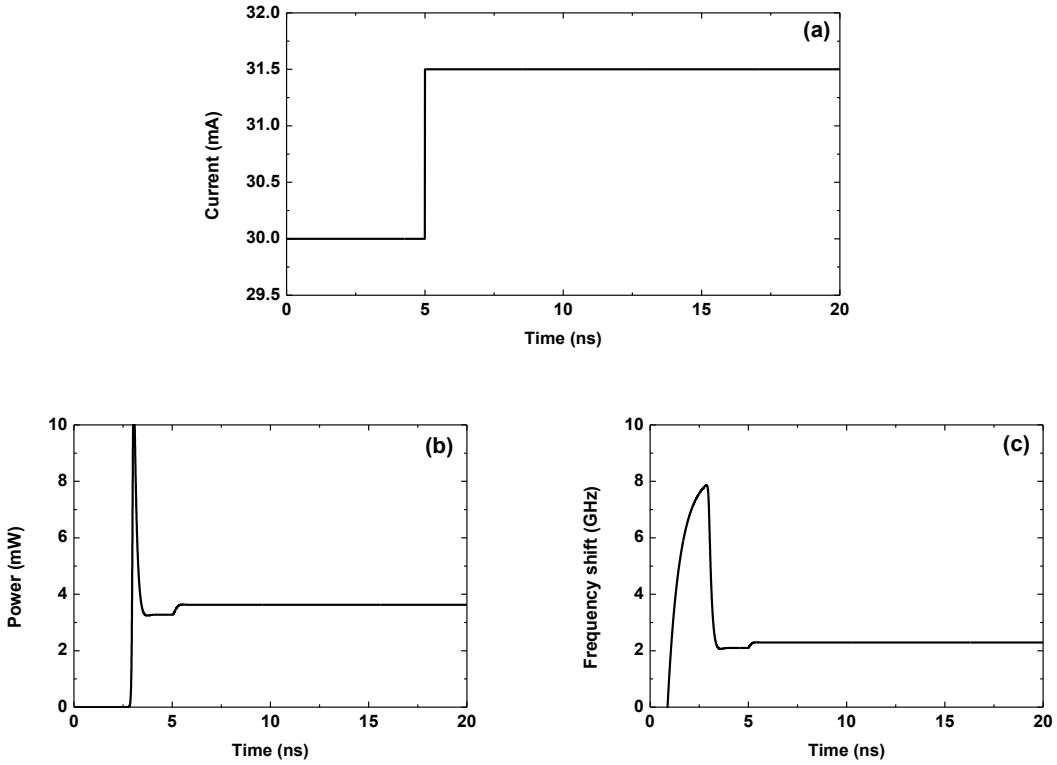

Fig. 3.37. Current, power and frequency shift of the laser field versus time. The transient power and frequency changes before 5 ns are due to the turn-on dynamics with a step current from 0 mA to 30 mA at 0 ns.

For the investigation of dynamic properties, we consider a single mode DFB laser. Therefore, we only need one rate equation in (3.64) for the optical mode group with lasing energy E_m=0.8 eV, which is in resonance with the GS recombination energy. In this study, we keep the bias current of the laser at I_{bias}=30 mA. In order to obtain the AM response and the frequency chirp we employ a purely numerical approach, which is different to the semi-analytical approach using the derivation of a full set of differential rate equations (see section 3.3). As shown in Fig. 3.37(a), a small step-function like current $I(t)$ (1.5 mA, corresponding to a typical RF power

of -10 dBm) is superimposed to the bias current at 5.0 ns, and the time integration lasts until 20 ns. Due to the fact that the Qdot laser's transient response is within 5.0 ns as illustrated in Fig. 3.37(b), the laser is ensured to be stable when the current step is imposed. Then, we calculate the response of the power $P(t)$ in Fig. 3.37(b) and the frequency shift $F_s(t)$ (see Eq. (3.73)) in Fig. 3.37(c) with respect to the current step in the time domain. Taking the differences $\Delta I(t)$, $\Delta P(t)$ and $\Delta F_s(t)$ and conducting the Fourier transform, we obtain the responses in the frequency domain, separately:

$$\begin{aligned} [t, \Delta I(t)] &\xrightarrow{FFT} [f, \Delta I(f)] \\ [t, \Delta P(t)] &\xrightarrow{FFT} [f, \Delta P(f)] \\ [t, \Delta F_s(t)] &\xrightarrow{FFT} [f, \Delta F_s(f)] \end{aligned} \tag{3.74}$$

Employing $\Delta I(f)$, $\Delta P(f)$ and $\Delta F_s(f)$, we can study the small-signal characteristics on the AM response, the CPR as well as the FM-to-AM index.

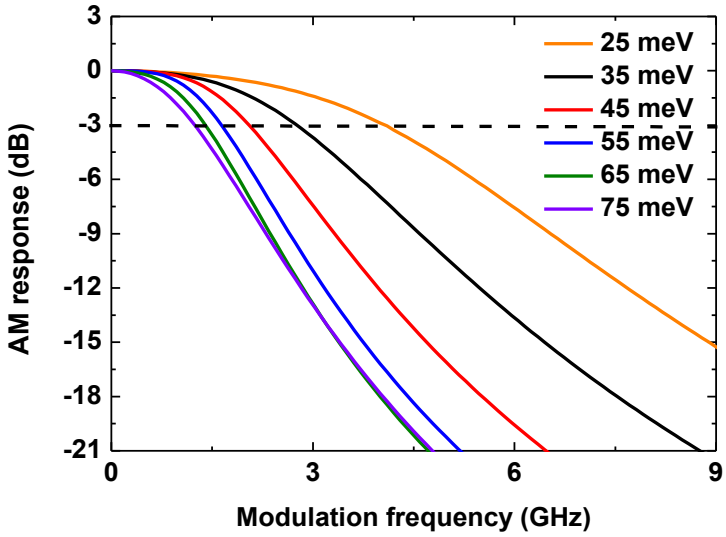

Fig. 3.38. AM response for various values of inhomogeneous broadenings.

The QD laser under study shows flat responses due to the large damping factor as shown in Fig. 3.38. The inhomogeneous broadening reduces the 3-dB modulation bandwidth from 4.1 GHz for a broadening of 25 meV down to 1.2 GHz for the case of 75 meV. For the chirp properties depicted in Fig. 3.39, lasers with small broadening exhibits lower CPR both in the adiabatic and the transient regimes. In addition, the adiabatic chirp dominates up to a modulation frequency of 6 GHz for a low broadening of 25 meV whereas for the case of 75 meV, it only dominates lower than 2 GHz. From the evolution of the FM-to-AM index in Fig. 3.40, we can see the α-factor is increased by about 3 times by the inhomogeneous broadening.

The tendency is in agreement with the evolution of the α-factor at lasing threshold shown in Fig. 3.35.

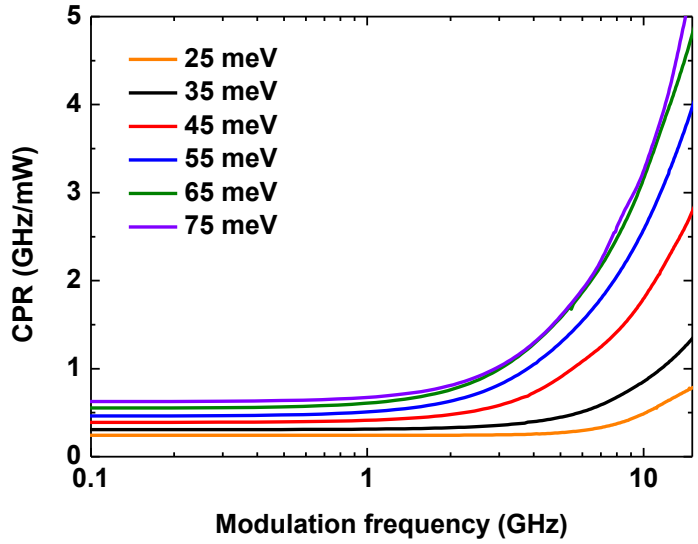

Fig. 3.39. CPR variation for different values of inhomogeneous broadenings.

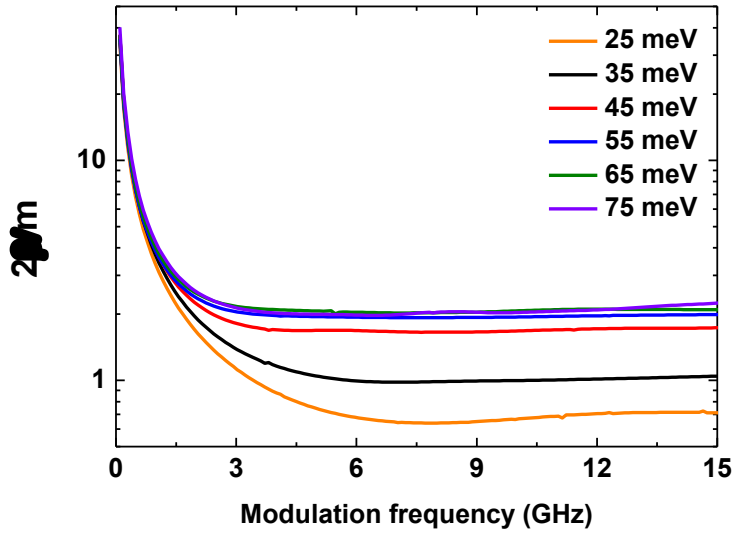

Fig. 3.40. FM-to-AM index ratio for various inhomogeneous broadenings.

3.8. Large-signal modulation

The large signal modulation of a semiconductor laser determines its capability for digital data transmission. The laser is usually biased above threshold and switched between two power levels, defining the low and the high digital optical signal level. The laser is not biased below threshold in order to avoid the influence of a long turn-on delay, although it may provide a large contrast between the high and the low signal levels. There is a close relationship between the

large and the small signal modulation responses. When the laser is underdamped, the small signal AM response shows a high resonance peak, and the large signal waveform exhibits overshoot because of the relaxation oscillation, which can degrade the signal quality. When the laser is overdamped, both the small and the large signal modulations show flat response. Generally, the maximum bit rate of the large signal modulation lies in the range of the maximum 3-dB bandwidth of the small-signal response. However, recent work reports that when the small signal modulation response is limited by gain compression, the laser can be modulated at much higher bit rates in the large signal regime provided that the optical gain is large enough [Gready12a], [Gready13].

There are several measures to evaluate the digital modulation performance of a laser system: the eye diagram, the time-resolved chirp profile, and the bit error rate (BER). This work focuses on the former two properties. The latter is the number of bit errors divided by the total number of transferred bits during a studied time interval. In the optical communication system, the BER may be affected by transmission channel noise, interference, distortion, bit synchronization problems, attenuation, spectral instabilities, etc [Grillot10].

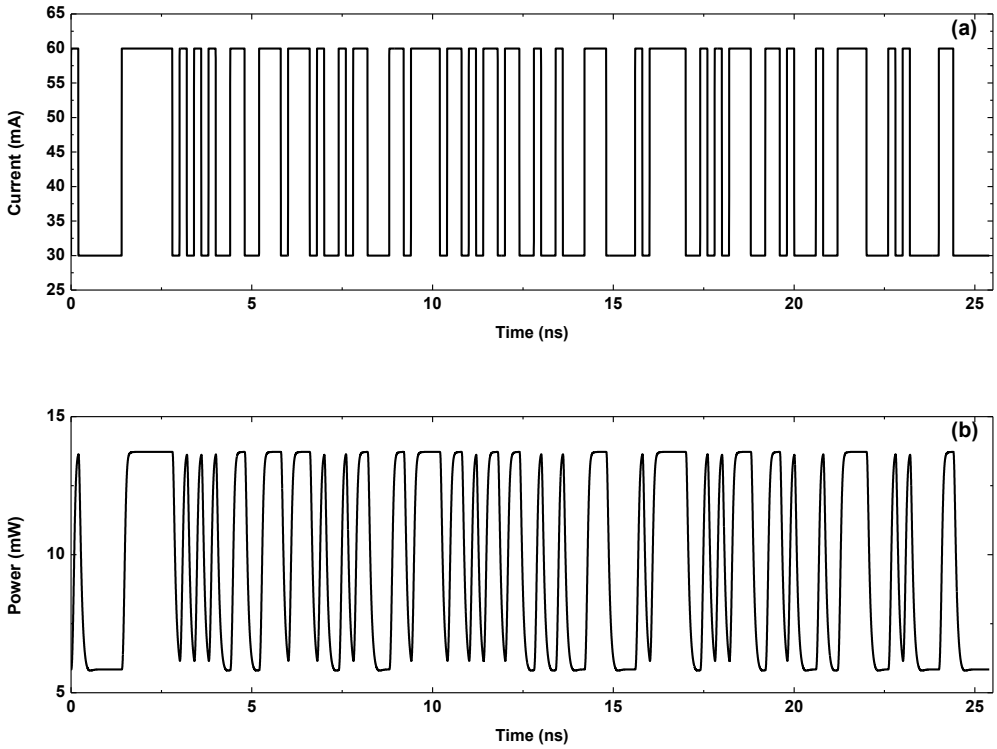

Fig. 3.41. One PRBS7 sequence of modulation current and the time-resolved intensity profile. The data modulation bit rate is 5.0 Gbps.

When testing a laser system, a pseudo random binary sequence (PRBS) is required, which has a quasi-continuous spectrum in the frequency domain [SHF04]. PRBS signal has a long

periodicity with a sequence of N bits consisting of 0 and 1. Thus, in the frequency domain, the signal has very dense discrete spectral components distributes over the entire transmission bandwidth and are therefore very similar to completely random signals. For a PRBS-k pattern with index k, its full number of elements is $N=2^k-1$, which includes all the possibilities of k bits except k-bit zeros. The commonly used PRBS signals have index k=7, 15, 23, and 31. The larger the index k is, the closer the PRBS signal is to completely random signals. In order to obtain a reasonable test as well as to save the computation time, we employ a PRBS-7 signal in this work, and use the non-return-to-zero (NRZ) line encoding scheme.

Figure 3.41(a) illustrates one full pattern of PRBS-7 current signal with a modulation bit rate of 5.0 Gbps. The total duration of the signal is $(2^7-1)/(5.0\ \text{Gbps})= 25.4$ ns. The rise and fall times of the signal is set to a typical value of 80 ps. By integrating rate equations (3.59)-(3.64) over the time duration, we obtain the time-resolved intensity waveform in Fig. 3.41(b). An alternative way of displaying the digital intensity signal is the so-called eye diagram (eye pattern) [Onsemi14]. The eye diagram is a methodology to represent and analyze a high-speed digital signal. It is constructed from the intensity waveforms by folding the parts of the waveform corresponding to each individual bit into a signal graph with signal amplitude on the vertical axis and time on horizontal axis. By repeating this construction over samples of the waveform, the resultant graph will represent the average statistics of the signal and will resemble an eye. The eye diagram provides plenty of information such as overshoot, ringing, noise, jitter rise and fall times, etc. This work focuses on one of the most important features--- the *openness* of the eye pattern, which is evaluated qualitatively in this section. However, the openness of the eye diagram can be quantified by the *eye height* and the *eye width.* The quality of an eye diagram is measured by the Q-factor, which is based on the histogram of the amplitude. The noise, overshoot and ringing will increase the standard deviation and therefore decrease the Q-factor as well as increase the BER [Onsemi14]. However, in this work we do not consider the noise effect. In the followings, we will investigate the influences of the carrier scattering rates and the inhomogeneous broadening on the eye diagram and on the time-resolved frequency chirp. In the simulations, the low bias current is set at 30 mA and the high one is at 60 mA. The modulation bit rate is set at 5.0 Gbps.

A) Influence of the carrier capture process

Figure 3.42(a) shows the eye diagrams for difference capture times from the RS to the ES_2. A characteristic feature is the low distortion of the high and low levels due to the strong damping of the laser oscillation in contrast to Qwell lasers. For fast carrier capture rates (top), the laser has a smaller damping factor, and shows an overshoot in the eye diagram. Slow capture rate

enlarges the damping factor and thus suppresses the overshoot (bottom). On the other hand, the eye diagram becomes close due to the reduction of the modulation bandwidth as shown in Fig. 3.25.

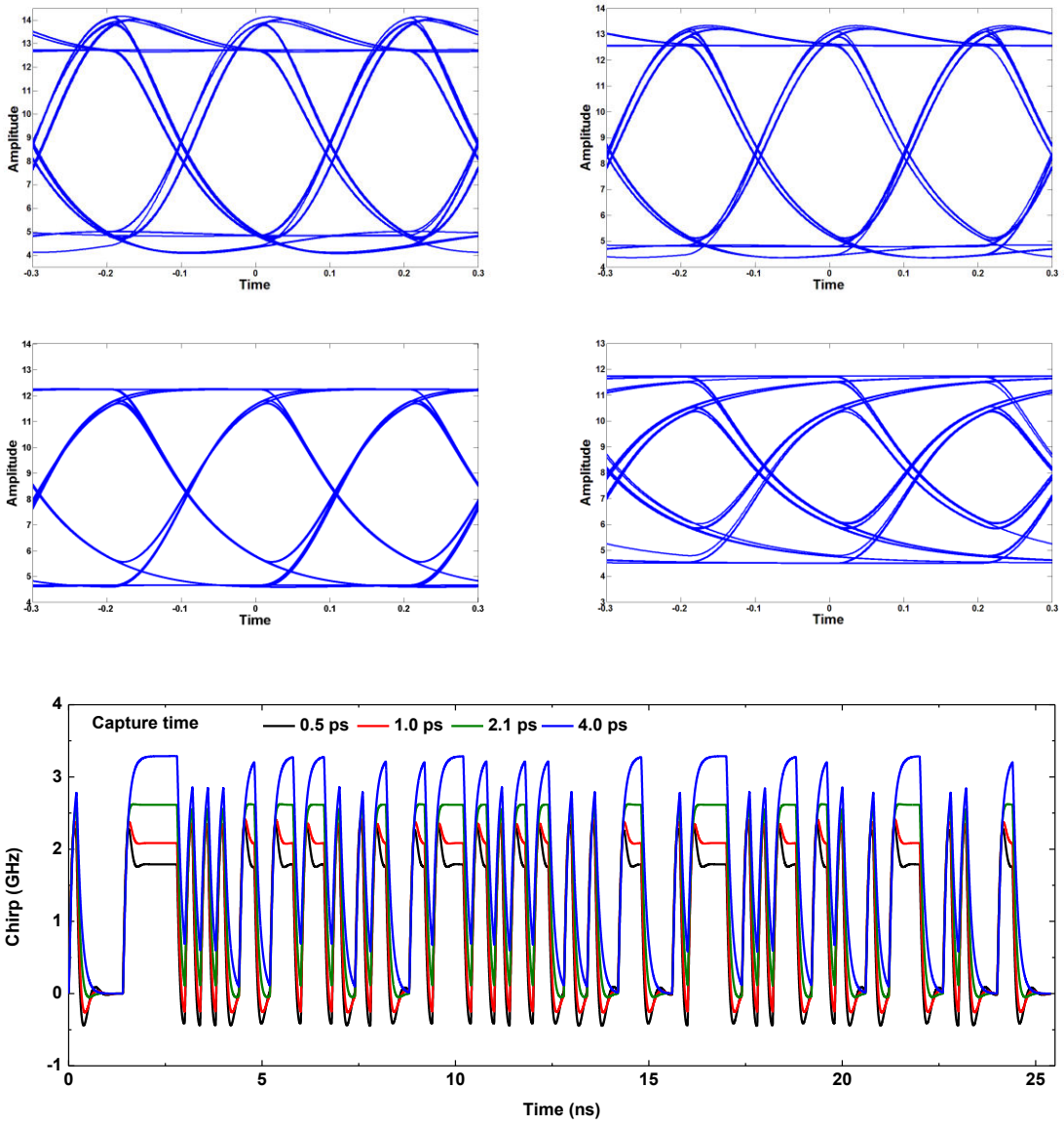

Fig. 3.42. (a) Eye diagram for different capture times (τ_{ES2}^{RS}): 0.5 ps (top left), 1.0 ps (top right), 2.1 ps (bottom left), 4.0 ps (bottom right). (b) Time-resolved chirp profiles for the same capture times. The chirp profile is offset such that the chirp value at t=0 ns is set to zero. The relaxation times are fixed at $\tau_{ES1}^{ES2} = \tau_{GS}^{ES1}$ =1.2 ps. The inhomogeneous broadening is 45 meV.

In a laser device, the frequency variation can be modeled as the sum of the phase shift and the frequency shift terms. An abrupt shift in phase becomes a transient in frequency. The two terms are generally referred to as transient and adiabatic chirps, respectively. A very general form of the chirp equation is [Koch84]:

$$\Delta f(t) = a_{transient}\frac{dP(t)}{dt} + a_{adiabatic}P(t) \tag{3.75}$$

The transient term is that part of the chirp that correlates to dP(t)/dt while the adiabatic term is linked to P(t) directly. For the laser rate equation, we calculate the frequency chirp using Eq. (3.73) through the variation of the refractive index.

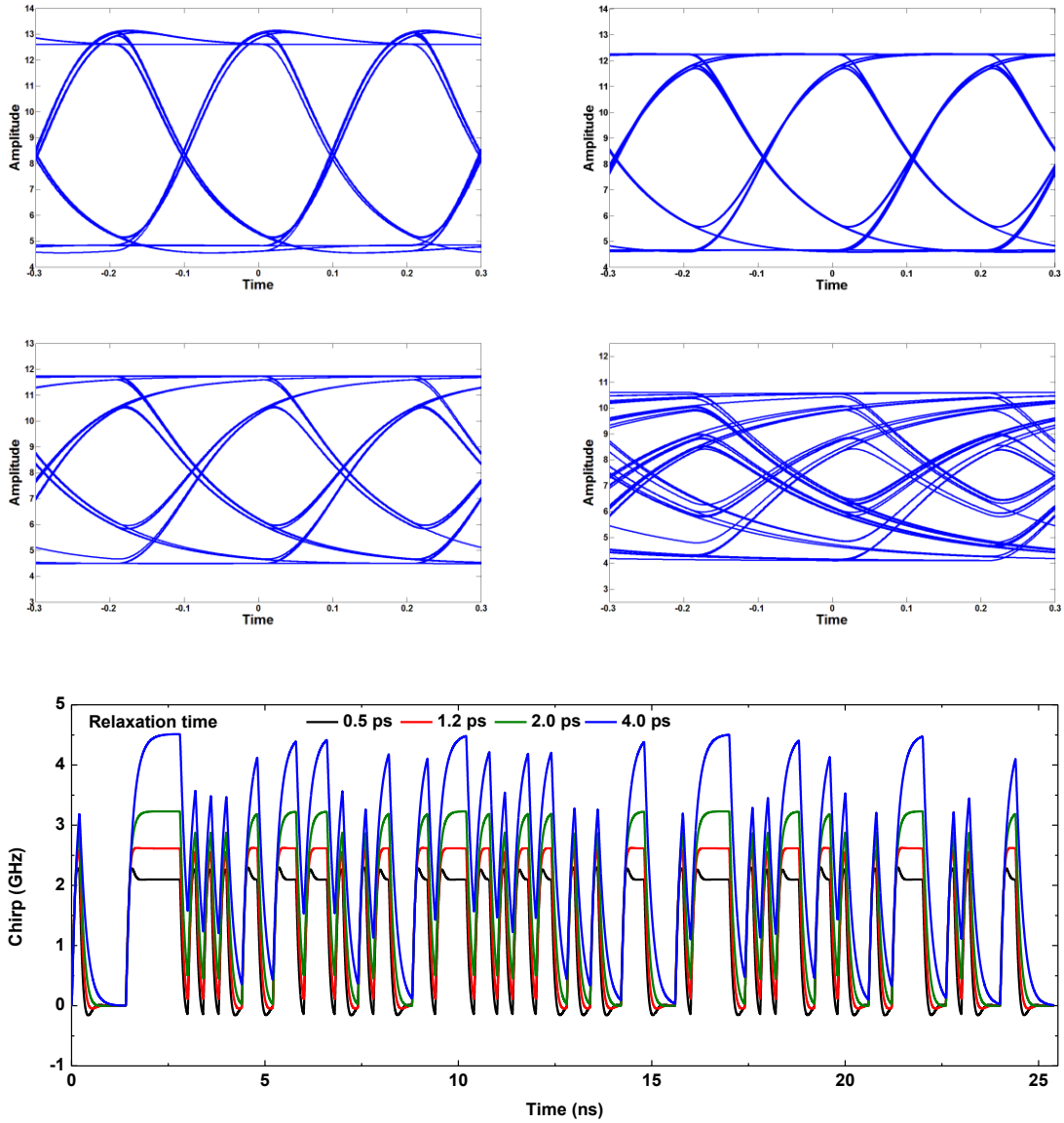

Fig. 3.43. (a) Eye diagram for different relaxation times ($\tau_{ES1}^{ES2} = \tau_{GS}^{ES1}$): 0.5 ps (top left), 1.2 ps (top right), 2.0 ps (bottom left), 4.0 ps (bottom right); (b) Time-resolved chirp profiles for different relaxation times. The capture time is fixed at τ_{ES2}^{RS} =2.1 ps. The inhomogeneous broadening is 45 meV.

In Fig. 3.42(b), the time-resolved chirp with fast capture rate shows overshoot (transient chirp) in the high level due to the relaxation oscillation. The adiabatic chirp is increased from 1.8 GHz for τ_{ES2}^{RS} =0.5 ps to 3.3 GHz for τ_{ES2}^{RS} =4.0 ps. Thus, slow carrier capture process enlarges

the adiabatic chirp of the laser device, which is in agreement with the small-signal CPR analysis in Fig. 3.27.

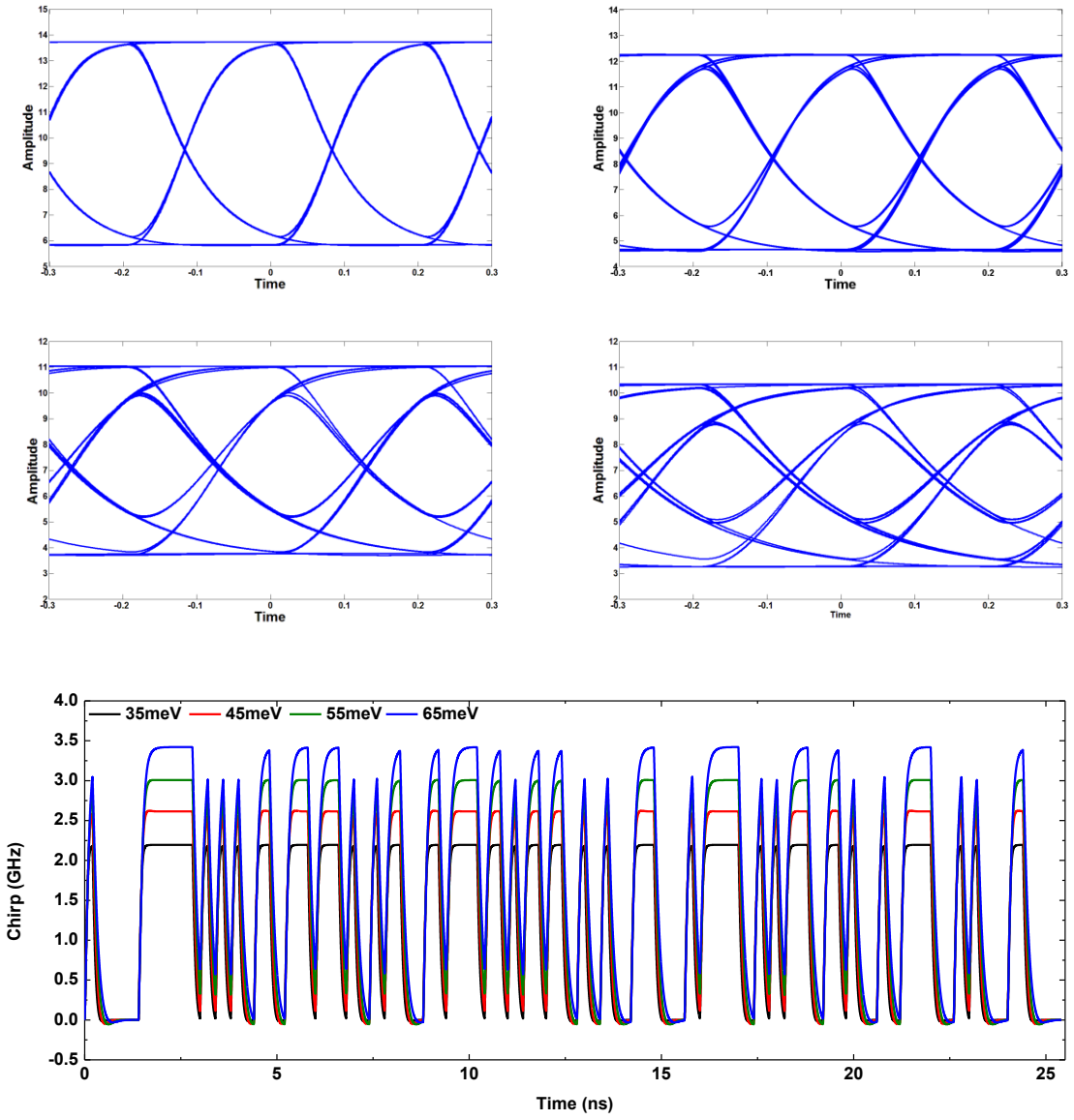

Fig. 3.44. (a) Eye diagram for different inhomogeneous broadening values: 35 meV (top left), 45 meV (top right), 55 meV (bottom left), 65 meV (bottom right). (b) Time-resolved chirp profiles for different inhomogeneous broadenings. The capture times τ_{ES2}^{RS}=2.1 ps. The relaxation times are $\tau_{ES1}^{ES2}=\tau_{GS}^{ES1}$=1.2 ps.

B) Influence of the intradot carrier relaxation process

Figure 3.43(a) shows the influence of the intra-dot carrier relaxation process on the openness of the eye diagram. Similarly as the capture process, fast carrier relaxation induces overshoot in the diagram due to the relaxation oscillation. Slow relaxation reduces the openness of the eye. The variation of the chirp profile for the relaxation process in Fig. 3.43(b) is similar to that for the capture process in Fig. 3.42 (b). Compared to the carrier capture process, the large signal response of a Qdot laser is more sensitive to the relaxation process. In addition, scattering times

beyond 5.0 ps lead to stronger deleterious effect on the eye diagrams, which are not presented in this section.

C) Influence of the inhomogeneous broadening

Figure 3.44(a) clearly shows that the inhomogeneous broadening degrades the quality of the eye diagram. For a broadening of 35 meV (top left) the eye openness is quite good, and it becomes very poor for the broadening of 65 meV (bottom right). On the other hand, the peak-to-peak chirp in Fig. 3.44(b) increases from 2.2 GHz up to 3.4 GHz.

Conclusion of chapter 3: this chapter investigated the modulation dynamics of free-running Qdot lasers based on a semi-analytical method. The AM bandwidth is found to be limited by the carrier capture and relaxation processes as well as the Pauli blocking effect, which are also responsible for the large damping factor often observed in Qdot lasers. An improved rate equation model is developed taking into account carrier contributions of off-resonant state on the refractive index change and allowing to study the α-factor properties of nanostructure lasers. It is proved that the α-factor of nanostructure lasers is strongly dependent on the modulation frequency [Lingau14]. For instance, the α-factor values calculated at low modulation frequencies are higher than that at high ones obtained by the FM/AM technique. In addition, it is shown that ES laser offers superior dynamic properties than the GS laser, including broader AM bandwidth, smaller α-factor as well as lower frequency chirp. The impacts of the carrier capture and relaxation times on the modulation dynamics are also investigated. Lastly, employing a MPRE model, we have analyzed the effects of inhomogeneous broadening as well as the large-signal modulation performances of the nanostructure lasers.

Chapter 4. Modulation dynamics of optically injection-locked Qdot lasers

Optical injection-locking semiconductor laser system involves two lasers referred to the master and the slave lasers as shown in Fig. 4.1, illustrating the light transmission diagram. The master laser is usually a single-mode tunable laser with a narrow spectral linewidth. The light of the master laser is coupled into the slave laser, which is the semiconductor laser under test. The dynamic characteristics of optically injection-locked lasers strongly depend on two vital parameters: the injection ratio, and the frequency detuning. The injection ratio is defined as the ratio of the master laser's power to that of the slave laser. The frequency detuning is the frequency offset between the master laser and the slave laser.

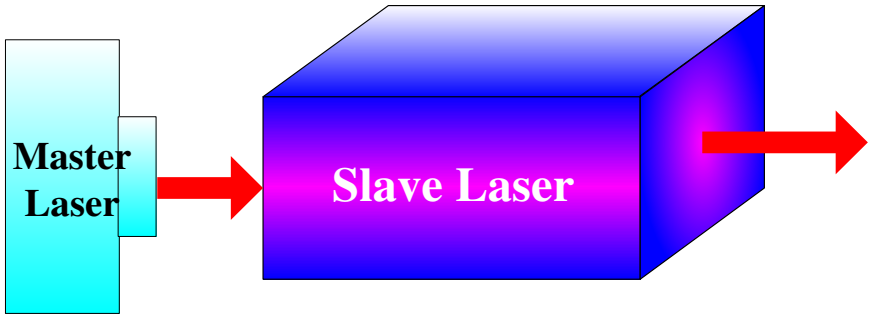

Fig. 4.1. Schematic diagram of an optically injection-locked semiconductor laser

Semiconductor lasers subject to optical injection are known to produce a large variety of dynamical behaviors including stable locking, locking-unlocking bistability, periodic oscillations, chaotic dynamics, and many other instabilities [Wieczorek05]. In the stable locking regime, the optical injection technique can improve a host of performance of semiconductor lasers, such as side-mode suppression [Iwashita82], bandwidth and relaxation oscillation enhancement [Murakami03], [Simpson95], reduced frequency chirping [Lin84], [Toba84], nonlinear distortion suppression [Meng98], reduction of relative intensity noise [Liu97], [Yabre00], increased link gain [Pochet14], and near single sideband modulation [Sung07]. Periodic oscillations have applications in photonic microwave generation [Hwang04], [Chan07], while chaotic dynamics can be used for chaotic communication [Lodi94] and random bit generation [Li12]. This chapter focuses on the simulation of dynamics in the stable locking regime, where the frequency of the slave laser is locked to that of the master laser with a constant phase offset. Chapter 5 will discuss nonlinear dynamics generated in the unstable locking regime.

4.1. Electric field under optical injection

Within the framework of the semi-classical laser theory, the time change of the electric field in the semiconductor laser subject to external optical injection is governed by the equation as [Lang82]:

$$\frac{d\varepsilon}{dt} = \frac{1}{2}(\Gamma v_g g - \frac{1}{\tau_p})\varepsilon + j\Delta\omega_N \varepsilon + k_c A_{inj} e^{j\Delta\omega_{inj} t} \tag{4.1}$$

where the first term on the right hand side gives the gain and the optical loss of the field. The second term ω_N is the carrier-induced frequency shift, and the expression is the same as the free running laser described in chapter 3. The last term is related to the external optical injection with A_{inj} the amplitude of the injected light, and k_c the external coupling coefficient between the master and the slave lasers:

$$k_c = \frac{v_g}{2L}\frac{1-R}{\sqrt{R}} \tag{4.2}$$

where L is the length of the laser cavity, R is the facet reflectivity, and $\Delta\omega_{inj}$ defines the detuning frequency as $\Delta\omega_{inj} = \omega_{master} - \omega_{slave}$. The phase information is contained in the complex electric field expression $\varepsilon(t) = A\exp\left[-j(\varphi_m - \varphi_s(t))\right]$, with $\varphi_s(t)$ and φ_m being the temporal laser phase and the constant injected phase, respectively [Murakami03]. The phase of the laser field $\varepsilon(t)$ is time-dependent and thus inconvenient for discussions. In order to remove the time dependence, we shift the phase using $E(t) = \varepsilon(t)\exp\left[-j\Delta\omega_{inj} t\right]$. Inserting this equation into Eq. (4.1) yields:

$$\frac{dE}{dt} = \frac{1}{2}(\Gamma v_g g - \frac{1}{\tau_p})E + j\Delta\omega_N E + k_c A_{inj} - j\Delta\omega_{inj} E \tag{4.3}$$

with $E(t) = A(t)\exp\left[-j(\varphi_m - \varphi_s(t)) - j\Delta\omega_{inj} t\right]$. Thus, the phase difference between the slave and the master lasers is given by $\phi(t) = \varphi_s(t) - \varphi_m - \Delta\omega_{inj} t$.

An alternative approach of the modeling is to describe the photon number S(t) and the phase $\phi(t)$, separately. Using $E(t) = \sqrt{S(t)}\exp\left[j\phi(t)\right]$, Eq. (4.3) can be replaced by

$$\frac{dS}{dt} = (\Gamma_p v_g g - \frac{1}{\tau_P})S + 2k_c\sqrt{S_{inj}S}\cos\phi + \beta_{SP}\frac{N}{\tau^{spon}} \tag{4.4}$$

$$\frac{d\phi}{dt} = \Delta\omega_N - \Delta\omega_{inj} - k_c\sqrt{\frac{S_{inj}}{S}}\sin\phi \tag{4.5}$$

where the spontaneous emission term is included in Eq. (4.4), and S_{inj} stands for the injected photon number. The internal injection ratio is defined as $R_{inj}=S_{inj}/S_0$, where S_0 is photon number of the free-running laser. Coupling Eqs. (4.4) and (4.5) with the rate equations describing the carrier dynamics of the Qdots (chapter 3), we obtain the full set of rate equations for the optically injection-locked Qdot laser system.

4.2. Stability diagram

Before discussing the modulation dynamics, it is important to firstly determine the stable locking regime where the modulation operation is meaningful. From the analysis of the steady-state solution of the rate equation system, we can obtain the phase across the stable locking range is approximately $\cot^{-1}\alpha_H$ to $-\pi/2$ from negative to positive frequency detuning edges [Lau08]. The accurate locking region is given by the local bifurcations of the Qdot laser, namely saddle-node and Hopf bifurcations [Wieczorek02], [Wieczorek05], [Sciamanna05]. The bifurcations can be obtained by an eigenvalue analysis of the fixed point, that is, if a single, real eigenvalue passes through the imaginary axis in the complex plane, one typically finds a *saddle-node* (SN) bifurcation while a pair of complex conjugate eigenvalues passing through the imaginary axis corresponds to a *Hopf* bifurcation. One distinguishes between bifurcations of attracting objects, which are called *supercritical*, and bifurcations of unstable objects, which are called *subcritical*. Note that subcritical bifurcations, which may not seem to be of immediate relevance from an experimental point of view, are generally necessary to obtain an overall and consistent dynamical picture. As a result of numerical continuation one obtains a bifurcation curve as a boundary between two regions of qualitatively different dynamics of the laser [Wieczorek05].

The bifurcations can be efficiently predicted by the approach of numerical continuation, which is implemented by the continuation package *MATCONT* in this work [Dhooge03]. *MATCONT* is a *MATLAB* package for numerical bifurcation analysis of ordinary differential equations (ODEs). It allows one to compute curves of equilibria, saddle-node points (limit points), Hopf points, limit cycles, period doubling bifurcation points of limit cycles, and fold bifurcation points of limit cycles. All curves are computed by the same function that implements a prediction-correction continuation algorithm based on the Moore-Penrose matrix pseudo-inverse. The continuation of bifurcation points of equilibria and limit cycles is based on bordering methods and minimally extended systems.

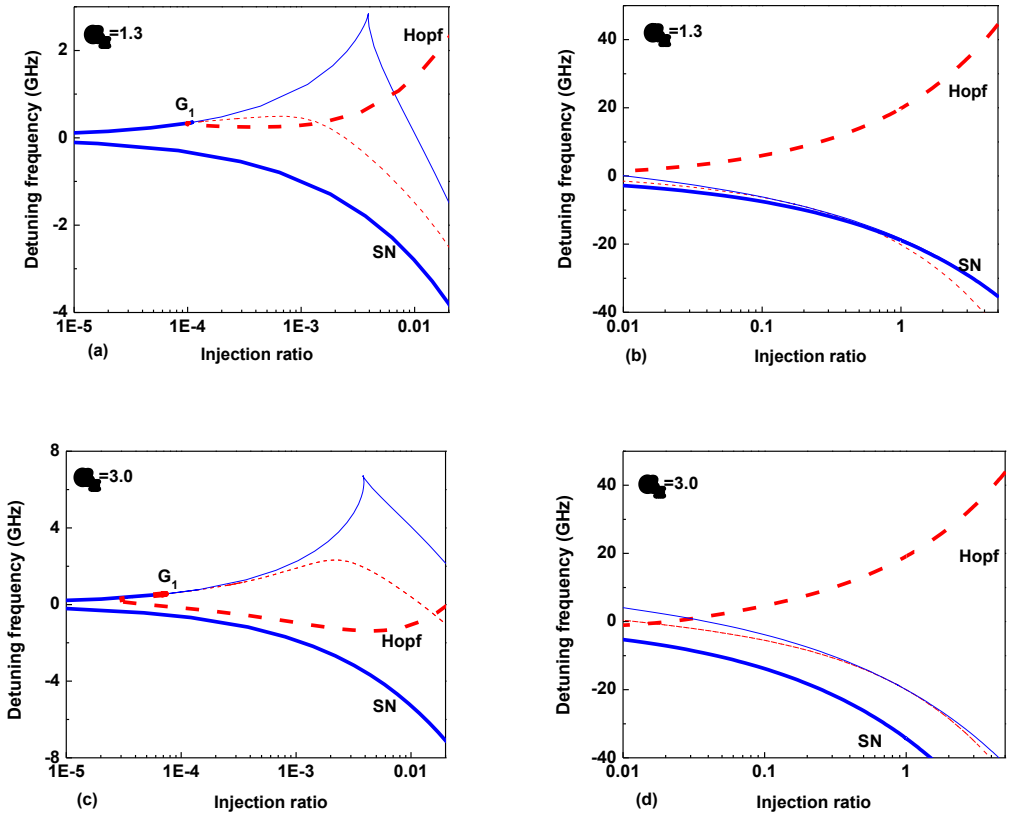

Fig. 4.2. Local bifurcation diagrams as a function of the injection ratio and the detuning frequency for α-factor α_H =1.3 (a) and (b); and for α-factor α_H=3.0 (c) and (d). Solid line is the saddle-node (SN) bifurcation and dashed line is the Hopf bifurcation. The supercritical bifurcation is denoted by thick lines while subcritical bifurcation by thin lines. The stable locking regime is bounded by the supercritical bifurcations.

Figure 4.2 shows the SN (solid lines) and Hopf (dashed lines) bifurcations of the Qdot laser. The stable locking regime is bounded by the supercritical bifurcations (both solid and dashed thick lines) [Wieczorek99]. This regime is enlarged under high injection level as shown in the right part of Fig. 4.2. At low injection strength ((a) and (c)), the intersection of the Hopf and SN curves produces a codimension-two point G_1 where the bifurcations change from supercritical (subcritical) to subcritical (supercritical) along both the Hopf and SN curves. It is known that the laser system can generate a variety of nonlinear dynamics around the G_1 point in its vicinity [Wieczorek99]. The supercritical bifurcation can be tracked in experiment while the subcritical bifurcation not. Nevertheless, the latter is important for understanding the global dynamical bifurcations [Wieczorek03]. In addition, Fig. 4.2 shows that the bifurcation diagram strongly depends on the value of the α-factor. A nonzero α-factor always leads to an asymmetric bifurcation, and a large α-factor shifts the stable-locked region to the negative side [Wieczorek05].

4.3. Modulation bandwidth enhancement

This section deals with the modulation characteristics of injection-locked lasers. As for the case of free running laser (see sections 3.1-3.3), we also study the modulation dynamics (AM and FM) of the injection-locked laser semi-analytically. Considering a Qdot laser operated on the GS, the rate equation model is described by Eqs. (4.4), (4.5) associated with Eqs. (3.40)-(3.42) in chapter 3. Through the small signal analysis, we linearize the rate equations, and yield

$$\begin{bmatrix} \gamma_{11}+j\omega & -\gamma_{12} & 0 & 0 & 0 \\ -\gamma_{21} & \gamma_{22}+j\omega & -\gamma_{23} & 0 & 0 \\ 0 & -\gamma_{32} & \gamma_{33}+j\omega & -\gamma_{34} & 0 \\ 0 & 0 & -\gamma_{43} & \gamma_{44}+j\omega & -\gamma_{45} \\ -\gamma_{51} & -\gamma_{52} & -\gamma_{53} & -\gamma_{54} & \gamma_{55}+j\omega \end{bmatrix} \begin{bmatrix} \delta N_{RS} \\ \delta N_{ES} \\ \delta N_{GS} \\ \delta S_{GS} \\ \delta\phi \end{bmatrix} = \frac{\delta I}{qV} \begin{bmatrix} 1 \\ 0 \\ 0 \\ 0 \\ 0 \end{bmatrix} \tag{4.6}$$

with

$$\gamma_{11} = \frac{1-\rho_{ES}}{\tau_{ES}^{RS}} + \frac{1}{\tau_{RS}^{spon}};\quad \gamma_{12} = \frac{1}{\tau_{RS}^{ES}} + \frac{1}{4N_B}\frac{N_{RS}}{\tau_{ES}^{RS}};\quad \gamma_{21} = \frac{1-\rho_{ES}}{\tau_{ES}^{RS}};$$

$$\gamma_{22} = \frac{1-\rho_{GS}}{\tau_{GS}^{ES}} + \frac{1}{\tau_{RS}^{ES}} + \frac{1}{\tau_{ES}^{spon}} + \frac{1}{4N_B}\frac{N_{RS}}{\tau_{ES}^{RS}} + \frac{1}{4N_B}\frac{N_{GS}}{\tau_{ES}^{GS}};\quad \gamma_{23} = \frac{1-\rho_{ES}}{\tau_{ES}^{GS}} + \frac{1}{2N_B}\frac{N_{ES}}{\tau_{GS}^{ES}};$$

$$\gamma_{32} = \frac{1-\rho_{GS}}{\tau_{GS}^{ES}} + \frac{1}{4N_B}\frac{N_{GS}}{\tau_{ES}^{GS}};\quad \gamma_{33} = \frac{1-\rho_{ES}}{\tau_{ES}^{GS}} + \frac{1}{\tau_{GS}^{spon}} + \frac{1}{2N_B}\frac{N_{ES}}{\tau_{GS}^{ES}} + v_g a S_{GS};$$

$$\gamma_{34} = -v_g g_{GS} + v_g a_P S_{GS};\quad \gamma_{43} = \Gamma_p v_g a S_{GS} + \frac{\Gamma_p \beta_{SP}}{\tau_{GS}^{spon}};$$

$$\gamma_{44} = -\Gamma_p v_g g_{GS} + \frac{1}{\tau_p} + \Gamma_p v_g a_P S_{GS} - k_c \cos\phi\sqrt{S_{inj}/S_{GS}};$$

$$\gamma_{45} = -2k_c \sin\phi\sqrt{S_{inj}S_{GS}};\quad \gamma_{51} = \Gamma_p v_g a_{RS} F_{RS};\quad \gamma_{52} = \frac{1}{4}\Gamma_p v_g a_{ES} F_{ES};\quad \gamma_{53} = \frac{1}{2}\Gamma_p v_g a \alpha_H^{GS};$$

$$\gamma_{54} = -\frac{1}{2}\Gamma_p v_g a_P \alpha_H^{GS} + \frac{k_c \sin\phi}{2S_{GS}}\sqrt{S_{inj}/S_{GS}};\quad \gamma_{55} = k_c \cos\phi\sqrt{S_{inj}/S_{GS}}; \tag{4.7}$$

Using the modulation transfer function $H(\omega) = \delta S_{GS}(j\omega)/(\delta I/qV)$, Fig. 4.3 presents the injection effect on the AM response for different injection ratios under the zero detuning condition, that is, the master and slave lasers are referenced to the same frequency. In Fig. 4.3(a), at low injection ratio, the response is under-damped and exhibits a high relaxation peak. Large injection ratio increases the damping factor and thereby the laser shows a broadband and flat response. Figure 4.3(b) shows that the 3-dB modulation bandwidth is increased by the optical injection in comparison with that of the free-running laser. The bandwidth of the injected laser reaches the maximum at an injection ratio of R_{inj}=2.0. The enhanced resonance frequency is generated by the transient interaction between the injection-locked field and the field

corresponding to the shifted cavity resonance [Murakami03]. This regime around zero detuning is more suitable for high-speed and broadband telecommunication applications [Naderi11].

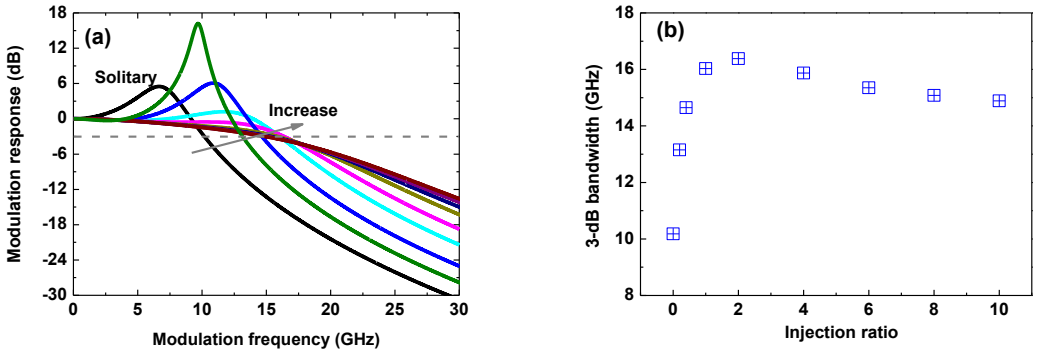

Fig. 4.3. (a) Amplitude response of the optically injection-locked QD laser for increasing values of the injection ratios of R_{inj}= 0, 0.2, 0.4, 1.0, 2.0, 4.0, 6.0, 8.0, 10. (b) 3-dB modulation bandwidth as a function of the injection ratio. The frequency detuning is fixed at Δf_{inj}=0 GHz.

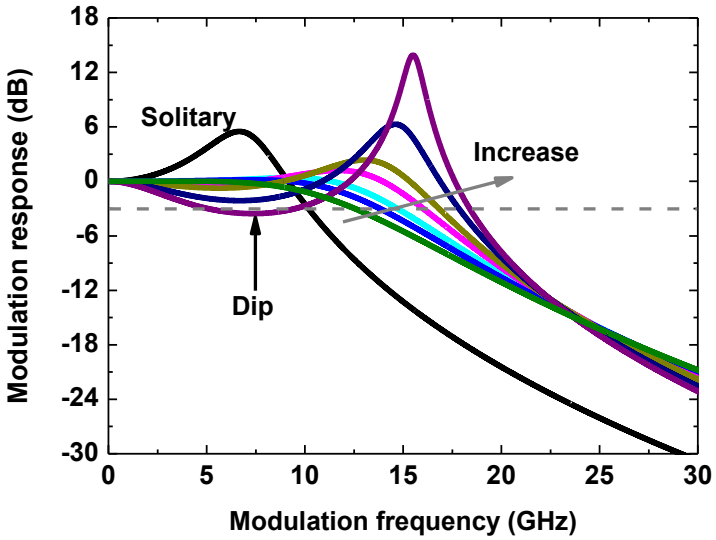

Fig. 4.4. Effect of frequency detuning on the modulation response. The detunings Δf_{inj}=-8, -5, -3, 0, 2, 5, 7 GHz. The injection ratio is fixed at R_{inj}=1.0.

Figure 4.4 illustrates the effect of frequency detuning on the modulation response within the stable locking region. At negative frequency detuning side, that is when the frequency of the master laser is smaller than that of the slave laser, the modulation response is highly damped, and thus yield quite linear curve. This regime has a high gain and can be used for low bandwidth applications that need low link loss or high linearity [Lau08]. At positive frequency detuning side, the laser shows a sharp and high resonance peak. In addition, there is usually a dip ahead of the resonance frequency, which limits the modulation bandwidth. This regime near the positive stable locking edge can be used for narrow band applications at extremely high frequencies, or for high-speed optoelectronic oscillators.

4.4. Frequency chirp reduction

Similarly to the chirp characterization of the free-running laser in Eq. (3.48), the CPR of the laser subject to optical injection is given by [Lau09]:

$$CPR_{inj}(\omega)=\omega\frac{\alpha_H(j\omega)}{2S_{GS}}\frac{(j\omega+1/\tau_p-\Gamma_p v_g g_{GS})+k_c\sqrt{S_{inj}/S_{GS}}\left(\sin\phi/\alpha_H(j\omega)-\cos\phi\right)}{j\omega+k_c\sqrt{S_{inj}/S_{GS}}\left(\cos\phi-\alpha_H(j\omega)\sin\phi\right)} \quad (4.8)$$

where $\alpha_H(j\omega)$ is given in Eq. (3.48). The above equation does not include the gain compression term for the sake of simplicity. However, the simulations in the following figures take into account the gain compression effect with a factor of 2×10^{-16} cm^3 as listed in Table 3.2. Without optical injection, Eq. (4.8) will reduce to be the same as Eq. (3.48) for the case of the free running laser. It is noted that we do not consider the thermal impact on the frequency chirp properties, which is known to increase the chirp level for modulation frequencies less than 0.01 GHz [Coldren95],[Kechaou12a].

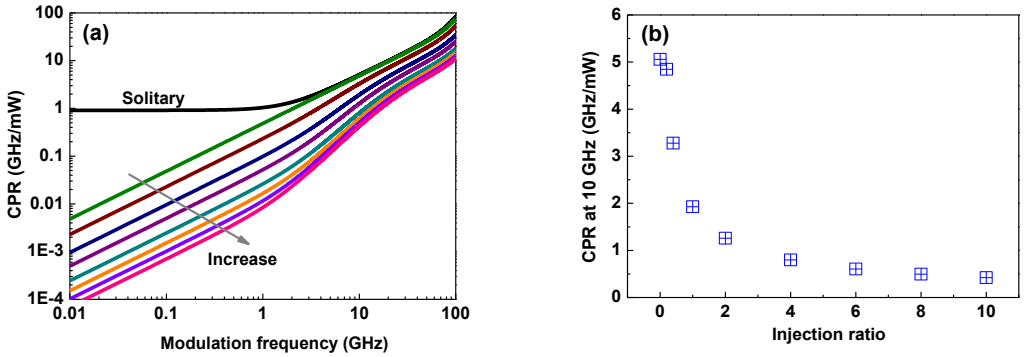

Fig. 4.5. (a) CPR of the optically injection-locked Qdot laser for increasing injection ratios of R_{inj}= 0, 0.2, 0.4, 1.0, 2.0, 4.0, 6.0, 8.0, 10. (b) CPR value at 10 GHz as a function of the injection ratio. The frequency detuning is fixed at Δf_{inj}=0 GHz. The gain compression effect is included with a factor of 2×10^{-16} cm^3.

Figure 4.5(a) shows the CPR of the injected laser at various injection ratios. At low modulation frequencies less than 1 GHz, the adiabatic chirp of the free-running laser remains constant at 1.0 GHz/mW. In contrast, the CPR of the injected laser is well reduced. This is attributed to the injection term shown in the denominator of Eq. (4.8). Therefore, optical injection suppresses the adiabatic chirp of the Qdot laser. At high modulation frequencies, the CPR is also reduced. Figure 4.5(b) presents the CPR value at 10 GHz as a function of the injection ratio. It is shown that the CPR is reduced from 5 GHz/mW for the free-running laser down to 0.5 GHz/mW at an injection ratio of R_{inj}=10.0. Figure 4.6 illustrates similar effect of frequency detuning on the CPR. It is shown that the CPR value is sensitive to the frequency detuning, and the minimum is obtained at a slightly negative detuning frequency (-3 GHz).

Experimental results discussed in section 5.3 confirm that the adiabatic chirp can be indeed almost completely removed by the optical injection.

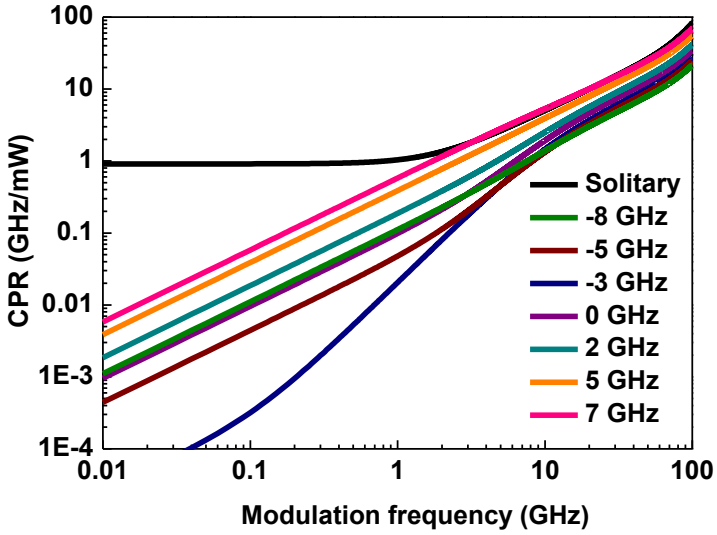

Fig. 4.6. Effect of frequency detuning on the CPR. The injection ratio is fixed at R_{inj}=1.0. The minimum CPR is obtained at a slightly negative detuning frequency (-3 GHz).

4.5. α-factor under optical injection

From the analysis in chapter 3, we know that in the free running laser the α-factor can be extracted from the ratio of the FM-to-AM indices referring to Eq. (3.49). However, the relation between the α-factor and the ratio 2β/m can be substantially modified by the optical injection. Indeed, from the small signal analysis of the differential equation Eq. (4.6) for the injected laser, we obtain

$$\left(\frac{2\beta(m)}{m(\omega)}\right)_{inj} = \alpha_H(j\omega)\frac{(j\omega+1/\tau_p-\Gamma_p v_g g_{GS})+k_c\sqrt{S_{inj}/S_{GS}}\left(\sin\phi/\alpha_H(j\omega)-\cos\phi\right)}{j\omega+k_c\sqrt{S_{inj}/S_{GS}}\left(\cos\phi-\alpha_H(j\omega)\sin\phi\right)} \quad (4.9)$$

In comparison with the free-running case in Eq. (3.49), the relation between the two parameters becomes more complex. An injection term appears in the numerator while another one in the denominator. Therefore, the behavior of 2β/m strongly depends on the injection condition. In addition, it is noted that the relation $(2\beta/m)_{inj} = 2S_{GS}CPR_{inj}/\omega$ is still valid as for the free running laser.

Figure 4.7 shows the variation of the ratio 2β/m at different injection strengths. As already discussed in the previous chapter, 2β/m of the free-running laser exhibits a giant value at low modulation frequency, which is mostly due to the gain compression in the numerator as well as the small value of modulation frequency in the denominator in Eq. (4.9). In contrast, with

optical injection, the giant value disappears due to the additional injection term in the denominator. For modulation frequencies less than 1 GHz, the ratio 2β/m of the injected laser remains almost constant at a rather low value (less than 1). Increasing the modulation frequency makes the 2β/m values converge towards the free-running case. Beyond a few GHz (10 GHz), the plateau gives the α-factor extracted by the FM/AM technique, which has already been discussed in chapter 3.

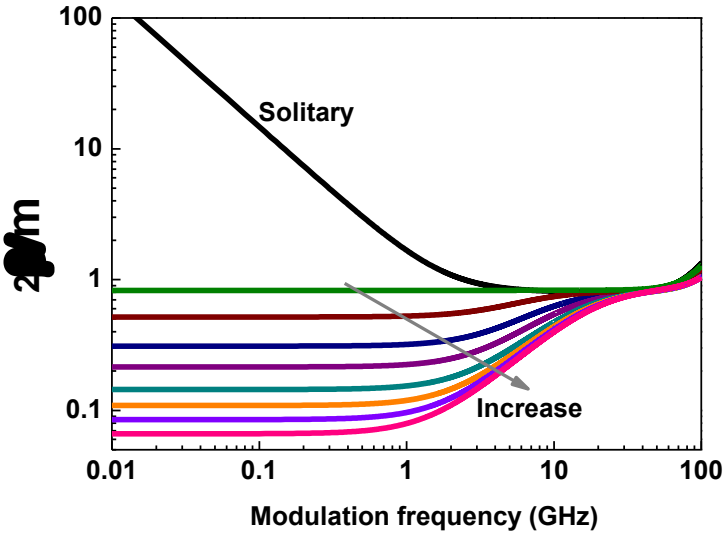

Fig. 4.7. FM-to-AM index ratio of the injection-locked Qdot laser for injection ratios of R_{inj}= 0, 0.2, 0.4, 1.0, 2.0, 4.0, 6.0, 8.0, 10. The frequency detuning is fixed at Δf_{inj}=0 GHz.

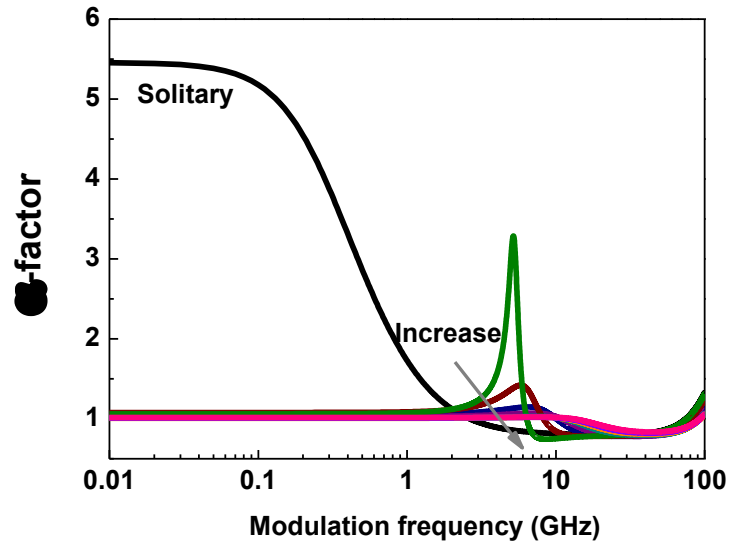

Fig. 4.8. Frequency dependence of the α-factor of the injection-locked Qdot laser for injection ratios of R_{inj}= 0, 0.2, 0.4, 1.0, 2.0, 4.0, 6.0, 8.0, 10. The frequency detuning is fixed at Δf_{inj}=0 GHz.

Correspondingly, Fig. 4.8 presents the variation of the α-factor as a function of the modulation frequency for different injection strengths. It is noted that the α-factor here is still

calculated by Eq. (3.48), since the optical injection can not change the α-factor definition. At low modulation frequency, the free-running laser has a first constant α-factor value around 5.5, which is consistent with the α-factor of the laser under the DC bias condition. In presence of optical injection, this low modulation-frequency α-factor is strongly reduced down to unity. As shown in Fig. 4.9, this effect can be explained by the difference of the carrier population variations between the off-resonant states (ES, RS) and the resonant GS, which is decreased by the optical injection, in comparison with the free-running laser case (see Fig. (3.9)). At high modulation frequencies, the α-factor of the free running laser decreases to a plateau, which is consistent with the 2β/m value in this range. Fig. 4.8 shows that the optical injection has little impact on the α-factor at this high modulation frequency regime except for low injection ratio, in which case a resonance-like peak occurs. This is attributed to the pre-resonance dip in the frequency response of the GS carrier density (Fig. 4.9). This kind of phenomenon occurs once there is a high relaxation peak in the AM response, which also happens at the positive detuning edge as described in the following.

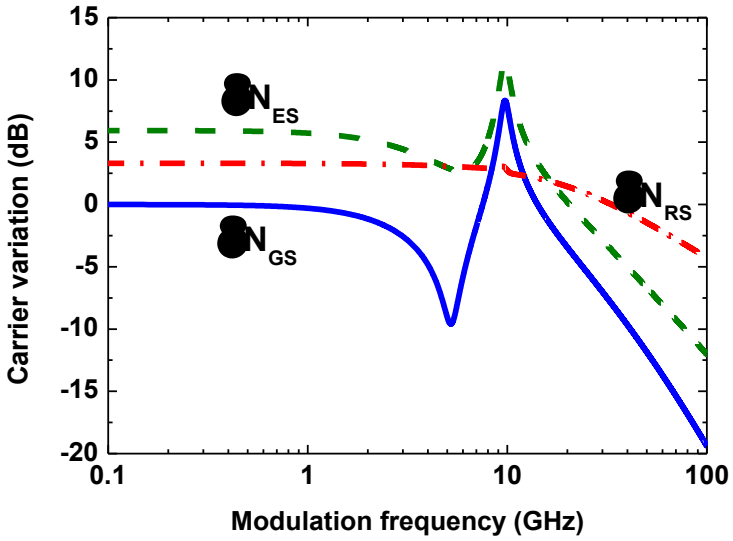

Fig. 4.9. Carrier density variations at an injection ratio of R_{inj}= 0.2. The frequency detuning is Δf_{inj}=0 GHz. The dip in the GS leads to the resonance-like peak in the α-factor. The carrier variation is normalized to the value δN_{GS} of 0.01 GHz.

Figure 4.10 shows that the ratio 2β/m also strongly depends on the frequency detuning. The minimum value occurs at a detuning of -3.0 GHz as for the CPR. Figure 4.11 demonstrates that the α-factor under low modulation frequency slightly decreases when varying the frequency detuning from negative to positive side.

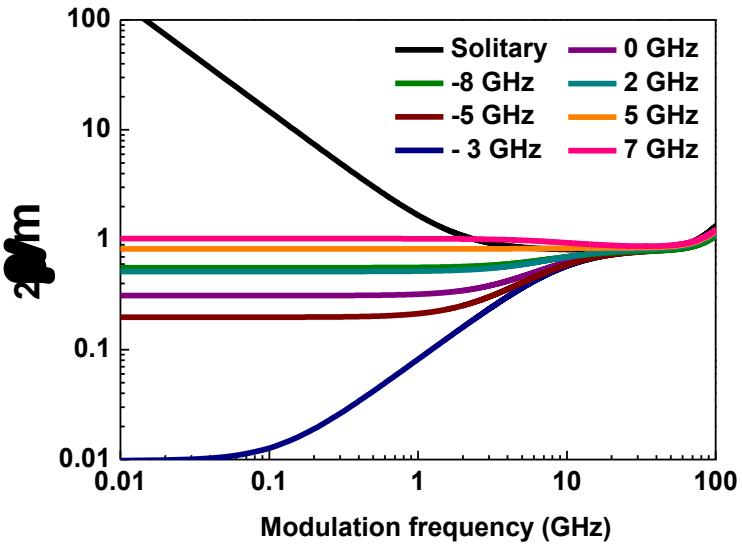

Fig. 4.10. Frequency detuning effect on the ratio of FM-to-AM indices. The injection ratio is fixed at R_{inj}=1.0.

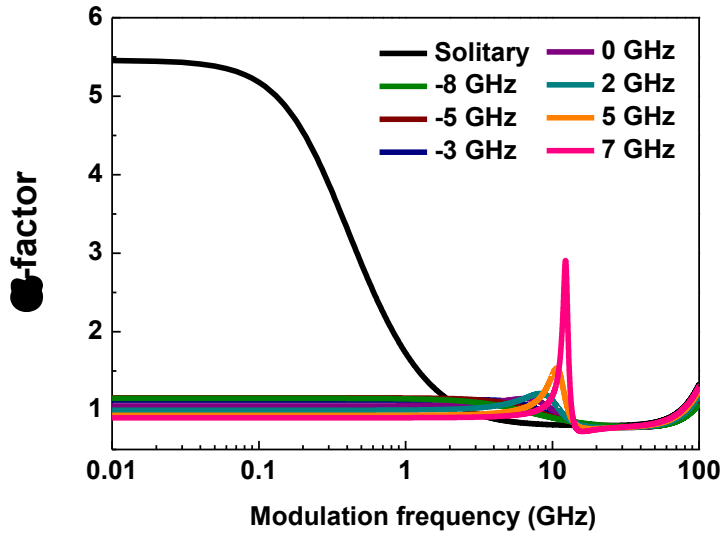

Fig. 4.11. Frequency detuning effect on the α-factor. The injection ratio is fixed at R_{inj}=1.0.

4.6. Improvement of large-signal performance

This section numerically studies the large-signal modulation characteristics of the injection-locked laser. In particular, it is shown that improvements of the eye diagram as well as the suppression of the time-resolved chirp are possible under proper injection-locking conditions. In this section, carrier dynamics including the SCH, the RS, as well as the ES_2, ES_1 and GS are described by Eqs. (3.59)-(3.63), while the injected laser (complex) field is expressed by Eq. (4.3). The laser under study is a Qdot DFB laser emitting at 1.55 μm as described in section 3.7. Taking advantage of the MPRE model, we firstly investigate the effect of optical injection

on the gain spectrum. Then in the second part we study the injection influence on the large signal modulation dynamics.

A) Effect of optical injection on the gain

The studied Qdot DFB laser is biased at 30 mA. Figure 4.12(a) shows that the carrier occupation probability of each discrete state in the dots decreases under strong injection strength. As an example, the GS occupation probability is 77% for the free running laser, while it decreases to 54% with an injection ratio R_{inj}=10. On the other hand, Fig 4.12(b) reveals that the carrier occupation also decreases at the negative frequency detuning side while increasing at the positive detuning side. Figure 4.13 shows that the lasing power is enhanced either by increasing the injection power and/or by tuning frequency of the master laser to the negative side. Figure 4.14 illustrates that the phase ϕ (see Eq. (4.5)) increases significantly at low injection ratio in comparison with the free running case, while at high injection ratio, the phase only changes slightly with the increased injection strength. On the other hand, positive frequency detuning reduces the phase value.

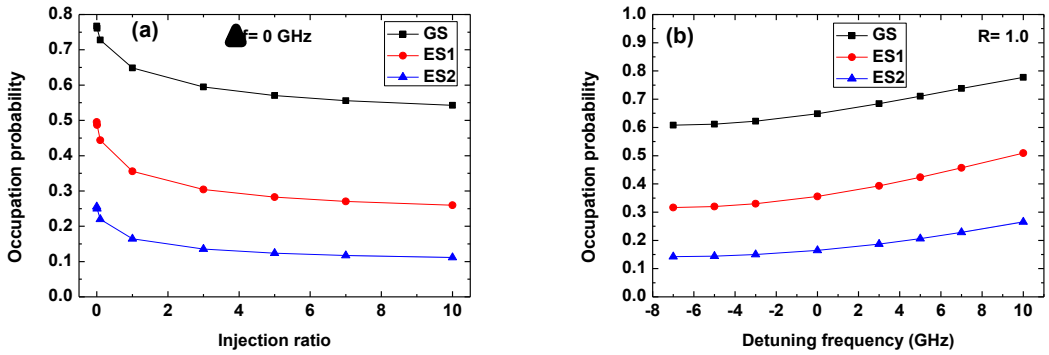

Fig. 4.12. Carrier occupation probability in each discrete Qdot states of injected laser. (a) Injection strength effect with fixed detuning Δf_{inj}=0 GHz. (b) Frequency detuning effect with fixed injection ratio R_{inj}=1.0.

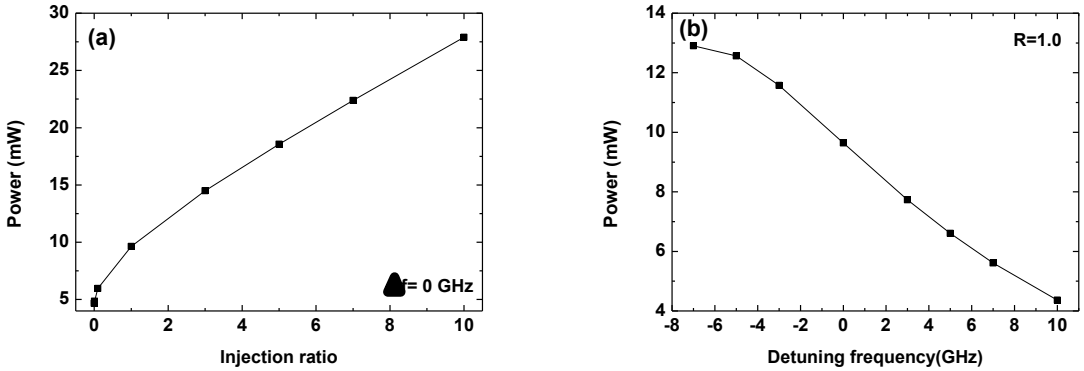

Fig. 4.13. (a) Influence of injection strength on the lasing power with fixed detuning Δf_{inj}=0 GHz. (b) Influence of frequency detuning on the lasing power with fixed injection ratio R_{inj}=1.0.

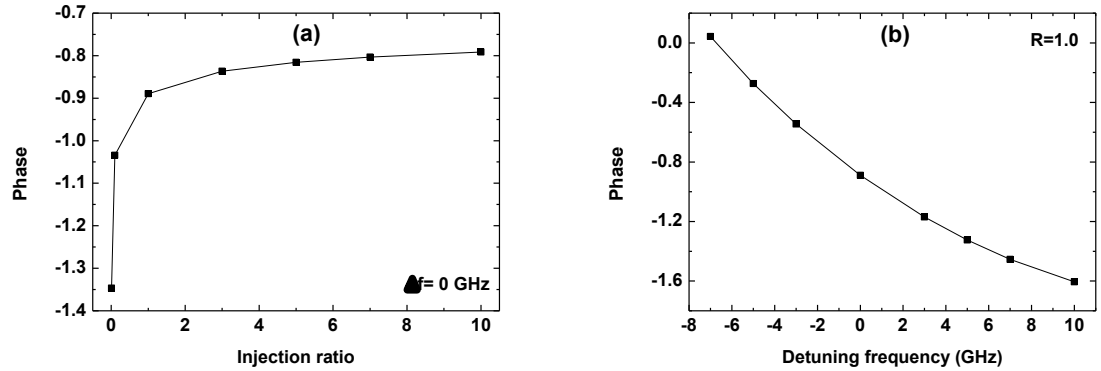

Fig. 4.14. (a) Influence of injection strength on the phase ϕ with fixed detuning Δf_{inj}=0 GHz. (b) Influence of frequency detuning on the phase with fixed injection ratio R_{inj}=1.0.

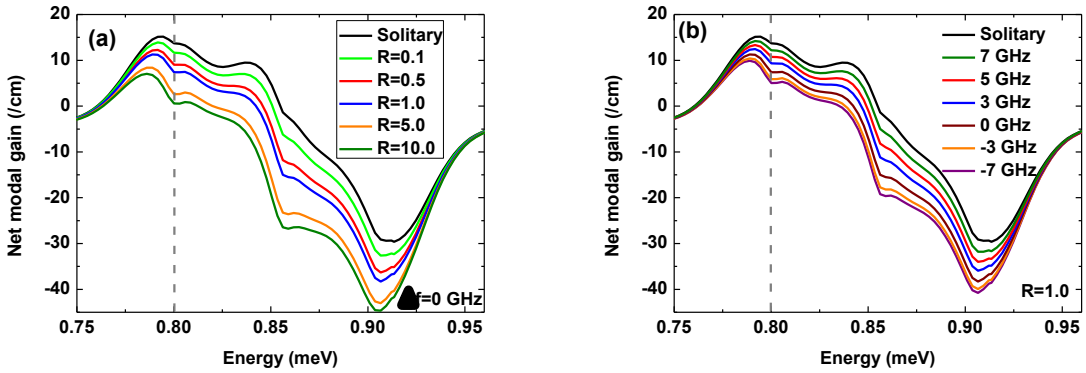

Fig. 4.15. Influence of optical injection on the net modal gain spectrum. (a) Influence of injection strength with fixed detuning Δf_{inj}=0 GHz. (b) Influence of frequency detuning with fixed injection ratio R_{inj}=1.0. The dashed line indicates the lasing energy of the DFB laser.

Finally, the effect of optical injection on the gain spectrum variation is given in Fig. 4.15. In consistence with the carrier occupation probability in Fig. 4.12, the whole gain spectrum is reduced by the optical injection. In addition, the gain decreases from positive to negative detuning side (Fig. 4.15(b)). This particular feature will be exploited in the next chapter to extract the α-factor with a novel experimental technique.

B) Effect of optical injection on the large-signal dynamics

As discussed in section 4.3, the injected laser at zero frequency detuning usually exhibit a broadband and flat modulation response, which is preferable in high-speed optical telecommunications. Positive detuning is not favourable due to the sharp relaxation peak and the pre-resonance dip while negative detuning is not either because of the small modulation bandwidth. Therefore, this section only discusses the effect of varying injection strength on the large signal performance at the zero detuning condition. In the simulation, the studied Qdot laser is modulated between 30 mA and 60 mA, and the modulation bit rate is set at 5.0 Gbps.

Figure 4.16 shows that the openness of the eye diagram are improved by the external optical injection, due to the enhancement of the modulation bandwidth. Figure 4.17 demonstrates that the adiabatic chirp is almost totally suppressed by the optical injection. In addition, the peak-to-peak transient chirp decreases with the increasing injection ratio.

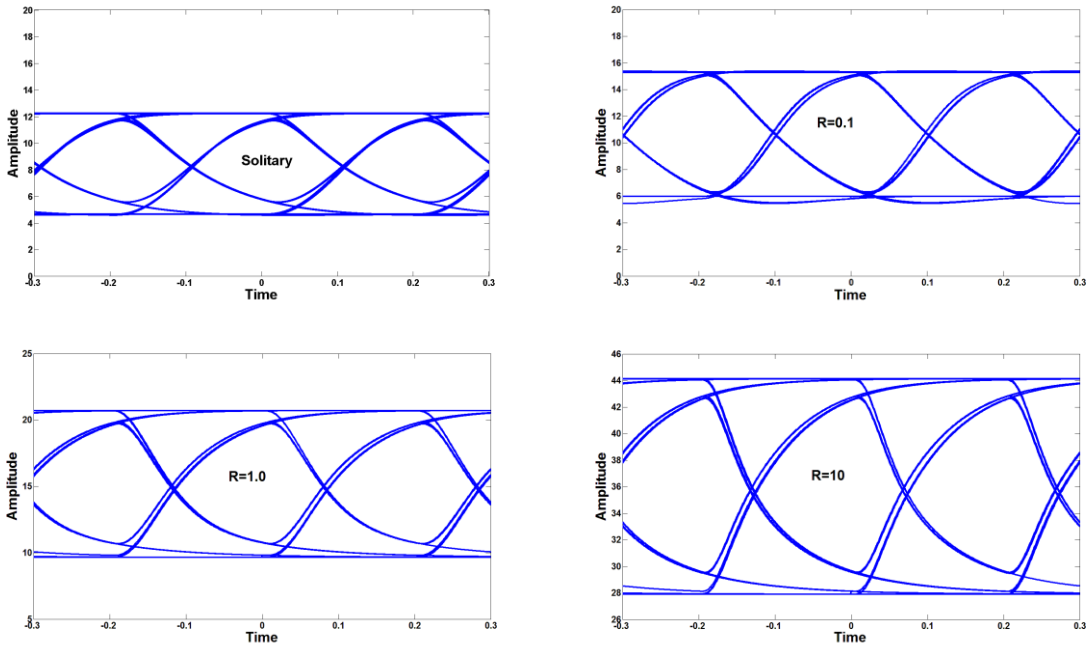

Fig. 4.16. Eye diagram of free-running and injected lasers modulated at 5.0 Gbps. The injections ratios are R_{inj}=0.1, 1.0, 10.0.

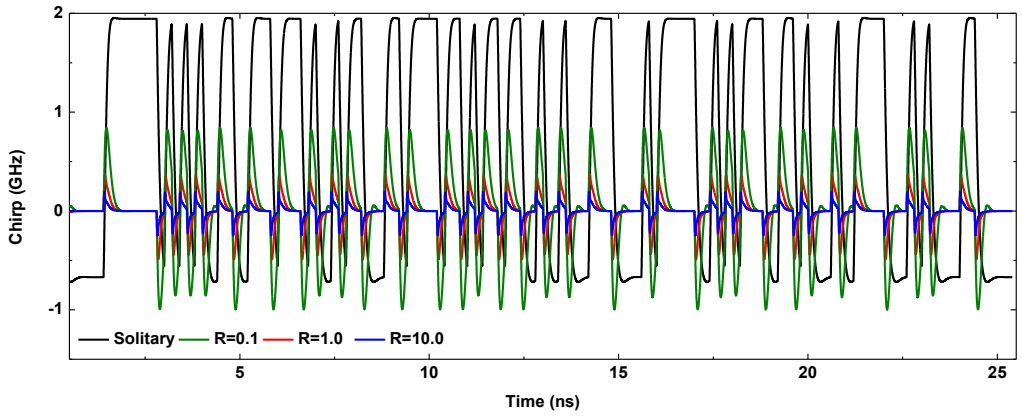

Fig. 4.17. Time-resolved chirp waveforms of free-running and injected lasers at 5.0 Gbps. Injections ratios are R_{inj}=0.1, 1.0, 10.0.

In summary, this chapter studies the effect of the optical injection as a function of the injection strength and the detuning frequency. The injection locking technique can improve the AM response as well as suppress the frequency chirp both in small and large modulation regimes. Numerical results also unveil that the optical injection also strongly alters the phase-amplitude coupling (driven by the α-factor) characteristics. Particularly, we show that the

optical gain spectrum can be tuned either by the injection strength or by the frequency detuning, which will be used in the following chapter to develop a novel experimental technique for the evaluation of the α-factor.

Chapter 5. Experimental investigation of modulation dynamics

5.1. Laser characterization under DC condition

The laser under test is a Qdot laser grown and fabricated at FOTON-INSA laboratory. Figure 5.1 illustrates the epitaxial layer structure of the Qdot laser. The Qdot structure was grown by gas source molecular beam epitaxy on a 2° misoriented (100) n-doped InP substrate [Elias09]. The misorientation allows the formation of Qdots instead of Qdashes which are traditionally formed on InP(100) oriented substrate [Lelarge07]. The active layer consists of six stacked layers of InAs dots, which are embedded into an InGaAsP quaternary alloy. The 4-µm wide (W) ridge waveguide was fabricated by selective wet and dry etching sequence based on a CH_4-H_2-Ar RIE plasma using a Ti-Au mask. Then, a benzocyclobutene (BCB) layer was spin-coated to planarize the mesa structure and dry-etched back to expose the top surface of the ridge. This self-alignment step enables the p-contact electrode to be defined by Ti-Au e-beam evaporation. The substrate was thinned to 150 µm and a backside n-type metallization was performed with an AuGe sputtered alloy. Finally, the device was cleaved into a 830-µm long (L) cavity, and the reflectivity of both facet is R_1=R_2=0.32.

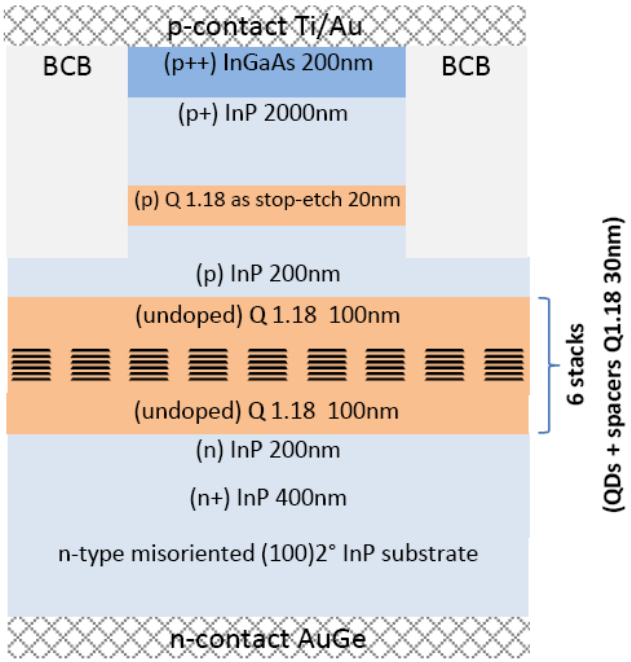

Fig. 5.1. The epitaxial layer structure of the InAs/InP(100) Qdot laser grown at FOTON-INSA laboratory. 'Q1.18' denotes that the quaternary alloy $In_{0.8}Ga_{0.2}As_{0.435}P_{0.565}$ emits at 1.18 µm. The stop-etch layer is used to control the etch depth. 'BCB' denotes benzocyclobutene, and '+' or '++' indicates the doping level.

5.1.1. Static characteristics

The experimental investigations were performed at the Optoelectronics Lab, Télécom ParisTech. Figure 5.2 shows the experimental setup for the static characterization of the free-running laser. A DC current source is used to drive the Qdot laser device through a DC probe. The laser bar is mounted to an aluminum heat sink. The temperature is controlled by a thermo-electric cooler (TEC) and is set to 293 K. The laser output is collected by a single mode lensed fiber, and the coupling efficiency is about 43%. The power is monitored by a power meter and a high resolution (10 pm) optical spectrum analyzer (OSA) is used to record the optical spectra.

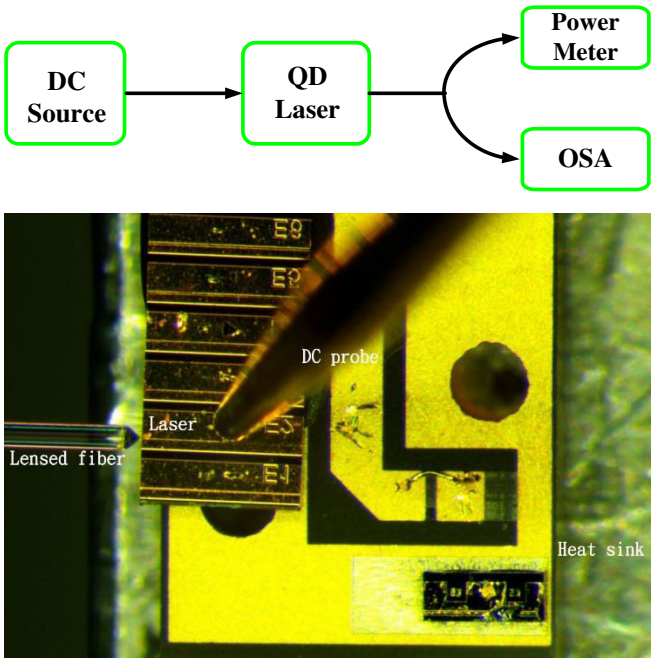

Fig. 5.2. Experimental setup (up) and image of mounting (bottom) for CW operation of the free-running QD laser

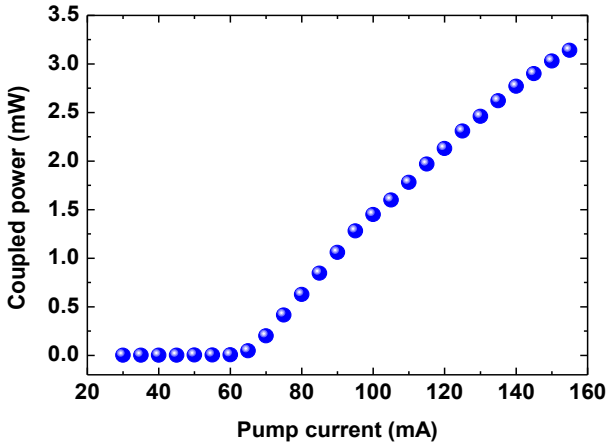

Fig. 5.3. Light-current characteristics (L-I) curve at room temperature (293 K). The lasing threshold is I_{th}=64 mA

Figure 5.3 shows the coupled laser power from a single facet versus the pump current. The lasing threshold is I_{th}=64 mA. The external slope efficiency per facet is 0.086 mW/mA taking into account the fiber's coupling efficiency (43%). Figure 5.4 illustrates the optical spectrum at a bias current of 80 mA. The lasing peak centers around 1635 nm. The average longitudinal mode spacing is 0.458 nm. From the mode spacing and the cavity length, the group refractive index of the laser is calculated through the relation $n_g = \lambda^2 / (2L^* \Delta\lambda)$, and the result is shown in Fig. 5.5. The average value of the refractive index is about 3.50. Considering an internal loss of α_i =6.0 cm^{-1}. The photon lifetime in the cavity is estimated to be 6 ps [Coldren95].

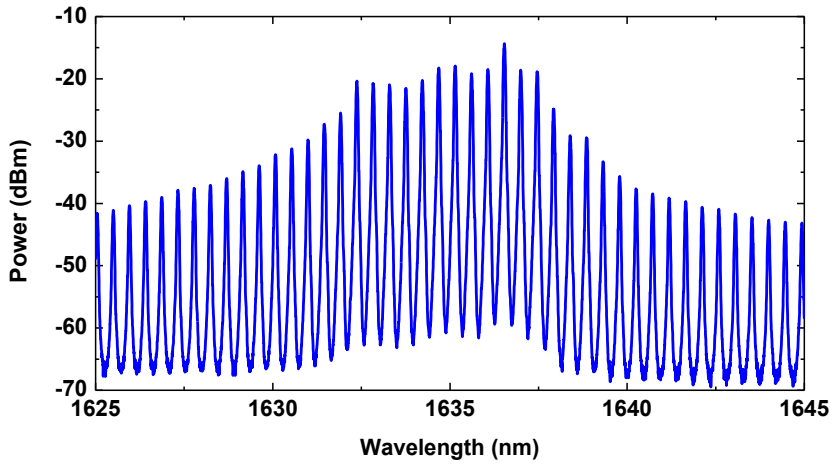

Fig. 5.4. Optical spectrum at I_{bias}=80 mA. The lasing peak centers around 1635 nm.

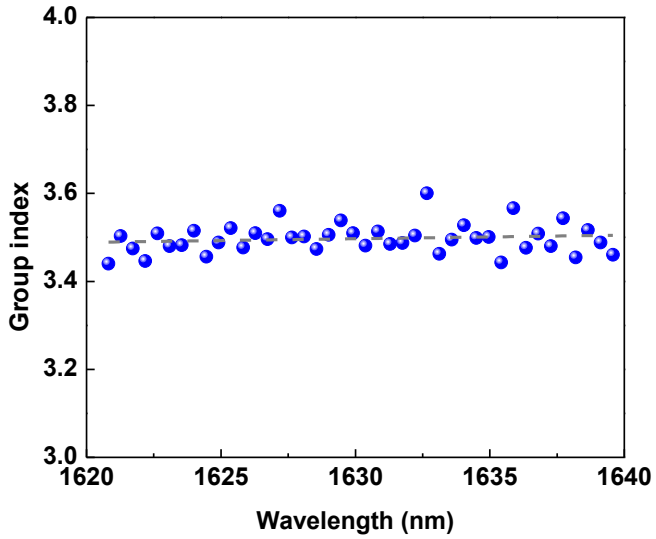

Fig. 5.5. Group refractive index. The average value is n_g=3.497.

Below threshold, the optical gain of the laser increases with the pump current, while it is clamped above threshold. By measuring the evolution of both the wavelength and the gain for

various bias currents, the below threshold α-factor of the laser can be determined by [Raghuraman93]

$$\alpha_H = -\frac{2\pi}{L\Delta\lambda}\frac{d\lambda/dI}{dg_{net}/dI} \tag{5.1}$$

where g_{net} is the net modal gain, which can be obtained from the Hakki-Paoli method. This method is based on the peak-to-valley ratio of the amplified spontaneous spectrum (ASE), and the net modal gain g_{net} is extracted using the following relationship [Hakki75]:

$$g_{net} = \Gamma_p g - \alpha_i = \frac{1}{L}\ln\left(\frac{1}{R}\frac{\sqrt{x}-1}{\sqrt{x}+1}\right) \tag{5.2}$$

where g is the material gain and Γ_p is the optical confinement factor. x is the ratio of the peak-to-valley intensity levels. Figure 5.6 shows the net modal gain variation of the Qdot laser under test from I_{bias}=54.5 mA to I_{bias}=63.5 mA with a current step of 0.5 mA. The laser device exhibits a wide gain spectrum with a full-width at half maximum (FWHM) of about 81 nm and a maximum gain of 14.4 cm^{-1} at 63.5 mA.

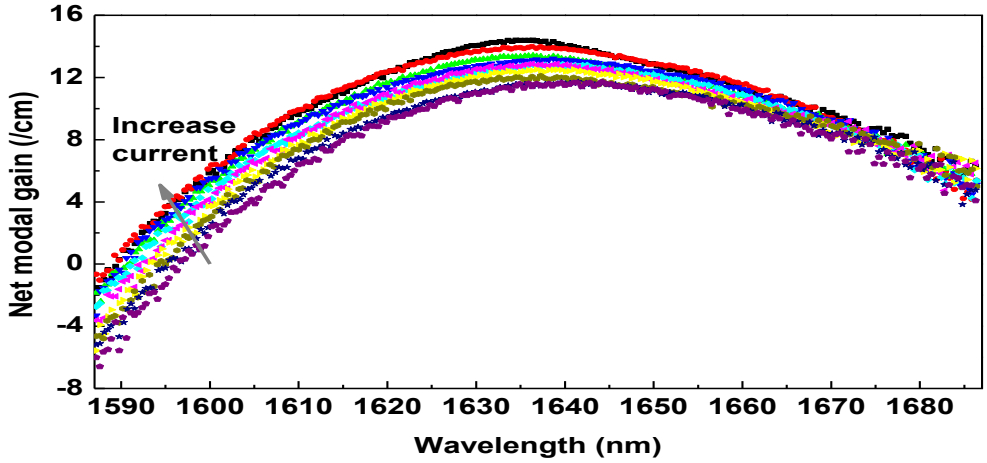

Fig. 5.6. Net modal gain evolution from 54.5 mA to 63.5 mA. The current step is 0.5 mA.

The wavelength evolution with the pump current can be directly tracked from the OSA. The wavelength is blue-shifted because of the band filling effects driven by the carrier injection, that is, $d\lambda/dI < 0$. However, thermal effects will red-shift the wavelength and affect the accuracy of the measurement. In order to attenuate the thermal effects, the DC current source is operated in pulsed mode. The pulse width is set at 10 μs, and the duty cycle is set as 10%. Further reducing the pulse width and the duty cycle is even better for substantially removing the thermal effect but resulting in too weak spectral signals to track. Through Eq. (5.2), the measured α-factor is shown in Fig. 5.7. Generally, the α-factor increases with the optical wavelength, in consistent with the calculation in chapter 3.

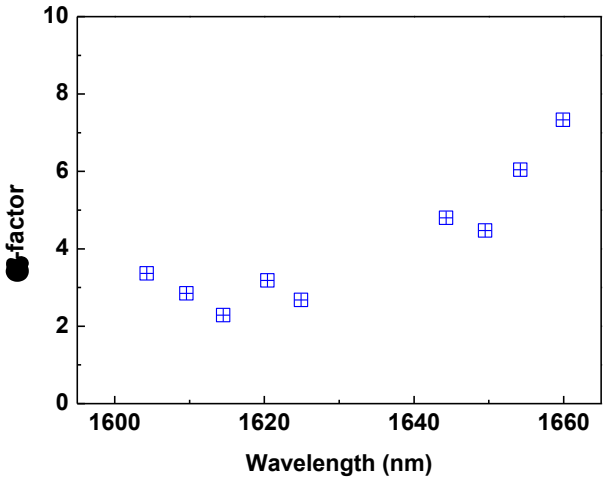

Fig. 5.7. Wavelength dependence of the below threshold α-factor of the Qdot laser measured using the Hakki-Paoli method.

5.1.2. Nonlinear dynamics in injection-locked laser

This section qualitatively studies the nonlinear dynamics of the Qdot laser subject to an external optical injection. Figure 5.8 shows the experimental setup for the characterization. A single-mode external cavity laser is used as the tunable master laser source, and it is injected into the Qdot laser (slave laser) through an optical circulator. The polarization of the master laser is controlled by the polarization controller to align with that of the slave laser, and the injected power is tuned and is monitored by a power monitor. The light is inverted to electric signal through a high-speed photodiode (12 GHz), followed by an electrical spectrum analyzer (ESA) tracking the electric spectrum and by a high-speed digital oscilloscope (20 GHz, Tektronix) recording the time series. This time-resolved signal is post-processed in a computer, where the electric spectrum is reproduced through the Fourier transform. In addition, the phase portrait is extracted from the amplitude (A(t)) and its difference (Diff(A)=A(t_{k+1})-A(t_k)).

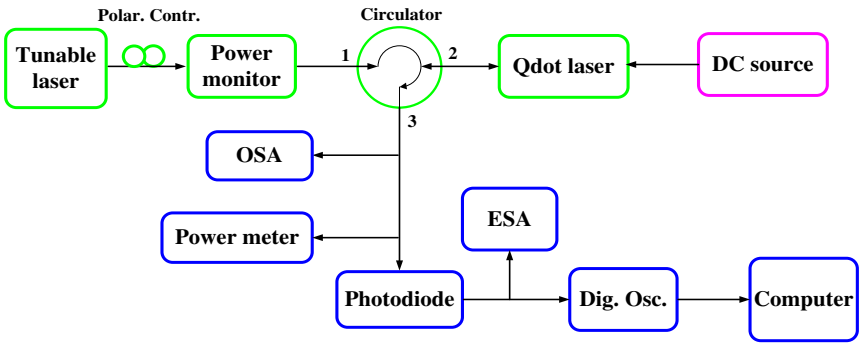

Fig. 5.8. Experimental setup for the characterization of the Qdot laser nonlinear dynamics subject to optical injection. OSA: optical spectrum analyzer; ESA: electronic spectrum analyzer.

Figure 5.9 shows an optical spectrum of the Fabry-Perot Qdot laser subject to optical injection (stably locked) at bias current I_{bias}=80 mA. The injected mode is amplified while other longitudinal modes are well suppressed, the side mode suppression ratio (SMSR) is more than 50 dB. This is because that the gain value over the whole spectra is reduced by the optical injection as discussed in Chapter 4, therefore all the side modes fall below the lasing threshold condition and the residual power owes to the spontaneous emission. It is noted that the residual side modes are all red-shifted due to the reduction of the injected carriers.

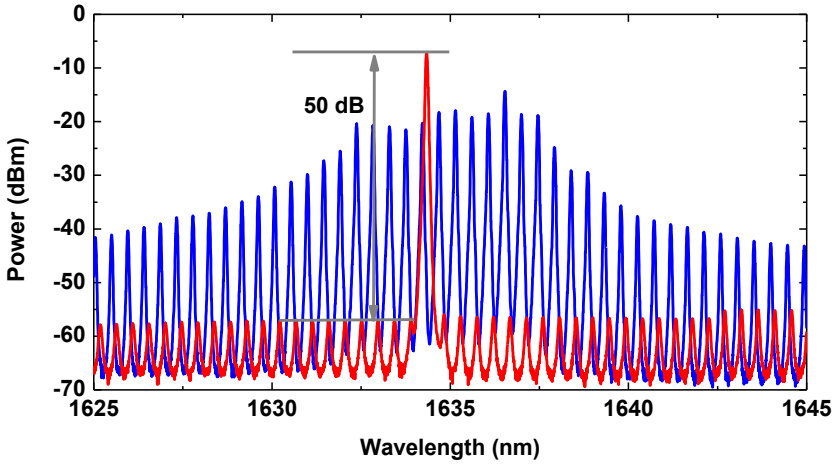

Fig. 5.9. Optical spectra of the optically injected laser (red) and the free-running laser (blue).

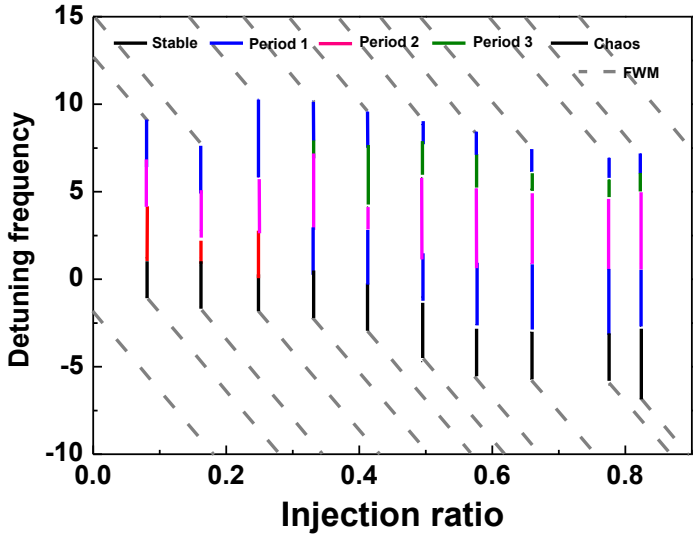

Fig. 5.10. Stability diagram of the Qdot laser subject to optical injection. The bias current is 80 mA, and the free-running wavelength is1637.11nm. The injection ratio is operated up to R_{inj}=0.82, limited by the power of the master laser device.

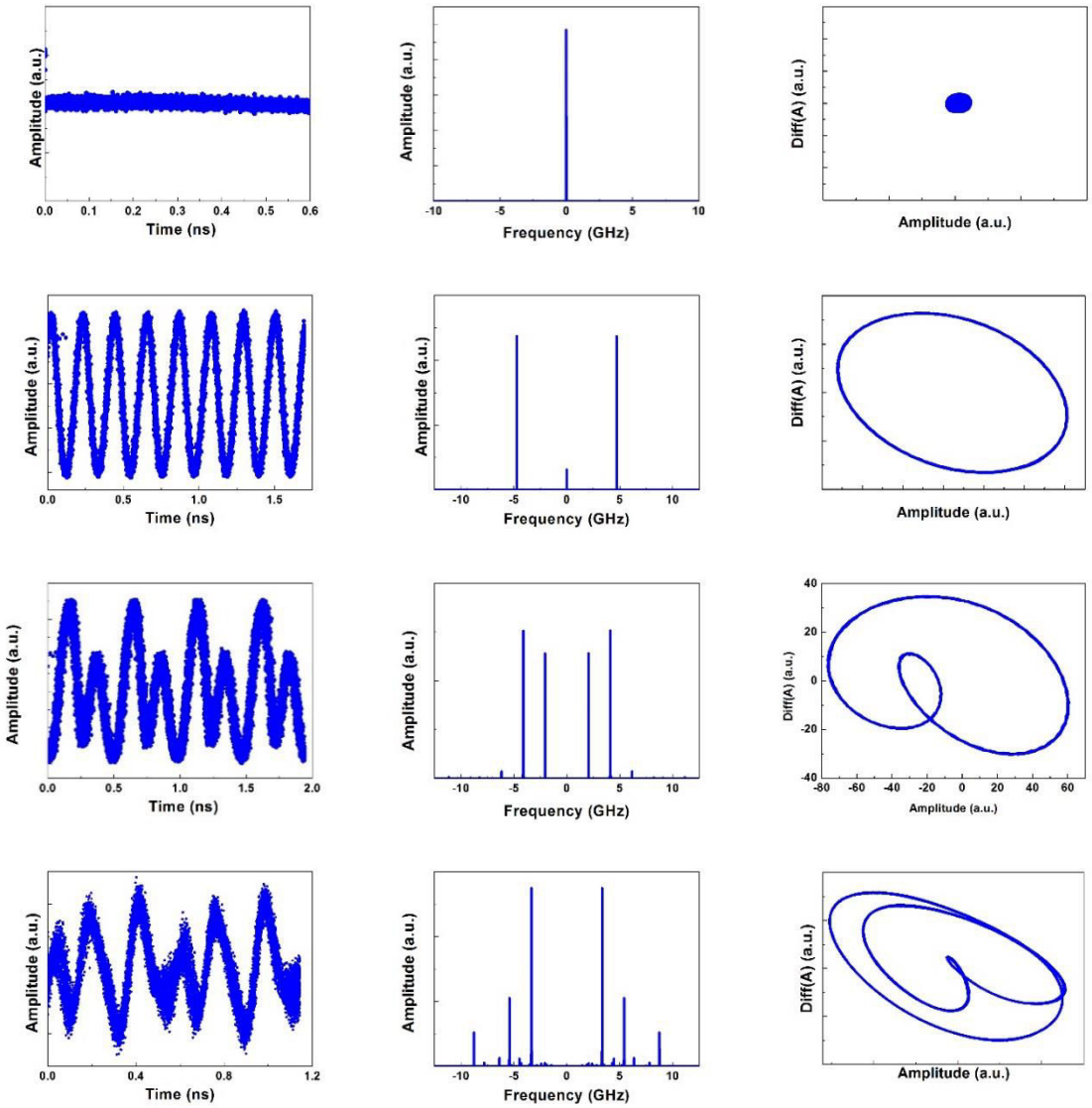

Fig. 5.11. Time series (α-factort), electronic spectrum (middle), and phase portrait (right) for different dynamics subject to optical injection: stable locking (row 1), period 1 (row 2), period 2 (row 3), period 3 (row 4).

Figure 5.10 shows the measured stability map of the optically injected Qdot laser. The generated nonlinear dynamics is a function of the detuning frequency as well as the injection ratio. In the diagram, we identified the stable-locked, periodic, chaotic, and four-wave mixing (FWM) regions. Some of the dynamics are recorded in Fig. 5.11:

a) Stable-locked region (row 1). In this region, both the frequency and the phase of the slave laser are synchronized to the master laser. The intensity of laser output is a constant. Thus, the electric spectrum only has a zero frequency component. The stable locking regime creates a point in the phase portrait. In the following sections, we will study the modulation dynamics of injection-locked lasers operated in this regime.

b) Period 1 oscillations (row 2). The laser output intensity oscillates with one period, i.e., one maximum and one minimum. The slave laser frequency is shifted according to the

new average carrier density caused by injection. Superposition of the shifted laser field and the injected field, which have different frequencies, results in beating, that is, the signal oscillates with the optical frequency but is modulated on a scale determined by the detuning between the component fields [Wieczorek05]. The oscillation frequency also strongly depends on the injection strength and the frequency detuning [Hwang04]. The electric spectrum exhibits one non-zero peak, and the phase portrait creates a limit cycle.

c) Period 2 dynamics (row 3). The laser intensity has two maxima and two minima. Another frequency component is born in the electric spectrum, which is half of the basic frequency. Two limit cycles are created in the phase portrait.

d) Period 3 dynamics (row 4). The laser output has threes maxima and three minima. The electric spectrum has three non-zero components, and there are three limit cycles in the phase portrait.

Unluckily, the nonlinear dynamics of chaos and FWM are not recorded in this work. For the latter, the slave laser is not locked to the master laser, and thus out of the locking regime. In the next section, it will be seen that a dual-mode injection-locking technique can be a promising solution to generate efficient FWM dynamics.

5.1.3. Four-wave mixing using dual-mode injection

Optical wavelength conversion plays an important role in wavelength division multiplexed (WDM) systems. The nondegenerate four-wave mixing (NDFWM) in semiconductor gain media is a desirable technique for wavelength conversion due to its ultrafast nature and transparency to the modulation format of the signals [Tatham93], [Geraghty97]. In addition, since the converted signal is the phase-conjugate replica of the input signal, it also provides the possibility for fiber dispersion compensation in long distance transmission systems [Tatham94], [Marcenac97]. NDFWM in semiconductor optical amplifiers (SOAs) and DFB lasers have been extensively studied and much effort has been devoted to enhance the conversion efficiency (the ratio of the output-converted signal power to the input-signal power) and the optical signal-to-noise ratio [Kim07], [D'Ottavi96], [Simoyama98], [Kim12], [Su05]. Generally, the SOA has a larger linear gain, which provides high conversion efficiency, whereas it also generates additional amplified spontaneous emission noise. In this way, there is an optimum linear gain for the maximum conversion efficiency to noise ratio [Kim07], while a compromise on the pump-wave power is also required to obtain a better performance [D'Ottavi96]. In DFB lasers, the lasing mode itself is used as a pump wave, and the NDFWM is enhanced by the cavity

resonance. A higher conversion efficiency associated with a lower noise level can be achieved from a laser with a long cavity and a small grating coupling coefficient. A high lasing power is also favorable for obtaining higher conversion efficiency [Simoyama98], [Kim12], [Su05]. As for the nonlinear gain medium, in contrast to the Qwell material, Qdots offer various advantages such as a wider gain spectrum [Li00], ultrafast carrier dynamics [Nielsen10], higher nonlinear gain effect and thus a larger three-order nonlinear susceptibility [Akiyama00], [Lu06]. In addition, due to the reduced α-factor, Qdots have the possibility of eliminating destructive interference among the nonlinear processes and also offer an enhanced efficiency in the wavelength up-conversion [Akiyama02], [Flayyih13]. In order to improve the dynamical performance of semiconductor lasers, the optical injection-locking technique has been widely used to reduce the spectral linewidth, frequency chirp as well as to suppress relative intensity noise and nonlinear distortion [Yabre96], [Simpson95], [Meng99]. In particular, it has been reported that the α-factor value can be reduced under strong optical injection as well [Lingnau12], [Lin13], which is quite beneficial for further suppressing the destructive interference. Employing a dual-mode injection-locking scheme in this work, we report the efficient NDFWM generation in a Qdot Fabry-Perot laser, in which one tone of the injected CW beams is used as the pump wave, while the other one plays the role of the probe wave. Each of these locks a longitudinal mode of the FP laser within the stable-locking range.

Figure 5.12 shows the experimental setup, where two tunable CW lasers ($TL_{1,2}$: Yenista Optics, T100S) are injected into the Qdot laser via an optical circulator. The Qdot laser output is collected from port 3 of the circulator, which is followed by a 90/10 fiber splitter. The 10% port is connected with a power meter to monitor the output power while the 90% port is used to analyze the optical spectrum with an OSA. The polarization of the tunable lasers is controlled to align with the slave laser through the polarization controller. The temperature of the Qdot laser is kept constant at 293 K throughout the experiment using a thermo-electric cooler.

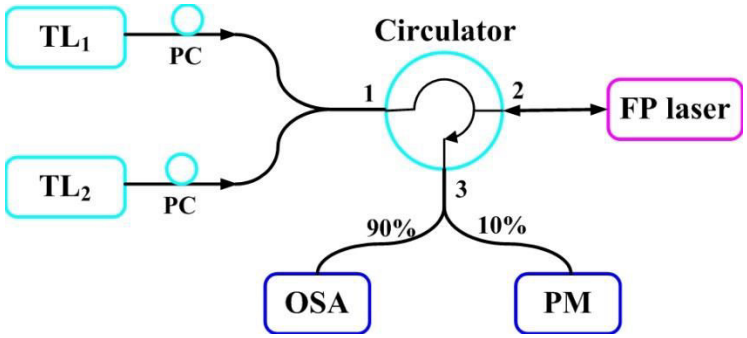

Fig. 5.12. Schematic of the experimental setup. $TL_{1,2}$: Tunable laser ; PC : Polarization controller ; OSA : Optical spectrum analyzer ; and PM : Power meter.

The Qdot laser structure and basic static properties are already described in section 5.1.1. In the study of the NDFWM performance, the Qdot laser is biased at 110 mA with a fiber-coupled power of 2.0 mW. Each of the two tunable lasers is set at the maximum achievable power around 1.4 mW (1.43 mW for $TL_1$and 1.38 mW TL_2), which are measured at port 2 of the circulator. Assuming a power coupling efficiency of 60% [Naderi09], the injection ratio for each of the master lasers to the slave laser is calculated to be 0.42, meaning that the strength of the optical injection remains at a relatively low level. The wavelength of the master laser TL_1 is fixed around 1628.5 nm and acts as the pump wave, while TL_2 is tuned to a longer wavelength and acts as the probe wave.

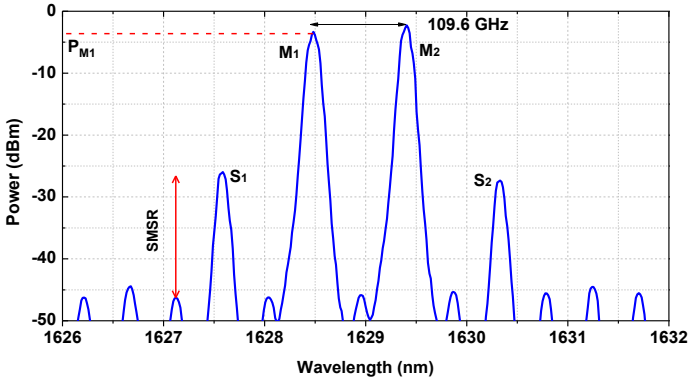

Fig. 5.13. Optical spectrum with FWM. $M_{1,2}$ are the stably locked modes by the tunable master lasers. The frequency difference between the locked modes is 109.6 GHz. $S_{1,2}$ are the newly converted signals.

Figure 5.13 shows an optical spectrum of the dual-mode injection-locked Qdot laser. Each injected wavelength selects a longitudinal mode within the free-running FP multimodes, while all other modes are well suppressed. M_1 and M_2 are the stable locked modes by TL_1 and TL_2, respectively. Due to the third-order nonlinear susceptibility $\chi^{(3)}$, new waves S_1 and S_2 are generated as the converted conjugate signal of M_2 and M_1. Assuming the frequency difference between M_1 and M_2 is $\Delta f = f_{M1} - f_{M2}$, the FWM process is governed by the carrier density pulsation (CDP) mechanism for Δf within a few GHz [Agrawal88], which creates temporal carrier modulation. For larger frequency detunings up to THz range, spectral hole burning (SHB) and carrier heating (CH) dominates. In the SHB mechanism, the injected signals create a hole and change the intraband carrier distribution, producing a modulation of the occupation probability of carriers within the energy band [Kikuchi92]. In the case of Qdot lasers, the slow interdot processes on the order of a few to tens of picoseconds allow for the creation of deeper spectral holes and thus for more efficient FWM [Nielsen10]. The CH mechanism is caused by the stimulated emission from the ground state, which removes the lowest energy carriers, while free carriers absorb photons leading to higher energy [Nielsen10], [Kikuchi92]. The frequencies

of the two newly generated signals respectively are $f_{S1} = f_{M1} + \Delta f$ and $f_{S2} = f_{M2} - \Delta f$. Then the corresponding susceptibilities are [Akiyama02]:

$$\chi^{(3)}(f_{S_1}) = \sum_B \chi_B^{(3)}(\Delta f = 0)\left(1 - i2\pi\Delta f \tau_B\right)^{-1}$$
$$\chi^{(3)}(f_{S_2}) = \sum_B \chi_B^{(3)}(\Delta f = 0)\left(1 + i2\pi\Delta f \tau_B\right)^{-1} \quad (5.3)$$

where B denotes the contributions from SHB, CH and CDP, and τ_B is the corresponding time constant. The electric field of the FWM signal is proportional to the induced polarization $D(f)$ [Park04]:

$$D(f_{S_1}) = \varepsilon_0 \chi^{(3)}(f_{S_1}) E^2(f_{M_1}) E^*(f_{M_2})$$
$$D(f_{S_2}) = \varepsilon_0 \chi^{(3)}(f_{S_2}) E^2(f_{M_2}) E^*(f_{M_1}) \quad (5.4)$$

The normalized conversion efficiency (NCE) is then found to be [Kolchanov96]:

$$\eta_{S1} = \frac{P_{S1}}{P_{M1}^2 P_{M2}}; \quad \eta_{S2} = \frac{P_{S2}}{P_{M2}^2 P_{M1}} \quad (5.5)$$

where P_X (X=$M_{1,2}$,$S_{1,2}$) is the corresponding wave output power, which can be extracted from the optical spectrum.

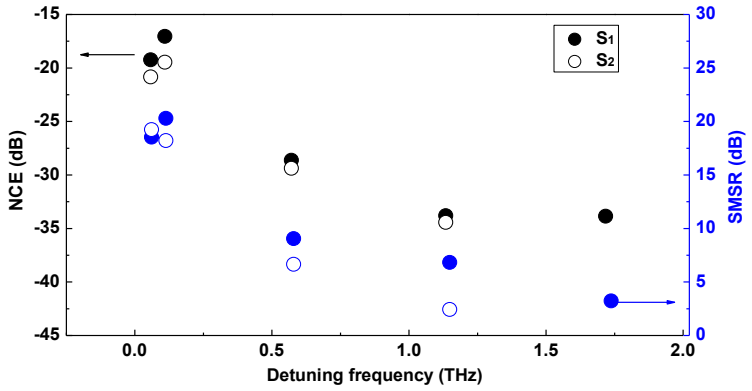

Fig. 5.14. The normalized conversion efficiency (NCE) η_{S1}, η_{S2} (black) and SMSR (blue) as a function of the detuning frequency. S_1 is denoted by the full circle, and S_2 is by the open circle. Note that signal S_2 at 1.72 THz is invisible because it is submerged in the residual FP modes.

Following the above definitions, the normalized conversion efficiency (black) of the FWM in the Qdot laser is presented in Fig. 5.14. The interval of the detuning frequency Δf is mainly determined by the mode spacing, which is 0.46 nm in the Qdot laser under study. The detuning frequency is then operated from the minimum 57.6 GHz up to 1.72 THz. For even larger detunings up to 5.7 THz, the FWM signal is submerged in the residual FP modes or noise and disappears. Due to the asymmetric gain spectrum as shown in Fig. 5.6 and carrier populations in higher energy non-lasing states, the Qdot laser has a non-zero α-factor parameter [Grillot08].

The measured below-threshold α-factor of the Qdot laser device under study is found to be 2.6 at 1625 nm as shown in Fig. 5.7. Representing the susceptibilities $\chi_{CDP}^{(3)}$, $\chi_{SHB}^{(3)}$ and $\chi_{CH}^{(3)}$ as complex phasors [Akiyama02], it is found that this finite α-factor value causes the phasors to be oriented in different directions at zero detuning. When the frequency difference is tuned, on one hand $\chi_{CDP}^{(3)}$ begins to rotate and its direction becomes closer to that of $\chi_{SHB}^{(3)}$ and $\chi_{CH}^{(3)}$. On the other hand, the magnitude of each susceptibility becomes smaller as expressed in equation (5.3). Then η increases and reaches the peak value when the norm of the three additive susceptibilities is the largest. In the experiment under study, this situation is achieved at the detuning frequency Δf =109.6 GHz with a normalized conversion efficiency of -17 dB (η_{S1}). Beyond that, the direction of $\chi_{CDP}^{(3)}$ deviates away and the conversion efficiency decreases with the detuning frequency. When Δf is tuned above the characteristic rates (1 THz) of the SHB and CH processes, $\chi_{SHB}^{(3)}$ and $\chi_{CH}^{(3)}$ also begin to rotate making η nearly constant at about -34 dB from Δf =1.13 THz to 1.72 THz in the experiment. It is noted that at a detuning frequency around 1.1 THz, the NCE of the studied Qdot laser is more than 15 dB larger than that of a Qwell SOA reported in [Koltchanov96]. From Eqs. (5.3)-(5.5), it can be derived that η_{S1}= η_{S2}. However, the experimental results depicted in Fig. 5.14 show that η_{S2} is slightly smaller than η_{S1}, which is attributed to the assertion that the SHB effect contributes less to the wavelength up-conversion [D'Ottavi94]. In addition, Fig. 5.14 also presents the variation of side mode suppression ratio (SMSR, blue) with respect to each converted signal S_1 and S_2 since the residual modes act as optical noise to the converted signals. The SMSR decreases with the detuning frequency and the highest ratio is 20.3 dB at Δf =109.6 GHz. The SMSR of S_2 is smaller in comparison with S_1, which can be partly attributed to the lower power of S_2. On the other hand, the amplitude of the residual FP modes at the longer wavelength side is higher when the laser is injection locked. This is because the gain at the right side of the pump wave M_1 is larger than that at the left side. Since the gain spectrum is almost clamped above threshold [Gioannini06], this trend can be partially reflected by the sub-threshold gain shown in Fig. 5.6.

Lastly, it is important to note that in the experiment both the pump wave and the probe signal are operated in the stable-locked regime. However, for an arbitrary probe wavelength the temperature of the FP laser can be controlled to tune one of the FP modes within the stable-locking range of the probe signal. In addition, because the converted signal is enhanced by the cavity resonance, it is important to make the converted signal coincide with one of the resonance frequency peaks in the laser cavity [Li93]. This can be achieved by tuning the pump wave since

it typically has a large power and thus a wide locking range. Furthermore, the normalized conversion efficiency can be enhanced by a larger bias current to the FP laser, since the output power is mainly determined by the slave laser. The SMSR can be improved by a higher injection ratio [Li93], which can be achieved by coupling an amplifier into the configuration to amplify the pump wave power. Unfortunately, the impact of the injection strength on the FWM was not studied in this work due to the power limitation of the devices.

5.2. Optical Injection-Hakki-Paoli method for α-factor extraction

In the previous section, it has been shown that the Hakki-Paoli method is only applicable to the below-threshold condition for the measurement of the α-factor. One of the major drawbacks of this method is the thermal effect. Lelarge *et al.* introduced a thermal correction method assuming that the thermal effect below threshold is the same as that above threshold. Besides, it is also assumed that carriers are all clamped above threshold [Lelarge05]. However, this is not true for nanostructure semiconductor lasers, since carriers in off-resonant states remains increase with pump current. Consequently, the measurement usually requires the pulsed current operation. Shorter pulse (< 1μs) results in less thermal effect, however it also leads to rather weak optical signal. Therefore, there is a tradeoff between the reduction of thermal effect and the tracked optical power. Once the laser is operated above threshold, the gain is clamped hindering the application of the Hakki-Paoli method. Modulation techniques including FM/AM method [Harder83] (see Chapter 3) and fiber transfer function method [Devaux93] are commonly used for the above-threshold α-factor measurement. However, both techniques require high-speed modulation operation, and thus increase the complexity of the experimental setup. In this section, we propose a novel approach to measure the α-factor of semiconductors under DC condition, with the help of optical injection. Here we name this approach as *Optical Injection-Hakki-Paoli* method. Particularly, this method is applicable for both below and above threshold operations. Moreover, it is insensitive to the thermal effects. In the following, we present the preliminary investigations using this novel approach.

From the study of the optical injection effect on the gain spectrum (see Fig. 4.15), it was shown that the gain of the laser can be tuned either by the injection strength or by the frequency detuning. This effect is similar to that of tuning the pump current in the Hakki-Paoli method. When the laser is operated within the stably-locked area, Fig. 5.9 shows that except the injected mode, all other side modes are well suppressed, and the residual power is supported by the ASE. Therefore, a novel method related to the Hakki-Paoli technique can be developed for the gain extraction of suppressed side modes both below and above the threshold. In accordance with

the α-factor definition using Hakki-Paoli method in Eq. (5.1), we replace the pump current I in the original definition either by the injection ratio R_{Inj} or the frequency detuning F_{Inj}. In such way, we can recast the definition of the α-factor through the two following two relationships:

By tuning the injection ratio R_{Inj}:

$$\alpha_H = -\frac{2\pi}{L\Delta\lambda}\frac{d\lambda / dR_{Inj}}{dg_{net} / dR_{Inj}} \tag{5.6}$$

Or by varying the frequency detuning F_{Inj}:

$$\alpha_H = -\frac{2\pi}{L\Delta\lambda}\frac{d\lambda / dF_{Inj}}{dg_{net} / dF_{Inj}} \tag{5.7}$$

Depending on the available master laser sources, it is possible to utilize either of the above two definitions. If the master laser has a poor tunability but the power can be varied in a large scale, the method of tuning the injection power is applicable (Eq. 5.6). If the master laser has a good tunability, the method of tuning the frequency can be employed instead (Eq. 5.7). In this work, we use the latter approach since the master laser source is a tunable external cavity laser.

The laser device under study is based on the InAs/InP Qdash nanostructure, consisting of five stacked layers of self-assembled InAs dashes. The laser structure is grown by the CBE onto an InP substrate. The waveguide is 1 mm long, 2 μm width and both facets of the laser are as cleaved. The laser is provided by the National Research Council (NRC), Canada. Figure 5.15 illustrates the experimental setup for the measurement of the α-factor with the help of external optical injection. The schematic description is similar to that of Fig. 5.8. The laser device is operated at room temperature (293 K). The power of the tunable master laser is fixed at 9.3 mW. We tune the wavelength of the master laser, and record the output optical spectrum of the injected laser system using the OSA, which has a resolution of 10 pm.

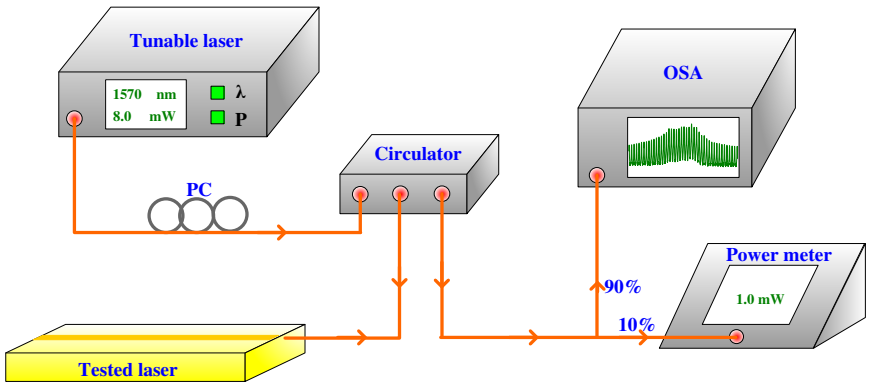

Fig. 5.15. Experimental setup for the measurement of the α-factor using the Optical Injection-Hakki-Paoli method. The tunable external cavity laser is used to inject the tested laser through an optical circulator. The output light is collected by a high resolution (10 pm) OSA for post-processing. A polarization controller (PC) is adjusted to align the polarization of the tunable laser with that of the tested laser.

Figure 5.16 shows the L-I curve of the free-running Qdash laser. It has a lasing threshold of 46 mA at room temperature. Figure 5.17 presents the optical spectra of the free-running laser biased at 80 mA. The lasing modes peak around 1550 nm. We aim to study the α-factor of the laser for wavelengths in the range from 1545 to 1555 nm. The injection can be operated at any mode outside of the target span. In this work, the injected mode is chosen around 1570 nm, which is 20 nm away from the gain peak. The optical injection is conducted in the stable locking regime. As shown in Fig. 5.18(a), the frequency detuning is operated from the positive frequency detuning (shorter wavelength) to the negative frequency detuning (longer wavelength) sides. Figure 5.18(b) illustrates the variation of the side modes around 1550 nm under optical injection. When the master laser is tuned from shorter to longer wavelengths, the side modes are red shifted and the amplitude is reduced, which indicates the reduction of the optical gain.

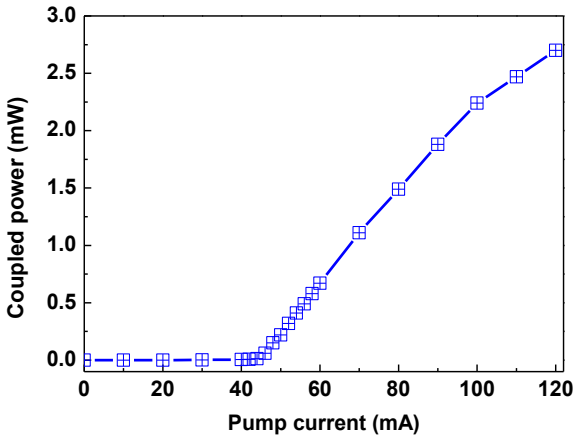

Fig.5.16. L-I curve of the Qdash laser operated at room temperature (293 K). The lasing threshold is 46 mA.

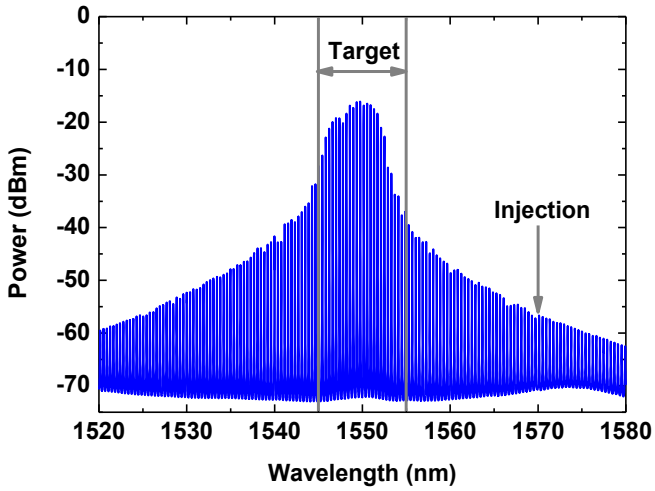

Fig. 5.17. Optical spectra of the free-running Qdash laser biased at 80 mA. The target span of α-factor measurement is between1545 and 1555 nm. The injected mode is fixed around 1570 nm.

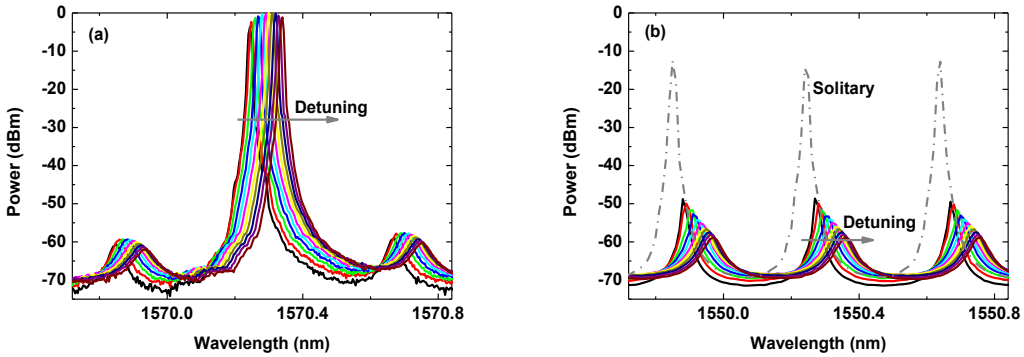

Fig. 5.18. (a) Optical spectra of injected laser mode around 1570 nm, and (b) Side modes around 1550 nm at various frequency detunings. The detuning step is 10 pm, and the injected power is fixed at 9.3 mW.

Based on the optical spectra of side modes, we can apply the Hakki-Paoli method to extract the net modal gain of the Qdash laser as presented in Fig. 5.19. It is shown that the gain decreases from positive to negative frequency detunings, which are always lower than that of the free-running laser. Figure 5.20 shows an illustration of the wavelength variation as a function of the net modal gain, which is tuned by the frequency detuning. When the injected laser is tuned to the positive frequency side, the wavelength is blue-shifted while the gain is increased. Through linear fitting, we obtain the value $d\lambda / dg_{net}$. We point out that this value does exclude the impact of the thermal effect, since the operation is conducted at a fixed bias current. In addition, the knowledge of the exact value of the frequency detuning is not needed. Last but not least, this approach is applicable for lasers operated both below and above threshold operations.

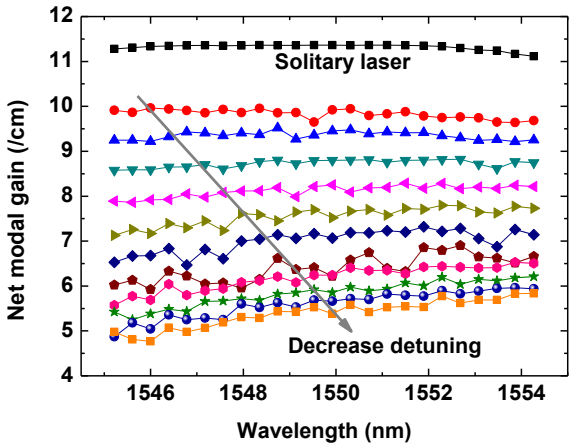

Fig. 5.19. Net modal gain spectra under optical injection for various frequency detunings from 1570.21 nm to 1570.35 nm. The detuning step is 10 pm, and the injected power is fixed at 9.3 mW.

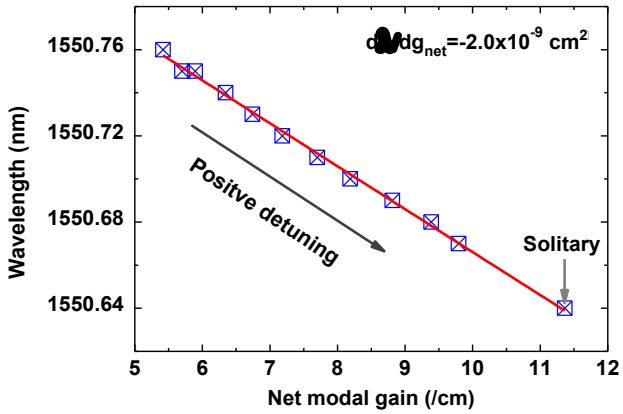

Fig. 5.20. Wavelength variation versus the net modal gain, which is tuned by the frequency detuning.

Figure 5.21 shows the measured α-factor of the Qdash laser for various bias currents, both above and below thresholds. Generally, the α-factor increases with the bias current because more carriers are populated in the off-resonant states. In addition, the α-factor increases from shorter to longer wavelengths.

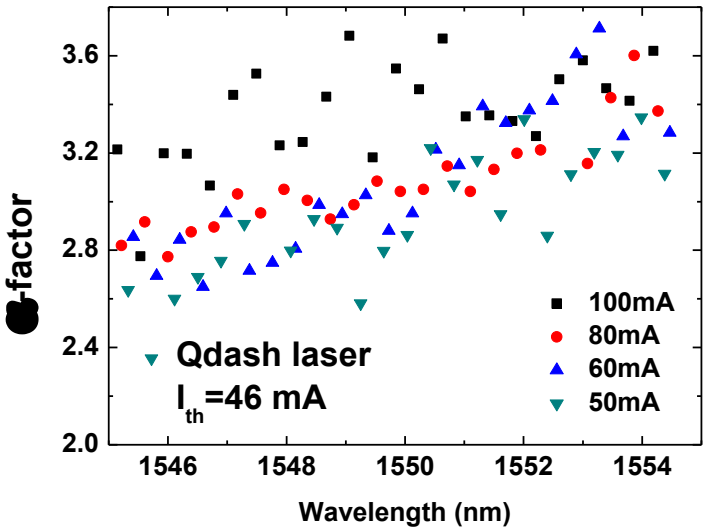

Fig. 5.21. Measured α-factor of the Qdash laser for different bias currents using the Optical Injection-Hakki-Paoli method. A gap occurs for α-factor values between above and below thresholds. The lasing threshold is 46 mA.

In addition, we investigated another nanostructure Qdot laser as well as a commercial Qwell laser using this *Optical Injection-Hakki-Paoli* method. The Qdot laser is also based on the InAs/InP system, consisting of 5 stack layers (fabricated at NRC, Canada). The laser structure is grown by CBE, and the waveguide has a length of 1 mm, and a width of 3 μm. The Qdot laser has a threshold of 43 mA, and the Qwell laser has one of 23 mA at room temperature. Figure 5.22 shows the measured α-factor of the Qdot laser, which is generally smaller than that

of the Qdash laser (Fig. 5.21). Figure 5.23 shows that this novel developed method is well applicable to the Qwell laser as well.

It is noted that all the α-factors measured in the three kinds of laser devices are operated above threshold. During the the writing of this thesis, the measurement below threshold is still ongoing.

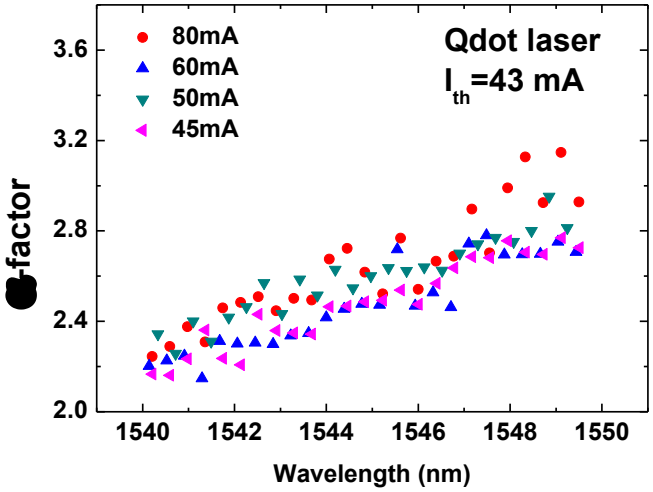

Fig. 5.22. Measured α-factor of a Qdot laser for different bias currents with the Optical Injection-Hakki-Paoli method. A gap occurs for α-factor values between above and below thresholds. The lasing threshold is 43 mA.

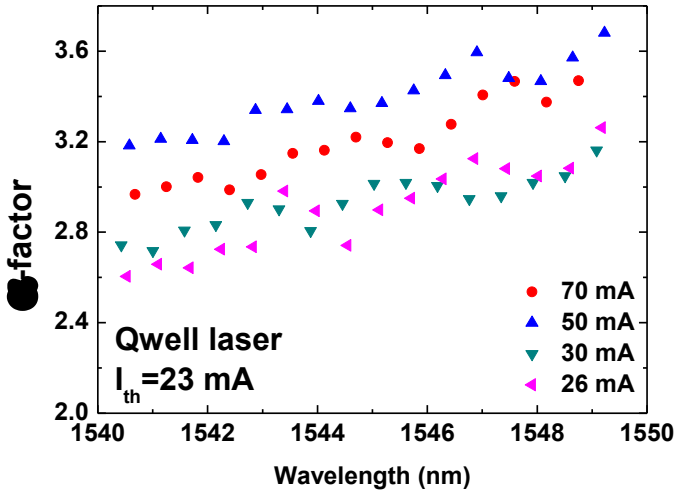

Fig. 5.23. Measured α-factor of a Qwell laser for different bias currents. No gap occurs for α-factor values around the lasing threshold. The lasing threshold is 23 mA.

On the other hand, we theoretically study the α-factor variations for pump currents both below and above threshold dusing its efinition in Eq. (3.48). The calculated α-factor as a function of the modulation frequency ranging from 1 Hz up to 10^{11} Hz is presented in Fig. 5.24 (a). As already discussed in section 3.2 (see Fig. 3.9), the α-factor remains constant at low

modulation frequencies less than 10^7 Hz, which is consistent with the value under DC condition ($\alpha_{H,QD}^{DC}$). The α-factor obtained by the FM/AM technique ($\alpha_{H,QD}^{FM/AM}$) at high modulation frequencies increases continuously from below to above threshold, as was shown in Fig. 3.10. Since the developed Optical Injection-Hakki-Paoli method provides the DC α-factor value $\alpha_{H,QD}^{DC}$, we illustrate the simulated value in Fig. 5.24(b) as a function of the normalized pump current. The simulation demonstrates for the first time the discontinuity of the DC α-factor value $\alpha_{H,QD}^{DC}$ at threshold. It is noted that this plot is different to the one in Fig. 3.10 showing the high modulation frequency α-factor $\alpha_{H,QD}^{FM/AM}$ given by the FM/AM technique.

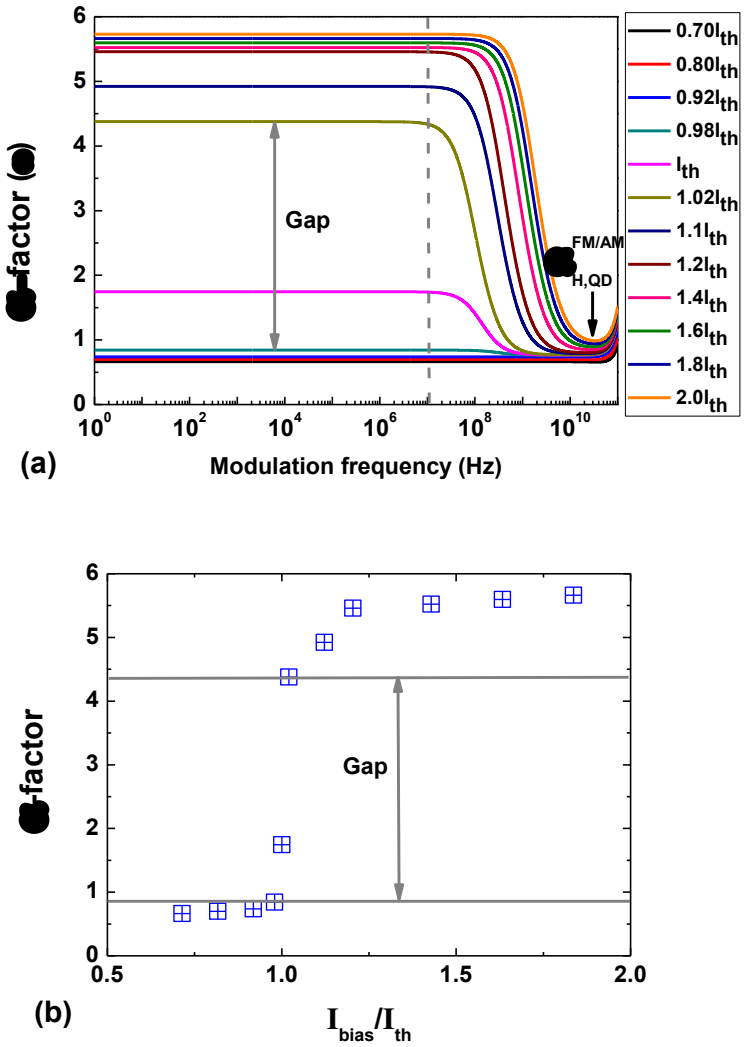

Fig. 5.24. (a) Simulated α-factor as a function of the modulation frequency for different bias currents using Eq. (3.48). The constant value at low modulation frequencies (<10^7 Hz) is consistent with the DC value $\alpha_{H,QD}^{DC}$. In contrast, the FM/AM value $\alpha_{H,QD}^{FM/AM}$ is given at high modulation frequency. (b) The simulated DC α-factor $\alpha_{H,QD}^{DC}$ as a function of the normalized pump current. The gap behavior at threshold is qualitatively in agreement with the experimental observations in Figs. 5.21 and 5.22.

This special feature of nanostructure lasers can be attributed to the different carrier responses below and above threshold as shown in Fig. 5.25. Below threshold ($I=0.8\times I_{th}$), the carrier populations in the GS and in the ES vary in a high level around 25 dB (at 0.01 GHz), while carriers in the RS varies at a lower level. This results in a small DC α-factor according to the analytical expression (3.48). Once above threshold ($I=1.2\times I_{th}$), the carrier variation in the GS is strongly suppressed to a low level less than -5 dB, which is 30 dB smaller than the below threshold case. This is due to the gain clamping of the laser emission above threshold. However, carrier variations in the ES and in the RS remain at a high level, which leads to a higher value of the DC α-factor.

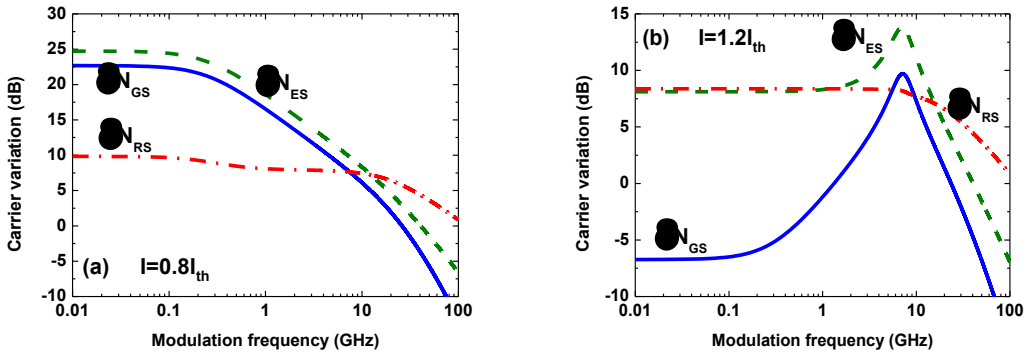

Fig. 5.25. Carrier variations (a) below threshold at $I_{bias}=0.8\times I_{th}$, and (b) above threshold at $I_{bias}=1.2\times I_{th}$. The carrier variations are normalized to the value δN_{GS} of 0.01 GHz at lasing threshold I_{th}.

Therefore, the discontinuity behavior of the DC α-factor at the lasing threshold in nanostructure lasers is attributed to the clamping of the resonant GS carrier populations as well as to the unclamped carrier populations in the off-resonant ES and RS. Since there is no discrete off-resonant state in Qwell lasers, this kind of phenomenon does not occur in the measurement shown in Fig. 5.23. The α-factor gap in nanostructure lasers retains the effort of reduing its value towards zero. Alternative approaches such as p-doping, tunnel injection as well as lasing operation on the ES are possible scenarios to reduce the α-factor [Mollet14], [Bhowmick14].

Lastly, it is noted that the above discussions are based on our preliminary measurements. Further investigations are currently ongoing in order to further verify these first results.

5.3. Dynamical characterization under direct modulation

In the previous two sections, we studied the nanostructure semiconductor laser properties under DC condition. This section deals with the laser characteristics operating under direct modulation. The laser under study is the Qdash laser described in section 5.2. In section 5.3.1, we discuss the modulated free-running laser in the frequency domain, including the AM response and the CPR properties. In section 5.3.2, the modulated injection-locked laser is

investigated in the time domain. In section 5.3.3, we analyze the large-signal modulation properties of both the free-running laser and the injected laser.

5.3.1. Modulated free-running laser

For the direct modulation operation of the semiconductor laser, a high-speed microwave probe is required instead of the DC probe to modulate the laser. In this work, we use high-speed a ground-signal-ground (GSG) pico-probe for the measurement as illustrated in Fig. 5.26.

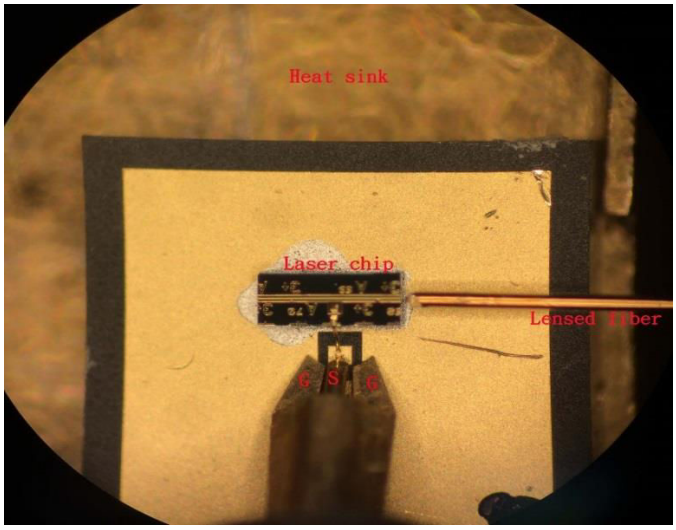

Fig. 5.26. Image of the laser mounting for modulation operation. A high-speed ground-signal-ground (GSG) pico-probe is used for the modulation.

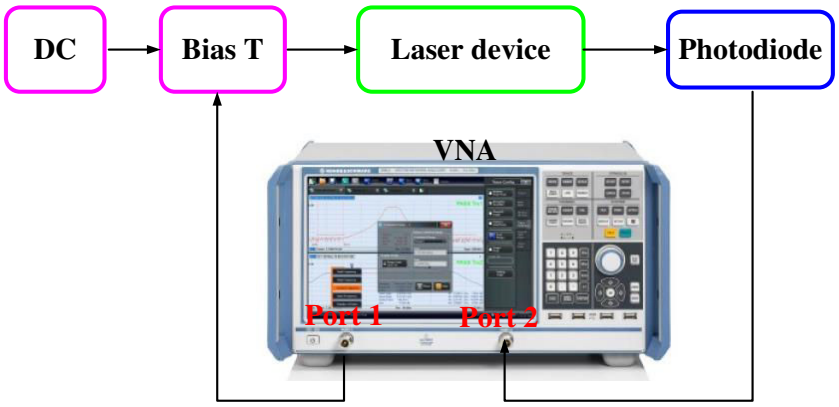

Fig. 5.27. Experimental setup used for the measurement of the AM response.

A) Amplitude modulation response

Figure 5.27 presents the schematic of the experimental setup for the characterization of the laser's small-signal AM response in the frequency domain. The measurements require the use of the vector network analyzer (VNA), which combines a microwave generator and an ESA in one. From Port 1, the VNA generates an electrical sine wave signal with swept frequency, which is imposed to the DC current via a bias-T and is sent to the laser diode. Collection of the reflected signal from the laser chip in Port 1 (S_{11}), the frequency-dependent impedance of the

laser diode can be obtained [Kuntz06]. The laser output is converted to an electrical signal through a high-speed photodiode, and then the signal is collected in Port 2. The combined modulation response of the laser diode (H_{21}) and the parasitic circuits (P_{21}) is given by the transmission function S_{21}.

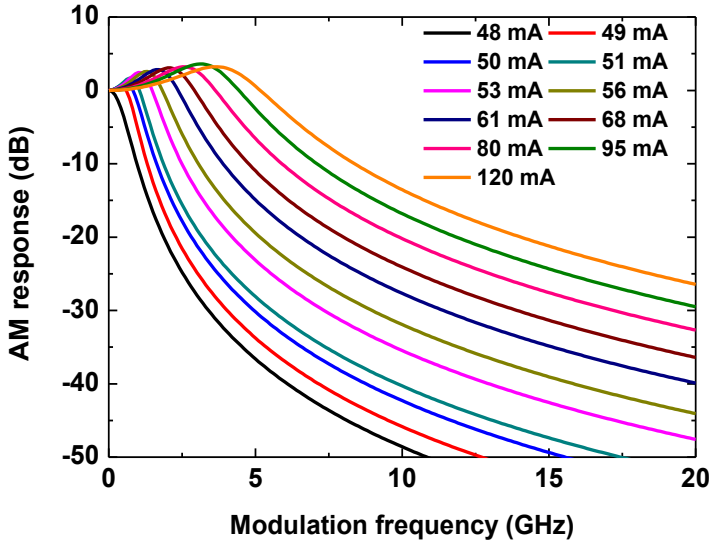

Fig. 5.28. Reproduced intrinsic modulation response H_{21} after Eq. (5.10).

The sole intrinsic response H_{21} of the laser diode can be extracted through a subtraction method eliminating the parasitic effect [Morton92]. The approach assumes that the parasitic components are independent of the pump current. Thus, for two different bias currents I_1 and I_2 we have relation:

$$\begin{aligned} S_{21}(I_1) &= H_{21}(I_1) + P_{21} \\ S_{21}(I_2) &= H_{21}(I_2) + P_{21} \end{aligned} \tag{5.8}$$

Subtracting $S_{21}(I_2)$ by $S_{21}(I_1)$, we obtain

$$D_{21} = S_{21}(I_2) - S_{21}(I_1) = H_{21}(I_2) - H_{21}(I_1) \tag{5.9}$$

Thus, the parasitic effects are eliminated using this formula. The intrinsic modulation transfer function $H_{21}(f)$ of the semiconductor laser [Coldren95] is given by

$$H_{21}(f) = 10\log\left(\frac{f_R^4}{\left(f^2 - f_R^2\right)^2 + \Gamma_D^2 f^2}\right) \tag{5.10}$$

Correspondingly, the subtraction response $D_{21}(f)$ is

$$D_{21}(f) = 10\log\left(\frac{f_{R2}^4}{\left(f^2 - f_{R2}^2\right)^2 + \Gamma_{D2}^2 f^2} \frac{\left(f^2 - f_{R1}^2\right)^2 + \Gamma_{D1}^2 f}{f_{R1}^4}\right) \tag{5.11}$$

where $f_{R2,1}$ and $\Gamma_{D2,1}$ are the resonance frequency and the damping factor of each bias current, respectively. By curve fitting the subtracted response using Eq. (5.11), the resonance frequency and the damping factor of the laser are extracted.

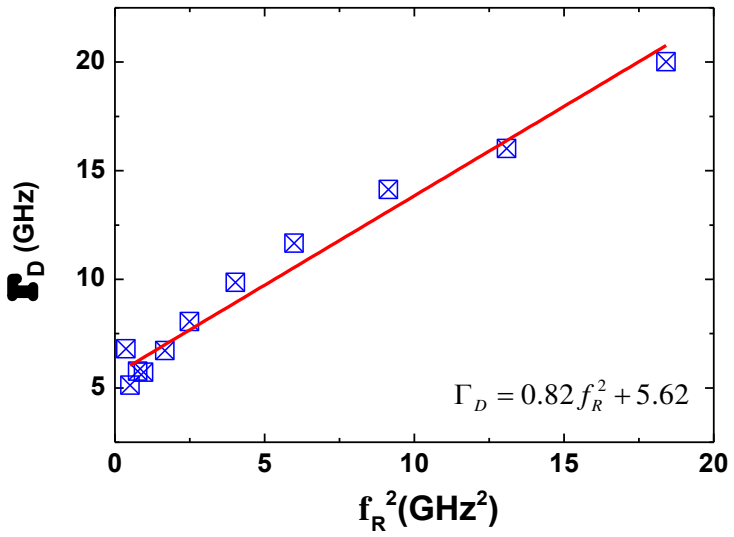

Fig. 5.29. Damping factor versus the square of the resonance frequency of the Qdash laser. Linear fitting gives the K-factor of 0.82 ns, and the offset of 5.62 GHz.

Table. 5.1. Damping factor offset of QD lasers reported in the literature

Reference	Laser type	K-factor	Γ_0
[Kuntz06]	InGaAs/GaAs (FP)	1.20 ns	17.0 GHz
[Zhukov13]	InAs/InGaAs (DFB)	1.02 ns	9.9 GHz
[Naderi11]	InAs/GaAs (FP)	1.51 ns	9.0 GHz
[Pochet10]	InAs/GaAs (FP)	1.44 ns	7.5 GHz
[Martinez08]	InAs/InP(311)B (FP)	0.63 ns	3.0 GHz
[Su04]	InAs/GaAs (DFB)	0.23 ns	1.7 GHz

Using the extracted dynamic parameters, Fig. 5.28 reproduces the intrinsic modulation response of the Qdash laser for different bias currents. The damping factor and the resonance frequency of the laser are linked by the K-factor as factor as $\Gamma = Kf_R^2 + \Gamma_0$ with Γ_0 the damping factor offset at threshold, and the reciprocal $1/\Gamma_0$ gives the effective carrier lifetime of the laser device [Coldren95]. In Qwell lasers, the typical value of Γ_0 is 1~2 GHz, which is determined by the spontaneous emission and the non-radiative transition processes [Coldren95]. For the measured Qdash laser, linear fitting in Fig. 5.29 shows that the K-factor is 0.82 ns, and Γ_0 is 5.62 GHz. It is demonstrated that the damping factor offset of the Qdash laser is larger than that of Qwell lasers. Similar phenomenon was also found in Qdot lasers as reported in literatures

[Su04], [Kuntz06], [Martinez08], [Pochet10], [Naderi11], [Zhukov13], and is summarized in Table 5.1.

This result is also consistent with our theoretical study described in section 3.1. Therefore, nanostructure semiconductor lasers generally have a smaller carrier lifetime in comparison with Qwell lasers. This is attributed to the slow intradot carrier relaxation process from the ES to the GS as well as to the carrier escape process [Lingnau12a], which increases the effective carrier lifetime of the GS.

B) Frequency chirp

The frequency chirping properties of semiconductor lasers can be characterized using optical discriminators. The purpose of the discriminator is to convert optical frequency variations into detectable intensity variations. Optical slope discriminator may be realized using interferometers [Provost11], optical fibers [Consoli11], and so on. In principle, any linear optical component with wavelength-dependent transmission characteristics may serve as a discriminator. In this section, we examine in detail the Mach-Zehnder (MZ) interferometer, which has two paths with different optical length. The field in the longer path is a delayed replica of the field in the short path. Assuming the time delay is τ, the electric field in each path is [Sorin92]:

$$\begin{aligned} E(t) &= \sqrt{P(t)}e^{j(\omega_0 t+\varphi(t))} \\ E(t-\tau) &= \sqrt{P(t-\tau)}e^{j(\omega_0(t-\tau)+\varphi(t-\tau))} \end{aligned} \tag{5.12}$$

where the optical power is P(t), the angular optical frequency is ω_0, and the optical phase is $\varphi(t)$. The output power of the interferometer is given by

$$\begin{aligned} P_{out}(t) &= \left|E(t)+E(t-\tau)\right|^2 \\ &= P(t)+P(t-\tau)+2\sqrt{P(t)P(t-\tau)}\cos(\Delta\varphi(t)+\omega_0\tau) \end{aligned} \tag{5.13}$$

where the third term is due to the interference of the two optical field. The phase difference is

$$\Delta\varphi(t) \equiv \varphi(t)-\varphi(t-\tau) \tag{5.14}$$

Assuming the phase difference is small $\Delta\varphi(t) << 1$, that is, the differential time delay τ is small enough in comparison with the signal coherent time, then we get the approximation

$$\Delta\varphi(t) \approx \frac{d\varphi(t)}{dt}\tau = 2\pi\Delta\nu(t)\tau \tag{5.15}$$

where $\Delta\nu(t)$ is the frequency shift of the electrical field. Figure 5.30 illustrates a sketch of the transfer function of a MZ interferometer. In the absence of any frequency chirp, $\Delta\varphi(t)$ is zero.

However, any changes in the frequency of the signal at the interferometer input will create a change of $\Delta\varphi(t)$, which in turn changes the output optical power.

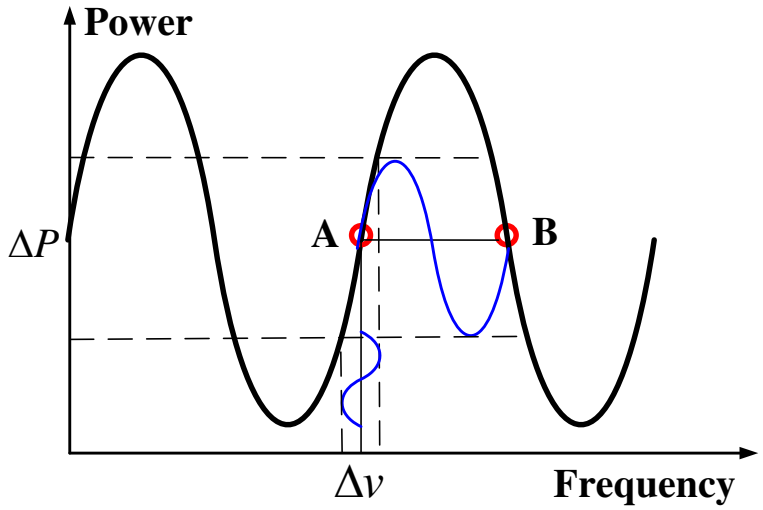

Fig. 5.30 Transfer function of MZ frequency discriminator

The free spectral range (FSR) of the interferometer is an important parameter for the MZ interferometer, which is defined as the change in optical frequency, to obtain a phase shift of 2π between the two combining fields, i. e., the frequency difference between the two peaks shown in Fig. 5.30. The FSR is given by the reciprocal of interferometer differential delay $1/\tau$. By adjusting the differential delay, the interferometer can be operated at the quadrature point A at the positive slope, which results in the relation $\omega_0\tau = -\pi/2 + 2k\pi$, and thus yields

$$P_{out}^{A}(t) = P(t) + P(t-\tau) + 2\sqrt{P(t)P(t-\tau)}\sin(2\pi\Delta v(t)\tau) \tag{5.16}$$

Then tune the time delay by half a wavelength to the quadrature point B at the negative slope, the relation becomes $\omega_0\tau = \pi/2 + 2k\pi$, and correspondingly we obtain

$$P_{out}^{B}(t) = P(t) + P(t-\tau) - 2\sqrt{P(t)P(t-\tau)}\sin(2\pi\Delta v(t)\tau) \tag{5.17}$$

Since the powers of the two paths are usually the same, the time-resolved intensity profile AM(t) is given by [Saunders94]

$$AM(t) = \frac{1}{2}\left(P_{out}^{A}(t) + P_{out}^{B}(t)\right) \tag{5.18}$$

While the time-resolved frequency chirp is calculated by

$$\Delta v(t) = \frac{FSR}{2\pi}\sin^{-1}\left[\frac{P_{out}^{A}(t) - P_{out}^{B}(t)}{P_{out}^{A}(t) + P_{out}^{B}(t)}\right] \tag{5.19}$$

It is noted that in the chirp measurement using a MZ interferometer, the differential delay between the two paths must be carefully selected considering several requirements [Hui09]: a) Coherence requirement. It needs the time delay to be small enough than the coherent time t_{coh}

such that $\tau << t_{coh}$. b) Sensitivity requirement, which prefers a longer delay. This is because the conversion is proportional to $\sin(2\pi\Delta v(t)\tau)$. c) Frequency bandwidth requirement, which desires a short delay. To maintain a linear conversion, the delay is set as $\tau < 1/(8*2\pi\Delta\upsilon_{\max})$. This allows the intensity to be made proportional to the frequency change. 4) Modulation frequency requirement, which requires short delay. The delay must be smaller than the inverse of the maximum modulation speed, that is, $\tau << 1/(f_m)_{\max}$.

The time domain analysis above is applicable for both small and large input signals. This can be manipulated using an oscilloscope in the experiment. For the small-modulation signal, an alternative efficient approach is to study the chirp in the frequency domain. This can be realized by a network analysis measurement. Assuming that the signal is modulated at a frequency ω_m, the optical power is given by

$$P(t) = P_0[1 + m\cos(\omega_m t)] \tag{5.20}$$

where m is the AM index. Similarly, the optical phase is also modulated and is written as

$$\varphi(t) = \beta\cos(\omega_m t + \psi) \tag{5.21}$$

where β is the FM index, and ψ is the phase difference between the FM and the AM modulations.

$$\begin{aligned} P_{out}^{A,B} &= 2P_0\left[1 + \frac{m}{2}\left(\cos(\omega_m t) + \cos(\omega_m(t-\tau))\right)\right] \\ &\pm 2P_0\sqrt{\left(1 + m\cos(\omega_m t)\right)\left(1 + m\cos(\omega_m(t-\tau))\right)}\sin(\Delta\varphi(t)) \end{aligned} \tag{5.22}$$

Only consider the first order terms and neglect the continuous and higher order terms of modulation frequency, we obtain:

$$P_{out}^{A,B}(t) \approx 2P_0\left[m\left(\cos(\omega_m t) + \cos(\omega_m(t-\tau))\right) \pm \Delta\varphi(t)\right] \tag{5.23}$$

where the relation $\sin(\Delta\varphi(t)) \approx \Delta\varphi(t)$ is used in the above equation. In the frequency domain, this formula is transferred to [Sorin92]:

$$P_{out}^{A,B}(f_m) \approx 2P_0\left[m(f_m)T_{AM}(f_m) \pm \Delta v(f_m)T_{FM}(f_m)\right] \tag{5.24}$$

where $\Delta v(f_m) = jf_m\beta(f_m)$. In the above formula, the AM transfer function of the MZ interferometer is:

$$T_{AM}(f_m) = \cos(\pi f_m\tau)e^{-j\pi f_m\tau} \tag{5.25}$$

and its FM transfer function is :

$$T_{FM}(f_m)=\frac{2\sin(\pi f_m\tau)}{f_m}e^{j(-\pi f_m\tau+\pi/2+\psi)} \tag{5.26}$$

Thus, we can obtain the AM modulation index in the frequency domain:

$$m(f_m)=\frac{P_{out}^{A}(f_m)+P_{out}^{B}(f_m)}{4P_0\cos(\pi f_m\tau)e^{-j\pi f_m\tau}} \tag{5.27}$$

and the FM modulation index:

$$\beta(f_m)=\frac{P_{out}^{A}(f_m)-P_{out}^{B}(f_m)}{j4P_0\left[2\sin(\pi f_m\tau)\right]e^{j(-\pi f_m\tau+\pi/2+\psi)}} \tag{5.28}$$

Then, the ratio of the FM-to-AM index is given by [Provost11]

$$\frac{2\beta(f_m)}{m(f_m)}=\frac{1}{\tan(\pi f_m/FSR)}\frac{P_{out}^{A}(f_m)-P_{out}^{B}(f_m)}{P_{out}^{A}(f_m)+P_{out}^{B}(f_m)}e^{-j(\pi/2+\psi)} \tag{5.29}$$

Correspondingly, we can obtain the chirp-to-power ratio (CPR) through the relationship

$$CPR(f_m)=\frac{f_m}{2(2P_0)}\frac{2\beta(f_m)}{m(f_m)} \tag{5.30}$$

It is noted that the total input power into both paths of the MZ interferometer is $2P_0$.

Based on the above analysis, Fig. 5.31 illustrates the experimental setup at III-V lab for the frequency chirping analysis in the frequency domain. A MZ interferometer is used as the frequency discriminator. $P_{out}^{A}(f_m)$ and $P_{out}^{B}(f_m)$ are recorded on a VNA. The recorded data is post-processed using Eqs. (5.29) and (5.30) to calculate the ratio of FM-to-AM index and the CPR.

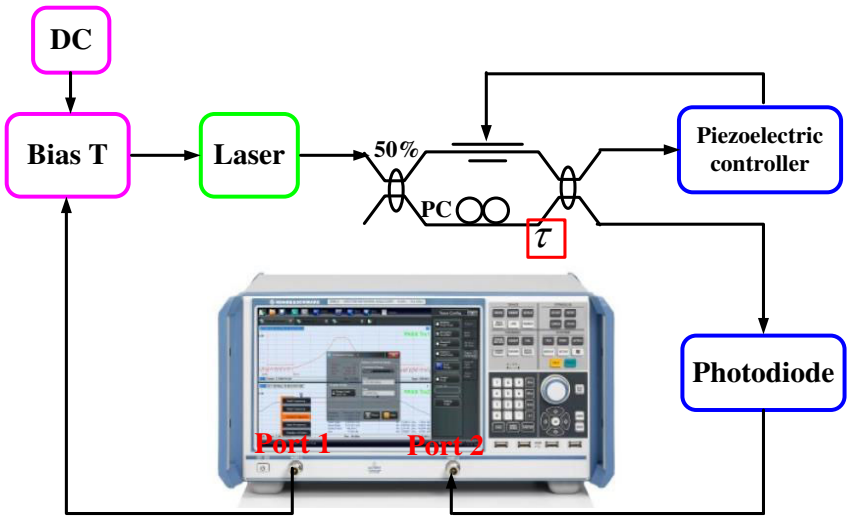

Fig. 5.31. FM-to-AM index ratio and CPR measurement in the frequency domain. A MZ interferometer is used as a frequency discriminator, and the VNA is used to measure the FM and AM responses.

Figure 5.32(a) shows the measured FM-to-AM index ratio. As the simulation in chapter 3, $2\beta/m$ has a large value at low modulation frequency, and decreases to a plateau with

increasing modulation speed. The plateau gives the α-factor value of the Qdash laser, which is 5.5 at 1549 nm. Figure 5.32(b) presents the CPR of the Qdash laser. The adiabatic chirp at low modulation frequencies is about 2.6 GHz/mW, while the CPR increases almost linearly with the modulation frequency beyond 5.0 GHz.

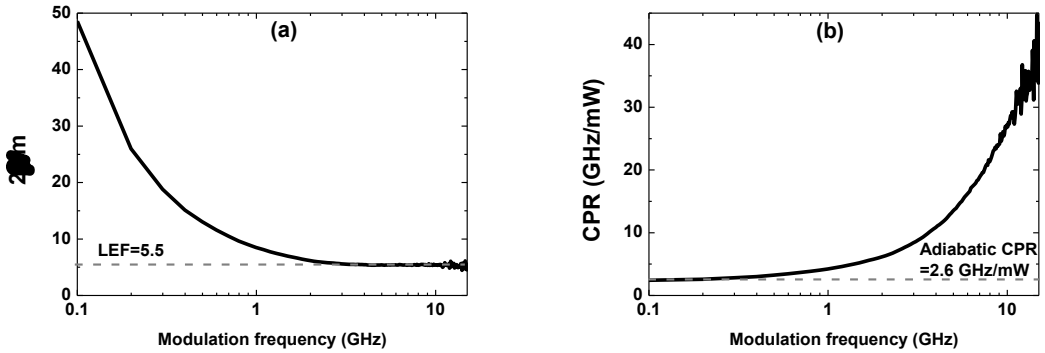

Fig. 5.32. (a) Measured ratio of FM-to-AM index of the Qdash laser. The horizontal line indicates that the α-factor of the laser is 5.5; (b) Measured CPR of the Qdash laser. The CPR due to the adiabatic chirp is about 2.6 GHz/mW as indicated by the horizontal line. The bias current is at 80 mA, and the mode under study is at 1549.0 nm.

5.3.2. Modulated injection-locked laser

In Chapter 4, we have theoretically presented that the ratio of FM-to-AM index of injection-locked semiconductor laser has a different behavior in comparison with the free-running laser. In this section, we show experimental demonstrations in the time domain.

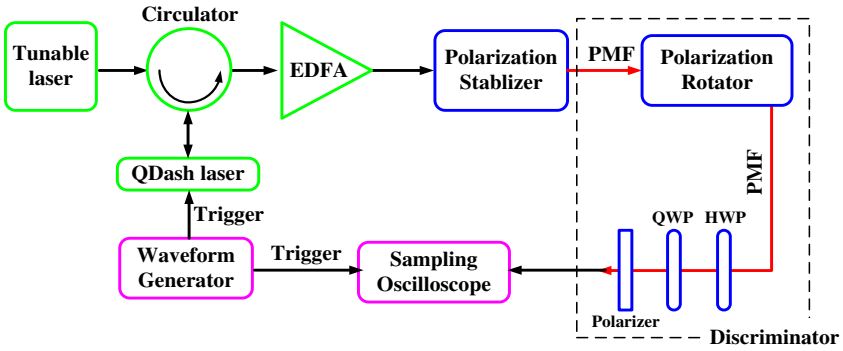

Fig. 5.33. Experimental setup used for the time-resolved AM and FM responses. PMF: polarization maintaining fibre; HWP: half-wave plate; QWP: quarter-wave plate.

Figure 5.33 shows the experimental setup developed at Télécom ParisTech for the time-resolved intensity and chirp measurement of the injection-locked Qdash laser. The optical frequency discriminator in this setup is a fibre-based interferometer, which consists of polarization maintaining fibers (PMFs) and a phase shifter unit (including a half wave plate, a quarter wave plate and two polarizers) [Consoli11], [Chaibi15]. Its transfer function is similar to that of MZ interferometer, and the intensity as well as the chirp responses is extracted in the same way as well [Provost11]. Instead of a VNA, a waveform generator is used to generate the

sine-wave signal with a certain frequency to modulate the Qdash laser. A high-speed sampling oscilloscope is required to record the time series $P_{out}^{A,B}(t)$, which is synchronized with the waveform generator. The Qdash laser is biased above threshold at 80 mA at room temperature, and the optical mode under study is at 1550.6 nm.

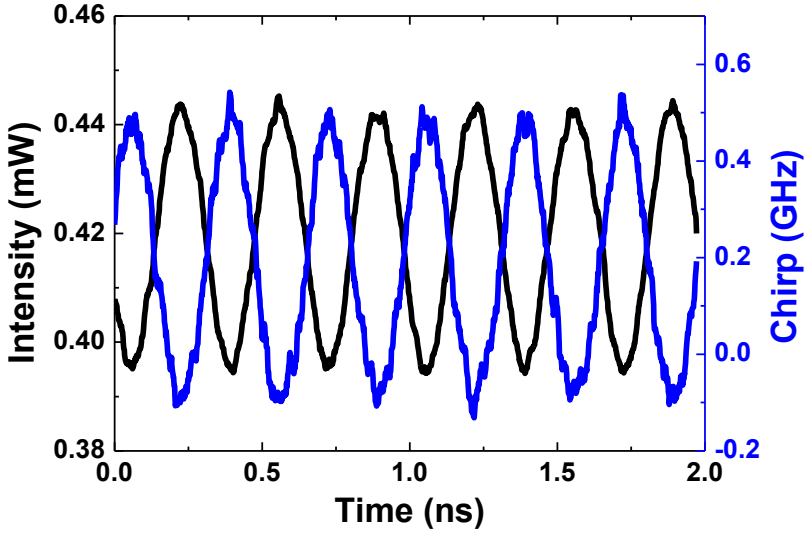

Figure 5.34. Time-resolved intensity (black) and chirp (blue) waveforms recorded for a modulation frequency of 6 GHz.

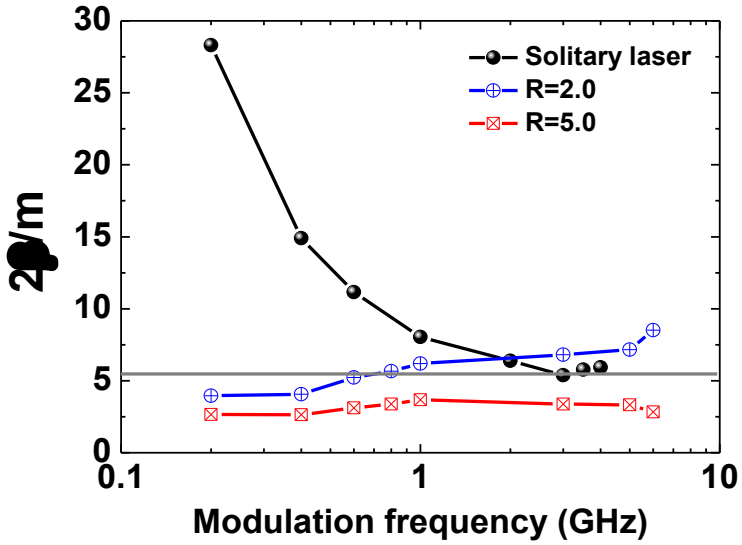

Fig. 5.35. Ratio of FM-to-AM index of the free-running laser, and of the injection-locked laser with injection ratios of R=2.0 and R=5.0. The ratio is obtained from the time domain analysis. The frequency detuning of the master laser with respect to the slave laser is fixed at -4.0 GHz. The horizontal line gives the α-factor of the free-running Qdash laser.

Figure 5.34 shows an example of the measured time-resolved intensity profile AM(t) and the frequency chirp $\Delta\upsilon(t)$. The AM (m) and the FM (β) indices are extracted by fitting the

waveforms using the sine function. By varying the modulation frequency, we can obtain the ratio 2β/m for each frequency, and the results are reported in Fig. 5.35. For the free-running laser, the curve of 2β/m extracted from the time domain analysis is similar to that shown in Fig. 5.32, which is obtained from the frequency analysis. The ratio 2β/m gives the α-factor of 5.4 around f_m=3 GHz. When the laser is subjected to optical injection, the behavior of 2β/m becomes quite different. The injected laser shows a much lower value instead of a giant one at low modulation frequencies, which is even smaller than the α-factor of the free-running laser. For an injection of R=2.0, 2β/m increases from 4.0 for f_m=0.2 GHz up to 8.5 for f_m=6.0 GHz. In contrast, for R=5.0, 2β/m remains almost constant around 3.0. The experimental observation is qualitatively consistent with the simulations in Chapter 4.

5.3.3. Large-signal modulation

This section deals with the large signal behavior of the modulated Qdash laser for both the free running case and for the laser subject to optical injection. The large signal analysis is operated in the time domain, and the experimental setup is the same one as in Fig. 5.33. The Qdash laser is biased at 80 mA at room temperature.

Figure 5.36(a) shows the intensity and chirp profiles of the free-running Qdash laser at a modulation rate of 2.5 Gbps. The transient chirp is related with the overshoot in the modulation response, which is attributed to the relaxation oscillation. It is also shown that the adiabatic chirp of the free-running laser is more than 2.0 GHz due to the gain compression as well as the spontaneous emission.

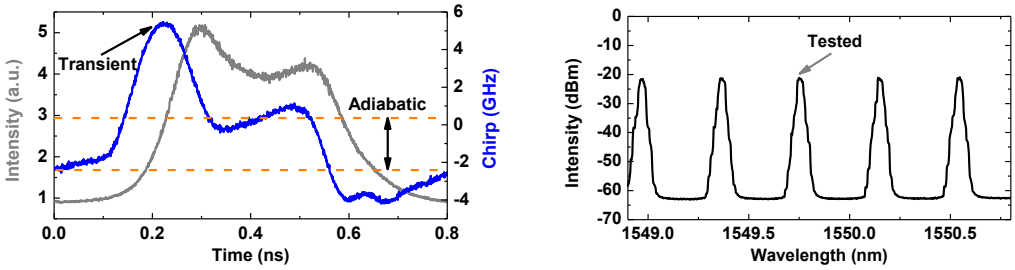

Fig. 5.36. (a) Large-signal intensity (black) and chirp (blue) profiles of the free-running Qdash laser; (b) Optical spectrum under large signal modulation. The laser mode under study is at 1549.75 nm. The modulation rate is 2.5 Gbps, and the modulation depth is Vpp=2.5 V.

Figure 5.37 presents the effect of optical injection on the intensity and chirp profiles. It is shown that the relaxation oscillation in the intensity waveform becomes stronger with the decreased (increased) wavelength (frequency) detuning. Correspondingly, the transient chirp increases as well. It is noted that for all frequency detuning conditions, the adiabatic chirp is

almost completely suppressed by the optical injection, which is in agreement with the simulations in section 4.4.

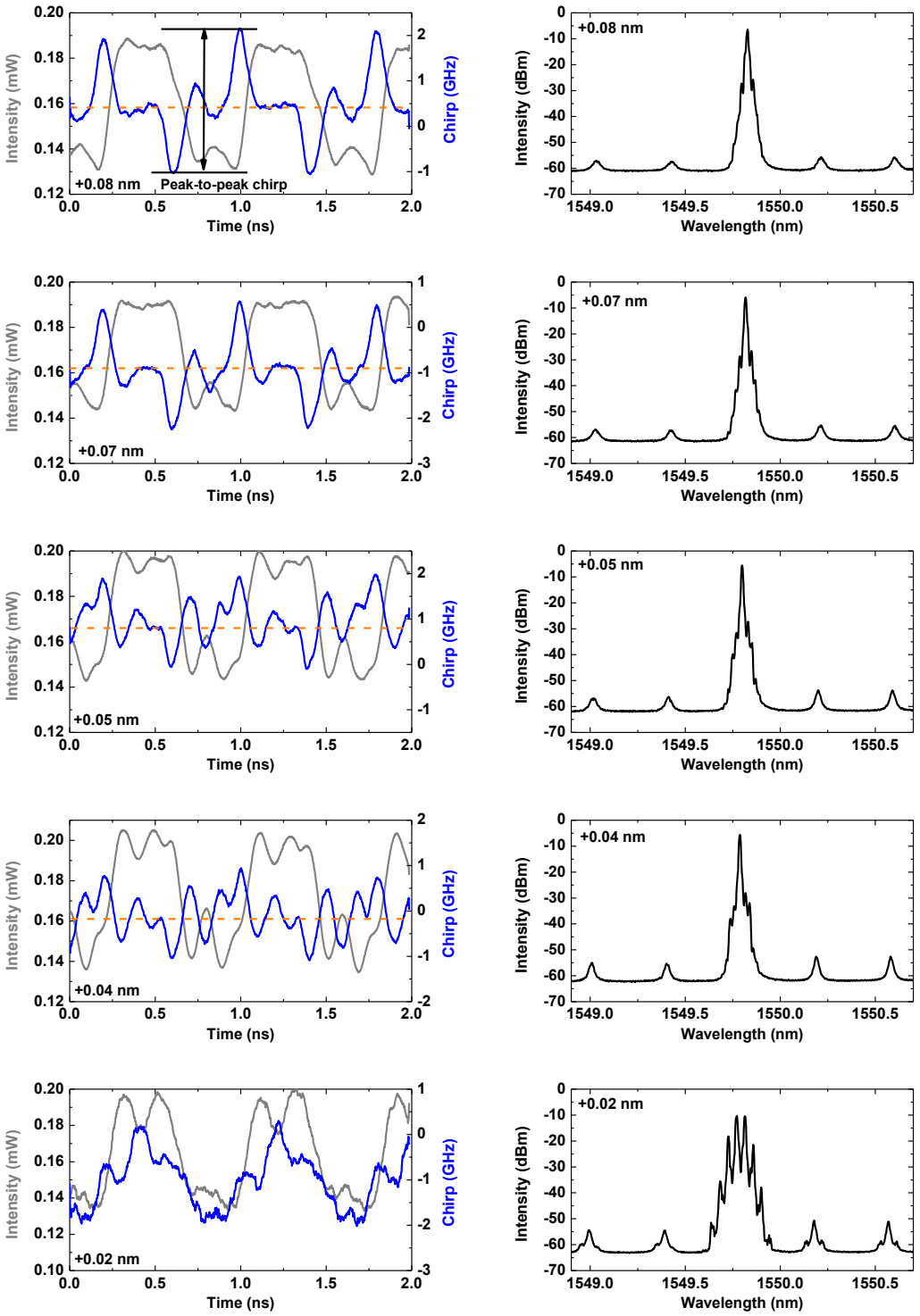

Fig. 5.37. Intensity, chirp profiles (α-factort) and optical spectra (right) of the injection-locked Qdash laser at various detunings. The power of the tunable master laser is fixed at 10 mW. The bottom case is period one dynamics.

Figure 5.38 shows that peak-to-peak chirp increases with the wavelength detuning, from 2.0 GHz for detuning of +0.04 nm up to 3.2 GHz for detuning of 0.08 nm, which are smaller than that of the free-running laser. Therefore, in addition to the elimination of adiabatic chirp, optical injection suppresses the peak-to-peak chirp as well.

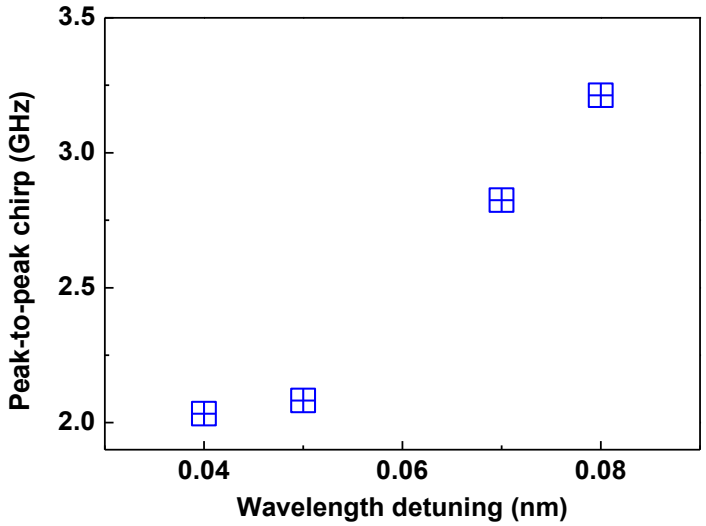

Fig. 5.38. Peak-to-peak chirp as a function of wavelength detuning. The peak-to-peak chirp of the free-running laser is 4.3 GHz.

In summary, this chapter characterizes the modulation dynamics of nanostructure Qdash and Qdot lasers. The AM and FM responses of the free-running laser are studied in the frequency domain. Using optical injection, various nonlinear regimes are identified. In particular, the stable locked area is leveraged to our benefits in order to study the phase-amplitude coupling and the frequency chirp. The high efficiency FWM properties generated in the Qdot laser employing dual-mode injection are investigated. Under optical injection, the NDFWM is operated up to a detuning range of 1.7 THz with a low injection ratio of 0.42. The normalized conversion efficiency and the side-mode suppression ratio with respect to the converted signal are analyzed. The highest NCE of -17 dB associated with a SMSR of 20.3 dB is achieved at detuning of 110 GHz. Under direct current modulation, the phase-amplitude coupling properties of the laser are found to be strongly altered by the external optical injection. In addition, optical injection also well suppresses the time-resolved large-signal chirp. These findings are of prime importance for the realization of chirp-free laser devices. From an implementation perspective the slave laser can be referenced to the proper wavelength locker, facilitating implementation in a compact butterfly package suitable for high-speed applications in optical fiber links.

Particularly, a novel Optical Injection-Hakki-Paoli method is proposed to extract the α-factor of semiconductor laser under DC operation. In contrast to the Hakki-Paoli method operated

only below threshold, this technique that is insensitive to the thermal effect is applicable to both below and above threshold measurements. Further measurements are ongoing to better explore this technique and to understand the physical mechanisms. In addition, for the first time we theoretically demonstrate the existence of a discontinuity of the α-factor in nanostructure lasers at the lasing threshold. This phenomenon is attributed to the carrier clamping of the resonant GS, as well as the unclamped carrier populations in the off-resonant states. In contrast, this behavior does not occur in Qwell lasers, since there are no discrete off-resonant states. Such a discontinuity is a fundamental limitation, preventing the reduction of the α-factor towards zero. This new result is significant for the future improvement of Qdot devices with reduced α-factor.

Part II. Quantum Cascade (QC) Laser

Chapter 6. Introduction to QC lasers

Bipolar semiconductor lasers described in Part I are based on the interband electronic transitions in heterostructures. The lasing spectrum usually lies in the near-infrared (NIR, 0.8~3 μm) regime (see Fig. 6.1). It is hard to extend its wavelength to the mid-infrared (MIR, 3~30 μm) region due to the band gap limitation of the semiconductor materials. Quantum cascade (QC) lasers, however, are unipolar semiconductor lasers relying on intersubband transitions. This kind of lasing mechanism extends the lasing spectra from MIR up to Terahertz regime (THz, 100 μm~1000 μm, or 0.3~3 THz). So far, most QC lasers are built using either InGaAs-AlInAs grown on InP substrates or AlGaAs-GaAs on GaAs substrates. High-performance devices are based on multi-quantum well design or on chirped superlattices [Blaser01a].

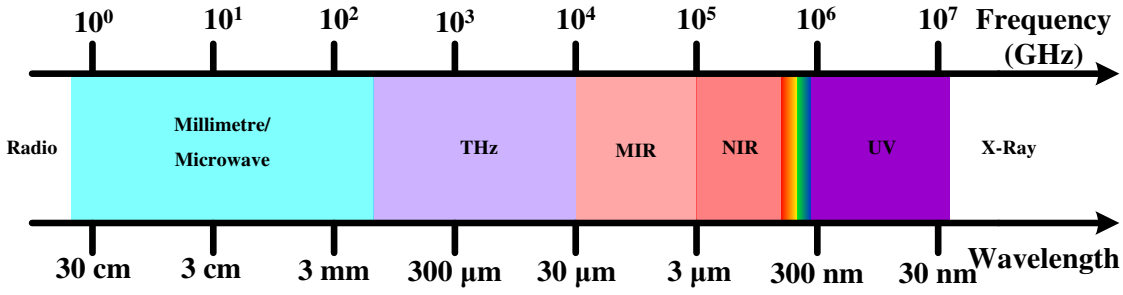

Fig. 6.1. Position of NIR, MIR, and THz regimes in the electromagnetic spectrum

6.1. Brief history and applications

The first demonstration of an intersubband semiconductor lasers, named quantum cascade (QC) laser, was reported in 1994 by Faist and coworkers in Capasso's group at Bell Labs, USA [Faist94]. The great invention was built upon a couple of breakthroughs in earlier years. In 1970, heterojunction superlattices (SLs) and associated transport properties were investigated by Esaki and Tsu [Esaki70]. In 1971, Kazarinov and Suris first proposed to use the intersubband transitions in a SL structure for electromagnetic radiation amplification [Kazarinov71]. This intersubband emission was observed by West in 1985 [West85]. In 1986, the first sequential resonant tunneling through a multi-quantum-well SL was reported by Capasso *et al.* [Capasso86]. The first QC laser reported by Faist was grown by MBE and has an emission wavelength of 4.3 μm. After that, the development of QC lasers has kept progressing rapidly. Pulsed mode [Faist96] and continuous wave operations [Faist96a] at room temperature operation were demonstrated one by one. The first step towards the realization of a terahertz QC laser was supported by the observation of a 4.5 THz electroluminescence from a QC structure in 1998 [Rochat98]. The first THz QC laser emitting at 4.4 THz was reported in 2002

using a chirped superlattice based structure in a low-loss semi-insulating surface plasmon waveguide [Kohler02]. Nowadays, the QC laser field keeps mushrooming quickly, and has brought significant impact to the scientific world. The laser devices are coming to the market and are expected to bring wide range of applications.

A) Gas spectroscopy.

Absorption spectroscopy based sensing is one key application for QC lasers. A lot of molecules have strong vibrational/rotational absorption lines in the MIR or the THz ranges. The gas sensing technology can be used in, for instance, the air pollutant and greenhouse gas monitoring, breath analysis for medical diagnostics, explosive and hazardous materials detection, and industrial process monitoring [Weidmann04], [Manne06], [Fuchs10], [Wysocki05]. THz spectroscopy systems have been applied to various materials in order to understanding the basic characteristics and to demonstrate potential applications in sending and diagnostics. Especially, astronomy and space researches are strong drivers for THz research because the interstellar dust clouds contains a huge amount of information, in which the molecules can be probed in the THz regime [Siegel02].

B) Terahertz imaging

THz imaging is attractive because it has the possibility to generate phase-sensitive spectroscopic images, which can be applied for material identification. Dielectric substances like paper, plastics and ceramics, are relatively non-absorbing in this frequency range. Different materials can be easily identified based on the analysis of their refractive index, which is extracted from the THz phase information. Therefore, the imaging systems find applications in security screening and manufacturing quality control. Particularly, 3D tomographic THz imaging system is of great interest. In addition, studies of cellular structure using THz imaging is also increasing [Hu95], [Loffler01], [Ferguson02], [Mitrofanov01], [Han00].

C) Free space optical (FSO) communication [Ajili07], [Majumdar08]

FSO communication links have received attention in the research and commercial communities because of their high bandwidth with relatively high security to eavesdropping but without the complexity of installing optical fiber. Commercially available systems have been mostly based on telecommunication components in the NIR spectral region. However, the atmospheric optical channel has quite different characteristics from fiber-based channels. Molecular absorption, light scattering from suspended particulates, fog, rain and snow all conspire to make the FSO transmission systems more complex and less controlled. The choice of source wavelength is thus a critical parameter in the design of such systems. In

the MIR wavelength range, the atmosphere has two windows of 3-5 μm and 8-14 μm, which make QC lasers promising for FSO communication links. Particularly, the intrinsic lasing mechanism makes QC laser have a large modulation bandwidth on the order of several hundreds of gigahertz, which is potential to realize ultrahigh speed optical transmission. Martini succeeded in transmission of radio/video images over 70 m under lab conditions [Martini01]. Later, Blaser demonstrated an optical data link between two different buildings separated by 350 m using a 9.3 μm QC laser [Blaser01]. In addition, QC lasers can be also employed in LIDAR systems for remote sensing [Paschke10].

6.2. Fundamentals of QC lasers

Quantum cascade lasers are unipolar semiconductor devices based on intersubband transitions instead of interband transitions like in bipolar semiconductor lasers. The radiative transition occurs between confined electronic states usually in the conduction band. Figure 6.2 compares the difference between the interband and intersubband transitions. Interband QW lasers have a staircase-like density of states for energies larger than the transition energy E_{21}. In contrast, intersubband transitions have an atomic-like density of states peaking at E_{21}, leading to a very narrow gain spectrum. Because the initial and final subbands have the same curvature, the gain linewidth only depends on the collision processes [Maulini06]. Another fundamental characteristic of the intersubband transitions is the short carrier lifetime (~1 ps), which is three orders of magnitude faster than that of interband transitions (~1 ns).

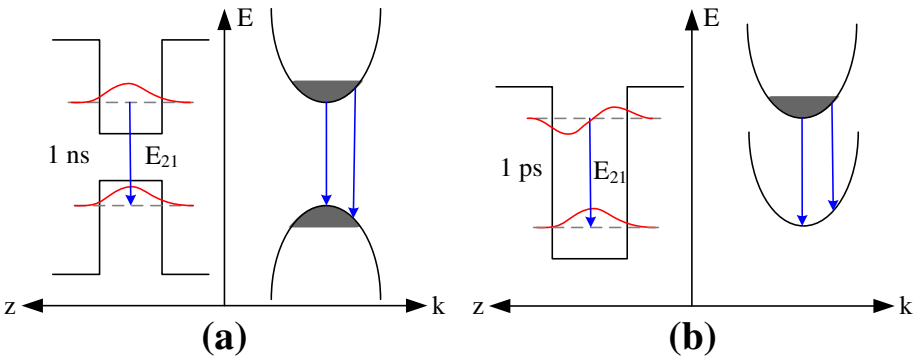

Fig. 6.2. Band diagram and in-plane energy dispersion of (a) interband transition and of (b) intersubband transition.

Figure 6.3 shows the band structure of a typical QC laser. The basic structure of QC lasers consists of the active region and the injector region, which form one stage of the laser. The QC lasers typically have 20-50 repeated identical stages.

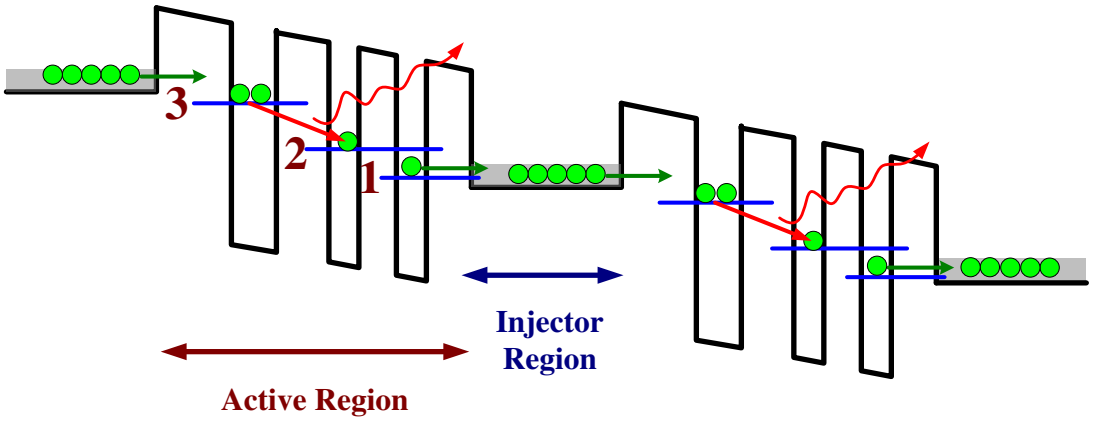

Fig. 6.3. Schematic structure of a QC laser. Each stage consists of an active region and an injector region. The active region is a three-level laser system. The radiation occurs between level-3 and level-2. The injector region is used to collect carriers from level-1 of one stage and to inject carriers to the following stage.

The active region provides the optical gain for the laser emission. The active region relies on multiple-QW structures as shown in Fig. 6.3. The electronic structure of the active region consists of at least 3 energy levels. Electrons are injected into the upper laser level-3. The carrier population inversion occurs between level-3 and level-2, where the laser radiation takes place. Carriers in the lower laser level-2 are depopulated into the bottom level 1 via optical phonon assisted non-radiative transition. In order to meet the condition of the population inversion, the lifetime of the upper laser level-3 must be longer than that of the level-2. On one hand, the lifetime of level-3 is increased (on the order of 1 ps) by employing a transition with a reduced spatial overlap of the wavefunctions (diagonal transition). On the other hand, the lifetime of level-2 is minimized (on the order of 0.1 ps) by making the spacing with level-1 resonant with the optical phonon energy.

An important parameter in the QC laser design is the oscillator strength R_{ij}, which is defined as [Weisbuch91], [Liu00]:

$$R_{ij} = \frac{2m_0}{\hbar^2}(E_i - E_j)\langle\psi_i|Z|\psi_j\rangle = \frac{2m_0}{\hbar^2}(E_i - E_j)z_{ij}^2 \tag{6.1}$$

where m_0 is the electron mass, E_{ij} is the state energy, and z_{ij} is the dipole matrix element. In the effective one-band model [Wittmann09], the wavefunction in the conduction band satisfies the Schrödinger equation:

$$\left[\frac{\hbar^2}{2}\frac{\partial}{\partial z}\frac{1}{m^*(E,z)}\frac{\partial}{\partial z} + V(z)\right]\psi(z) = E\psi(z) \tag{6.2}$$

where the contribution of the valence band is taken into account by an energy dependent effective mass [Nelson87]:

$$m^*(E,z) = m^*(z)\left(1+\frac{E-V(z)}{E_{g,eff}}\right) \tag{6.3}$$

where the effective bandgap $E_{g,eff} = \hbar^2/(2\zeta m^*(z))$ is related to the nonparabolicity coefficient ζ. The energy levels E_{ij} in the conduction band can be obtained by solving Eq. (6.2). Finally, the matrix element of the optical transition between the initial and final states is given by [Sirtori94]:

$$z_{ij} = \frac{-i\hbar}{2(E_i - E_j)}\left\langle \psi_i \middle| p_z \frac{1}{m^*(E_i,z)} + \frac{1}{m^*(E_j,z)} p_z \middle| \psi_j \right\rangle \tag{6.4}$$

where the momentum operator is defined as $p_z = -i\hbar\frac{\partial}{\partial z}$.

The injector region bridges the adjacent active regions. The band structure is another multi-QW structure or a superlattice structure. Carriers tunneled out from the bottom level of one stage are collected here and then are injected to the upper lasing level of the following stage by resonant tunneling. The injection region also introduces an additional energy drop between the lower lasing level and the bottom state of the period. Therefore, it reduces the thermal backfilling of the former. Finally, the injector region is doped to act as an electron reservoir, insuring that the integrated negative charge in the structure is compensated by the positive donors, even in the situation of strong electrical injection to prevent the formation of space-charge domains [Maulini06].

After the birth of the QC laser concept, various architectures of both active region and injector region were proposed, which led to dramatic improvements of the laser's performances. The first QC laser was composed of three coupled Qwells, where the radiation relies on the diagonal transition in the real space. Later, the vertical transition design was introduced aiming to be less sensitive to interface roughness and impurity fluctuations [Faist95]. The injection efficiency of the injector region is maximized by introducing a thin well, which increases the overlap between the bottom state and the upper lasing state of the following period [Faist96]. In 1997, Scamarcio et al. brought a completely different concept using the superlattice (SL) active region instead of discrete energy levels. In this design, electrons transit between two superlattice conduction bands (miniband), and the photon energy follows that of the energy gap (minigap). A distinctive feature of the architecture is the high oscillator strength of the optical transition at the mini-Brillouin zone boundary of the superlattice [Scamarcio97]. The performance is further improved by a chirped SL active region design, which overcomes the need of doping in the active region [Tredicucci98]. This kind of structures improves the carrier

extraction efficiency from the lower lasing state to the bottom state. Today, two active designs are the most promising: The bound (or continuum)-to-continuum (or bound) design [Faist01], [Yao10], [Yao10a], and the two-phonon resonance design [Hofstetter01].

Finally, we summarize the fundamental features of the QC lasers in contrast to the interband semiconductor lasers:

A) The transition energy is determined by the confinement energy of the electrons in the quantum well rather than the band gap energy of the material. Thus, it is possible to tune the lasing wavelength by adjusting the Qwell thickness. The covered wavelength range can be up to 50% of the conduction band offset using the same material system.

B) Multiple cascade stages. The electrons are recycled from one stage to the subsequent, that is, one electron can trigger lots of photons while passing all the stages. This results in high differential quantum efficiency. Although the threshold current of QC lasers is usually very high due to the ultra-short non-radiative lifetime, its value can however be reduced since the threshold current density is inversely proportional to the number of cascades.

C) The short carrier lifetime on the order of 1 ps. It is even smaller than the photon lifetime (> 5 ps). In contrast, the interband laser has a much longer carrier lifetime (~ 1 ns) than the photon lifetime. This main difference brings new dynamical characteristics like broadband modulation bandwidth up to several hundreds of GHz without any relaxation oscillation.

D) Narrow gain spectrum. This is due to the discrete atomic-like density of states in QC lasers. The symmetric gain shape also leads to a near-zero α-factor (typically -1~1).

In the following, Chapter 7 discusses the dynamic properties of the free running QC laser, and Chapter 8 investigates the QC laser subject to optical injection.

Chapter 7. Free-running QC laser

7.1. Rate equations and static solutions

From the introduction in chapter 6, it is known that the QC laser is a three-level laser system with many repeated stages. Since the stages can be slightly different from one to another, the laser system can be in principle macroscopically described by a full set of rate equations including three equations of carriers and one of photons for each stage [Rana02]. Assuming the QC laser has N_{pd} (20~50) periods, the total number of coupled rate equations are $4\times N_{pd}$, which means there are 80~200 equations describing one QC laser system. In order to simplify the analysis, here it is assumed that all the gain stages are identical. That is, every stage has the same carrier number and the same time constants. Finally, the simplified rate equation system is given by [Harder05]:

$$\frac{dN_3}{dt} = \eta\frac{I}{q} - \frac{N_3}{\tau_{32}} - \frac{N_3}{\tau_{31}} - \Gamma_p v_g g S \tag{7.1}$$

$$\frac{dN_2}{dt} = \frac{N_3}{\tau_{32}} - \frac{N_2}{\tau_{21}} + \Gamma_p v_g g S \tag{7.2}$$

$$\frac{dN_1}{dt} = \frac{N_3}{\tau_{31}} + \frac{N_2}{\tau_{21}} - \frac{N_1}{\tau_{out}} \tag{7.3}$$

$$\frac{dS}{dt} = N_{pd}\Gamma_p v_g g S - \frac{1}{\tau_P} S + \beta N_{pd}\frac{N_3}{\tau_{sp}} \tag{7.4}$$

where N3,2,1 respectively denote the carrier numbers in the upper lasing subband, lower lasing subband and the bottom state, S denotes the photon number, η is the current injection efficiency, $\tau_{32}, \tau_{31}, \tau_{21}$ are the relaxation times among the three levels , τ_{out} is the tunneling out time, τ_p is the photon lifetime, τ_{sp} is the spontaneous emission time, Γ_p is the optical confinement factor, v_g is the group velocity of the light, and the gain stage number is N_{pd}. The optical gain g of each stage is defined as [Petijean11]:

$$g = a\frac{\Delta N}{Lw} \tag{7.5}$$

where $\Delta N = N_3 - N_2$ is the population inversion, L is the cavity length and w is the cavity width. In a parabolic band approximation for the electronic dispersion in the conduction band, the differential gain a is given by [Gmachl99]:

$$a = \frac{1}{L_p}\frac{4\pi q z_{32}^2}{\varepsilon_0 n_r \lambda(2\gamma_{32})} \tag{7.6}$$

where z_{32} is the optical dipole matrix element, ε_0 is the vacuum dielectric constant, n_r is the refractive index of the optical mode, λ is the lasing wavelength, $(2\gamma_{32})$ is the full width at half maximum (FWHM) of the optical transition, and L_p is the length of a single gain stage.

A) Below threshold

The steady-state solution to the rate equations can be obtained by setting all the time derivatives to zero. Below the lasing threshold, the photon emission is only owing to the spontaneous emission and is small, thereby it is often assumed that S=0. Then, we obtain the carrier numbers of each state as a function of the injected current:

$$N_3 = \eta \frac{I}{q} \frac{1}{1/\tau_{32} + 1/\tau_{31}} \tag{7.7}$$

$$N_2 = \eta \frac{I}{q} \frac{1}{1/\tau_{32} + 1/\tau_{31}} \frac{\tau_{21}}{\tau_{32}} \tag{7.8}$$

$$N_1 = \eta \frac{I}{q} \tau_{out} \tag{7.9}$$

In order to realize population inversion, i. e, $N_3 > N_2$, the carrier lifetime of the lower lasing level must be smaller than that of the upper lasing level $\tau_{21} < \tau_{32}$.

B) Above threshold

Once the laser is operated above the lasing threshold, the gain is clamped at

$$N_{pd}\Gamma_p v_g g \approx \frac{1}{\tau_P} \tag{7.10}$$

Using this condition, the steady-state solutions above threshold are solved as

$$N_3 = \left(\eta \frac{I}{q} + \frac{Lw}{N_{pd}\Gamma_p v_g a} \frac{1}{\tau_p} \frac{1}{\tau_{21}} \right) \frac{1}{1/\tau_{31} + 1/\tau_{21}} \tag{7.11}$$

$$N_2 = \left(\eta \frac{I}{q} - \frac{Lw}{N_{pd}\Gamma_p v_g a} \frac{1}{\tau_p} \frac{1}{\tau_{31}} \right) \frac{1}{1/\tau_{31} + 1/\tau_{21}} \tag{7.12}$$

$$N_1 = \eta \frac{I}{q} \tau_{out} \tag{7.13}$$

and the population inversion is

$$\Delta N = \frac{Lw}{N_{pd}\Gamma_p v_g a} \frac{1}{\tau_p} \tag{7.14}$$

From Eq. (7.2), the photon number is expressed as

$$S = N_{pd}\tau_p \frac{\tau_{31}}{\tau_{32}(\tau_{31}+\tau_{21})}\left[\eta\frac{I}{q}(\tau_{32}-\tau_{21}) - \frac{Lw}{N_{pd}\Gamma_p v_g a}\frac{1}{\tau_p}\frac{(\tau_{32}+\tau_{31})}{\tau_{31}}\right] \tag{7.15}$$

Setting the photon number to zero in the above equation, we obtain the threshold current:

$$I_{th} = \frac{q}{\eta}\frac{Lw}{N_{pd}\Gamma_p v_g a}\frac{1}{\tau_p}\frac{(\tau_{32}+\tau_{31})}{\tau_{31}(\tau_{32}-\tau_{21})} \tag{7.16}$$

Using this relation, the photon number expression (7.15) is replaced by

$$S = \eta\eta_r N_{pd}\tau_p \frac{I - I_{th}}{q} \tag{7.17}$$

with the radiative quantum efficiency

$$\eta_r = \frac{\tau_{31}(\tau_{32}-\tau_{21})}{\tau_{32}(\tau_{31}+\tau_{21})} \tag{7.18}$$

The radiative quantum efficiency for a QC laser is defined as the fraction of the total number of electrons into each gain stage per second that contributes to the photon emission. Equation (7.18) shows that if the lifetime of the lower lasing level τ_{21} is much smaller than both the non-radiative lifetimes τ_{32} and τ_{31}, the radiative quantum efficiency would be close to unity.

Table 7.1. QC laser parameters used in the simulation [Sirtori02], [Rana02], [Faist04], [Harder05], [Gensty05], [Petijean11]

Parameter	Symbol	Value	Parameter	Symbol	Value
Lasing frequency	υ	2.9 THz (103 μm)	Differential gain	a	5×10^{-8} cm
Stage number	N_{pd}	30	Spontaneous emission factor	β	1×10^{-6}
Optical confinement factor	Γ_p	0.27	Current injection efficiency	η	0.15
Cavity length	L	3 mm	Carrier lifetime from level 3 to 2	τ_{32}	2.0 ps
Cavity width	w	80 μm	Carrier lifetime from level 3 to 1	τ_{31}	2.4 ps
Facet reflectivity	R	0.29	Carrier lifetime from level 2 to 1	τ_{21}	0.5 ps
Group index	n_r	3.3	Tunneling out time	τ_{out}	0.5 ps
Cavity loss	α_i	24 cm^{-1}	Photon lifetime	τ_P	3.7 ps
Spontaneous emission time	τ_{sp}	7 ns			

In the simulations, all the parameters are listed in Table 7.1. Figure 7.1 shows the steady-state solutions of the QC laser. In contrast to interband semiconductor lasers, carrier populations in the lasing states 3 and 2 keep increasing beyond their threshold values. As a result, an increase in the injected current of the QC laser not only leads to an increase in the photon emission rate but it also leads to an increase in the rate of non-radiative transitions. This property is indicated in Eqs. (7.11) and (7.12). However, the population inversion as well as the gain is clamped above threshold as described in Eq. (7.14). Carriers in the bottom state N_1 increases linearly with the pump current.

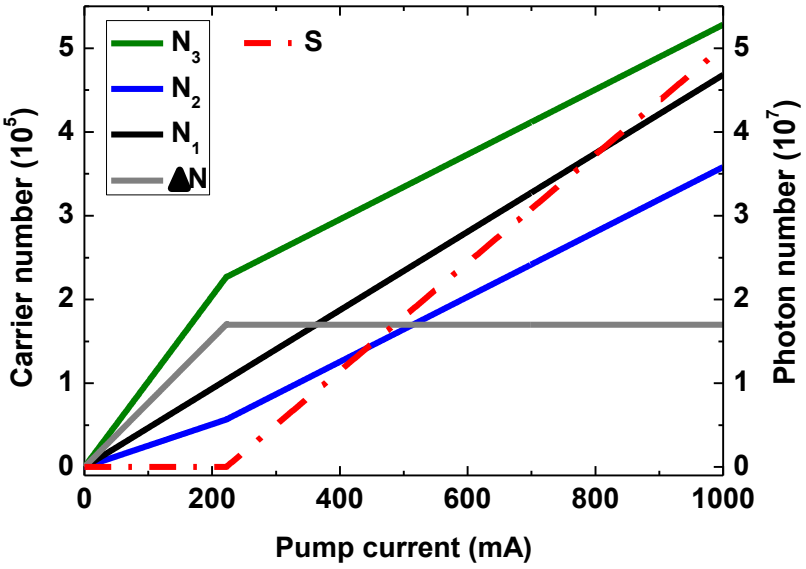

Fig. 7.1 Steady-state solutions of the QC laser. The threshold current is 223 mA. The carrier population inversion is clamped beyond threshold. The radiative efficiency of the laser is $\eta_r = 0.62$ (see Eq. (7.18)).

7.2. Modulation dynamics

In the modulation response of QC lasers, one particular feature is the absence of the relaxation oscillation, which is owing to its shorter carrier lifetime as compared to the photon lifetime. The short non-radiative lifetime suppresses the relaxation oscillation resulting in an over-damped class-A oscillator with carrier equilibrium completely restored after one photon roundtrip. On the other hand, because of the ultrafast carrier lifetime on the order of 1 ps, QC lasers lead to an ultra-broad modulation bandwidth, which is highly desirable for free-space short-range communications [Mustafa99]. Assuming a simplified set of rate equations, the AM bandwidth was predicted to be as large as of 100 GHz [Cheung97]. Values up to terahertz were even theoretically calculated in intersubband semiconductor lasers based on a triple quantum well structure [Donovan01], [Haldar05]. However, these values are lowered to tens of gigahertz

when using a full rate equation approach taking into account the QCL periods as well as the ground level from which electrons leave the active region into the injector of the next stage [Rana02], [Petijean11] Experimentally, Paiella et al. reported a QCL emitting at 8 μm with a 10 GHz AM bandwidth and no relaxation oscillation resonance [Paiella01]. Besides AM bandwidths up to 13 GHz and 24 GHz have also been measured on terahertz QCLs using a test bench technique [Barbieri07], [Maineult10]. In this section, we study both the amplitude and frequency modulation response properties through the small-signal analysis.

Considering that the laser is directly modulated by a small current δI with a given modulation frequency, the carriers and the photon will be modulated correspondingly $\delta N_{1,2,3}$ and δS . Finally, the differential rate equation system is given by

$$\begin{bmatrix} j\omega+\gamma_{11} & -\gamma_{12} & 0 & -\gamma_{14} \\ -\gamma_{21} & j\omega+\gamma_{22} & 0 & -\gamma_{24} \\ -\gamma_{31} & -\gamma_{32} & j\omega+\gamma_{33} & 0 \\ -\gamma_{41} & -\gamma_{42} & 0 & j\omega+\gamma_{44} \end{bmatrix} \begin{bmatrix} \delta N_3 \\ \delta N_2 \\ \delta N_1 \\ \delta S \end{bmatrix} = \frac{\eta \delta I}{q} \begin{bmatrix} 1 \\ 0 \\ 0 \\ 0 \end{bmatrix} \tag{7.19}$$

with

$$\begin{aligned} &\gamma_{11} = G_0 S + \frac{1}{\tau_{32}} + \frac{1}{\tau_{31}};\ \ \gamma_{12} = G_0 S;\ \ \gamma_{14} = -G_0 (N_3 - N_2) \\ &\gamma_{21} = G_0 S + \frac{1}{\tau_{32}};\ \ \gamma_{22} = G_0 S + \frac{1}{\tau_{21}};\ \ \gamma_{24} = G_0 (N_3 - N_2) \\ &\gamma_{31} = \frac{1}{\tau_{31}};\ \ \gamma_{32} = \frac{1}{\tau_{21}};\ \ \gamma_{33} = \frac{1}{\tau_{out}}; \\ &\gamma_{41} = N_{pd} G_0 S + N_{pd} \frac{\beta}{\tau_{sp}};\ \ \gamma_{42} = -N_{pd} G_0 S;\ \ \gamma_{44} = \frac{1}{\tau_p} - N_{pd} G_0 (N_3 - N_2) \end{aligned} \tag{7.20}$$

where $G_0 = \Gamma_p v_g a / (Lw)$, and $\gamma_{44} \approx 0$ ignoring the spontaneous emission and the gain compression.

A) AM response

The modulation transfer function is then given by

$$H(\omega) = \frac{N_{pd} G_0 S \left(j\omega + A \right)}{-j\omega^3 - B\omega^2 + j\omega C + D} \tag{7.21}$$

with

$$A=\frac{1}{\tau_{21}}-\frac{1}{\tau_{32}};\quad B=2G_0S+\frac{1}{\tau_{32}}+\frac{1}{\tau_{31}}+\frac{1}{\tau_{21}}$$
$$C=G_0S\left(\frac{1}{\tau_{31}}+\frac{1}{\tau_{21}}+\frac{2}{\tau_p}\right)+\left(\frac{1}{\tau_{32}}+\frac{1}{\tau_{31}}\right)\frac{1}{\tau_{21}} \tag{7.22}$$
$$D=\frac{G_0S}{\tau_p}\left(2G_0S+\frac{1}{\tau_{31}}+\frac{1}{\tau_{21}}\right)$$

Both the numerator and the denominator are multiplied by the same term $\left(j\omega+1/\tau_{out}\right)$, resulting in a cancellation in Eq. (7.21). Through the above modulation transfer function, Fig. 7.2 shows the normalized AM response of the QC laser for various bias currents. It demonstrates that the QC laser indeed has a broadband response with a bandwidth of tens of GHz as reported in the measurements [Barbieri07], [Maineult10]. The 3-dB bandwidth increases from several GHz near the lasing threshold up to 60 GHz at the bias current of 4.5×I_{th}. In addition, the responses remain quite flat with no resonance peak in comparison with the interband semiconductor lasers. This is attributed to the ultra-fast carrier lifetime, which is even shorter than the photon lifetime.

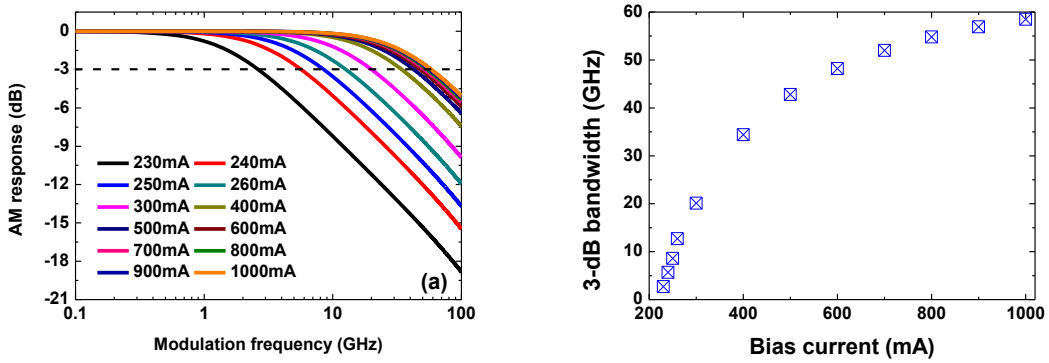

Fig. 7.2. (a) AM response of the QC laser for different bias currents. (b) 3-dB modulation bandwidth as a function of bias current. The threshold current of the laser is 223 mA.

In order to gain an intuitive insight of the AM response behavior, we analyze the zero and the poles (eigenvalues) of the modulation transfer function (7.21). The QC laser system only has one constant zero given by

$$z=-\left(1/\tau_{21}-1/\tau_{32}\right) \tag{7.23}$$

From Table 7.1, the zero of the QC laser system is z=-1.5×10^{12} rad/s. In Class-B type interband semiconductor lasers have a pair of conjugate complex poles, determined by the damping factor Γ and the resonance frequency ω_R as

$$p_{1,2}=-\left(\frac{1}{2}\Gamma\pm j\omega_R\right) \tag{7.24}$$

In contrast, the poles of the QC laser at the bias current of $1.5\times I_{th}$ respectively are $p_1 = -9.60\times10^{10}$ rad/s, $p_2 = -1.02\times10^{12}$ rad/s, and $p_3 = -2.57\times10^{12}$ rad/s. From the knowledge of the Bode plot analysis, the modulation bandwidth is mainly determined by the smallest pole p_1 (15.3 GHz). In addition, it is shown that all poles of the QC laser are real values, which is a feature of class-A laser. No complex eigenvalue of the laser system indicates that the QC laser has not relaxation oscillation in consistent with the experimental observation [Paiella01].

B) FM response

In order to study the FM behavior of the QC laser, one additional equation of the phase variation of the electric field is coupled with the rate equations (7.1)-(7.4):

$$\frac{d\phi}{dt} = \frac{\alpha_H}{2}\left(N_{pd}\Gamma_p v_g g - \frac{1}{\tau_P} \right) \tag{7.25}$$

where α_H is the linewidth enhancement factor of the QC laser. The gain compression effect has to be taken into account, by replacing the gain in the rate equations as follows

$$g \rightarrow g(1-\xi S / V_p) \tag{7.26}$$

where ξ is the gain compression factor, and V_p is the photon volume. The gain compression effect is responsible for the adiabatic chirp and the bending of L-I curve of the QC laser as already observed in the experiment [Hangauer14]. Potential mechanisms of the gain compression of the QC laser are the spectral and spatial hole burning as well as the carrier heating as for interband semiconductor lasers [Willatzen91], [Klotzkin14], [Morthier91]. However, a full identification of the physical effects still requires further studies.

From the small-signal analysis of the differential rate equations, the CPR of the QC laser is derived as

$$CPR(\omega) = \frac{j\omega\delta\phi}{\delta S} = \frac{\alpha_H}{2S}\left(j\omega + \frac{1}{\tau_P} - N_{pd}G_0(N_3 - N_2)(1-\xi S / V_p) \right) \tag{7.27}$$

where the spontaneous emission is neglected. It is shown that the CPR of the QC laser is very similar to that of interband lasers, except the gain expression. The FM response of the QC laser is then given by

$$FM(\omega) = \frac{j\omega\delta\phi}{\eta\delta I / q} = CPR(\omega)H(\omega) \tag{7.28}$$

Figure 7.3 shows the CPR of the QC laser decreases with the increasing bias current, because the CPR is inversely proportional to the laser power. The adiabatic chirp due to the gain compression at low modulation frequency is around 0.05 GHz/mW. At high modulation frequencies, the CPR increases linearly proportional to the value of the linewidth enhancement

factor. Figure 7.4 presents for the first time the FM response of the QC laser. Surprisingly, the FM bandwidth is on the order of tens of THz, which is three orders of magnitude larger than that of the AM bandwidth (Fig. 7.2). On the other hand, a resonance-like peak occurs in the FM response. Through the Bode plot analysis of Eq. (7.28), this peak is attributed to the spontaneous emission and the gain compression. In the future work, it is necessary to perform experimental investigations on the FM behavior to verify these theoretical predictions.

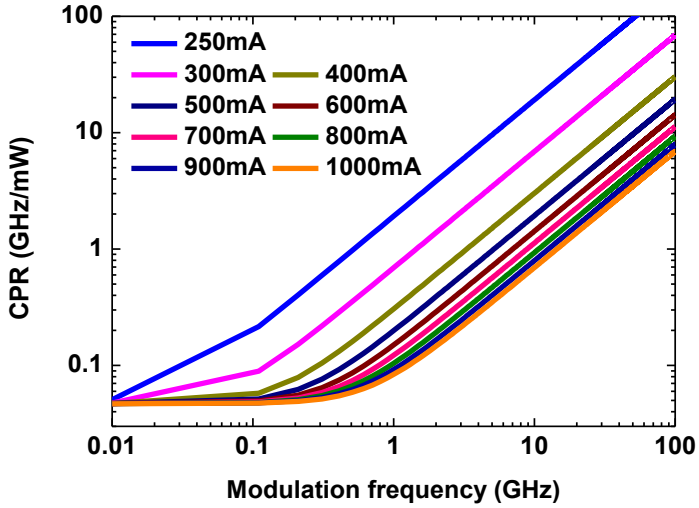

Fig. 7.3. CPR of the QC laser for different bias currents. The gain compression factor is assumed to be $\xi = 5\times10^{-17}$ cm^3.

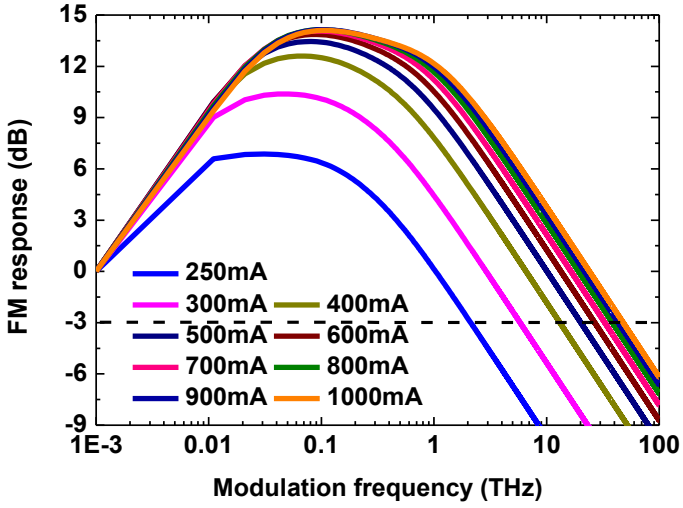

Fig. 7.4. FM response of the QC laser for different bias currents. The gain compression factor is assumed to be $\xi = 5\times10^{-17}$ cm^3.

In summary, this chapter studied the static and dynamic properties of free-running QC lasers based on a set of coupled rate equations. Semi-analytical analyses show that the QC lasers exhibit a flat and broadband AM response with a bandwidth on the order of tens of GHz.

Particularly, the QC lasers do not have any relaxation oscillation. On the other hand, the FM response of QC lasers exhibits an ultra-broad bandwidth on the order of tens of THz, three orders of magnitude higher than the AM response. These properties make the QC laser very promising for modulation applications such as free space communications.

Chapter 8. Injection-locking of QC lasers

The optical injection locking architecture has been a powerful engine for establishing tunable photonic oscillators and high bandwidth radio frequency links. For intersubband QC laser geometries, the suppression of residual amplitude modulation was observed [Taubman04], as well as power scaling, linewidth reduction and frequency noise suppression of frequency combs [Borri12]. The AM bandwidth enhancement effect by optical injection was theoretically reported via a simple model without taking into account gain stage cascading [Meng12]. This chapter first introduce the rate equation models describing the injection-locked QC laser and the steady-state solutions. Secondly, the local bifurcation diagram will be presented. Thirdly, we analyze both the AM and FM properties of the QC laser subject to optical injection locking.

8.1. Static characteristics

As in interband semiconductor lasers, the optical injection of the QC laser can be described by replacing the photon and phase equations (7.4), (7.25) using

$$\frac{dS}{dt} = \left(N_{pd}\Gamma_p v_g g - 1/\tau_P\right)S + \beta N_{pd}\frac{N_3}{\tau_{sp}} + 2k_c\sqrt{S_{inj}S}\cos\Delta\phi \tag{7.29}$$

$$\frac{d\Delta\phi}{dt} = \frac{\alpha_H}{2}\left(N_{pd}\Gamma_p v_g g - 1/\tau_P\right) - \Delta\omega_{inj} - k_c\sqrt{\frac{S_{inj}}{S}}\sin\Delta\phi \tag{7.30}$$

where the phase difference between the slave and the master lasers is $\Delta\phi = \phi_{slave} - \phi_{master}$ with $\phi_{master}, \phi_{slave}$ being the phases of the master and slave lasers, respectively. The frequency detuning is $\Delta\omega_{inj} = \omega_{master} - \omega_{slave}$,where ω_{master} is the angular frequency of the master laser and ω_{slave} that of the slave laser, and k_c denotes the coupling rate of the master into the slave. The injection ratio is defined as $R_{inj}=S_{inj}/S_{FR}$, where S_{inj} is the injected photon number and S_{FR} is the photon number of the free running laser. All parameters used in the computations are outlined in Table 7.1.

The steady-state solutions of the injection-locked laser system is given by

$$N_3 - N_2 = \frac{Lw}{N_{pd}\Gamma_p v_g a}\left(\frac{1}{\tau_p} - 2k_c\sqrt{\frac{S_{inj}}{S}}\cos\Delta\phi\right) \tag{7.31}$$

$$N_1 = \eta\frac{I}{q}\tau_{out} \tag{7.32}$$

$$S = S_{inj}\left[\frac{2k_c \cos\Delta\phi}{1/\tau_p - N_{pd}\Gamma_p v_g g}\right]^2 \tag{7.33}$$

$$\Delta\phi = \sin^{-1}\left[\frac{-\Delta\omega_{inj}}{k_c\sqrt{1+\alpha_H^2}}\sqrt{\frac{S}{S_{inj}}}\right] - \tan^{-1}\alpha_H \tag{7.34}$$

From Eq. (7.31), it is shown that the total modal gain of the laser is reduced by $2k_c\sqrt{S_{inj}/S}\cos\Delta\phi$ and is dependent on both the injection ratio and the detuning frequency. Figure 7.5 shows that optical injection reduces the threshold current. The lasing power is increased (a), while the carrier population inversion (N_3-N_2) is reduced (b).

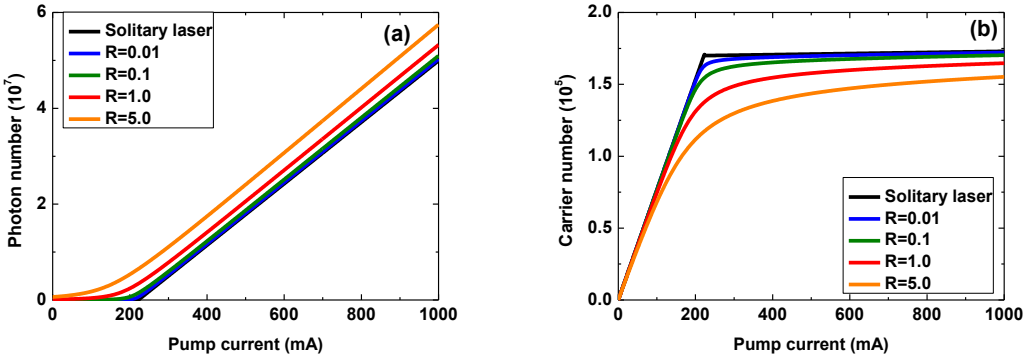

Fig. 7.5. Injection strength effect on the photon number (a), and on the carrier population inversion (N_3-N_2) (b) for a QC laser. The injection ratio is with respect to the photon number of the free running laser at $1.5\times I_{th}$, that is, $S_{FR}=7.26\times10^6$ (0.52 mW). The frequency detuning is fixed at zero.

8.2. Stability diagram

The bifurcation diagrams are useful to identify nonlinear dynamics such as period doubling and chaos in optically injected semiconductor lasers [Wieczorek05]. In this section, we investigate the main saddle-node (SN) and Hopf bifurcations of the injection-locked QC laser using the continuation package *Matcont* as introduced in section 4.2 [Dhooge03]. It is known that the bifurcation diagram strongly depends on the value of the α-factor. Due to the nature of intersubband transitions, QC lasers are expected to exhibit a narrow and symmetric gain spectrum, leading to a zero α-factor at the gain peak according to the Kramers-Krönig relation. However, many body Coulomb interactions, coherence of resonant-tunneling transport and electronic dispersion non-parabolicity yields to a non-zero α-factor in real QC laser devices. Experimentally reported α-factor values range from -2.0 up to 3.0 [Kumazaki08], [Liu13]. Nevertheless, in most cases, the α-factor of QC lasers is much smaller than that of interband semiconductor lasers.

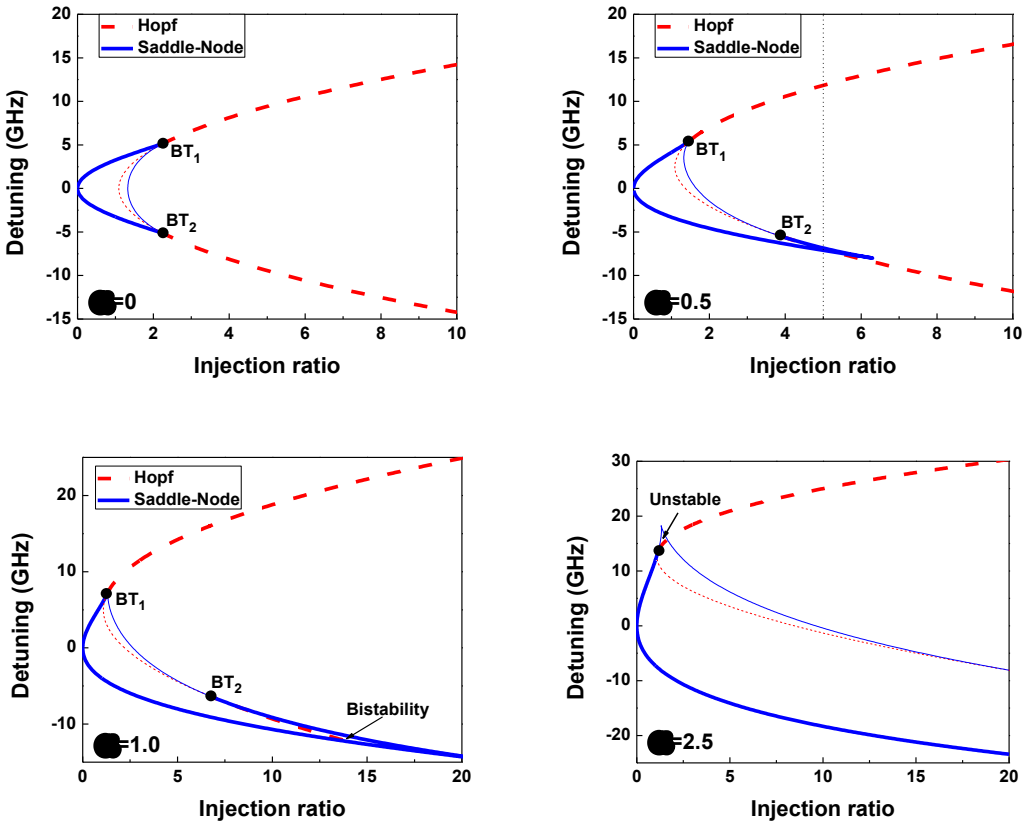

Fig. 7.6. Local bifurcation diagram of an injection-locked QC laser for α-factor values of 0, 0.5, 1.0 and 2.5. Solid line is the saddle-node (SN) bifurcation and dashed line is the Hopf bifurcation. The supercritical bifurcation is denoted by thick lines while subcritical bifurcation by thin lines. The stable locking regime is bounded by the supercritical bifurcations. The investigated laser is operating in the stable locked region of the bifurcation diagram with an α-factor of 0.5, where the vertical dotted line indicates an injection ratio of 5.0.

The simulated stability diagrams are shown in Fig.7.6 for several α-factors. The stable locking regime is bounded by the supercritical bifurcations, which is enlarged by increasing the α-factor from 0 to 2.5. In contrast to the case of interband lasers (see Fig. 4.2), the zero frequency detuning case is always stable even under low injection level. Besides, the codimension-two SN-Hopf points are of Bogdanov-Takens (BT) form instead of Zero-Hopf (ZH) form [Pausch12], where the bifurcations change criticality. Complex nonlinear dynamics usually arise around these codimension-two points [Wieczorek05]. With a larger α-factor, BT_1 moves toward the negative axis of injection ratio associated with the positive axis of detuning, while BT_2 moves oppositely. For a zero α-factor α_H=0, the bifurcation diagram is symmetric, while a non-zero one leads to an asymmetry. A bistability region emerges near the cusp point at the negative detuning side for α_H =1.0, which is not exhibited in conventional interband semiconductor lasers [Kelleher12]. For an α-factor of α_H=2.5, a small unstable locked area appears at the positive detuning side. When compared to interband lasers, all above differences

in the bifurcation diagram can be directly attributed to the high ratio of the photon lifetime to the carrier lifetime in QC lasers (τ_p/τ_{32}=1.85) [Kelleher12], [Erneux13].

8.3. Modulation dynamics

A) AM response enhancement

With the bifurcation diagram, the modulation properties of the injection-locked QC laser can be studied within the stable locked regime. To investigate the AM response, we linearize the rate equations via the standard approach of small signal analysis. The modulation transfer function of the injection-locked QC laser can be expressed as follows:

$$H(\omega) = \frac{p_1 p_2 p_3 p_4 p_5}{z_1 z_2 z_3} \frac{\prod_{k=1}^{3}(j\omega - z_k)}{\prod_{k=1}^{5}(j\omega - p_k)} \tag{7.35}$$

where z_k, p_k are respectively the zeros and poles of the steady-state polynomials, which are useful in the modulation response's behavior analysis with respect to the Bode plots. Among the zeros, z_1 is the smallest one and is expressed as:

$$z_1 = k_c \sqrt{S_{inj}/S}(\cos\phi - \alpha_H \sin\phi) \tag{7.36}$$

From chapter 7, it is known that the free running QC lasers exhibit a rather flat AM response without resonance peak due to their ultrafast carrier lifetime [Maineult10]. The modulation bandwidth can be enhanced by increasing bias current but at the price of the excess heating and the degradation of spectral properties. The inset of Fig. 7.7 illustrates that the injection-locked laser at zero detuning does not present resonance peak as well. Fig. 7.7 also shows that the 3-dB modulation bandwidth increases with the optical injection strength, however, the bandwidth tends to saturate at high injection ratios. The possible underlying physical mechanism to this saturation is the finite carrier and photon lifetimes, which remains open for further investigation in the future.

In Fig. 7.8, we present the detuning effect on the modulation response. The detuning range is controlled in the stable locked regime with respect to the bifurcation diagram. It is seen that the 3-dB bandwidth is enhanced by both positive and negative detunings, while the former is more efficient. From the inset, under both detunings it is found that peaks arise in the response. However, from the Bode plot analysis the underlying mechanisms are different. For the positive detuning, a pair of complex conjugate poles appears which surprisingly give rise to a resonance originating from the interaction between the locked field and the shifted cavity-resonance field [Murakami03]. The resonance combined with the small zero z_1 results in the peak in the

modulation response. In the case of negative detuning, all the poles remain real indicating there is no resonance. The appearance of the peak is due to the fact that the zero z_1 is smaller than any of the poles (in the Bode plot). In addition, the simulation in Fig. 7.9 shows that a large α-factor also increases the peak amplitude in the modulation response. However, the modulation bandwidth is hardly influenced.

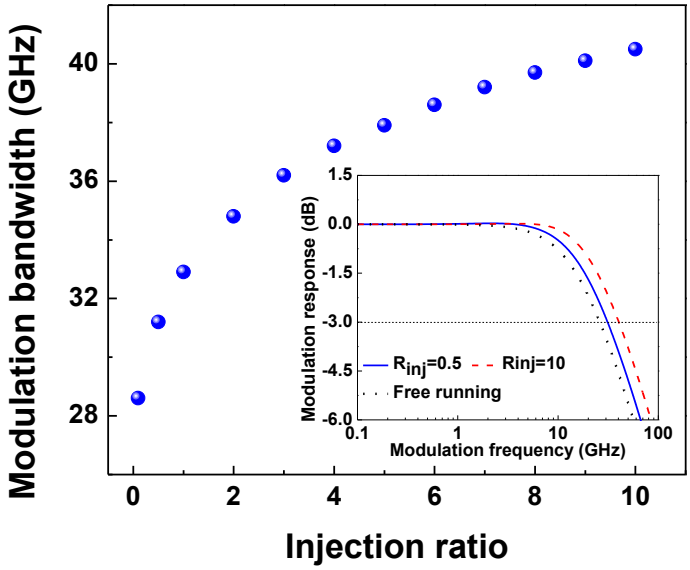

Fig. 7.7. The 3-dB modulation bandwidth as a function of injection ratio (for zero detuning and α-factor=0.5). Inset: The related AM response. Note the absence of any peaks.

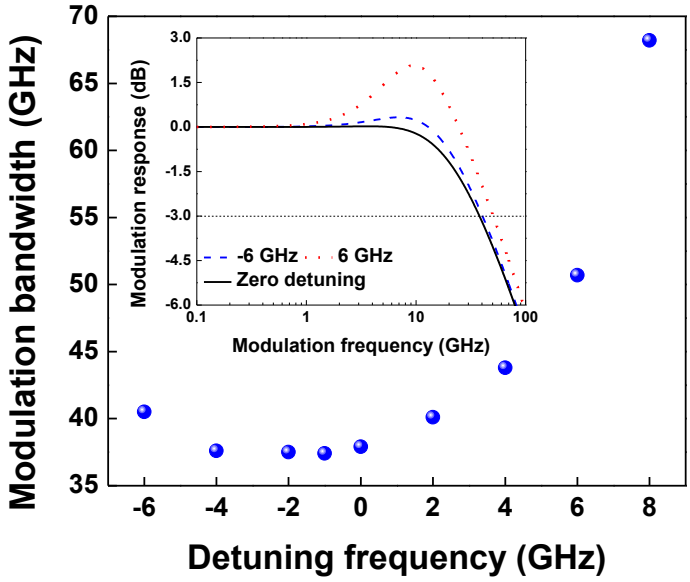

Fig. 7.8. The 3-dB modulation bandwidth as a function of detuning (for R_{inj}=5.0 and α-factor=0.5). Inset: The AM response under various detuning conditions. The peak at positive detuning is due to the resonance while the one at negative detuning is not.

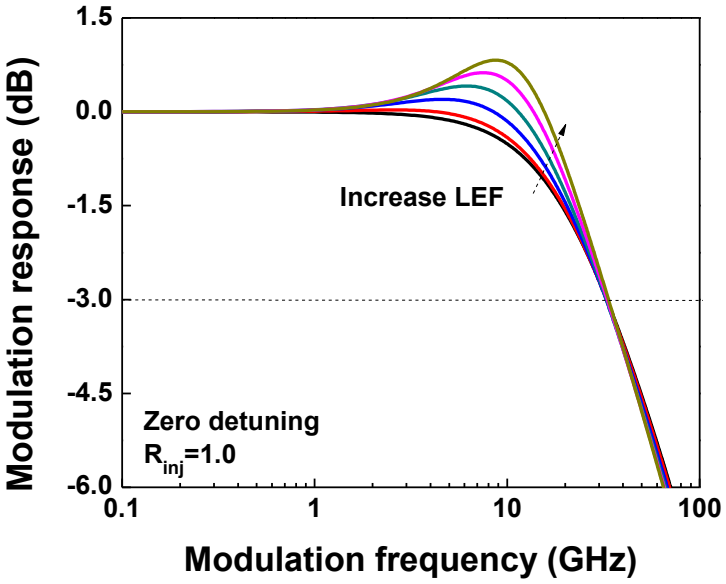

Fig. 7.9. Modulation response at zero detuning with R_{inj}=1.0 for various α-factor values 0.1, 0.5, 1.0, 1.5, 2.0, 2.5.

One fundamental feature of QC lasers is the multistage cascade scheme, where electrons contribute to the gain and the photon emission in each period, leading to a radiative quantum efficiency proportional to the period number [14]. We therefore study the influences of the cascade gain stage number on the AM response. Surprisingly, it is shown that the response is little impacted by the stage number, both in free running and injection-locked lasers under the same bias-threshold current ratio (I_{bias}=1.5×I_{th}). However, when all the responses are normalized to the DC value with N_{pd}=30 as shown in Fig. 7.10, it is found that the amplitude of the response increases with a larger stage number which means more power is obtained in the modulation, while the response shape remains similar. In contrast, the inset of Fig. 7.10 presents that the steady-state property is strongly impacted by the stage number. With more gain stages in the QC laser, both carriers in the upper and lower subbands decrease, while the photon number remains almost constant. Additionally, the threshold current of the free running laser is substantially reduced while the external differential efficiency (dS/dI) is enhanced, as reported in [Faist98]. When compared to the free running laser, the carrier number of the upper subband (N_3) in the locked laser decreases while that of the lower subband (N_2) slightly increases. The population in the bottom state remains constant at $N_1 = \tau_{out}\eta I / q$. Besides, the laser power is scaled up. On the other hand, laser devices with more stages require higher operating voltage, which is useful to reduce the undesired potential drops in the injector region, but it also leads to poor heat-removal efficiency from the active region [Tournié12].

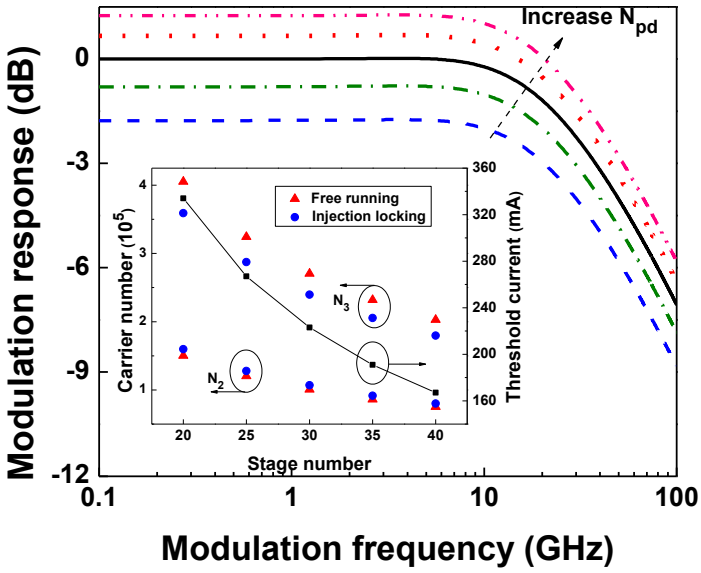

Fig. 7.10. AM response for various gain stage number increasing from 20 to 40, note that it is normalized to the case with N_{pd}=30 (under zero detuning and R_{inj}=5.0). Inset is steady-state result for I_{bias}=1.5×I_{th}.

B) Frequency chirp reduction

Figure 7.11 shows the calculated CPR for the QC laser with and without optical injection. For the free running laser, the CPR remains almost constant in the modulation range 0.01~0.1 GHz. In this region, the adiabatic chirp dominates the chirp level originating from the gain compression as well as from the spontaneous emission. For higher frequencies than 0.1 GHz, the CPR increases almost linearly with the modulation frequency, and the slope is then determined by the linewidth enhancement factor and the laser output power. For the laser operating under optical injection, the constant CPR region vanishes, which value is determined by the injection ratio, phase difference and the linewidth enhancement factor. At zero detuning, the optical injection remarkably reduces the CPR level, especially for modulation frequencies less than 10 GHz. At the frequency of 1.0 GHz, the optical injection substantially decreases the free-running CPR from 480 MHz/mW down to 30 MHz/mW with an injection ratio of 10. For frequencies higher than 10 GHz, the modulation frequency dominates the CPR value, and more than half of the chirp is reduced. Figure 7.12 presents the impact of frequency detuning under an injection ratio of 5.0. It shows that the frequency detuning in either direction increases the CPR value. In contrast to the interband laser, the CPR can be even larger than the free-running laser case for detunings near the stable-locked regime edges. The minimum CPR is obtained at zero detuning. Since the detuning also enhances the AM bandwidth, a trade-off is required in the optical injection to simultaneously reach a low frequency chirp and a large modulation bandwidth.

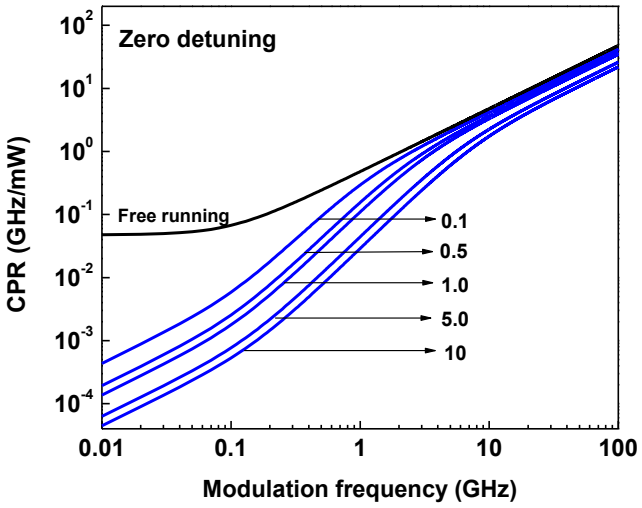

Fig. 7.11. The CPR level for the free-running QC laser and the laser with optical injection at zero detuning. The injection ratio increases from 0.1 up to 10.

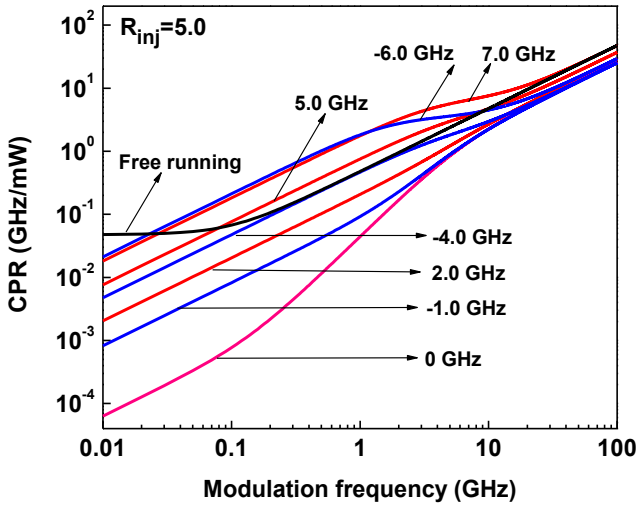

Fig. 7.12. Impacts of frequency detuning to the CPR of the injection-locked QC laser with an injection ratio of 5.0.

To summarize, this chapter investigated the dynamic properties of optical injection-locked QC lasers both on bifurcation diagrams and modulation responses. It is demonstrated that the stable locking regime widens as the α-factor value increases. Meanwhile, both bistable and unstable locked regions are found in this dynamical system. Increasing either the injection ratio or the master-slave frequency difference enhances the 3-dB AM modulation bandwidth. In addition, optical injection reduces the CPR of QC lasers as for interband lasers. These findings are of prime importance for the performance enhancement of future integrated QC lasers.

Chapter 9. Summary and outlook

In this thesis, we studied the modulation dynamics of nanostructured Qdot semiconductor lasers in the first part and of QC lasers in the second part.

The small-signal modulation dynamics are studied in a semi-analytical approach based on a set of coupled rate equations, incorporating the special features of nanostructures. The carrier scattering processes (capture and relaxation) are found to be the main limitation of the 3-dB modulation bandwidth. We also improved the model by taking into account the contribution of carrier populations of off-resonant states on the refractive index change. This model allows us to study the α-factor properties of nanostructure lasers, which are compared with common experimental approaches used to measure it. Results quantitatively unveil that carrier populations of off-resonant states strongly increase the α-factor of Qdot lasers. Therefore, enlarging the energy separation between the resonant and off-resonant states helps to reduce its magnitude. On the other hand, fast carrier scattering rates also leads to a smaller α-factor. In contrast to the usual GS emission, ES lasing Qdot lasers exhibit superior dynamic performances, including broader modulation bandwidth, lower frequency chirping. Particularly, calculations reveal that the α-factor of an ES laser is only half of that in a GS laser. Through proper energy band engineering, it is of high potential for the realization of chirp-free emitters with zero or even negative α-factor values using the ES emission. Employing a multi-population rate equation model, we also numerically studied the inhomogeneous broadening impacts both on the small and large signal analysis. It strongly limits the modulation performances of Qdot lasers, such as reducing the modulation bandwidth and degrading the eye diagram quality, raising the α-factor as well as the frequency chirp.

The optical injection-locking technique does improve the dynamic characteristics of nanostructure lasers. Depending on the injection conditions, calculations show that the modulation bandwidth is strongly enhanced while the frequency chirp is well suppressed. In addition, the phase-amplitude coupling properties of the nanostructure laser are significantly altered by the optical injection.

The modulation dynamics of nanostructure lasers are characterized in the experiments both for the free-running and for the injection-locking operations. Particularly, based on the simulations of the optical gain in presence of optical injection, a novel *Optical Injection-Hakki-Paoli* method has been developed based on the preliminary results. This experimental technique does not suffer from thermal effects and offers the possibility to extract both the below and above threshold α-factor of semiconductor laser simply by adjusting the injection ratio or the

frequency detuning. In addition, we theoretically revealed for the first time the occurrence of a threshold discontinuity of the α-factor in nanostructure (Qdot and Qdash) lasers while it does not in Qwell lasers. This behavior is attributed to the unclamped carrier populations in the off-resonant states, and thus retains the efforts of reducing the α-factor and thus the frequency chirp of nanostructure lasers.

In the second part, we investigated the modulation dynamics of the QC lasers. Owing to its intersubband optical transition and the ultrafast carrier lifetime (on the order of 1 ps), the dynamic properties of the QC lasers are different to those of interband semiconductor lasers. The AM response has a broad modulation bandwidth on the order of tens of GHz without any relaxation resonance, while the FM response shows an ultra-broad bandwidth on the order of tens of THz. When the QC laser is injection-locked, the bifurcation diagram is substantially different to the case of interband lasers with an enhanced stability. In addition, the modulation bandwidth can be enhanced not only at the positive frequency detuning side but also at the negative one. All these properties offer promising perspectives that can be explored for future development of free-space communications.

In future works, various experimental demonstrations are required to verify the theoretical predictions presented in this thesis, such as the reduction of α-factor through band structure engineering in nanostructure lasers, and the superior dynamic performance of lasers operating on the ES. The proposed *Optical Injection-Hakki-Paoli* method in this work deserves further theoretical and experimental investigations. Modulation dynamics of injection-locked QC lasers needs experimental investigations as well. Furthermore, tunnel injection and p-doped schemes can be possible solutions to enhance the dynamical performances of nanostructure semiconductor lasers.

In addition to the modulation dynamics, it is also important to study the intensity and phase noise characteristics of the nanostructure and QC lasers both theoretically and experimentally, which have significant influences on their applications. Especially, optical injection locking technique can well improve the noise properties of both kind lasers [Simos14], [Juretzka15].

Moreover, in the rate equation modeling we used the exciton approximation. However, this approximation has some limitations in predicting behaviors such as the so-called GS quenching when Qdot lasers exhibit simultaneous GS and ES lasing, which is attributed to the asymmetry of electrons and holes [Gioannini12], [Rohm15]. In future works, it will be interesting to investigate influences of the de-synchronization between electrons and holes on the lasers' static and dynamic characteristics.

As for the injection-locked lasers, this work mainly focus on the stably locking regime, but as mentioned in chapter 5, the technique also produces a large variety of nonlinear dynamics such as periodic oscillation and chaos. It will be interesting to further characterize the behaviors and to explore the physical mechanisms in the nanostructure and QC lasers. Particularly, the QC lasers are expected to exhibit different and interesting dynamics owing to its ultrafast carrier lifetimes. Nanostructure and QC lasers subject to optical feedback as well as mode-locked lasers for optical clock distribution are interesting field to explore. Investigation on modulation dynamics of silicon based emitters [Liang10], [Duan14], [Rickman14] is a promising topic as well.

Bibliography

[A]

[Agrawal86] G. P. Agrawal and N. K. Dutta, *Long Wavelength Semiconductor Lasers*. New York: Van Nostrand Reinhold, 1986.

[Agrawal88] G. P. Agrawal, "Population pulsations and nondegenerate four-wave mixing in semiconductor lasers and amplifiers," J. Opt. Soc. Am. B 5, 147 (1988).

[Ajili07] L. Ajili, *Quantum Cascade Lasers at Terahertz Frequencies*, Ph. D thesis, Neuchatel, 2007.

[Akahane10] K. Akahane, N. Yamamoto ,and T. Kawanishi, "Wavelength tunability of highly stacked quantum dot laser fabricated by a strain compensation technique," in Proceeding of the 22nd IEEE International Semiconductor Laser Conference (ISLC), 37 (2010).

[Akahane12] K. Akahane, N. Yamamoto ,and T. Kawanishi, "The dependence of the characteristic temperature of highly stacked InAs quantum dot laser diodes fabricated using a strain-compensation technique on stacking layer number," in Proceeding of the 22nd IEEE International Semiconductor Laser Conference (ISLC), 82 (2012).

[Akiyama00] T. Akiyama, O. Wada, H. Kuwatsuka, T. Simoyama, Y. Nakata, K. Mukai, M. Sugawara, and H. Ishikawa, "Nonlinear processes responsible for nondegenerate four-wave mixing in quantum-dot optical amplifiers," Appl. Phys. Lett. 77, 1753 (2000).

[Alferov63] Z. I. Alferov and R. F. Kazarinov, "Semiconductor Laser with Electric Pumping," Inventor's Certificate 181737 in Russian, Appl. 950840, priority as of March 30, 1963.

[Alghoraibi04] I. Alghoraibi, L. Joulaud, C. Paranthoen, A. le Corre, O. Dehaese, N. Bertru, H. Folliot, P. Caroff, and S. Loualiche, "InAs self-assembled quantum dot and quantum dash lasers on InP for 1.55 μm optical telecommunications," J. Appl. Phys. 95, 1074 (2004).

[Alghoraibi06] I. Alghoraibi, T. Rochel, N. Bertru, A. Le Corre, A. Létoublon, P. Caroff, O. Dehaese, and S. Loualiche, "Self-assembled InAs quantum dots grown on InP(311)B substrates: Role of buffer layer and amount of InAs deposited," J. Cryst. Growth 293, 263 (2006).

[Allen05] C. N. Allen, P. Poole, P. Barrios, P. Marshall, G. Pakulski, and S. Raymond, "External cavity quantum dot tunable laser through 1.55 μm," Physica E 26, 372 (2005).

[Anantathanasarn06] S. Anantathanasarn, R. Notzel, P. J. van Veldhoven, F. W. M. van Otten, Y. Barbarin, G. Servanton, T. de Vries, E. Smalbrugge, E. J. Geluk, T. J. Eijkemans, E. A. J. M. Bente, Y. S. Oei, M. K. Smit, and J. H. Wolter, "Lasing of wavelength-tunable (1.55 μm region) InAs/InGaAsP/InP (100) quantum dots grown by metal organic vapor-phase epitaxy," Appl. Phys. Lett. 89, 073115 (2006).

[Arakawa82] Y. Arakawa and H. Sakaki, "Multidimensional quantum well laser and temperature dependence of its threshold current," Appl. Phys. Lett. 40, 939 (1982).

[Agrawal89] G. P. Agrawal, "Intensity dependence of the linewidth enhancement factor and its implications for semiconductor lasers," IEEE Photon. Tech. Lett. 1, 212 (1989).

[Arakawa01] Y. Arakawa, "Progress in growth and physics of nitride-based quantum dots," Phys. Stat. Sol. (a) 188, 37 (2001).

[Arecchi84] F. T. Arecchi, G. L. Lippi, G. P. Puccioni, and J. R. Tredicce, "Deterministic chaos in laser with injected signal," Opt. Commun. 51, 308 (1984).

[Arsenijevi14] D. Arsenijevi, A. Schliwa, H. Schmeckebier, M. Stubenrauch, M. Spiegelberg, D. Bimberg, V. Mikhelashvili, and G. Eisenstein, “Comparison of dynamic properties of ground- and excited-state emission in p-doped InAs/GaAs quantum-dot lasers,” Appl. Phys. Lett. 104, 181101 (2014).
[Asada86] M. Asada, Y. Miyamoto, and Y. Suematsu, “Gain and the threshold of three-dimensional quantum-box lasers,” IEEE J. Quantum Electron. 22, 1915 (1986).
[Asryan96] L. V. Asryan and R. A. Suris, “Inhomogeneous line broadening and the threshold current density of a semiconductor quantum dot laser,” Semicond. Sci. Technol. 11, 554 (1996).
[Asryan11] L. V. Asryan, Y. C. Wu, and R. A. Suris, “Carrier capture delay and modulation bandwidth in an edge-emitting quantum dot laser,” Appl. Phys. Lett. 98, 131108 (2011).

[B]

[Barbieri07] S. Barbieri, W. Maineult, S. S. Dhillon, C. Sirtori, and J. Alton, “13 GHz direct modulation of terahertz quantum cascade lasers,” Appl. Phys. Lett. 91, 143510 (2007).
[Berg01] T. W. Berg, S. Bischoff, I. Magnusdottir, and J. Mørk, “Ultrafast gain recovery and modulation limitations in self-assembled quantum-dot devices,” IEEE Photon. Tech. Lett. 13, 541 (2001).
[Bertru10] N. Bertru, C. Paranthoen, O.Dehaese, H. Folliot, A. Le Corre, R. Piron, F. Grillot, W. Lu, J. Even, G. Elias, C. Levallois, S. Loualiche, M. Bozkurt, J. Ulloa, P. Koenraad, and A. Ponchet, “QD laser on InP substrate for 1.55 µm emission and beyond,” Proc. of SPIE 7608, 76081B (2010).
[Bhattacharyya99] D. Bhattacharyya, A. A. Avrutin, A. C. Bryce, J. H. Marsh, D. Bimberg, F. Heinrichsdorff, V. M. Ustinov, S. V. Zaitsev, N. N. Ledentsov, P. S. Kop’eV, Zh. I. Alferov, A. I. Onischenko, and E. P. O’Reilly, “Spectral and dynamic properties of InAs-GaAs self-organized quantum-dot lasers,” IEEE J. Sel. Top. Quantum Electron. 5, 648 (1999).
[Bhattacharya00] P. Bhattacharya, D. Klotzkin, O. Qasaimeh, W. Zhou, S. Krishna, and D. Zhu, “High-speed modulation and switching characteristics of In(Ga)As-Al(Ga)As self-organized quantum-dot lasers,” IEEE J. Sel. Top. Quantum Electron.6, 426 (2000).
[Bhattacharya00a] P. Bhattacharya, “Quantum well and quantum dot lasers: from strained-layer and self-organized epitaxy to high-performance devices,” Opt. Quantum Electron. 32, 211 (2000).
[Bhattacharya07] P. Bhattacharya and Z. Mi, “Quantum-dot optoelectronic devices,” Proc. IEEE 95, 1723 (2007).
[Bhowmick14] S. Bhowmick, M. Z. Baten, T. Frost, B. S. Ooi, and P. Bhattacharya, “High performance InAs/$In_{0.53}Ga_{0.23}Al_{0.24}As$/InP quantum dot 1.55 µm tunnel injection laser,” IEEE J. Quantum Electron. 50, 7 (2014).
[Bimberg96] D. Bimberg, N. N. Ledentsov, M. Grundmann, N. Kirstaedter, O. G. Schmidt, M. H. Mao, V. M. Ustinov, A. Yu. Egorov, A. E. Zhukov, P. S. Kop’ev, Zh. I. Alferov, S. S. Ruvimov, U. Gosele, and J. Heydenreich, “InAs-GaAs quantum pyramid lasers: In situ growth, radiative lifetimes and polarization properties,” Jpn. J. Appl. Phys. 35, 1311 (1996).
[Bimberg98] D. Bimberg, M. Grundmann, and N. N. Ledentsov, *Quantum Dot Heterostructures*, New York: Wiley, 1998.
[Blaser01] S. Blaser, D. Hofstetter, M. Beck, and J. Faist, “Free-space optical data link using Peltier-cooled quantum cascade laser,” Electron. Lett. 37, 778 (2001).

[Blaser01a] S. Blaser, L. Diehl, M. Beck, J. Faist, U. Oesterle, J. Xu, S. Barbieri, and F. Beltram, "Characterization and modeling of quantum cascade lasers based on a photon-assisted tunneling transition," IEEE J. Quantum Electron. 37, 448 (2001).

[Bockelmann92] U. Bockelmann and T. Egeler, "Electron relaxation in quantum dots by means of Auger processes," Phys. Rev. B 46, 15574 (1992).

[Borri12] S. Borri, I. Galli, F. Cappelli, A. Bismuto, S. Bartalini, P. Cancio, G. Giusfredi, D. Mazzotti, J. Faist, and P. De Natale, "Direct link of a mid-infrared QCL to a frequency comb by optical injection," Optics Letter 37, 1011 (2012).

[C]

[Capasso86] F. Capasso, K. Mohammed, and A. Y. Cho, "Resonant tunneling thourgh double barriers, perpendicular quantum transport phenomena in superlattices, and their device applications," IEEE J. Quantum. Electron. 22, 1853 (1986).

[Carlin91] J. F. Carlin, R. Houdré, A. Rudra, and M. Ilegems, "Island formation in ultra-thin InAs/InP quantum wells grown by chemical beam epitaxy," Appl. Phys. Lett. 59, 3018 (1991).

[Caroff05] P. Caroff, C. Paranthoen, C. Platz, O. Dehaese, H. Folliot, and N. Bertru, "High-gain and low-threshold InAs quantum-dot lasers on InP," Appl. Phys. Lett. 87, 243107 (2005).

[Chaibi15] M. E. Chaibi, H. T. Nguyen, C. Gosset, F. Grillot, and D. Erasme, "Time resolved chirp measurement based on a polarization-maintaining fiber," Opt. Lett., (2015).

[Chan07] S. C. Chan, S. K. Hwang, and J. M. Liu, "Period-one oscillation for photonic microwave transmission using an optically injected semiconductor laser," Opt. Express 15, 14921 (2007).

[Chang03] F. Y. Chang, C. C. Wu, and H. H. Lin, "Effect of InGaAs capping layer on the properties of InAs/InGaAs quantum dots and lasers," Appl. Phys. Lett. 82, 4477 (2003).

[Cheung97] C. Y. L. Cheung, P. S. Spencer, and K. A. Shore, "Modulation bandwidth optimisation for unipolar intersubband semiconductor lasers," IEEE proceedings Optoelectronics 144, 44 (1997).

[Chimot13] N. Chimot, S. Joshi, G. Aubin, K. Merghem, S. Barbet, A. Accard, A. Ramdane, and F. Lelarge, "1550nm InAs/InP quantum dash based directly modulated lasers for next generation passive optical network," in *2012 International Conference on IPRM,* 177, 2013.

[Chow99] W. W. Chow and S. W. Koch, *Semiconductor-Laser Fundamentals*, Berlin: Springer, 1999.

[Chow05] W. W. Chow and S. W. Koch, "Theory of semiconductor quantum-dot laser dynamics," IEEE J. Quantum Electron. 41, 495 (2005).

[Chow11] W. W. Chow, M. Lorke, and F. Jahnke, "Will quantum dots replace quantum wells as the active medium of choice in future semiconductor lasers," IEEE J. Sel. Top. Quantum Electron. 17, 1349 (2011).

[Chow13] W. W. Chow and F. Jahnke, "On the physics of semiconductor quantum dots for applications in lasers and quantum optics," Progress in Quantum Electronics, 37,109 (2013).

[Cisco10] Cisco Data Center Interconnect Design and Deployment Guide, Cisco Press, 2010.

[Coldren95] L. A. Coldren and S. W. Corzine, *Diode Lasers and Photonic Integrated Circuits*, New York: Wiley, 1995.

[Consoli11] A. Consoli, J. M. G. Tijero, and I. Esquivias, "Time resolved chirp measurement of gain switched semiconductor laser using a polarization based optical differentiator," Opt. Express 19, 10805 (2011).

[Cornet04] C. Cornet, C. Labbé, H. Folliot, N. Bertru, O. Dehaese, J. Even, A. Le Corre, C. Paranthoën, C. Platz, and S. Loualiche, "Quantitative investigations of optical absorption in InAs/InP (311)B quantum dots emitting at 1.55 μm wavelength," Appl. Phys. Lett. 85, 5685 (2004).

[Cornet05] C. Cornet, C. Platz, P. Caroff, J. Even, C. Labbé, H. Folliot, A. Le Corre, "Approach to wetting-layer-assisted lateral coupling of InAs/InP quantum dots," Phys. Review B 72, 035342 (2005).

[Cornet06] C. Cornet, A. Schliwa, J. Even, F. Doré, C. Celebi, A. Létoublon, E. Macé, C. Paranthoën, A. Simon, P. M. Koenraad, N. Bertru, D. Bimberg, and S. Loualiche, "Electronic and optical properties of InAs/InP quantum dots on InP(100) and InP(311)B substrates: Theory and experiment," Phys. Rev. B 74, 035312 (2006).

[Cornet06a] C. Cornet, M. Hayne, P. Caroff, C. Levallois, L. Joulaud, and E. Homeyer, "Increase od charge-carrier redistribution efficiency in a laterally organized superlattice of coupled quantum dots," Phys. Review B 74, 245315 (2006).

[Crowley12] M. T. Crowley, N. A. Naderi, H. Su, F. Grillot and L. F. Lester, "GaAs Based Quantum Dot Lasers," in *Semiconductors and Semimetals: Advances in Semiconductor Lasers*, 2012.

[D]

[Dagens05] B. Dagens, A. Markus, J. X. Chen, J. G. Provost, D. Make, O. Le Gouezziou, J. Landreau, A. Foire, and B. Thedrez "Gaint linewidth enhancement factor and purely frequency modulated emission from quantum dot laser," Electron. Lett. 41, 323 (2005).

[Dagens05] B. Dagens, A. Markus, J. X. Chen, J. G. Provost, D. Make, O. Le Gouezigou, J. Landreau, A. Fiore, and B. Thedrez, Gain linewidth enhancement factor and purely frequency modulated emission from quantum dot laser," Electron. Lett. 41, 323 (2005).

[Devaux93] F. Devaux, Y. Sorel, and J. F. Kerdiles, "Simple measurement of fiber dispersion and of chirp parameter of intensity modulated light emitter," J. Lightwave Tech. 11, 1937 (1993).

[Dery05] H. Dery and G. Eisenstein, "The impact of energy band diagram and inhomogeneous broadening on the optical differential gain in nanostructure lasers," IEEE J. Quantum Electron. 41, 26 (2005).

[Dhooge03] A. Dhooge, W. Govaerts, and Y. A. Kuznetsov, "MATCONT: A MATLAB package for numerical bifurcation analysis of ODEs," ACM Transactions on Mathematical Software 29, 141 (2003).

[Dingle76] R. Dingle and C. H. Henry, "Quantum Effects in Heterostructure Lasers," U.S. Patent No. 3,982,207, filed on March 7, 1975, issued Sept. 21, 1976.

[Dong14] P. Dong, Y.-K. Cheng, G.-H. Duan, and D. T. Neilson, "Silicon photonic devices and integrated circuits," Nanophotonics 3, 215 (2014).

[Donovan01] K. Donovan, P. Harrison, and R. W. Kelsall, "Self-consistent solutions to the intersubband rate equations in quantum cascade lasers: Analysis of a GaAs/$Al_xGa_{1-x}As$ device," J. Appl. Phys., 89, 3084 (2001).

[D'Ottavi94] A. D'Ottavi, E. Iannone, A. Mecozzi, S. Scotti, P. Spano, J. Landreau, A. Ougazzaden, and J. C. Bouley, "Investigation of carrier heating and spectral hole burning in semiconductor amplifiers by highly nondegenerate four-wave mixing," Appl. Phys. Lett. 64, 2492 (1994).

[Duan87] G. Duan, P. Gallion, and G. Gebarge, "Analysis of frequency chirping of semiconductot lasers in presence of optical feedback," Opt. Lett. 12, 800 (1987).

[Duan90] G. H. Duan, P. Gallion, and G. Debarge, “Analysis of the phase-amplitude coupling factor and spectral linewidth of distributed feedback and composite-cavity semiconductor lasers,” IEEE J. Quantum Electron. 26, 32 (1990).
[Duan92] G.-H. Duan, P. Gallion, and G. P. Agrawal, “Effective nonlinear gain in semiconductor lasers,” IEEE Photon. Tech. Lett. 4, 218 (1992).
[Duan14] G.-H. Duan, C. Jany, A. L. Liepvre *et al.*, “Hybrid III-V on silicon lasers for photonic integrated circuits on silicon,” IEEE J. Sel. Top. Quantum Electron. 20, 6100213 (2014).

[E]

[Elias09] G. Elias, A. Létoublon, R. Piron, I. Alghoraibi, A. Nakkar, N. Chevalier, K. Tavernier, A. Le Corre, N. Bertru and S. Loualiche, “Achievement of high density InAs/GaInAsP quantum dots on misoriented InP(001) substrates emitting at 1.55 µm, ” Jpn. J. Appl. Phys. 48, 070204 (2009).
[Erasme14] D. Erasme, T. Anfray, M. E. Chaibi, K. Kechaou, J. Petit, G. Aubin, K. Merghem, C. Kazmierski, J-G. Provost, P. Chanclou, and C. Aupetit-Berthelemot, “The dual-electroabsorption modulated laser, a flexible solution for amplified and dispersion uncompensated networks over standard fiber,” J. Lightwave Tech. 32, 4068 (2014).
[Erneux13] T. Erneux, V. Kovanis, and A. Gavrielides, “Nonlinear dynamics of an injected quantum cascade laser,” Phys. Rev. E 88, 032907 (2013).
[Esaki70] L. Esaki and R. Tsu, “Superlattice and negative differential conductivity in semiconductors,” IBM J. Res. Develop. 14, 61 (1970).
[Even04] J. Even and S. Loualiche, “Exact analytical solutions describing quantum dot, ring and wire wavefunctions,” J. Phys. A: Math. Gen. 37, L289 (2004).
[Even08] J. Even, F. Dré, C. Cornet, and L. Pedesseau, “Semianalytical model for simulation of electronic properties of narrow-gap strained semiconductor quantum nanostructures,” Phys. Rev. B 77, 085305 (2008).

[F]

[Faist94] J. Faist, F. Capasso, D. L. Sivco, C. Sirtori, A. L. Hutchinson, and A. Y. Cho, “Quanutm cascade laser,” Science 264, 553 (1994).
[Faist95] J. Faist, F. Capasso, C. Sirtori, D. L. Sivco, A. L. Hutchinson, and A. Y. Cho, “Vertical transition quantum cascade laser with Bragg confined excited-state,” Appl. Phys. Lett. 66, 538 (1995).
[Faist96] J. Faist, F. Capasso, C. Sirtori, D. L. Sivco, J. N. Baillargeon, A. L. Hutchinson, S. G. Chu, and A. Y. Cho, “High power mid-infrared quantum cascade lasers operating above room temperature,” Appl. Phys. Lett. 68, 3680 (1996).
[Faist96a] J. Faist, F. Capasso, C. Sirtori, D. L. Sivco, A. L. Hutchinson, and A. Y. Cho, “Rom temperature mid-infrared quantum cascade lasers,” Electron. Lett. 32, 560 (1996).
[Faist98] J. Faist, A. Tredicucci, F. Capasso, C. Sirtori, D. L. Sivco, J. N. Baillargeon, A. L. Hutchinson, and A. Y. Cho, “High-power continuous-wave quantum cascade lasers,” IEEE J. Quantum Electron. 34, 336 (1998).
[Faist01] J. Faist, M. Beck, T. Aellen, and E. Gini, “Quantum-cascade lasers based on a bound-to-continuum transition,” Appl. Phys. Lett. 78, 147-149 (2001).

[Faist04] J. Faist, L. Ajili, G. Scalari, M. Giovannini, M. Beck, M. Rochat, H. E. Beere, A. G. Davies, E. H. Linfield, and D. A. Ritchie, "Terahertz quantum cascade laser," Phil. Trans. R. Soc. Lond. A 362, 215 (2004).

[Fathpour05] S. Fathpour, Z. Mi, and P. Bhattacharya, "High-speed quantum dot lasers," J. Phys. D: Appl. Phys. 38, 2103 (2005).

[Ferguson02] B. Ferguson, S. H. Wang, D. Gray, D. Abbot, and X. C. Zhang, "T-ray computed tomography," Opt. Lett. 27, 1312 (2002).

[Ferreira99] P. Ferreira and G. Bastard, "Phonon assisted capture and intra-dot Auger relaxation in quantum dots," Appl. Phys. Lett. 74, 2818 (1999).

[Flayyih13] A. H. Flayyih and A. H. Al-Khursan, "Four-wave mixing in quantum dot semiconductor optical amplifiers," Appl. Opt. 52, 3156-3165 (2013).

[Fuchs10] F. Fuchs, S. Hugger, M. Kinzer, R. Aidam, W. Bronner, R. Loesch, Q. Yang, "Imaging standoff detection of explosives using widely tunable midinfrared quantum cascade lasers," Optic. Engineering 49, 111127 (2010).

[G]

[Garcie97] J. M. Garcie, G. Medeiros-Ribeiro, K. Schmidt, T. Ngo, J. L. Feng , A. Lorke, J. Kotthaus, and M. Petroff, "Intermixing and shape changes during the formation of InAs Self-assembled quantum dots," Appl. Phys. Lett. 71, 2014 (1997).

[Gensty05] T. Gensty and W. Elsaber "Semiclassical model for relative intensity noise of intersubband quantum cascade lasers," Opt. Comm. 256, 171 (2005).

[Geraghty97] D. F. Geraghty, R. B. Lee, M. Verdiell, M. Ziari, A. Mathur, and K. J. Vahala, "Wavelength conversion for WDM communication systems using four-wave mixing in semiconductor optical amplifiers," IEEE J. Sel. Top. Quantum. Electron. 3, 1146 (1997).

[Gerhard08] S. Gerhard, C. Schilling, F. Gerschutz, M. Fischer, J. Koeth, I. Krestnikov, A. Kovsh, M. Kamp, S. Hofling, and A. Forchel, "Frequency-dependent linewidth enhancement factor of quantum-dot lasers," IEEE Photon. Tech. Lett. 20, 1736 (2008).

[Gilfert11] C. Gilfert, V. Ivanov, N. Oehl, M. Yacob, and J. Reithmaier, "High gain 1.55 μm diode lasers based on InAs quantum dot like active regions," Appl. Phys. Lett. 98, 201102 (2011).

[Gioannini06] M. Gioannini, A. Sevega, and I. Montrosset, "Simulations of differential gain and linewidth enhancement factor of quantum dot semiconductor lasers," Optic. Quantum Electron. 38, 381 (2006).

[Gioannini07] M. Gioannini and I. Montrosset, "Numerical analysis of the frequency chirp in quantum-dot semiconductor lasers," IEEE J. Quantum Electron. 43, 941 (2007).

[Gioannini11] M. Gioannini and M. Rossetti, "Time-domain traveling wave model of quantum dot DFB lasers," IEEE J. Sel. Top. Quantum Electron. 17, 1318 (2011).

[Gioannini12] M. Gioannini, "Ground-state power quenching in two-state lasing quantum dot lasers," J. Appl. Phys. 111, 043108 (2012).

[Gmachl99] C. Gmachl, F. Capasso, A. Tredicucci, D. L. Sivco, R. Kohler, A. L. Hutchinson, and A. Y. Cho, "Dependence of the device performance on the number of stages in quantum-cascade lasers," IEEE J. Sel. Top. Quantum Electron. 5, 808 (1999).

[Gong08] M. Gong, K. Duan, C. F. Li, R. Magri, A. Narvaez, and L. He, "Electronic structure of self-assembled InAs/InP quantum dots: Comparison with self-assembled InAs/GaAs quantum dots," Phys. Rev. B 77, 045326 (2008).

[Gready11] D. Gready and G. Eisenstein, "Effects of homogeneous and Inhomogeneous broadening on the dynamics of tunneling injection quantum dot lasers," IEEE J. Quantum Electron. 47, 944 (2011).

[Gready12] D. Gready, G. Eisenstein, C. Gilfert, V. Ivanov, and J. P. Reithmaier, "High-speed low-noise InAs/InAlGaAs/InP 1.55-μm quantum-dot lasers" IEEE Photon. Tech. Lett. 24, 809 (2012).

[Gready12a] D. Gready, G. Eisenstein, C. Gilfert, V. Ivanov, J. P. Reithmaier, D. Arsenijevic, H. Schmeckebier, M. Stubenrauch, and D. Bimberg, "Relation between small and large signal modulation capabilities in highly nonlinear quantum dot lasers for optical telecommunication," *IEEE Photonics* C*onference (IPC)*, 48, 2012.

[Gready13] D. Gready, G. Eisenstein, M. Gioannini, I. Montrosset, D. Arsenijevic, H. Schmeckebier, M. Stubenrauch, and D. Bimberg, "On the relationship between small and large signal modulation capabilities in highly nonlinear quantum dot lasers," Appl. Phys. Lett. 102, 101107 (2013).

[Gready14] D. Gready, G. Eisenstein, V. Ivanov, C. Gilfert, F. Schnabel, A. Rippien, J. P. Reithmaier, and C. Bornholdt, "High speed 1.55 μm InAs/InAlGaAs/InP quantum dot laser," IEEE Photon. Tech. Lett. 26, 11 (2014).

[Grillot08] F. Grillot, B. Dagens, J. G. Provost, H. Su, and L. F. Lester, "Gain compression and above-threshold linewidth enhancement factor in 1.3 μm InAs-GaAs quantum-dot lasers," IEEE J. Quantum Electron. 44, 946 (2008).

[Grillot09] F. Grillot, K. Veselinov, M. Gioannini, I. Montrosset, J. Even, R. Piron, E. Homeyer, and S. Loualiche, "Spectral analysis of 1.55 μm InAs–InP(113)B quantum-dot lasers based on a multipopulation rate equations model," IEEE J. Quantum Electron. 45, 872 (2009).

[Grillot10] F. Grillot, *Diodes Lasers pour les Systèmes de Communications Optiques*, Editions Universitaires Europeennes, 2010.

[Grillot11] F. Grillot, N. A. Naderi, J. B. Wright, R. Raghunathan, M. T. Crowley, and L. F. Lester, "A dual-mode quantum dot laser operating in the excited state," Appl. Phys. Lett. 99, 1110 (2011).

[H]

[Haegeman02] B. Haegeman, K. Engelborghs, D. Roose, D. Pierous, and T. Erneux, "Stability and rupture of bifurcation bridges in semiconductor lasers subject to optical feedback," Phys. Rev. E 66, 046216 (2002).

[Hakki75] B. W. Hakki, and T. L. Paoli, "Gain spectra in GaAs double-heterostucture injection lasers," J. Appl. Phys. 46, 1299 (1975).

[Han00] P. Y. Han, G. C. Cho, and X. C. Zhang, "Time-domain transillumination of biological tissues with terahertz pulses," Opt. Lett. 25, 242 (2000).

[Hangauer14] A. Hangauer and G. Wysocki, "Gain compression in a quantum cascade laser: Connection between high frequency tuning and bending of LI curve," JW2A.76, CLEO, 2014.

[Harder83] C. Harder, K. Vahala, and A. Yariv, "Measurement of the linewidth enhancement factor α of semiconductor lasers," Appl. Phys. Lett. 42, 328 (1983).

[Harder05] M. K. Harder, "A simplified analysis of direct intensity modulation of quantum cascade lasers," IEEE J. Quantum Electron. 41, 1349 (2005).

[Haug98] H. Haug and S. W. Koch, *Quantum Theory of the Optical and Electronic Properties of Semiconductors,* World Scientific, Singapore, 1998.

[Hegarty05] S. P. Hegarty, B. Corbett, J. G. McInerney, and G. Huyet, "Free-carrier effect on index change in 1.3 µm quantum-dot lasers," Electron. Lett. 41, 416 (2005)

[Hein07] S. Hein, V. von Hinten, W. Kaiser, S. Hofling, and A. Forchel, "Dynamic properties of 1.5 µm quantum dash lasers on (100) InP," Electron. Lett. 43, 1093 (2007).

[Henry82] C. H. Henry, "Theory of the linewidth of semiconductor lasers," IEEE J. Quantum Electron. QE-18, 259 (1982).

[Hofstetter01] D. Hofstetter, M. Beck, T. Aellen, J. Faist, U. Oesterle, M. Ilegems, E. Gini, and H. Melchior, "Continuous wave operation of a 9.3 µm quantum cascade laser on a Peltier cooler," Appl. Phys. Lett. 78, 1964 (2001).

[Homeyer07] E. Homeyer, R. Piron, F. Grillot, O. Dehaese, K. Tavernier, E. Macé, A. Le Corre, and S. Loualiche, "First demonstration of a 1.52 µm RT InAs/InP (311)B laser with an active zone based on a single QD layer," Semicond. Sci. Technol. 22, 827 (2007).

[Homeyer07a] E. Homeyer, R. Piron, F. Grillot, O. Dehaese, K. Tavernier, and E. Macé, "Demonstration of a low threshold current in 1.54 µm InAs/InP (311)B quantum dot laser with reduced quantum dot stacks," Jpn. J. Appl. Phys. 46, 6903 (2007).

[Hu95] B. B. Hu and M. C. Nuss, "Imaging with terahertz waves," Opt. Lett. 20, 1716 (1995).

[Huffaker98] D. L. Huffaker, G. Park, Z. Zou, O. B. Shchekin, and D. G. Deppe, "1.3 µm room-temperature GaAs-based quantum-dot laser," Appl. Phys. Lett. 73, 2564 (1998).

[Hui09] R. Hui and M. O'Sullivan, *Fiber Optic Measurement Techniques*, Elsevier, 2009.

[Hwang04] S. K. Hwang, J. M. Liu, and J. K. White, "Characteristics of period-one oscillations in semiconductor lasers subject to optical injection," IEEE J. Sel. Top. Quantum Electron. 10, 974 (2004).

[I]

[Ignatiev00] I. V. Ignatiev, I. E. Kozin, S. V. Nair, H. W. Ren, S. Sugou, and Y. Masumoto, "Carrier relaxation dynamics in InP quantum dots studied by artificial control of nonradiative losses," Phys. Rev. B 61, 15633 (2000).

[Iwashita82] K. Iwashita and K. Nakagawa, "Suppression of mode partition noise by laser diode light injection," IEEE Trans. Microwave Theory Tech. 30, 1657 (1982).

[J]

[Joshi14] S. Joshi, N. Chimot, L. A. Neto, A. Accard, and J. G. Provost, "Quantum dahs based directly modulated lasers for long-reach acces networks," Electron. Lett. 50, 534 (2014).

[Joshi14a] S. Joshi, N. Chimot, A. Ramdane, and F. Lelarge, "On the nature of the linewidth enhancement factor in p-doped quantum dash based lasers," Appl. Phys. Lett. 105, 241117 (2014).

[Joyce02] P. B. Joyce, T. J. Krzyzewski, P. H. Steans, G. R. Bell, J. H. Neave, and T. S. Jones, "Variations in critical coverage for InAs/GaAs quantum dot formation in bilayer structures," J. Cryst. Growth 244, 39 (2002).

[Juretzka15] C. Juretzka, H. Simos, A. Bogris, D. Syvridis, W. Elsäßer, and M. Carras, "Intensity noise properties of mid-infrared injection locked quantum cascade lasers: II. Experiments," IEEE J. Quantum Electron. 51, 2300208 (2015).

[K]

[Kaiser05] W. Kaiser, K. Mathwig, S. Deubert, J. P. Reithmaier, F. Forchel, O. Parillaud, M. Krakowski, D. Hadass, V. Mikhelashvili, and G. Eisenstein, "Static and dynamic properties of laterally coupled DFB lasers based on InAs/InP Qdash structures," Electron. Lett. 41, (2005).

[Kazarinov71] R. F. Kazarinov and R. A. Suris, "Possibility of the amplification of electromagnetic waves in a semiconductor with a superlattice," Sov. Phys. Semicond. 5, 707 (1971).

[Kechaou12] K. Kechaou, T. Anfray, K. Merghem, C. Aupetit-Berthelemot, G. Aubin, C. Kazmierski, C. Jany, P. Chanclou, and D. Erasme, "Improved NRZ transmission distance at 20 Gbit/s using dual electroabsoprtion modulated laser," Electron. Lett. 48, 335 (2012)

[Kechaou12a] K. Kechaou, F. Grillot, J. G. Provost, B. Thedrez, and D. Erasme, "Self-injected semiconductor distributed feedback lasers for frequency chirp stabilization," Opt. Express 20, 26062 (2012).

[Kelleher12] B. Kelleher, S. P. Hegarty, and G. Huyet, "Optically injected lasers: The transition from class B to class A lasers," Phys. Review E 86, 066206 (2012).

[Khan14] M. Z. M. Khan, T. K. Ng, and B. S. Ooi, "Self-assembled InAs/InP quantum dots and quantum dashes: Material structures and devices," Progress in Quantum Electronics (2014).

[Kikuchi92] K. Kikuchi, M. Kakui, C. E. Zah, and T. P. Lee, "Observation of highly nondegenerate four-wave mixing in 1.5 μm traveling-wave semiconductor optical amplifiers and estimation of nonlinear gain coefficient," IEEE J. Quantum Electron. 28, 151 (1992).

[Kim96] A. D'Ottavi, F. Martelli, P. Spano, A. Mecozzi, S. Scotti, R. D'Ara, J. Eckner, and G. Guekos,"Very high efficiency four-wave mixing in a single semiconductor traveling wave amplifier," Appl. Phys. Lett. 68, 2186 (1996).

[Kim04] J. S. Kim, J. H. Lee, S. U. Hong, W. S. Han, H. S. Kwack, and C. W. Lee, "Long-wavelength laser based on self-assembled InAs quantum dots in InAlGaAs on InP(001)," Appl. Phys. Lett. 85, 1033 (2004).

[Kim04a] J. S. Kim, J. H. Lee, S. U. Hong, W. S. Han, H. S. Kwack, and C. W. Lee, "Room-temperature operation of InP-based quantum dot laser," IEEE Photon. Tech. Lett. 16, 1607 (2004).

[Kim07] H. J. Kim, H. J. Song, and J. I. Song, "All-optical frequency up-conversion technique using four-wave mixing in semiconductor optical amplifiers for radio-over-fiber applications," Microwave Symposium. IEEE/MTT-S International, 67, 2007.

[Kim12] H. J. Kim and J. I. Song, "All-optical frequency down conversion technique utilizing a four-wave mixing effect in a single semiconductor optical amplifier for wavelength division multiplexing radio-over-fiber applications," Opt. Express 20, 8047 (2012).

[Kirstaedter94] N. Kirstaedter, N. N. Ledentsov, M. Grundmann, D. Bimberg, V. M. Ustinov, S. S. Ruvimov, M. V. Maximov, P. S. Kop'ev, and Zh. I. Alferov, "Low threshold, large T_0 injection laser emission from (InGa)As quantum dots," Electron. Lett. 30, 1416 (1994).

[Klaime13] K. Klaime, C. Clo, R. Piron, C. Paranthoen, D. Thiam, and T. Batte, "23 and 39 GHz low phase noise monosection InAs/InP (113)B quantum dots mode-locked lasers," Opt. Express 21, 29000 (2013).

[Klotzkin14] D. J. Klotzkin, *Introduction to Semiconductor Lasers for Optical Communications*, Springer, 2014.

[Koch84] T. L. Koch and J. E. Bowers, "Nature of wavelength chirping in directly modulated semiconductor lasers," Electron. Lett. 20, 1038 (1984).

[Kohler02] R. Kohler, A. Tredicucci, F. Beltram, H. E. Beere, E. H. Linfield, A. G. Davies, D. A. Ritchie, R. C. Iotti, and F. Rossi, "Terahertz semiconductor-heterostructure laser," Nature 417, 156 (2002).

[Koltchanov96] I. Koltchanov, S. Kindt, K. Petermann, S. Diez, R. Ludwig, R. Schnabel, and H. G. Weber, "Analytical theory of terahertz four-wave mixing in semiconductor-laser amplifiers," Appl. Phys. Lett. 68, 2787 (1996).

[Koltchanov08] F. Grillot, B. Dagens, J. G. Provost, H. Su, and L. F. Lester, "Gain compression and above-threshold linewidth enhancement factor in 1.3 μm InAs-GaAs quantum-dot lasers," IEEE J. Quantum. Electron. 44, 946 (2008).

[Kotani09] J. Kotani, P. J. van Veldhoven, T. de Vries, B. Smalbrugge, E. A. J. M. Bente, M. K. Smit, and R. Notzel, "First demonstration of single-layer InAs/InP (100) quantum-dot laser: continuous wave, room temperature, ground state," Electron. Lett. 45, 1317 (2009).

[Krebs01] R. Krebs, F. Klopf, S. Rennon, J.P. Reithmaier, and A. Forchel, "High frequency characteristics of InAs/ GalnAs quantum dot distributed feedback lasers emitting at 1.3 μm," Electron. Lett. 37, 1223 (2001).

[Kroemer57] H. Kroemer, "Theory of a wide-gap emitter for transistors," Proc. IRE 45, 1535 (1957).

[Kumazaki08] N. Kumazaki, Y. Takagi, M. Ishihara, K. Kasahara, A. Sugiyama, N. Akikusa, and T. Edamura, "Detuning characteristics of the linewidth enhancement factor of a midinfrared quantum cascade laser," Appl. Phys. Lett. 92, 121104 (2008).

[Kuntz02] M. Kuntz, N. N. Ledentsov, D. Bimberg, A. R. Kovsh, and V. M. Ustinov, "Spectrotemporal response of 1.3 μm quantum-dot lasers," Appl. Phys. Lett. 81, 3846 (2002).

[Kuntz06] M. Kuntz, *Modulated InGaAs/GaAs Quantum Dot Lasers*, Ph. D thesis (Berlin, 2006).

[L]

[Lam94] Y. Lam and J. Singh, "Monte Carlo simulation of gain compression effects in GRINSCH quantum well laser structures," IEEE J. Quantum Electron. 30, 2435 (1994).

[Lang82] R. Lang, "Injection locking properties of a semiconductor laser," IEEE J. Quantum Electron. QE-18, 976 (1982).

[Lau08] E. K. Lau, L. J. Wong, X. Zhao, Y. K. Chen, C. J. Chang-Hasnain, and M. C. Wu, "Bandwidth enhancement by master modulation of optical injection-locked lasers," J. Lightwave Tech. 26, 2584 (2008).

[Lau09] E. K. Lau, L. J. Wong, and M. C. Wu, "Enhanced modulation characteristics of optical injection-locked lasers: A tutorial," IEEE J. Sel. Top. Quantum. Electron. 15, 618 (2009).

[Ledentsov96] N. N. Ledentsov, V. A. Shchukin, M. Grundmann, N. Kirstaedter, J. Bohrer, O. G. Schmidt, D. Bimberg, V. M. Ustinov, A. Yu. Egorov, A. E. Zhukov, P. S. Kop'ev, S. V. Zaitsev, N. Yu. Gordeev, and Zh. I. Alferov, "Direct formation of vertically coupled quatum dots in Stranski-Krastanow growth," Phys. Rev. B 54, 8743 (1996).

[Lee11] C. S. Lee, P. Bhattacharya, T. Frost, and W. Guo, "Characteristics of a high speed 1.22 μm tunnel injection p-doped quantum dot excited state laser," Appl. Phys. Lett. 98, 011103 (2011).

[Lelarge05] F. Lelarge, B. Rousseau, B. Dagens, F. Poingt, F. Pommereau, and A. Accard, "Room temperature continuous-wave operation of buried ridge stripe lasers using InAs-InP(100) quantum dots as active core," IEEE Photon. Tech. Lett. 17, 1369 (2005).

[Lelarge07] F. Lelarge, B. Dagens, J. Renaudier, R. Brenot, A. Accard, F. van Dijk, D. Make, O. Le Gouezigou, J. Provost, F. Poingt, J. Landreau, O. Drisse, E. Derouin, B. Rousseau, F. Pommereau, G.-H. Duan, "Recent advances on InAs/InP quantum dash based semiconductor lasers and optical amplifiers operating at 1.55 μm," IEEE J. Sel. Top. Quantum Electron. 13, 111 (2007).

[Li93] L. L. Li and K. Petermann, "Small-signal analysis of THz optical-frequency conversion in an injection-locked semiconductor laser," IEEE J. Quantum. Electron. 29, 2988 (1993).

[Li00] Y. F. Li, F. Q. Liu, B. Xu, X. L. Ye, D. Ding, Z. Z. Su, W. H. Jiang, H. Y. Liu, Y. C. Zhang, Z. G. Wang, "Two-dimensional ordering of self-assembled InAs quantum dots grown on (311)B InP substrate," J. Cryst. Growth 219, 17 (2000).

[Li00a] H. Li, G. T. Liu, P. M. Varangis, T. C. Newell, A. Stintz, B. Fuchs, K. J. Malloy, and L. F. Lester, "150-nm tuning range in a grating-coupled external cavity quantum-dot laser," IEEE Photon. Technol. Lett. 12, 759, (2000).

[Li12] X. Z. Li and S. C. Chan, "Random bit generation using an optically injected semiconductor laser in chaos with oversampling," Optics Lett. 37, 2163 (2012).

[Li13] S. G. Li, Q. Gong, C. F. Cao, X. Z. Wang, J. Y. Yan, Y. Wang, and H. L. Wang, "The developments of InP-based quantum dot lasers," Infrared Physics & Technology 60, 216 (2013).

[Liang10] D. Liang and J. E. Bowers, "Recent progress in lasers on silicon," Nature Photonics 4, 511-517 (2010).

[Lin84] C. Lin and F. Mengel, "Reduction of frequency chirping and dynamic linewidth in high-speed directly modulated semiconductor lasers by injection locking," Electron. Lett. 20, 1073 (1984).

[Lin12] G. Lin, P. Y. Su, and H. C. Cheng, "Low threshold current and widely tunable external cavity lasers with chirped multilayer InAs/InGaAs/GaAs quantum-dot structure," Opt. Express 20, 3941 (2012).

[Lin13] C. H. Lin and F. Y. Lin, "Four-wave mixing analysis on injection-locked quantum dot semiconductor lasers," Opt. Express 21, 21242 (2013).

[Lingnau12] B. Lingnau, K. Lüdge, W. W. Chow, and E. Schöll, "Failure of the α factor in describing dynamical instabilities and chaos in quantum-dot lasers," Phys. Rev. E 86, 065201(R) (2012).

[Lingnau12a] B. Lingnau, K. Lüdge, W. W. Chow, and E. Schöll, "Influencing modulation properties of quantum-dot semiconductor lasers by carrier lifetime engineering," Appl. Phys. Lett. 101, 131107 (2012).

[Lingnau13] B. Lingnau, W. W. Chow, E. Schöll, and K. Lüdge, "Feedback and injection locking instabilities in quantum-dot lasers: A microscopically based bifurcation analysis," New J. Phys. 15, 093031 (2013).

[Lingau14] B. Lingnau, W. W. Chow, and K. Lüdge,"Amplitude-phase coupling and chirp in quantum-dot lasers: Influence of charge carrier scattering dynamics," Opt. Express 22, 4867 (2014).

[Liu97] J. M. Liu, H. F. Chen, X. J. Meng, and T. B. Simpson, "Modulation bandwidth, noise, and stability of a semiconductor laser subject to strong injection locking," IEEE Photon. Tech. Lett. 9, 1325 (1997).

[Liu99] G. T. Liu, A. Stintz, H. Li, K. J. Malloy, and L. F. Lester, "Extremely low room-temperature threshold current density diode lasers using InAs dots in InGaAs quantum well," Electron. Lett. 35, 1163 (1999).

[Liu00] H. C. Liu and F. Capasso, *Intersubband Transitions in Quantum Wells: Physics and Device Applications I,* Academic Press, San Diego, CA, 2000.

[Liu04] H. Y. Liu, K. M. Groom, D. T. D. Childs, D. J. Robbins, T. J. Badcock, M. Hopkinson, D. J. Mowbray, and M. S. Skolnick, "1.3 μm InAs/GaAs multilayer quantum-dot laser with extremely low room temperature threshold current density," Electron. Lett. 40, 1412 (2004).

[Liu13] T. Liu, K. E. Lee, and Q. J. Wang, “Importance of the microscopic effects on the linewidth enhancement factor of quantum cascade lasers,” Opt. Express 21, 27804 (2013).
[Lodi94] A. Lodi, S. Donati, and M. Manna, “Chaos and locking in a semiconductor laser due to external injection,” IEEE J. Quantum Electron. 30, 1537 (1994).
[Loffler01] T. Loffler, T. Bauer, K.J. Siebert, H.G. Roskos, A. Fitzgerald, and S. Czasch, “Terahertz dark-field imaging of biomedical tissue,” Opt. Express 9, 616 (2001).
[Lorke06] M. Lorke, T. R. Nielsen, J. Seebeck, P. Gartner, and F. Jahnke, “Influence of carrier-carrier and carrier-phonon correlations on optical absorption and gain in quantum-dot systems,” Phys. Rev. B 73, 085324 (2006).
[Lu02] T. Akiyama, H. Kuwatsuka, N. Hatori, Y. Nakata, H. Ebe, and M. Sugawara, “Symmetric highly efficient (~0 dB) wavelength conversion based on four-wave mixing in quantum dot optical amplifiers,” IEEE Photon. Technol. Lett. 14, 1139 (2002).
[Lu06] Z. G. Lu, J. R. Liu, S. Raymond, P. J. Poole, P. J. Barrios, D. Poitras, F. G. Sun, G. Pakulski, P. J. Bock, and T. Hall, “Highly efficient non-degenerate four-wave mixing process in InAs/InGaAsP quantum dots,” Electron. Lett. 42, 1112 (2006).
[Lüdge09] K. Lüdge and E. Schöll, “Quantum-dot lasers--- Desynchronized nonlinear dynamics of electrons and holes,” IEEE J. Quantum. Electron. 45, 1396 (2009).
[Lüdge10] K. Lüdge, R. Aust, G. Fiol, M. Stubenrauch, D. Arsenijevi´c, D. Bimberg, and E. Schöll, “Large signal response of semiconductor quantum-dot lasers,” IEEE J. Quantum Electron. 46, 1755 –1762 (2010).
[Lüdge11] K. Lüdge, and H. G. Schuster, *Nonlinear Laser Dynamics: From Quantum Dots to Cryptography*, New York: Wiley, 2011.
[Lv10] X. Q. Lv, P. Jin, W. Y. Wang, and Z. G. Wang, “Broadband external cavity tunable quantum dot lasers with low injection current density,” Opt. Express 18, 8916 (2010).

[M]

[Magnusdottir03] I. Magnusdottir, S. Bischoff, A. V. Uskov, and J. Mork, “Geometry dependence of Auger carrier capture rates into cone-shaped self-assembled quantum dots,” Phys. Rev. B 67, 205326 (2003).
[Maineult10] W. Maineult, L. ding, P. Gellie, P. Filloux, and C. Sirtori, “Microwave modulation of terahertz quantum cascade lasers: a transmission-line approach,” Appl. Phys. Lett. 96, 021108 (2010).
[Majumdar08] A. K. Majumdar and J. C. Ricklin, *Free Space Laser Communication: Principles and Advances*, Springer (2008).
[Maksimov04] M.V. Maksimov, Y. M. Shernyakov, N. V. Kryzhanovskaya, A. G. Gladyshev, Y. G. Musikhin, N. N. Ledentsov, A. E. Zhukov, A. P. Vasilev, A. R. Kovsh, S. S. Mikhrin, E. S. Semenova, N. A. Maleev, E. V. Nikitina, V. M. Ustinov, and Z. I. Alferov, “High-power 1.5 μm InAs-InGaAs quantum dot lasers on GaAs substrates,” Semiconductors 38, 732 (2004).
[Malic06] E. Malic, K. J. Ahn, M. J. P. Bormann, P. Hövel, E. Schöll, A., Knorr, M. Kuntz, and D. Bimberg, “Theory of relaxation oscillations in semiconductor quantum dot lasers, ” Appl. Phys. Lett. 89, 101107 (2006).
[Manne06] J. Manne, O. Sukhorukov, W. Jäger, and J. Tulip, “Pulsed quantum cascade laser-based cavity ring-down spectroscopy for ammonia detection in breath,” Appl. Optics 45, 9230 (2006).

[Marcenac97] D. D. Marcenac, D. Nesset, A. E. Kelly, M. Brierly A. D. Elllis, D. G. Moodie, and C. W. Ford, "40 Gbit/s transmission over 406 km of NDSF using mid-span spectral inversion by four-wave mixing in a 2 mm long semiconductor optical amplifier," Electron. Lett. 33, 879 (1997).

[Marcinkevicius99] S. Marcinkevicius and R. Leon, "Carrier capture and escape in $In_xGa_{1-x}As$/GaAs quantum dots: Effects of intermixing," Phys. Rev. B 59, 4630 (1999).

[Markus03] A. Markus, J. X. Chen, O. Gauthier-Lafaye, J. G. Provost, C. Paranthoen, and A. Fiore, "Impact of intraband relaxation on the performance of a quantum-dot laser," IEEE J. Sel. Top. Quantum Electron. 9, 1308 (2003).

[Martinez08] A. Martinez, K. Merghem, S. Bouchoule, G. Moreau, A. Ramdane, J. G. Provost, F. Alexandre, F. Grillot, O. Dehaese, R. Piron, and S. Loualiche, "Dynamic properties of InAs/InP(311B) quantum dot Fabry-Perot lasers emitting at 1.52-μm," Appl. Phys. Lett. 93, 021101 (2008).

[Martini01] R. Martini, C. Gmachl, J. Falciglia, F. G. Curti, C. G. Bethea, F. Capasso, E. A. Whittaker, R. Paiella, A. Tredicucci, A. L. Hutchinson, D. L. Sivco, and A. Y. Cho, "High-speed modulation and free-space optical audio/video transmission using quantum cascade lasers," Electron. Lett. 37, 102 (2001).

[Massé07] N. F. Massé, E. Homeyer, A. R. Adams, S. J. Sweeney, Dehaese, O. R. Piron, F. Grillot, and S. Loualiche, "Temperature and pressure dependence of the recombination processes in 1.5μm InAs/InP (311)B quantum dot lasers, " Appl. Phys. Lett. 91, 131113 (2007).

[Maulini06] R. Maulini, *Broadly Tunable Mid-Infrared Quantum Cascade Lasers for Spectroscopic Applications,* Ph. D thesis, Neuchatel, 2006.

[Maximov04] M. V. Maximov and N. N. Ledentsov, "Quantum Dot Lasers", in *Dekker Encyclopedia of Nanoscience and Nanotechnology*, CRC Press, 3109 (2004).

[Melnik06] S. Melnik, G. Huyet, and A. V. Uskov, "The linewidth enhancement factor α of quantum dot semiconductor lasers," Opt. Express 14, 2950 (2006).

[Meng98] X. J. Meng, T. Chau, D. T. K. Tong, and M. C. Wu, "Suppression of second harmonic distortion in directly modulated distributed feedback lasers by external light injection," Electron. Lett. 34, 2040 (1998).

[Meng99] X. J. Meng, T. Chau, and M. C. Wu, "Improved intrinsic dynamic distortions in directly modulated semiconductor lasers by optical injection locking," IEEE Trans. Microw. Theory Tech. 47, 1172 (1999).

[Meng12] B. Meng and Q. J. Wang, "Theoretical investigation of injection-locked high modulation bandwidth quantum cascade lasers," Optics Express 20, 1450 (2012).

[Mi05] Z. Mi, P. Bhattacharya and S. Fathpour, "High-speed 1.3 μm tunnel injection quantum-dot lasers," Appl. Phys. Lett. 86, 153109 (2005).

[Mi06] Z. Mi and P. Bhattacharya, "DC and dynamic characteristics of p-doped and tunnel injection 1.65 μm InAs quantum-dash lasers grown on InP(001)," IEEE J. Quantum Electron. 42, 1224 (2006).

[Mi07] Z. Mi and P. Bhattacharya, "Analysis of the linewidth-enhancement factor of long-wavelength tunnel-injection quantum-dot lasers," IEEE J. Quantum Electron. 43, 363 (2007).

[Mikhrin05] S. S. Mikhrin, A. R. Kovsh, I. L. Krestnikov, A. V. Kozhukhov, D. A. Livshits, N. N. Ledentsov, Yu M. Shernyakov, I. I. Novikov, M. V. Maximov, V. M. Ustinov, and Zh. I. Alferov, "High power temperature-insensitive 1.3 μm InAs/InGaAs/GaAs quantum dot lasers," Semicond. Sci. Technol. 20, 340 (2005).

[Miska02] P. Miska, C. paranthoën, J. Even, O. Dehaese, N. Bertru, SL Loualiche, M. Senes, and X. Marie, "Optical properties of double cap grown InAs/InP quantum dots emitting at 1.55 μm," Semicond. Sci. Technol. 17, L63 (2002).

[Miska03] P. Miska, J. Even, C. Paranthoën, O. Dehaese, H. Folliot, S. Loualiche, M. Senes, and X. Marie, "Optical properties and carrier dynamics of InAs/InP(113)B quantum dots emitting between 1.3 and 1.55 μm for laser applications," Physica E 17, 56 (2003).

[Miska04] P. Miska, J. Even, C. Platz, B. Salem, and T. Benyattou, "Experimental and theoretical investigation of carrier confinement in InAs quantum dashes grown on InP(001)," J. Appl. Phys. 95, 1074 (2004).

[Miska08] P. Miska, J. Even, O. Dehaese, and X. Marie, "Carrier relaxation dynamics in InAs/InP quantum dots," Appl. Phys. Lett. 92, 191103 (2008).

[Mitrofanov01] O. Mitrofanov, M. Lee, J. W. Hsu, I. Brener, R. Harel, J. F. Federici, J. D. Wynn, L. N. Pfeiffer, and K. W. West, "Collection-mode near-field imaging with 0.5 THz pulses," IEEE J. Select. Topics Quantum Electron. 7, 600 (2001).

[Molina06] J. Molina, H. H. Nilsson, J. Z. Zhang, and I. Galbraith, Linewidth enhancement factor of quantum-dot optical amplifiers, IEEE J. Quantum Electron. 42, 986 (2006).

[Mollet14] O. Mollet, A. Martinez, K. Merghem, S. Joshi, J.-G. Provost, F. Lelarge, and A. Ramdane, "Dynamic characteristics of undoped and p-doped Fabry-Perot InAs/InP quantum dash based ridge waveguide lasers for access/metro networks," Appl. Phys. Lett. 105, 141113 (2014).

[Morthier91] G. Morthier, F. Libbrecht, K. David, P. Vankwikelberge, and R. G. Baets, "Theoretical investigation of the second-order harmonic distortion in the AM response of 1.55 F-P and DFB lasers," IEEE J. Quantum Electron. 27, 1990 (1991).

[Morton92] P. A. Morton, T. Tanbun-Ek, R. A. Logan, A. M. Sergent, P. F. Sciortino, and D. L. Coblentz, "Frequency response subtraction for simple measurement of intrinsic laser dynamic properties," IEEE Photon. Tech. Lett. 4, 133 (1992).

[Murakami03] A. Murakami, K. Kawashima, and K. Atsuki, "Cavity resonance shift and bandwidth enhancement in semiconductor lasers with strong light injection," IEEE J. Quantum Electron. 39, 1196 (2003).

[Murphy10] E. Murphy, "Enabling optical communication," Nature Photonics 4, 287 (2010).

[Mustafa99] N. Mustafa, L. Pesquera, C. Y. L. Cheung, and K. A. Shore, "Terahertz bandwidth prediction for amplitude modulation response of unipolar intersubband semiconductor lasers," IEEE Photon. Technol. Lett. 11, 527 (1999).

[N]

[Nagarajan92] R. Nagarajan, M. Ishikawa, T. Fukushima, R. Geels, and J. Bowers, "High speed quantum well lasers and carrier transport effects," IEEE J. Quantum Electron. 28, 1990 (1992).

[Naderi09] N. A. Naderi, M. Pochet, F. Grillot, N. B. Terry, V. Kovanis, and L. F. Lester, "Modeling the injection-locked behavior of a quantum dash semiconductor laser," IEEE J. Sel. Top. Quantum. Electron. 15, 563 (2009).

[Naderi10] N. A. Naderi, F. Grillot, K. Yang, J. B. Wright, A. Gin, and L. F. Lester, "Two-color multi-section quantum dot distributed feedback laser," Opt. Express 18, 27028 (2010).

[Naderi11] N. A. Naderi, *External Control of Semiconductor Nanostructure Lasers*, Ph. D thesis from University of New Mexico, 2011).

[Nelson87] D. F. Nelson, R. C. Miller, D. A. Kleinman, “Band nonparabolicity effects in semiconductor quantum wells,” Phys. Rev. B 35, 7770 (1987).
[Newell99] T. C. Newell, D. J. Bossert, A. Stintz, B. Fuchs, K. J. Malloy, and L. F. Lester, “Gain and linewidth enhancement factor in InAs quantum-dot laser diodes,” IEEE Photon. Tech. Lett. 11, 1527(1999).
[Nielsen04] T. R. Nielsen, P. Gartner, and F. Jahnke, “Many-body theory of carrier capture and relaxation in semiconductor quantum-dot lasers,” Phys. Rev. B 69, 235314 (2004).
[Ngo12] M. N. Ngo, H. T. Nguyen, C. Gosset, D. Erasme, Q. Deniel, and N. Genay, “Transmission performance of chirp-controlled signal emitted by electroabsorption modulator laser integrated with a semiconductor optical amplifier,” in Optical Fiber Communication Conference, US, 2012.
[Nilsson05] H. H. Nilsson, J. Z. Zhang, and I. Galbraith, “Homogeneous broadening in quantum dots due to Auger scattering with wetting layer carriers,” Phys. Rev. B 72, 205331 (2005).
[Nielsen10] D. Nielsen and S. L. Chuang, “Four-wave mixing and wavelength conversion in quantum dots,” Phys. Rev. B 81, 035305 (2010).
[Nishi98] K. Nishi, M. Yamada, T. Anan, A. Gomyo, and S. Sugou, “Long-wavelength lasing from InAs self-assembled quantum dots on (311)B InP,” Appl. Phys. Lett. 73, 526 (1998).
[Nozik08] A. J. Nozik, “Multiple exciton generation in semiconductor quantum dots,” Chem. Phys. Lett. 457, 3 (2008).

[O]

[O’Brien04] D. O’Brien, S. P. Hegarty, G. Huyet, and A. V. Uskov, “Sensitivity of quantum-dot semiconductor lasers to optical feedback,” Opt. Lett. 29, 1072 (2004).
[Ohnesorge96] B. Ohnesorge, M. Albrecht, J. Oshinowo, A. Forchel, and Y. Arakawa, “Rapid carrier relaxation in self-assembled InxGa1-xAs/GaAs quantum dots,” Phys. Rev. B 54, 11532 (1996).
[Oksanen03] J. Oksanen, and J. Tulkki, “Linewidth enhancement factor and chirp in quantum dot lasers,” J. Appl. Phys. 94, 1983 (2003).
[Onsemi14] *Understanding data eye diagram methodology for analyzing high speed digital signals*, ON semiconductor, USA, 2014.
[Oshinowo94] J. Oshinowo, M. Nishioka, S. Ishida, and Y. Arakawa, “Highly uniform InGaAs/GaAs quantum dots (15 nm) by metal organic chemical vapor deposition,” Appl. Phys. Lett. 65, 1421 (1994).
[Osinski87] M. Osiński and J. Buus, “Linewidth broadening factor in semiconductor lasers---An overview,” IEEE J. Quantum Electron. QE-23, 9 (1987).

[P]

[Paiella01] R. Paiella, R. Martini, F. Capasso, and C. Gmachl, “High-frequency modulation without the relaxation oscillation resonance in quantum cascade lasers,” Appl. Phys. Lett. 79, 2526 (2001).
[Panajotov12] K. Panajotov, M. Sciamanna, M. Arteaga, and H. Thienpont, “Optical feedback in vertical-cavity surface-emitting lasers,” IEEE J. Sel. Top. Quantum Electron. 19, 1700312 (2012).
[Paranthoën01] C. Paranthoën *et al*, “Height dispersion control of InAs/InP(113)B quantum dots emitting at 1.55 μm,” Appl. Phys. Lett. 78, 1751 (2001).

[Paranthoën03] C. Paranthoën, C. Platz, G. Moreau, N. Bertru, O. Dehaese, A. Le Corre, P. Miska, J. Even, H. Folliot, C. Labbe, J. C. Simon, and S. Loualiche, "Growth and optical characterizations on InAs quantum dots on InP substrate: toward sa 1.55 μm quantum dot laser," J. Cryst. Growth 251, 230 (2003).

[Park04] I. Park, I. Fischer, and W. Elsäßer, "Highly nondegenrate four-wave mixing in a tunable dual-mode semiconductor laser," Appl. Phys. Lett. 84, 5189 (2004).

[Paschke10] K. Paschke, P. Q. Liu, A. P. M. Michel, J. Smith, F. Moshary, and C. Gmachl, "Quantum cascade laser for elastic-backscattering LIDAR measurement," CLEO/QELS Conference, JThJ3 (2010).

[Pausch12] J. Pausch, C. Otto, E. Tylaite, N. Majer, E. Scholl, and K. Ludge, "Optically injected quantum dot lasers: Impact of nonlinear carrier lifetimes on frequency-locking dynamics," New J. Physics 14, 053018 (2012).

[Petijean11] Y. Petijean, F. Fabien, J-C, Mollier, and C. Sirtori, "Dynamic modeling of terahertz quantum cascade lasers," IEEE J. Select. Topics Quantum Electron. 17, 22 (2011).

[Peucheret09] C. Peucheret, *Direct and External Modulation of Light*, Technical University of Denmak, 2009.

[Pochet10] M. C. Pochet, *Characterization of the Dynamics of Optically-Injected Nanostructure Lasers*, Ph. D thesis from University of New Mexico, 2010.

[Pochet14] M. Pochet, N. G. Usechak, J. Schmidt, and L. F. Lester, "Modulation response of a long-cavity, gain-levered quantum-dot semiconductor laser," Optics Express 22, 1732 (2014).

[Poole09] P. J. Poole, K. Kaminska, P. Barrios, Z. Lu, and J. Liu, "Growth of InAs/InP-based quantum dots for 1.55 μm laser applications," J. Cryst. Growth 311, 1482 (2009).

[Provost11] J.-G. Provost and F. Grillot, "Measuring the chirp and the linewidth enhancement factor of optoelectronic devices with a Mach-Zehnder interferometer," IEEE Photon. Journal 3, 476 (2011).

[Q]

[QD Laser, Inc., 08] *New era of quantum dot lasers with evolution history of semiconductor lasers,* QD Laser Inc., 2008.

[R]

[Rana02] F. Rana and R. J. Ram, "Current noise and photon noise in quantum cascade lasers," Phys. Rev. B 65, 125313 (2002).

[Raz03] T. Raz, D. Ritter, and G. Bahir, "Formation of InAs self-assembled quantum rings on InP," Appl. Phys. Lett. 82, 1706 (2003).

[Raghuraman93] R. Raghuraman, N. Yu, R. Engelmann, H. Lee, and C. L. Shieh, "Spectral dependence of differential gain, mode shift, and linewidth enhancement factor in a InGaAs-GaAs strained-layer single-quantum-well laser operated under high-injection conditions," IEEE J. Quantum Electron. 29, 69 (1993).

[Reithmaier07] J. P. Reithmaier, G. Eisenstein, and A. Forchel, "InAs/InP quantum-dash lasers and amplifiers," Proc. IEEE 95, 1779 (2007).

[Rickman14] A. Rickman, "The commercialization of silicon photonics," Nature Photonics 8, 579 (2014).

[Rochat98] M. Rochat, J. Faist, M. Beck, U. Oesterle, and M. Ilegems. "Far-infrared (88 μm) electroluminescence in a quantum cascade structure," Appl. Phys. Lett. 73, 3724 (1998).

[Röhm15] A. Röhm, B. Lingnau, and K. Lüdge, "Understanding ground-state quenching in quantum-dot lasers," IEEE J. Quantum Electon. 51, 2000211 (2015).

[S]

[Saito00] H. Saito, K. Nishi, A. Kamei, and S. Sugou "Low chirp observed in directly modulated quantum dot lasers," IEEE Photon. Tech. Lett. 12, 1298 (2000).

[Saito01] H. Saito, K. Nishi, and S. Sugou, "Ground-state lasing at room temperature in long-wavelength InAs quantum-dot lasers on InP(311)B substrates," Appl. Phys. Lett. 78, 267 (2001).

[Saunders94] R. A. Saunders, J. P. King, and I. Hardcastle, "Wideband chirp measurement technique for high bit rate sources," Electron. Lett. 30, 1336 (1994).

[Scamarcio97] G. Scamarcio, F. Capasso, C. Sirtori, J. Faist, A. L. Hutchinson, D. Sivco, and A. Cho, "High-power infrared (8-mircometer wavelength) superlattice laser," Science 276, 773 (1997).

[Schneider02] H. C. Schneider, W. W. Chow, and S. W. Koch, "Anomalous carrier-induced dispersion in quantum-dot active media," Phys. Rev. B 66, 041310(R) (2002).

[Schneider04] H. C. Schneider, W. W. Chow, and S. W. Koch, "Excitation-induced dephasing in semiconductor quantum dots," Phys. Rev. B 70, 235308 (2004).

[Schuh13] K. Schuh, P. Gartner, and F. Jahnke, Combined influence of carrier-phonon and coulomb scattering on the quantum-dot population dynamics, Phys. Rev. B 87, 035301 (2013).

[Sciamanna04] M. Sciamanna, P. Mégret, and M. Blondel, "Hopft bifurcation cascade in small- α laser diodes subject to optical feedback," Phys. Review E 69, 046209 (2004).

[Sciamanna05] M. Sciamanna and K. Panajotov, "Two-mode injection locking in vertical-cavity surface-emitting lasers," Opt. Lett. 30, 2903 (2005).

[Seo02] J. H. Seo, Y. K. Seo, and W. Y. Choi, "Nonlinear distortion suppression in directly modulated distributed feedback lasers by sidemode optical injection locking," Jpn. J. of Appl. Phys. 41, L136 (2002).

[Seraphin65] B. O. Seraphin and N. Bottka, "Franz-Keldysh effect of the refractive index in semiconductors," Phys. Review 139, A560 (1965).

[SHF04] *Broadband Communication signals*, SHF Communication Technologies AG, Germany, 2004

[Sichkovskyi13] V. Sichkovskyi, M. Waniczek, and J. Reithmaier, "High-gain wavelength-stablized 1.55 μm InAs/InP(100) based lasers with reduced number of quantum dot active layers," Appl. Phys. Lett. 102, 221117 (2013).

[Siegel02] P. H. Siegel, "Terahertz technology," IEEE Trans. Microwave Theory Tech. 50, 910 (2002).

[Siegert05] J. Siegert, S. Marcinkevicius, and Q. X. Zhao, "Carrier dynamics in modulation-doped InAs/GaAs quantum dots," Phys. Rev. B 72, 085316 (2005).

[Simos14] H. Simos, A. Bogris, D. Syvridis, and W. Elsaßer, "Intensity noise properties of mid-infrared injection locked quantum cascade lasers: I. Modeling," IEEE J. Quantum Electon. 51, 2000211 (2014).

[Simoyama98] T. Simoyama, H. Kuwatsuka, and H. Ishikawa, "Cavity length dependence of wavelength conversion efficiency of four-wave mixing in λ/4-shifted DFB laser," FUJISU Sci. Tech. J. 34, 235 (1998).

[Simpson95] A. Murakami, K. Kawashima, and T. B. Simpon, and J. M. Liu, "Bandwidth enhancement and broadband noise reduction in injection-locked semiconductor lasers," IEEE photon. Technol. Lett. 7, 709 (1995).

[Simpson97] T. B. Simpson and J. M. Lu, "Enhanced modulation bandwidth in injection-locked semiconductor lasers," IEEE photon. Technol. Lett. 9, 1322 (1997).

[Sirtori94] C. Sirtori, F. Capasso, J. Faist, S. Scandolo, "Nonparabolicity and a sum rule associated with bound-to-bound and bound-to-continuum intersubband transitions in quantum wells," Phys. Rev. B 50, 8663 (1994).
[Sirtori02] C. Sirtori, *Quantum Cascade Laser: Fundamentals and Performances*, Les Ulis, France: EDP Science, 2002.
[Stevens09] B. J. Stevens, D. T. Childs , H. Shahid, and R. A. Hogg, "Direct modulation of excited quantum dot lasers," Appl. Phys. Lett. 95, 061101 (2009).
[Sorin92] W. C. Sorin, K. W. Chang, G. A. Conrad, and P. R. Hernday, "Frequency domain analysis of an optical FM discriminator," J. Lightwave Tech; 10, 787 (1992).
[Su92] C. B. Su, J. Eom, C. William, C. Rideout, H. Lange, C. B. Kim, R. B. Lauer, and J. S. Lacourse, "Characterization of the Dynamics of Semiconductor Lasers using Optical Modulation," IEEE J. Quantum Electron. 28, 118 (1992).
[Su04] H. Su, *Dynamic Properties of Quantum Dot Distributed Feedback Lasers*, Ph. D thsis (New Mexico, 2004).
[Su05] H. Su, H. Li, L. Zhang, Z. Zou A. L. Gray, R. Wang, P. M. Varangis, and L. F. Lester, "Nondegenerate four-wave mixing in quantum dot distributed feedback lasers," IEEE Phonon. Technol. Lett. 17, 1686 (2005).
[Sugawara00] M. Sugawara, K. Mukai, Y. Nakata, and H. Ishikawa, "Effect of homogeneous broadening of optical gain on lasing spectra in self-assembles $In_xGa_{1-x}As/GaAs$ quantum dot lasers," Phys. Rev. B 61, 7595 (2000).
[Sugawara05] M. Sugawara, N. Hatori, M. Ishida, H. Ebe, and Y. Arakawa, "Recent progress in self-assembled quantum-dot optical devices for optical telecommunication: Temperature-insensitive 10 Gbs-1 directly modulated lasers and 40 Gbs-1signal-regenerative amplifiers," J. Phys. D, Appl. Phys. 38, 2126 (2005).
[Sung07] H. K. Sung, E. K. Lau, and M. C. Wu, "Optical single sideband modulation using strong optical injection-locked semiconductor lasers," IEEE Photon. Tech. Lett. 19, 1005 (2007).

[T]

[Takahashi91] T. Takahashi and Y. Arakawa, "Nonlinear gain effects in quantum well, quantum well wire, and quantum well box lasers," IEEE J. Quantum Electron. 27, 1824 (1991).
[Tatham93] M. C. Tatham, G. Sherlock, and L. D. Westbrook, "20-nm optical wavelength conversion using nondegenerate four-wave mixing," IEEE Phonon. Technol. Lett. 5, 1303 (1993).
[Tatham94] M. C. Tatham, X. Gu, L. D. Westbrook, G. Sherlock and D. M. Spirit, "Transmission of 10 Gbit/s directly modulated DFB signals over 200 km standard fibre using mid-span spectral inversion," Electron. Lett. 30, 1335 (1994).
[Taubman04] M. S. Taubman, T. L. Myers, B. D. Cannon, and R. M. Williams, "Frequency stabilization of quantum cascade lasers by use of optical cavities," Spectrochimica Acta Part A 60, 3457 (2004).
[Toba84] H. Toba, Y. Kobayashi, K. Yanagimoto, H. Nagai, and M. Nakahara, "Injection locking technique applied to a 170 km transmission experiment at 445.8 Mbit/s," Electron. Lett. 20, 370 (1984).
[Tredicucci98] A. Tredicucci, F. Capasso, C. Gmachl, D. L. Sivco, A. L. Hutchinson, A. Y. Cho, J. Faist, G. Scamarcio, "High-power inter-miniband lasing in intrinsic superlattices," Appl. Phys. Lett. 72, 2388 (1998).
[Tournié12] E. Tournié and A. N. Baranov, "Advances in semiconductor lasers," Semiconductors and Semimetals 86, 183 (2012).
[Tucker11] R. S. Tucker, "Green optical communications---Part I: Energy limitions in transport," IEEE J. Sel. Top. Quantum Electron. 17, 245 (2011).

[U]

[Uskov97] A. V. Uskov, F. Adler, H. Schweizer, and M. H. Pilkuhn, “Auger carrier relaxation in self-assembled quantum dots by collisions with two-dimensional carriers,” J. Appl. Phys. 81, 7895 (1997).

[Uskov98] A. V. Uskov, J. McInerney, F. Adler, H. Schweizer, and M. H. Pilkuhn, “Auger carrier capture kinetics in self-assembled quantum dot structures,” Appl. Phys. Lett. 72, 58 (1998).

[Uskov04] A. V. Uskov, E. P. O’Reilly, D. McPeake, N. N. Ledentsov, D. Bimberg, and G. Huyet, “Carrier-induced refractive index in quatum dot structures due to transitions from discrete quantum dot levels to continuum states,” Appl. Phys. Lett. 84, 272 (2004).

[Ustinov98] V. Ustinov, A. Zhukov, A. Y. Egorov, A. Kovsh, S. Zaitsev, and N. Y. Gordeev, “Low threshold quantum dot injection laser emitting at 1.9 μm,” Electron. Lett. 34, 670 (1998).

[Ustinov98a] V. Ustinov, A. Kovsh, A. Zhukov, A. Y. Egorov, N. N. Ledentsov, and A. V. Lunev, “Low-threshold quantum-dot injection heterolaser emitting at 1.84 μm ,” Tech. Phys. Lett. 24, 22 (1998).

[V]

[van der Ziel75] J. P. van der Ziel, R. Dingle, R. C. Miller, W. Wiegmann, and W. A. Nordland, “Laser oscillations from quantum states in very thin GaAs-$Al_{0.2}Ga_{0.8}As$ multilayer structures,” Appl. Phys. Lett. 26, 463 (1975).

[Veselinov07] K. Veselinov, F. Grillot, C. Cornet, J. Even, A. Bekiarski, M. Gioannini, and S. Loualiche, “Analysis od the double laser emission occurring in 1.55-μm InAs-InP(113)B quantum-dot lasers,” IEEE J. Quantum Electron. 43, 810 (2007).

[Veselinov08] K. Veselinov, F. Grillot, M. Gioannini, I. Montrosset, E. Homeyer, R. Piron, J. Even, A. Bekiarski, and S. Loualiche, “Lasing spectra of 1.55 μm InAs/InP quantum dot lasers: theoretical analysis and comparison with the experiments,” Opt. Quant. Electron. 40, 227 (2008).

[W]

[Wang01] R. H. Wang, A. Stintz, P. M. Varangis, T. C. Newell, H. Li, K. J. Malloy, and L. F. Lester, “Room-temperature operation of InAs quantum-dash lasers on InP(001),” IEEE Photon. Tech. Lett. 13, 767 (2001).

[Weidmann04] D. Weidmann, F.K. Tittel, T. Aellen, M. Beck, D. Hofstetter, J. Faist, and S. Blaser, “Mid-infrared trace-gas sensing with a quasi-continuous-wave Peltier-cooled distributed feedback quantum cascade laser,” Appl. Phys. B 79, 907 (2004).

[Wentworth93] R. H. Wentworth, “Large-scale longitudinal spatial-hole burning contribution to laser gain compression,” IEEE J. Quantum Electron. 29, 2145 (1993).

[West85] L. C. West and S. J. Eglash, “First observation of an extremely large-diploe infrared transition within the conduction band of a gaas quantum well,” Appl. Phys. Lett. 46, 1156 (1985).

[Wieczorek99] S. Wieczorek, B. Krauskopf, T. B. Simpson, and D. Lenstra, “A unifying view of bifurcations in a semiconductor laser subject to optical injection,” Opt. Comm. 172, 279 (1999).

[Wieczorek02] S. Wieczorek, B. Krauskopf, and D. Lenstra, Multipulse excitability in a semiconductor laser with optical injection, Phys. Rev. Lett. 88, 063901 (2002).

[Wieczorek03] S. Wieczorek, T. B. Simpson, B. Krauskopf, and D. Lenstra, “Bifurcation transitions in an optically injected diode laser: theory and experiment,” Opt. Comm. 215, 125 (2003).

[Wieczorek05] S. Wieczorek, B. Krauskopf, T. B. Simpson, and D. Lenstra, "The dynamical complexity of optically injected semiconductor lasers," Physics Reports 416, 1 (2005).
[Weisbuch91] C. Weisbuch and B. Vinter, *Quantum Semiconductor Structures*, Academic Press, San Diego, CA, 1991.
[Willatzen91] M. Willatzen, A. Uskov, J. Mork, H. Olesen, B. Tromborg, and A. P. Jauho, "Nonlinear gain suppression in semiconductor lasers due to carrier heating," IEEE Photon. Tech. Lett. 3, 606 (1991).
[Wittmann09] A. Wittmann, *High-Performance Quantum Cascade Laser Sources for Spectroscopic Applications,* Ph. D thesis, Zurich, 2009.
[Wu13] Y. C. Wu, R. A. Suris, and L. V. Asryan, "Effect of excited states on the ground-state modulation bandwidth in quantum dot lasers," Appl. Phys. Lett. 102, 191102 (2013).
[Wu14] Y. Wu and L. V. Asryan, "Direct and indirect capture of carriers into the lasing ground state and the light-current characteristics of quantum dot lasers," J. Appl. Phys. 115, 103105 (2014).
[Wysocki05] G. Wysocki, A. A. Kosterev, and F. K. Tittel, "Spectroscopic trace-gas sensor with rapidly scanned wavelengths of a pulsed quantum cascade laser for in situ NO monitoring of industrial exhaust systems," Appl. Phys. B 80, 617 (2005).

[X]

[Xiao13] J. L. Xiao, C. C. Guo, H. M. Ji, P. F. Xu, Q. F. Yao, X. M. Lv, L. X. Zou, H. Long, T. Yang, and Y. Z. Huang, "Measurement of linewidth enhancement factor for 1.3 μm InAs/GaAs quantum dot lasers," IEEE Photon. Tech. Lett. 25, 488 (2013).
[Xu10] P. F. Xu, T. Yang, H. M. Ji, Y. L. Cao, Y. X. Gu, Y. Liu, W. Q. Ma, and Z. G. Wang, "Temperature-dependent modulation characteristics for 1.3 μm InAs/GaAs quantum dot lasers," J. Appl. Phys. 107, 013102 (2010).
[Xu12] P. F. Xu, H. M. Ji, J. L. Xiao, Y. Z. Huang, and T. Yang, "Reduced linewidth enhancement factor due to excited state transition of quantum dot lasers," Optics Lett. 37, 1298 (2012).

[Y]

[Yabre96] G. Yabre, "Effect of relatively strong light injection on the chirp-to-power ratio and the 3 dB bandwidth of directly modulated semiconductor lasers," J. Lightwave Tech. 14, 2367 (1996).
[Yabre00] G. Yabre, H. De Waardt, H. P. A. van den Boom, and G. D. Khoe, "Noise characteristics of single-mode semiconductor lasers under external light injection," IEEE J. Quantum Electron. 36, 385 (2000).
[Yao10] Y. Yao, W. O. Charles, T. Tsai, J. Chen, G. Wysocki, and C. F. Gmachl, "Broadband quantum cascade laser gain medium based on a "continuum-to-bound" active region design," Appl. Phys. Lett. 96, 211106 (2010).
[Yao10a] Y. Yao, X. Wang, J. Fan, and C. F. Gmachl, "High performance "continuum-to-continuum" quantum cascade lasers with a broad gain bandwidth of over 400 cm^{-1}," Appl. Phys. Lett. 97, 081115 (2010).

[Z]

[Zhou08] D. Zhou, R. Piron, F. Grillot, O. Dehaese, E. Homeyer, and M. Dontabactouny, "Study of the characteristics of 1.55 μm quantum dash/dot semiconductor lasers on InP substrate ," Appl. Phys. Lett. 93, 161104 (2008).

[Zhou09] D. Zhou, R. Piron, M. Dontabactouny, O. Dehaese, F. Grillot, and T. Batte, “Low threshold current density of InAs quantum dash laser on InP(100) through optimizing double cap technique,” Appl. Phys. Lett. 94, 081107 (2009).

[Zhukov12] A. Zhukov, M. Maksimov, and A. Kovsh, “Device characteristics of long-wavelength lasers based on self-organized quantum dots,” Semiconductors 46, 1225 (2012).

[Zhukov13] A. E. Zhukov, M. V. Maximov, A. V. Savelyev, Yu. M. Shernyakov, F. I. Zubov, V. V. Korenev, A. Martinez, A. Ramdane, J.-G. Provost, and D. A. Livshits, “Gain compression and its dependence on output power in quantum dot lasers,” J. Appl. Phys. 113, 233103 (2013).

[Zou10] Q. Zou, K. Merghem, S. Azouigui, A. Martinez, A. Accard, N. Chimot, F. Lelarge, and A. Ramdane, “Feedback-resistant p-type doped InAs/InP quantum-dash distributed feedback lasers for isolator-free 10 Gb/s tansmission at 1.55 μm,” Appl. Phys. Lett. 97, 231115 (1010).

Publications

[1] **C. Wang**, M. Osiński, J. Even, and F. Grillot, "Phase-amplitude coupling characteristics in directly modulated quantum dot lasers," Appl. Phys. Lett. 105, 221114 (2014).

[2] **C. Wang**, B. Lingnau, K. Lüdge, J. Even, and F. Grillot, "Enhanced dynamic performance of quantum dot semiconductor lasers operating on the excited state," IEEE J. Quantum Electron. 50, 723 (2014).

[3] **C. Wang,** F. Grillot, F. Y. Lin, I. Aldaya, T. Batte, C. Gosset, E. Decerle, and J. Even, "Nondegenerate four-wave mixing in a dual-mode injection-locked InAs/InP(100) nanostructure laser," IEEE Photon. Journal 6, 1500408 (2014).

[4] **C. Wang**, F. Grillot, V. I. Kovanis, J. D. Bodyfelt, and J. Even, "Modulation properties of optically injection-locked quantum cascade lasers," Opt. Lett. 38, 1975 (2013).

[5] **C. Wang**, F. Grillot, and J. Even, "Analysis of the frequency chirp of self-injected nanostructure semiconductor lasers," IET Optoelectron. 8, 51 (2014).

[6] **C. Wang**, F. Grillot, V. Kovanis, and J. Even, "Rate equation analysis of injection-locked quantum cascade lasers," J. Appl. Phys. 113, 063104 (2013).

[7] **C. Wang**, F. Grillot, and J. Even, "Impacts of wetting layer and excited state on the modulation response of quantum-dot lasers," IEEE J. Quantum Electon. 48, 1144 (2012).

[8] **C. Wang**, J. Even, and F. Grillot, "Near-threshold relaxation dynamics of a quantum dot laser," Proc. of SPIE 9134, 913404 (2014).

[9] F. Grillot, **C. Wang**, N. A. Naderi, and J. Even, "Modulation properties of self-injected quantum-dot semiconductor diode lasers," IEEE J. Sel. Topics in Quantum Electron.19, 1900812 (2013).

[10] I. Aldaya, C. Gosset, **C. Wang**, G. Gampuzano, F. Grillot, and G. Castanon, "Periodic and aperiodic pulse generation using an optically injected DFB laser," Electron. Lett. 51, 280 (2015).

[11] C. Gosset, I. Aldaya, **C. Wang**, H. Huang, X. You, J. Even, G. Campuzano, and F. Grillot, "Self-referenced technique for monitoring and analyzing the non-linear dynamics of semiconductor lasers," Opt. Express 22, 16528 (2014).

[12] **C. Wang**, F. Grillot, V. I. Kovanis, J. D. Bodyfelt, and J. Even, "Rate equation analysis of frequency chirp in optically injection-locked quantum cascade lasers," Proc. of SPIE 8980, 898014 (2014).

[13] **C. Wang**, F. Grillot, I. Aldaya, C. Gosset, T. Batte, E. Decerle, and J. Even, "Nondegenerate four-wave mixing in a dual-mode injection locked InAs/InP(100) quantum dot laser," Proc. of SPIE 8980, 89801K (2014).

[14] **C. Wang**, F. Grillot, and J. Even, "Intensity modulation response of injection-locked quantum cascade lasers," Proc. of SPIE 8619, 86191Q (2013).

[15] **C. Wang**, F. Grillot, and J. Even, "Impacts of carrier capture and relaxation rates on the modulation response of injection-locked quantum dot lasers," Proc. of SPIE 8619, 861908 (2013).

[16] **C. Wang**, F. Grillot, and J. Even, "Carrier escape from ground state and non-zero resonance frequency at low bias powers for semiconductor quantum-dot lasers," Proc. of SPIE 8432, 843225 (2012).

[17] **C. Wang**, M. Gioannini, I. Montrosset, J. Even, and F. Grillot, "Influence of inhomogeneous broadening on the dynamics of quantum dot lasers," Proc. of SPIE 9357 (2015).

[18] **C. Wang**, M. Osiński, J. Even, and F. Grillot, "Modulation-frequency dependent linewidth enhancement factor of quantum dot lasers," Semiconductor and Integrated Optoelectronics (SIOE), Cardiff, Wales, March, 2015.

[19] **C. Wang**, M. E. Chaibi, B. Lingnau, D. Erasme, K. Lüdge, P. Poole, J. G. Provost, J. Even, and F. Grillot, "Phase-amplitude coupling of optically injected nanostructure semiconductor lasers," IEEE Photonics Conference (IPC), San Diego, California USA, October, 2014.

[20] **C. Wang**, M. E. Chaibi, B. Lingnau, D. Erasme, K. Lüdge, P. Poole, J. G. Provost, J. Even, and F. Grillot, "Amplitude modulation and frequency chirp of an injection-locked quantum dash semiconductor laser," IEEE International Semiconductor Laser Conference (ISLC), Palma de Mallorca, Spain, September, 2014.

[21] **C. Wang**, B. Lingnau, E. Schöll, K. Lüdge, J. Even, and F. Grillot, "High performance excited-state nanostructure lasers---modulation response, frequency chirp and linewidth enhancement factor," CLEO: Applications and Technology, San Jose, California, United States, June, 2014.

[22] **C. Wang**, F. Grillot, and J. Even, "Nonlinear dynamics and modulation properties of optically injected quantum cascade lasers," CLEO/Europe, Munich, Germany, May, 2013.

[23] **C. Wang**, F. Grillot, and J. Even, "From basic physical properties of InAs/InP quantum dots to state of the art semi-empirical modelling of 1.55 μm directly modulated QD lasers: an overview," Semiconductor and Integrated Optoelectronics (SIOE), Cardiff, Wales, April, 2013.

[24] **C. Wang**, F. Grillot, and J. Even, "Self-injected quantum dot semiconductor lasers," Semiconductor and Integrated Optoelectronics (SIOE), Cardiff, Wales, April, 2013.

[25] **C. Wang**, F. Grillot, and J. Even, "Controlling the pre-resonance frequency dip in the modulation response of injection-locked quantum dot lasers," Nonlinear Dynamics in Semiconductor Lasers (NDSL), Berlin, Germany, September, 2012.

[26] **C. Wang**, F. Grillot, and J. Even, "Modelling the gain compression effects in semiconductor quantum-dot lasers through a new modulation transfer function," IEEE Photonics Conference (IPC), CA, USA, September, 2012.

[27] **C. Wang**, F. Grillot, and J. Even, "Nouvelle formulation de la function de transfer d'un laser à nanostructures quantiques pour les applications à la modulation haut-debit et aux phenomenes microscopiques non-lineaires," Journées Nationales d'Optique Guidée (JNOG), Lyon, France, July, 2012.

[28] **C. Wang**, F. Grillot, and J. Even, "Modulation response of semiconductor quantum dot lasers," Semiconductor and Integrated Optoelectronics (SIOE), Cardiff, Wales, April, 2012.

[29] **C. Wang**, M. Osiński, K. Schires, J. Even, and F. Grillot, "Modulation-Frequency Dependence of the Phase-Amplitude Coupling in Quantum Dot Lasers," CLEO: Applications and Technology, San Jose, California, United States, May, 2015.

[30] **C. Wang**, M. E. Chabi, H. M. Huang, D. Erasme, P. J. Poole, J. Even, and F. Grillot, "Linewidth enhancement factor in nanostructure semiconductor lasers subject to optical injection," Opt. Express, submitted (2015).

[31] **C. Wang**, K. Shires, M. Osiński, P. J. Poole, J. Even, and F. Grillot, "Threshold discontinuity of the linewidth broadening factor in nanostructure semiconductor lasrs," unpublished (2015).

Résumé

De nos jours, les lasers à semi-conducteurs jouent un rôle crucial dans le domaine dans le développement des communications optiques modernes. L'accroissement exponentiel du trafic de données dans les réseaux optiques est un moteur pour le développement de nouvelles technologies de lasers à semi-conducteurs. Depuis la première démonstration de laser à semi-conducteurs en 1962, les développements ont successivement porté sur les lasers à semi-conducteurs massifs (3D), sur les lasers à puits quantiques (Qwell, 2D) et à fils quantiques (Qwire, 1D), ou sur les lasers à nanostructures quantiques plus avancés tels que les îlots quantiques (Qdot ou Qdash suivant l'anisotropie de la géométrie). Les lasers à îlots quantiques dans la filière InAs/GaAs sont parfaitement adaptés pour la bande O (1260-1360 nm) des communications sur fibres optiques, alors que la filière InAs/InP développée plus récemment, est plus adaptée à la bande C (1530-1565 nm) et aux communications très longues distances.

Par comparaison avec les lasers à puits quantiques, les lasers à îlots quantiques présentent des caractéristiques statiques potentiellement supérieures telles que, de faibles courants de seuil [Liu99], des stabilités en température plus élevées [Mikhrin05], des gains matériaux importants [Maximov04], et des gains différentiels élevés [Bhattacharyya99]. Les îlots quantiques possèdent par ailleurs des niveaux d'énergie quantifiés, que l'on peut représenter de manière simplifiée au niveau composant par un état fondamental (GS) de paires électrons-trous, mais aussi des niveaux excités (ES) et un quasi-continuum d'états qui forme un réservoir de porteurs (RS). Les populations de ces états ainsi que les différents phénomènes de relaxation de porteurs, rendent l'analyse de la dynamique des composants lasers à îlots quantiques plus complexes que dans le cas des lasers à puits quantiques. Par ailleurs, les îlots quantiques obtenus par les approches « bottom-up » et le mode de croissance Stranski-Krastanow, présentent des élargissements inhomogènes des pics d'émission (30-80 meV) liés aux fluctuations de taille des îlots [Bhattacharya00], qui peuvent avoir un impact négatif sur les performances des lasers. Si les lasers à îlots quantiques peuvent potentiellement atteindre des coefficients de couplage phase-amplitude quasi-nul (facteur α) [Saito00], les valeurs expérimentales sont assez dispersées et dépassent même parfois 10 [Dagens05]. Par ailleurs, la bande passante des lasers à îlots modulés reste typiquement inférieure à 10 GHz (si on exclut le cas de l'injection tunnel ou des lasers à dopage p), et donc plus faible que celle des meilleurs lasers à puits quantiques [Bhattacharya00a].

Il est donc de la plus grande importance de caractériser finement la dynamique de ces lasers, et de mieux comprendre les phénomènes physiques à l'œuvre afin de proposer des pistes

d'amélioration. Dans ce but, la première partie de ce travail de thèse se focalise sur la dynamique des lasers à îlots quantiques sur substrats InP, incluant la modulation en amplitude (AM), en fréquence (FM) et les propriétés du facteur α. L'analyse de la dynamique des lasers à îlots quantiques est basée sur un modèle d'équations bilan, dérivé du couplage entre les équations de Bloch optiques et les équations de Maxwell [Chow03], après élimination de la polarisation. Ce modèle prend en compte les populations dans les états RS, ES and GS ainsi que les effets de champ électrique. Pour l'analyse petits-signaux, la dynamique des lasers a été étudiée à l'aide d'un modèle semi-analytique, dérivé de ces équations bilan.

A) Réponse AM

Pour un courant de modulation faible $\delta I(\omega)$ appliqué à un laser à îlots quantiques polarisé en continu, la population de photons induite est représentée par $\delta S(\omega)$. La réponse AM est alors caractérisée par la fonction de transfert:

$$\begin{aligned} H(\omega) &= \delta S(\omega) / \delta I(\omega) \\ &\approx H_1(\omega) H_0(\omega) \\ &= \left(\frac{\omega_R^2}{\omega_R^2 - \omega^2 + j\omega\Gamma} \right) \left(\frac{\omega_{R0}^2}{\omega_{R0}^2 - \omega^2 + j\omega\Gamma_0} \right) \end{aligned} \tag{A.1}$$

où ω_R, Γ sont la fréquence de résonance et le facteur d'amortissement associés à l'interaction entre la population de photons et la population de porteurs dans l'état GS. ω_{R0} et Γ_0 sont des paramètres permettant d'introduire les contributions des états ES et RS.

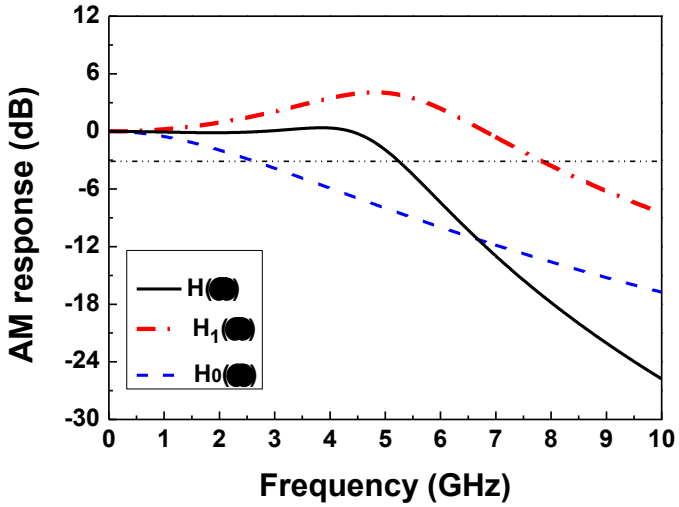

Fig. A.1. Réponse AM d'un laser à îlots quantiques. $H_1(\omega)$ est associé à l'interaction entre la population de photons et la population de porteurs dans l'état GS. $H_0(\omega)$ est attribué aux contributions des états ES et RS.

La figure A.1. montre la réponse AM d'un laser à îlot quantique. Les populations de porteurs des états RS et ES limitent la fonction de transfert à hautes fréquences. Ce résultat est attribué au temps de capture des porteurs de l'état RS vers l'état ES, au temps de relaxation time de l'état ES vers l'état GS et aux effets de remplissage liés au principe de Pauli. De plus, les simulations montrent que la fréquence de résonance et le facteur d'amortissement décroissent linéairement en fonction du temps de capture, alors que la dépendance en fonction du temps de relaxation est plus complexe.

B) Facteur α et chirp

Dans les lasers à semi-conducteurs, le facteur α décrit le couplage entre les variations des parties réelle (indice de réfraction) et imaginaire (gain) de la susceptibilité optique, induites par des variations des populations de porteurs. Ce facteur joue un rôle déterminant pour des propriétés des lasers telles que, la largeur spectrale [Duan90], la dérive de fréquence (« chirp ») [Duan87], la stabilité modale [Agrawal89], la dynamique non-linéaire sous injection optique [Wieczorek02] ou la rétroaction optique [Sciamanna04].

La relation de Kramers-Krönig permet de montrer qu'un élargissement du gain autour de la fréquence de résonance, donne une amplitude de gain plus faible et un spectre d'indice de réfraction étendu. Il est donc nécessaire, pour caractériser le facteur α des lasers à îlots quantiques, de prendre en compte les contributions des populations de porteurs dans les états ES et RS à l'indice de réfraction calculé à la résonance GS. A partir d'une analyse petits signaux, le facteur α à la résonance GS d'un laser à îlots quantiques est donné par la relation:

$$\alpha_{H,QD}^{GS}(\omega)=\frac{2}{\Gamma_P v_g}\frac{\delta\left[\Delta\omega_N^{LS}(N)\right]}{\delta g_{GS}(N)}\equiv\alpha_H^{GS}+\frac{1}{2}F_{ES}\frac{a_{ES}\delta N_{ES}}{a\delta N_{GS}}+2F_{RS}\frac{a_{RS}\delta N_{RS}}{a\delta N_{GS}} \qquad \text{(B.1)}$$

où $\Delta\omega_N^{LS}(N)$ est la déviation en fréquence du champ électrique et $g_{GS}(N)$ le gain optique. α_H^{GS} est la contribution associée aux porteurs dans l'état GS, $a_{ES,RS}$ les gains différentiels pour ES ou RS, et a le gain différentiel à GS incluant l'effet de compression du gain. $\delta N_{GS,ES,RS}$ sont les variations des populations de porteurs pour les différents états associées à la modulation du courant. La fonction $F_{ES,RS}$ incorpore les coefficients de pondération dépendant des écarts énergétiques GS/ES et GS/RS.

A partir de l'Eq. (B.1) et du modèle dynamique, on montre (Fig. B.1) que, contrairement aux lasers à puits quantiques, les lasers à îlots quantiques possèdent un facteur α qui dépend fortement de la fréquence de modulation. Aux faibles fréquences (< 0.1 GHz), le facteur α reste

à peu près constant à une valeur assez élevée (environ 5.5). Lorsqu'on augmente la fréquence de modulation, le facteur α atteint un plateau à 0.8, correspondant aux valeurs mesurées par la technique FM/AM. La figure Fig. B.1 montre aussi que la contribution ES est plus importante que la contribution RS en lien direct avec les valeurs des écarts énergétiques. Des analyses plus poussées montrent ainsi que le facteur α peut être réduit en augmentant ces écarts énergétiques et en favorisant des relaxations plus rapides des porteurs vers l'état GS.

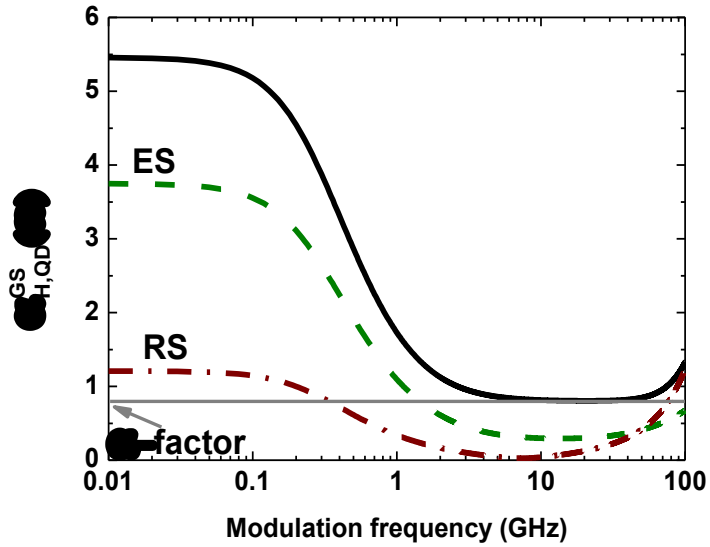

Fig. B.1. Variation du facteur α d'un laser à îlots quantiques en fonction de la fréquence de modulation (trait continu). Les contributions des porteurs dans les états ES (traits discontinus) et RS (traits/pointillés) sont aussi indiquées. La ligne grisée permet de repérer la valeur mesurable par la technique FM/AM.

Comme la modulation des populations de porteurs provoque l'apparition d'une modulation du gain mais aussi de l'indice de réfraction, la longueur effective de la cavité optique subit aussi une modulation ce qui se traduit par une modification de la fréquence de résonance. Ce phénomène de « chirp » en fréquence, couplé à la dispersion chromatique des fibres optiques, provoque une dégradation des signaux au sein des réseaux de fibres optiques. Le « chirp » au sein des lasers à îlots quantiques est caractérisé dans ce travail de thèse par le paramètre CPR (« chirp-to-power ratio ») qui est lié au facteur α selon la relation :

$$CPR(\omega) = \frac{\delta\omega_{LS}(\omega)}{\delta S_{GS}(\omega)} \approx \frac{\alpha_{H,QD}^{GS}(\omega)}{2S_{GS}}\left(j\omega + \Gamma_p v_g a_{GS}^p S_{GS}\right) \qquad \text{(B.2)}$$

où S_{GS} est la densité de photons et $a_{GS}^p = -\partial g_{GS} / \partial S_{GS}$. La figure B.2. montre l'effet du courant de polarisation sur le CPR. En régime adiabatique pour des fréquences de modulation inférieures à 1 GHz, le CPR reste constant (inférieur à 1 GHz/mW) et peu dépendant du courant.

Pour des fréquences plus élevées, le CPR augmente presque de manière parabolique en fonction de la fréquence. De plus, de forts courants de polarisation réduisent le CPR dans ce régime.

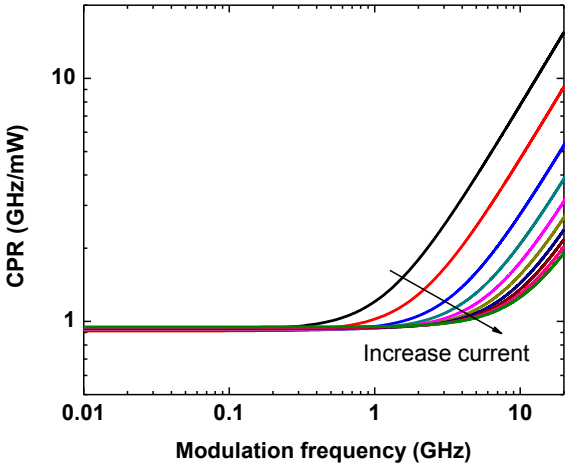

Fig. B.2. CPR d'un laser à îlots quantiques pour différents courants de polarisation de $1.1I_{th}$ à $2.9I_{th}$.

C) Effet laser sur l'état excité ES

L'émission laser sur l'état GS possède des limitations intrinsèques en termes de performances dynamiques, bande passante, facteur α et « chirp » en fréquence. Il est possible de proposer une alternative basée sur un effet laser ES au lieu de GS. Un tel effet laser peut être initié en jouant sur le courant de polarisation, la longueur de cavité, les facettes réflectrices ou en inscrivant un réseau optique [Parantheon03], [Grillot11], [Naderi10]. La figure C.1. présente les performances dynamiques d'un laser à îlots quantiques opérant sur l'état ES, comparées aux performances obtenues sur l'état GS. Si un effet laser ES correspond à un seuil plus élevé (x1.8), cela se traduit par contre par une bande passante plus large, un « chirp » en fréquence et un facteur α plus faibles. La bande passante plus large est due à une saturation du gain plus élevée et à des relaxations plus rapides à partir du réservoir de porteurs. Les performances peuvent être encore améliorées comme le montre le manuscrit par la suite.

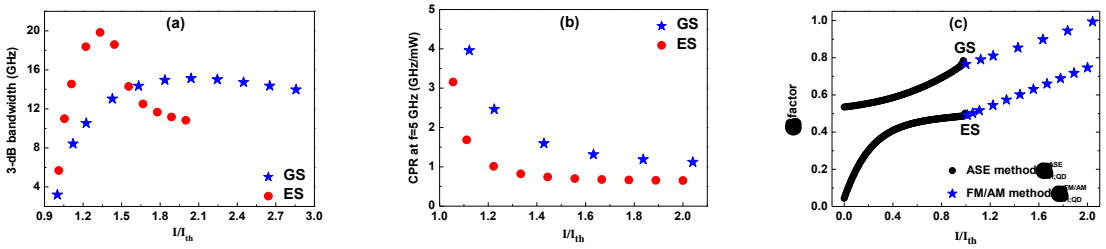

Fig. C.1. Performances dynamiques pour l'émission laser ES (a) bande passante à 3-dB, (b) CPR à la fréquence de modulation de 5 GHz, and (c) facteur α, comparées à l'émission laser GS. Le seuil en courant pour l'émission laser ES est d'environ 90 mA, soit 1.8 fois plus élevé que dans le cas GS.

D) Effets de l'élargissement inhomogène

Des îlots quantiques sont usuellement obtenus grâce au mode de croissance Stranski-Kratanov mode de croissance auto-organisée, qui provoque l'apparition de formes pyramidales ou coniques tronquées [Bimberg98]. La densité surfacique varie entre 10^9 et 10^{12} dots/cm^2. En raison des fluctuations de taille et de géométrie des îlots, le spectre de photoluminescence subit un élargissement inhomogène. L'élargissement inhomogène à température ambiante varie entre 30 et 80 meV [Bhattacharya00]. L'élargissement inhomogène augmente le seuil de courant pour l'effet laser, réduit le gain différentiel, augmente le facteur K, et dégrade donc les performances dynamiques du laser à îlots quantiques. La bande passante est réduite alors que le facteur α-factor et le « chirp » sont augmentés par l'élargissement inhomogène. La figure D.1 montre clairement que l'ouverture du diagramme de l'œil en modulation pour des signaux de grande amplitude est réduite par les effets d'élargissement inhomogène.

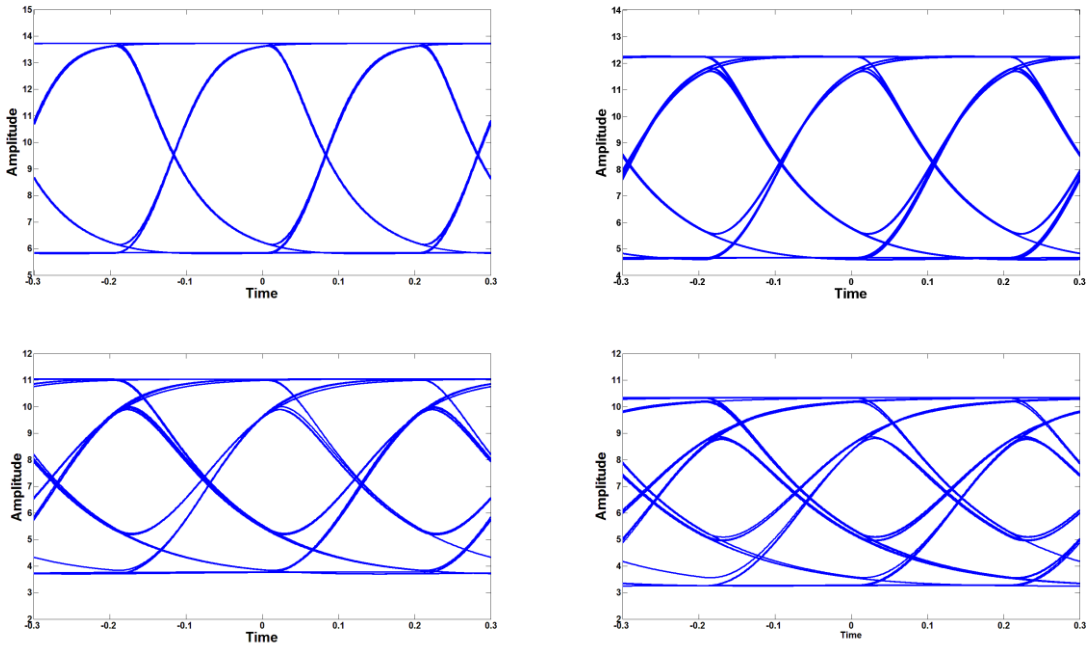

Fig. D.1. Diagramme de l'œil pour différentes valeurs d'élargissement inhomogène: 35 meV (haut à gauche), 45 meV (haut à droite), 55 meV (bas à gauche), 65 meV (bas à droite).

E) Lasers nanostructurés sous injection optique

L'injection optique dans les systèmes de lasers à semi-conducteurs implique deux lasers, un laser « maître » et un laser « esclave ». Le laser « maître » est habituellement un laser accordable monomode de faible largeur spectrale. Le faisceau du laser « maître » est couplé à celui du laser « esclave » étudié que l'on souhaite tester. Les caractéristiques dynamiques du système ainsi créé dépend de deux paramètres cruciaux: le taux d'injection et le désaccord en

fréquence. Le taux d'injection est défini comme le ratio entre la puissance du laser « maître » et celle du laser « esclave » Le désaccord en fréquence est la différence entre la fréquence du laser maître et la fréquence de résonance du laser « esclave ».

Les systèmes de lasers à semi-conducteurs sous injection optique sont connus pour présenter une grande variété de comportements dynamiques incluant : verrouillage stable, bistabilité, oscillations périodiques, dynamique chaotique, et bien d'autres instabilités [Wieczorek05]. Dans le régime de verrouillage stable, la technique d'injection optique peut améliorer de nombreuses performances des lasers à semi-conducteurs : suppression des modes latéraux[Iwashita82], augmentation de la bande passante et des oscillations de relaxation [Murakami03], [Simpson95], chirp en fréquence réduit [Lin84], [Toba84], suppression des distorsions non-linéaires [Meng98], réduction of bruit en intensité [Liu97], [Yabre00], augmentation du gain et amélioration de la modulation [Pochet14] [Sung07].

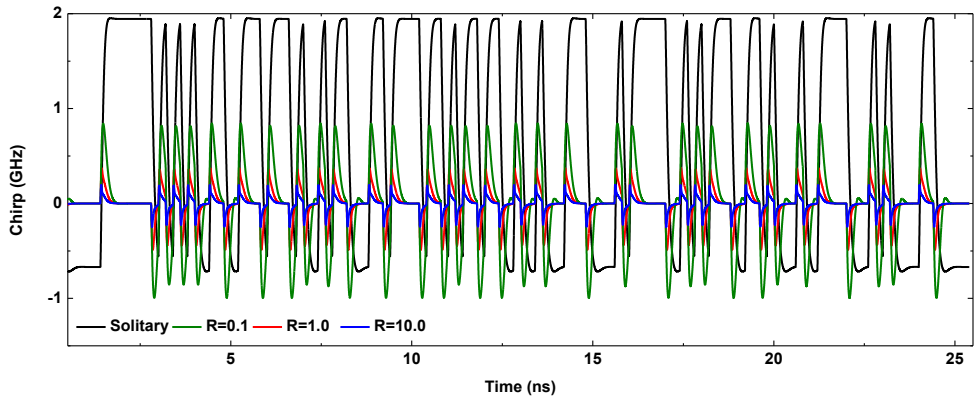

Fig. E.1. Forme du signal de chirp résolu en temps sous injection optique, pour plusieurs valeurs du taux d'injection et à 5.0 Gbps.

Cette partie se focalise plus particulièrement sur l'injection optique dans les lasers à îlots quantiques en verrouillage stable : accroissement de la bande passante, réduction du « chirp » en fréquence, et amélioration des caractéristiques de couplage phase-amplitude. L'injection optique réduit le facteur α dans le régime des faibles fréquences de modulation (<1 GHz), alors qu'elle a un impact plus faible dans le régime des fortes fréquences de modulation. Ce comportement est attribué à la dynamique des populations de porteurs sous injection optique. La figure E.1. montre l'effet de l'injection optique sur la forme du signal de « chirp » résolu en temps. Le « chirp » adiabatique est presque entièrement supprimé sous injection optique et le « chirp » transitoire (« peak-to-peak ») est aussi fortement réduit. De plus, cette analyse des effets de l'injection optique sur la dynamique s'appuie également sur une étude expérimentale.

F) Méthode Hakki-Paoli sous injection optique pour déterminer le facteur α : « Opitcal Injection-Hakki-Paoli method »

L'analyse des effets de l'injection optique basée sur le modèle MPRE (« multi-population rate equation ») [Gioannini06], révèle que l'ensemble du spectre de gain dépend du taux d'injection et du désaccord en fréquence, entrainant une variation concomitante de l'indice de réfraction. Nous avons développé une méthode nouvelle de détermination du facteur α, dénommée « *Optical Injection-Hakki-Paoli* method ». Cette approche est basée sur une polarisation en régime continu (DC), et peut s'appliquer au-dessous et au-dessus du seuil laser. Elle est insensible aux effets thermiques contrairement à la méthode Hakki-Paoli classique qui est de plus applicable seulement sous le seuil.

Dans un laser à semi-conducteurs de type Fabry-Pérot soumis à une injection optique, tous les modes optiques latéraux sont supprimés, contrairement au mode subissant l'injection, la puissance résiduelle étant reportée sous forme d'ASE (« amplified spontaneous emission »). A partir du spectre ASE, les variations du gain and de la longueur d'onde peuvent être reliées au désaccord en fréquence (ou du taux d'injection) à travers le facteur α :

$$\alpha_H = -\frac{2\pi}{L\Delta\lambda}\frac{d\lambda / d\mathrm{F}_{\mathrm{Inj}}}{dg_{net} / d\mathrm{F}_{\mathrm{Inj}}} \qquad \text{(F.1)}$$

où L la longueur de cavité, $\Delta\lambda$ l'écart entre modes longitudinaux, λ est la longueur d'onde du mode optique, g_{net} le gain modal net, et $\mathrm{F}_{\mathrm{Inj}}$ dépend du désaccord en fréquence entre les lasers maitre et esclave.

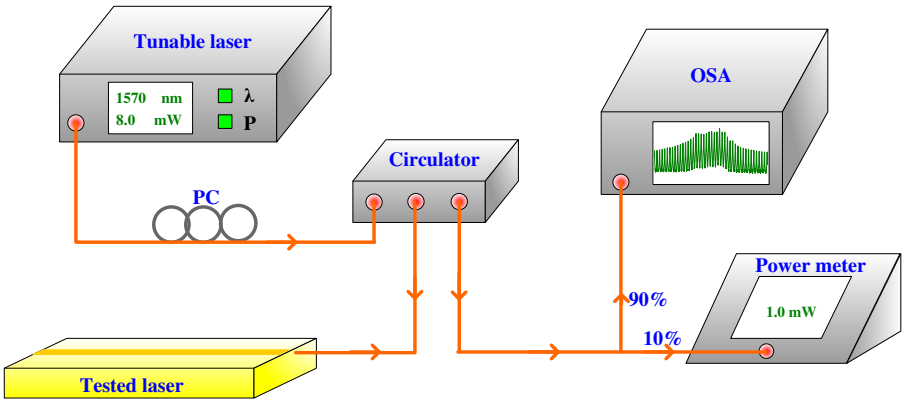

Fig. F.1. Représentation schématique du montage expérimental pour la mesure du facteur α par la méthode « Optical Injection-Hakki-Paoli ». Un laser accordable à cavité externe jouant le rôle du « laser maître» est couplé au laser testé par un circulateur optique. Les spectres optiques du laser testé sont mesurés en régime de verrouillage stable avec désaccords en fréquence positifs ou négatifs. La lumière est collectée et analysée grâce à un OSA de haute résolution (0.01 nm) OSA.

La figure F.1. est une représentation schématique du montage expérimental pour la mesure du facteur α par la méthode « Opitcal Injection-Hakki-Paoli ». Un laser accordable à cavité externe joue le rôle du « laser maître ». Les spectres optiques du laser testé sont mesurés en régime de verrouillage stable avec désaccords en fréquence positifs ou négatifs. A l'aide de ce montage, nous avons testé des lasers à îlots quantiques type Qdot ou Qdash et des lasers à puits quantiques (Fig. F.2).

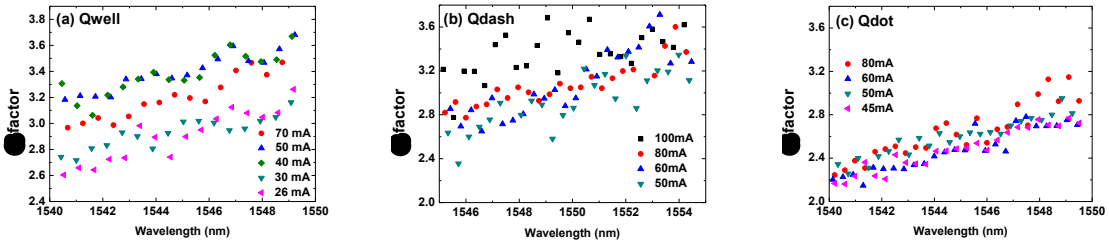

Fig. F.2. Facteur α pour différents courants de polarisation au-dessous et au-dessus du seuil. Au seuil, (a) le facteur α, d'un laser puits quantiques varie continument, alors que, pour un laser (b) Qdash ou (c) Qdot laser, il existe un gap pour le facteur α. Les seuils des lasers Qwell, Qdash, et Qdot sont égaux à 24, 46, et 43 mA, pour des longueurs d'onde de 1545, 1550, 1545 nm, respectivement.

La figure F.2. montre qu'au seuil, (a) le facteur α, d'un laser puits quantiques varie continument, alors que, pour un laser (b) Qdash ou (c) Qdot laser. Les seuils des lasers Qwell, Qdash, et Qdot sont égaux à 24, 46, et 43 mA, pour des longueurs d'onde de 1545, 1550, 1545 nm, respectivement.

G) Dynamique de modulation des lasers à cascades quantiques

Les lasers de type bipolaire analysés dans les parties précédentes, sont basés sur des transitions électroniques inter-bandes au sein d'hétérostructures à semi-conducteurs. Les spectres lasers sont usuellement situés dans le proche infrarouge (NIR, 0.8~3 μm). Il est difficile d'étendre ce concept de lasers aux longueurs d'onde dans le domaine du moyen infrarouge (MIR, 3~30 μm) en raison des gaps électroniques accessibles avec les matériaux semi-conducteurs classiques. Les lasers à cascades quantiques (QC), sont des lasers à semi-conducteurs unipolaires qui dépendent de transitions électroniques intra-bandes, dans la bande de conduction en général [Faist94]. Ce mécanisme particulier permet d'étendre le domaine accessible par effet laser du MIR au domaine Térahertz (THz, 100 μm~1000 μm / 0.3~3 THz). Les lasers QC présentent des potentialités variées pour l'analyse de gas [Weidmann04], l'imagerie térahertz [Hu95], ou les communications en espace libre [Ajili07]. Une autre caractéristique fondamentale des structures lasers QC est le temps de relaxation ultra-rapide des porteurs au sein des structures à la transition (~ 1 ps). Ces deux aspects fondamentaux sont illustrés schématiquement sur la Fig. G.1.

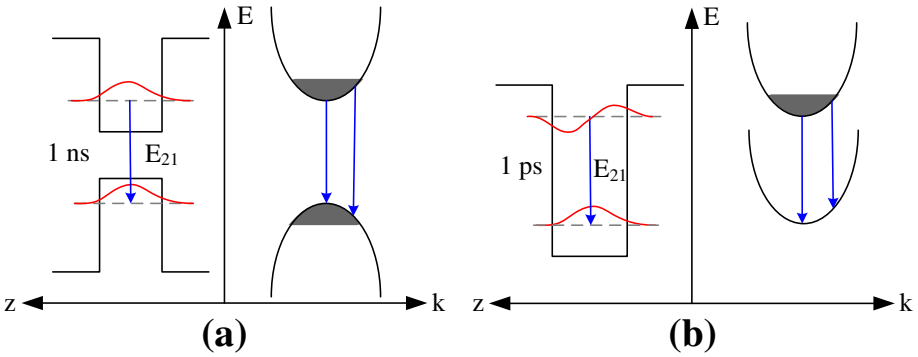

Fig. G.1. Représentation schématique des diagrammes de bandes et dispersions transverses pour des transitions (a) inter-bandes et (b) inter-sousbandes.

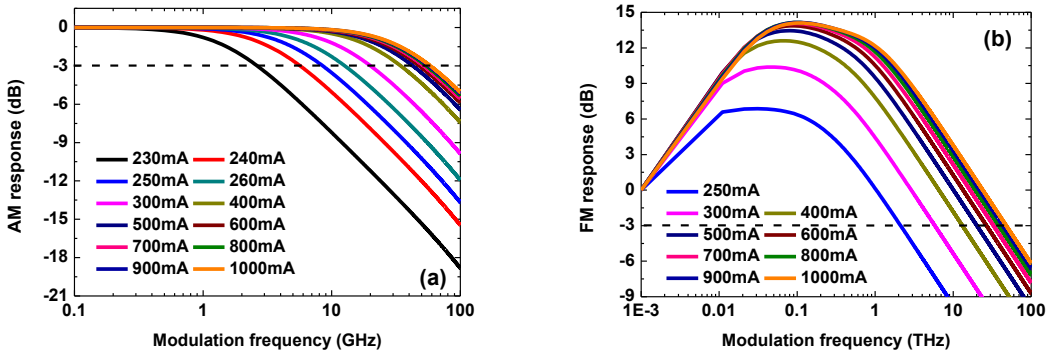

Fig. G.2. (a) Réponse AM et (b) réponse FM d'un laser QC pour différents courants de polarisation. Le seuil laser est égal à 223 mA.

De manière analogue aux lasers basés sur des transitions inter-bandes, nous étudions la dynamique de modulation des lasers QC à partir d'un système d'équations bilan, analysé sous une forme semi-analytique. La figure G.2(a) montre la réponse AM d'un laser QC. La bande passante AM est de l'ordre de quelques dizaines de GHz, un ordre de grandeur supérieur à celle des lasers inter-bandes. Par ailleurs, cette réponse AM ne présente pas de pic de résonance conformément aux résultats expérimentaux [Paiella01]. L'analyse aux valeurs propres montre en effet que les lasers QC ne présentent pas d'oscillations de relaxation. Ce phénomène est attribué aux relaxations très rapides, associées à des temps de vie très courts, plus courts que le temps de vie du photon dans la cavité laser. La figure G.2(b) présente la réponse FM d'un laser QC. De manière surprenante, la bande passante FM est de l'ordre de quelques dizaines de THz, trois ordres de grandeur supérieure à la bande passante AM. Par ailleurs un pic de résonance apparait dans la réponse FM. A partir d'un diagramme de Bode, ce pic est attribué à l'émission spontanée et à la compression du gain. Cependant, le comportement de la réponse FM nécessite des analyses théoriques et expérimentales plus poussées à l'avenir.

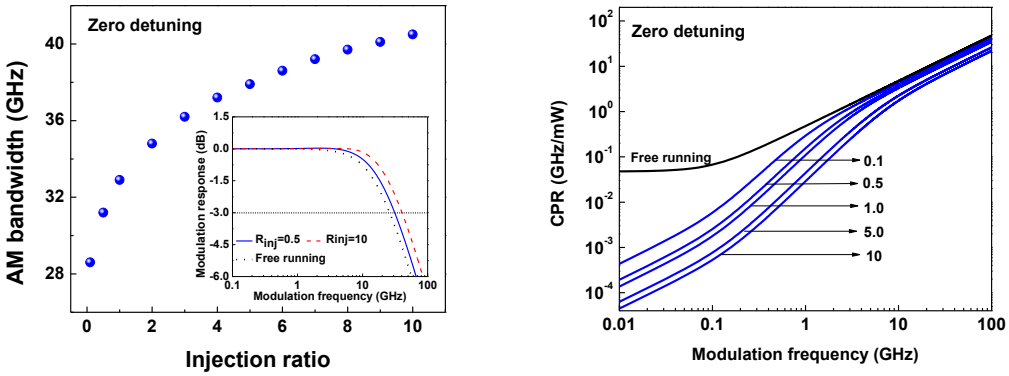

Fig. G.3. (a) Evolutions de la bande passante AM et (b) du CPR d'un laser QC lasers sous injection optique..

Quand un laser inter-sousbandes QC est soumis à une injection optique, la bande passante AM augmente et le CPR est fortement réduit par comparaison avec les lasers inter-bandes (Fig. G.3). Les simulations montrent qu'un désaccord en fréquence positif ou négative augmente la bande passante et exalte le pic de résonance en régime de modulation. Cela indique que les lasers QC, présente eux aussi potentiellement une grande richesse de comportements non-linéaires. Cette dynamique complexe sous injection optique nécessite des investigations plus poussées dans le fur.

INSA de RENNES
Service des Formations

AVIS DU JURY SUR LA REPRODUCTION DE LA THESE SOUTENUE

Titre de la thèse:
Dynamique de modulation de lasers nanostructurés sur subtrat InP et de lasers à cascade quantique

Nom Prénom de l'auteur : WANG CHENG

Membres du jury :
- Monsieur ERASME Didier
- Monsieur EVEN Jacky
- Monsieur SCIAMANNA Marc
- Monsieur DUAN Gang-Hua
- Monsieur OSINSKI Marek
- Madame GIOANNINI Mariangela
- Madame LÜDGE Kathy
- Monsieur GRILLOT Frédéric

Président du jury : D. ERASME

Date de la soutenance : 17 Mars 2015

Reproduction de la these soutenue

Thèse pouvant être reproduite en l'état
~~Thèse pouvant être reproduite après corrections suggérées~~

Fait à Rennes, le 17 Mars 2015

Signature du président de jury

Le Directeur,

M'hamed DRISSI

D. ERASME

Résumé

Le besoin incessant de débits toujours plus élevés dans les systèmes de télécommunications a un impact sur tous les éléments composant la chaine de transmission. Ainsi, pour faire face à l'augmentation croissante du volume de données échangées à travers le monde, le développement de nouvelles sources optiques semi-conductrices est absolument nécessaire. La modulation directe de lasers nanostructurés constitue une alternative bas coût et à faible consommation énergétique qui permettra de remplacer progressivement les diodes lasers à puits quantiques actuelles. De nombreux efforts en recherche ont été consacrés au cours des dernières années en vue d'améliorer les performances dynamiques des lasers nanostructurés notamment en terme de bande passante, de facteur de couplage phase-amplitude (facteur α) et de dérive de fréquence (chirp). Pour les applications aux très grands réseaux et systèmes de communication, la croissance d'îlots ou de fils quantiques déposés sur substrat InP permet de réaliser des dispositifs nanostructurés émettant dans le proche infra-rouge autours de 1550 nm.

Dans ce mémoire, la dynamique de modulation des lasers nanostructuré est étudiée en régime de modulation directe. Les caractéristiques analysées comprennent: la modulation en amplitude (AM) et en fréquence (FM), le chirp, et les réponses en régime grandsignal. Grâce à une approche semi-analytique, il est démontré que la bande passante et l'amortissement sont fortement limités par les phénomènes de capture et de relaxation des porteurs de charge dans les nanostructures. Afin d'étudier les propriétés du facteur α et du chirp, un nouveau modèle dynamique a été proposé, prenant en compte la contribution à l'indice optique des porteurs de charge dans des états hors résonance. Il est ainsi montré que, contrairement au cas des lasers à puits quantiques, le facteur α dépend fortement du courant de pompe et de la fréquence de modulation. Le facteur α reste constant à basses fréquences (<0,1 GHz) et supérieur aux valeurs obtenues à hautes fréquences (au-delà de quelques GHz) à partir de la technique FM/AM. Ces caractéristiques sont essentiellement attribuées aux contributions des porteurs dans les états hors résonance. Les simulations montrent que le facteur α peut être réduit en augmentant la séparation énergétique entre l'état fondamental résonant (GS) et les états hors résonance. En particulier, un effet laser sur 1'état excité des nanostructures (ES) constitue une solution prometteuse pour améliorer les performances dynamiques, en accroissant notamment la bande passante de modulation et en réduisant le facteur α d'environ 40%.

Les techniques d'injection optique sont également intéressantes pour régénérer les performances dynamiques des lasers. Le couplage phase-amplitude et le gain optique y sont substantiellement modifiés via le contrôle de l'amplitude et du désaccord en fréquence du faisceau injecté. Dans ce cadre, ce travail propose une nouvelle technique dérivée de la méthode Hakki-Paoli, permettant de mesurer, sous injection optique, le facteur α à la fois en dessous et au-dessus du seuil.

Les lasers à cascade quantique (QCL) sont basés sur des transitions électroniques inter-sous-bandes dans des hétérostructures à puits quantiques. Ces lasers présentent une bande passante (AM) relativement de quelques dizaines de GHz et sans résonance ce qui est prometteur pour les transmissions en espace libre. De manière surprenante, les calculs montrent que les QCL présentent une largeur de bande FM extrêmement large de l'ordre quelques dizaines de THz, environ trois ordres de grandeur supérieure à la largeur de bande AM. L'injection optique dans ces lasers présente les mêmes avantages que ceux procurés dans les lasers à transitions interbandes. Des désaccords positifs ou négatifs en fréquence augmentent notamment la largeur de la bande passante.

Abstract

High performance semiconductor lasers are strongly demanded in the rapidly increasing optical communication networks. Low dimensional nanostructure lasers are expected to be substitutes of their quantum well (Qwell) counterparts in the next-generation of energy-saving and high-bandwidth telecommunication optical links. Many efforts have been devoted during the past years to achieve nanostructure lasers with broad modulation bandwidth, low frequency chirp, and reduced linewidth enhancement factor. Particularly, 1.55-μm InP-based quantum dash (Qdash)/dot (Qdot) lasers are preferable for long-haul transmissions in contrast to the 1.3-μm laser sources.

In this dissertation, we investigate the dynamic characteristics of InPbased nanostructure semiconductor lasers operating under direct current modulation, including the amplitude (AM) and frequency (FM) modulation responses, the linewidth enhancement factor (also known as α-factor), as well as large-signal modulation responses. Using a semi-analytical analysis of the rate equation model, it is found that the modulation bandwidth of the quantum dot laser is strongly limited by the finite carrier capture and relaxation rates. In order to study the α-factor and chirp properties of the quantum dot laser, we develop an improved rate equation model, which takes into account the contribution of carrier populations in off-resonant states to the refractive index change. It is demonstrated that the α-factor of quantum dot lasers is strongly dependent on the pump current as well as the modulation frequency, in comparison to the case of Qwell lasers. The α-factor remains constant at low modulation frequencies (<0.1 GHz) and higher than the value derived at high modulation frequencies (beyond several GHz) from the FM/AM technique. These unique features are mostly attributed to the carrier populations in off-resonant states. Further simulations show that the α-factor can be reduced by enlarging the energy separation between the resonant ground state (GS) and off-resonant states. Lasing from the excited state (ES) can be a promising alternative to enhance the laser's dynamic performance. The laser exhibits a broader modulation response and the α-factor can be reduced by as much as 40%.

The optical injection technique is attractive to improve the laser's dynamical performance, including bandwidth enhancement and chirp reduction. These are demonstrated both theoretically and experimentally. The phase-amplitude coupling property is altered as well in comparison with the free-running laser and the optical gain depends on the injection strength and the frequency detuning. This work proposes a new method derived from the Hakki-Paoli method, enabling to measure the α-factor of semiconductor lasers under optical injection both below and above threshold. In addition, it is demonstrated theoretically that the α-factor in nanostructure lasers exhibits a threshold discontinuity, which is mainly attributed to the unclamped carrier populations in the off-resonant states. It is a fundamental limitation, preventing the reduction of the α-factor towards zero.

Quantum cascade (QC) lasers rely on intersubband electronic transitions in multi-quantum well heterostructures. QC lasers show flat broadband AM response (tens of GHz) without resonance, which constitutes promising features for free-space communications. Surprisingly, calculations show that the QC laser exhibits an ultrabroad FM bandwidth on the order of tens of THz, about three orders of magnitude larger than the AM bandwidth. Optically injection-locked QC lasers also exhibit specific characteristics by comparison to interband semiconductor lasers. Both positive and negative frequency detunings enhance the modulation bandwidth.

N° d'ordre : 15ISAR 09 / D15 - 09

Institut National des Sciences Appliquées de Rennes
20, Avenue des Buttes de Coësmes • CS 70839 • F-35708 Rennes Cedex 7
Tel : 02 23 23 82 00 - Fax : 02 23 23 83 96